NEW APPROACHES FOR THE STUDY OF DISSOLUTION KINETICS AT THE MICROSCOPIC LEVEL

by

Julie V. Macpherson

A thesis submitted for the degree of Doctor of Philosophy at the University of Warwick

Faculty of Science,
Department of Chemistry,
University of Warwick,
Coventry.
CV4 7AL

September 1996

For my mother without whose support none of this would have been possible

ACKNOWLEDGEMENTS

First and foremost I would like to express my gratitude to Dr. Patrick Unwin, who convinced me as a young undergraduate that electrochemistry would, most definitely, be good for me. His continued support and ever-present enthusiasm and optimism have always been a source of inspiration throughout the course of my studies.

A mention must also be given to the past and present members of the group, all of whom have contributed in some way to the work presented in this thesis. I would like to thank Mark Beeston, who has hence departed to the world of suited scientists, collectively called industrialists, for teaching me the finer qualities of cleanliness in a laboratory. I apologise now for an earlier acknowledgement to Mark which thanked him for proving electrochemistry does not work, I now realise it just takes time. To Rachel Martin ('rashers') thanks are due for keeping me fed during this write-up and aiding me in the understanding of the theory connected with this work. It would be boring to thank Nick Evans for his computing skills but unfortunately it is necessary along with thanks for the enumerate trips to the Coca-Cola machine he has made over the past year. To the last group member thanks are due to Chris Slevin for being very 'laid back' and quiet, in stark contrast to some members of the group, especially during 'thinking' time.

In addition thanks must go to Richard Lissaman for helping out with tricky mathematical problems.

I am eternally grateful to Harry Wiles, Ken Westwood and Norman Horner in the Workshop, Philip Roskelly and Nigel Burgess in Electronics and Alex Stuart the glassblower, for their skill, craftsmanship and willingness to accommodate to the pressures of getting equipment fixed and made yesterday.

Finally I would like to acknowledge the financial support of the EPSRC and NATO. The latter providing me with an opportunity to work at the University of Texas at Austin for one month.

DECLARATION

I hereby declare that the work contained in this thesis is entirely original and my own work, except where otherwise indicated.

Investigation of the dissolution mechanism of the (100) face of KBr, using the integrated electrochemical-atomic force microscope, was carried out at the University of Texas at Austin in collaboration with Dr. Andy Hillier and Prof. Allen J. Bard.

Parts of the work contained in this thesis have been accepted for publication in the scientific literature:

J. V. Macpherson, P. R. Unwin, A. C. Hillier and A. J. Bard, *In-situ* Imaging of Ionic Crystal Dissolution Using an Integrated Electrochemical-AFM Probe, *J. Am. Chem. Soc.*, 118, **1996**, 6445.

J. V. Macpherson and P. R. Unwin, Scanning Electrochemical Microscopy as a Probe of Silver Chloride Dissolution Rates, *J. Phys. Chem.*, 99, **1995**, 14824.

J. V. Macpherson and P. R. Unwin, Scanning Electrochemical Microscope Induced Dissolution: Rate Law and Reaction Rate Imaging for the Dissolution of the (010) Face of Potassium Ferrocyanide Trihydrate in Non-Stoichiometric Aqueous Solutions of the Lattice Ions, *J. Phys. Chem.*, 99, **1995**, 3338.

J. V. Macpherson, M. A. Beeston and P. R. Unwin, Imaging Local Mass Transfer Rates within an Impinging Jet and Studies of Fast Heterogeneous Electron Transfer Kinetics using the Microjet Electrode, *J. Chem. Soc., Faraday Trans.*, 91, **1995**, 899.

J. V. Macpherson and P. R. Unwin, Oscillatory Dissolution of an Ionic Single Crystal Surface Observed with the Scanning Electrochemical Microscope, *J. Phys. Chem.*, 98, **1994**, 3109.

J. V. Macpherson, S. Marcar and P. R. Unwin, Microjet Electrode: A Hydrodynamic Ultramicroelectrode with High Mass Transfer Rates, *Anal. Chem.*, 66, **1994**, 2175.

During the course of this thesis, work was carried out in other areas and the following papers have been accepted for publication in the scientific literature:

J. V. Macpherson, C. J. Slevin and P. R. Unwin, Probing the oxidative Etching Kinetics of Metals with the Feedback Mode of the Scanning Electrochemical Microscope, *J. Chem. Soc., Faraday Trans.*, in press.

P. R. Unwin and J. V. Macpherson, A New Look at Surface Reactions, *Chem. Ind.*, 21, **1995**, 874.

J. V. Macpherson, M. A. Beeston, P. R. Unwin, N. P. Hughes and D. Littlewood, Scanning Electrochemical Microscopy as a Probe of Local Fluid Flow through Porous Solids: Application to the Measurement of Convective Rates through a Single Dentine Tubule, *J. Chem. Soc., Faraday Trans.*, 91, **1995**, 1407.

J. V. Macpherson, M. A. Beeston, P. R. Unwin, N. P. Hughes and D. Littlewood, Scanning Electrochemical Microscopy as a Probe of Local Fluid Flow through Porous Solids: Application to the Measurement of Convective Rates through a Single Dentine Tubule, *J. Chem. Soc., Faraday Trans.*, 91, **1995**, 1407.

J. V. Macpherson and P. R. Unwin, Recent Advances in Kinetic Probes of the Dissolution of Ionic Crystals, *Progr. React. Kinet.*, 20, **1995**, 185.

P. R. Unwin and J. V. Macpherson, New Strategies for Probing Crystal Dissolution Kinetics at the Microscopic Level, *Chem. Soc. Rev.*, 24, **1995**, 109.

ABSTRACT

This thesis is concerned with the development, application and theoretical treatment of the scanning electrochemical microscope (SECM), with the aim of obtaining new insights into the kinetics and mechanisms of ionic crystal dissolution processes. The ultramicroelectrode (UME) probe of the SECM, placed at close distances to the surface of an ionic single crystal face in contact with a saturated solution, was used to induce and monitor the dissolution processes of interest. This was achieved by stepping the potential at the UME from a value at which no electrode reaction occurred to one where a component of the saturated solution was electrolysed at a diffusion-controlled rate. The resulting undersaturation induced the dissolution process and dissolving material, after traversing the tip/substrate gap, was subsequently collected at the UME probe. The current-time behaviour provided quantitative information on the local dissolution rate.

The SECM was successfully used to determine the dissolution characteristics of the (010) face of monoclinic potassium ferrocyanide trihydrate. A second-order dependence on the interfacial undersaturation was found, consistent with the classical Burton, Cabrera and Frank dissolution model. This investigation proved that the SECM was capable of delivering high mass transport rates under well-defined conditions and demonstrated that the dissolution of an unsymmetric salt could be described by classical theories. In addition, through the development of SECM dissolution rate imaging, it was shown that it was possible to map the dissolution activity across single pits in the crystal surface with micrometre resolution.

The kinetics and mechanism controlling the dissolution of silver chloride is a classical system which, despite a number of studies, remains unresolved. SECM studies of the dissolution of pellets and electrochemically grown films of AgCl in aqueous solutions, both in the absence and presence of supporting electrolyte (where the supporting electrolyte does not contain a ion common to AgCl), were carried out and the corresponding mass transfer theories developed. In the latter case dissolution was found to be diffusion-controlled, due to the build up of electroinactive ions in the tip/substrate gap, suppressing the attainment of high interfacial undersaturations. In contrast, in the absence of supporting electrolyte, where the principle of electroneutrality prevented this process, the dissolution kinetics were determined unequivocally.

In order to significantly increase the spatial resolution of electrochemically induced SECM imaging, a new integrated electrochemical-atomic force microscopy (IE-AFM) probe was developed, which simultaneously measured the topography of the surface while electrochemically inducing dissolution under conditions which closely mimicked those of SECM experiments. Using this technique, it was demonstrated, for the first time, that dissolution of an ionic crystal surface (the (100) face of potassium bromide), under conditions of very low interfacial undersaturation, occurred by the dynamic unwinding of steps at the sites of screw dislocations.

Through use of the high spatial resolution and well-defined mass transport characteristics of the SECM, it was possible to determine the dissolution characteristics, in an area of a crystal surface devoid of dislocations and defects, *i.e.* a 'perfect' surface. Studies on the (100) face of copper sulfate pentahydrate demonstrated that dissolution, in low dislocation density areas, occurred via an oscillatory mechanism.

A new hydrodynamic technique, the microjet electrode, was developed and found to be capable of achieving mass transfer coefficients up to 0.82 cm s^{-1}. The ability of the technique to characterise fast surface processes was demonstrated through kinetic studies of the oxidation of ferrocyanide ions at a Pt electrode. Possible modifications to the technique in order to facilitate the characterisation of dissolution processes were considered.

CONTENTS

5. Silver Chloride Dissolution Kinetics In Aqueous Solution With and Without Supporting Electrolyte

CHAPTER 1

INTRODUCTION

This chapter outlines the fundamental processes involved in the dissolution of an ionic solid and the questions which need to be addressed in any mechanistic and kinetic study of the process. A critical review of the different experimental methodologies which have been applied to study the dissolution of ionic solids is given, and the need for new approaches is highlighted. The principles, instrumentation and applications of the scanning electrochemical microscope are described. Techniques based on this device are proposed as new approaches for studying dissolution kinetics, which overcome the limitations of existing methodologies.

1.1 The Nature Of Dissolution Reactions

The dissolution of ionic solids is a fundamental reaction,[1-4] which plays a key role in many natural,[5,6] technological [7] and biological [8] processes. The process of dissolution of an ionic crystal involves the transfer of ions from the surface of the solid material to an undersaturated solution. This process is often represented by a simple chemical equation, for example, the dissolution of a crystal, M_yX_z, in an aqueous solution could be written:

$$M_yX_{z\,(s)} \Leftrightarrow yM^{z+}_{(aq)} + zX^{y-}_{(aq)} \qquad (1.1)$$

Equation (1.1) defines the net result of dissolution, *i.e.* the transfer of ions from a solid M_yX_z to an undersaturated solution, but masks the complexity of dissolution mechanisms.

When a solid dissolves in a liquid, the overall reaction may be represented in terms of some or all of the series of elementary events illustrated schematically in Figure 1.1. The following events are involved: (a) detachment of ions or molecules from a dissolution site; (b) surface diffusion of the detached species; (c) desorption (and adsorption); (d) mass transfer away from the crystal. The latter step is usually the movement of material into the bulk of the solution (by diffusion, convection and perhaps migration) but may also include diffusion through a porous layer at the solid surface. Steps (a) to (c) are surface processes and when any of these steps is slow compared to the transport processes, the dissolution reaction is said to be kinetically *surface controlled.* Conversely, when the surface processes are fast compared to the transport processes, the reaction is termed *transport controlled.*

The picture of dissolution given in Figure 1.1 is further complicated when the nature of a typical crystal is considered in more detail. For many crystalline materials, the morphology is such that a variety of crystal faces are exposed. As generally recognised in surface science, faces of a crystalline material with different arrangements of atoms, ions or molecules (depending on the nature of the material) are often characterised by different reactivities.[9] Furthermore, as illustrated schematically in Figure 1.2, even on a single crystal face there is a considerable variety of defects and surface microstructure, such as steps, terraces, kink sites, vacancies and ad-ions, all of which have characteristic free energies of dissolution.

Additionally, crystals often contain a number of defects which affect the surface properties. These disruptions to the lattice structure usually occur either as a consequence of impurities becoming incorporated into the crystal lattice during the growth process, or as a result of fast imperfect growth of the crystal. The two most common crystal defects are referred to as *screw* and *edge* dislocations[3] and are shown in Figure 1.3. They are line defects which propagate throughout the bulk crystal.

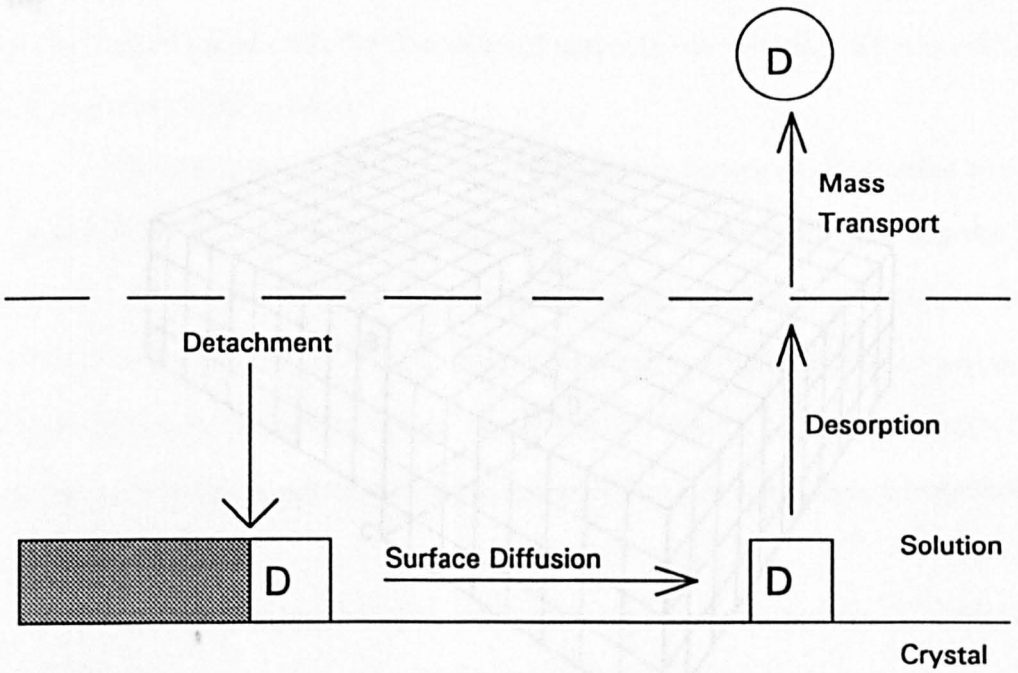

Figure 1.1. Elementary steps involved in dissolution processes. D represents a dissolution unit (ion or molecule).

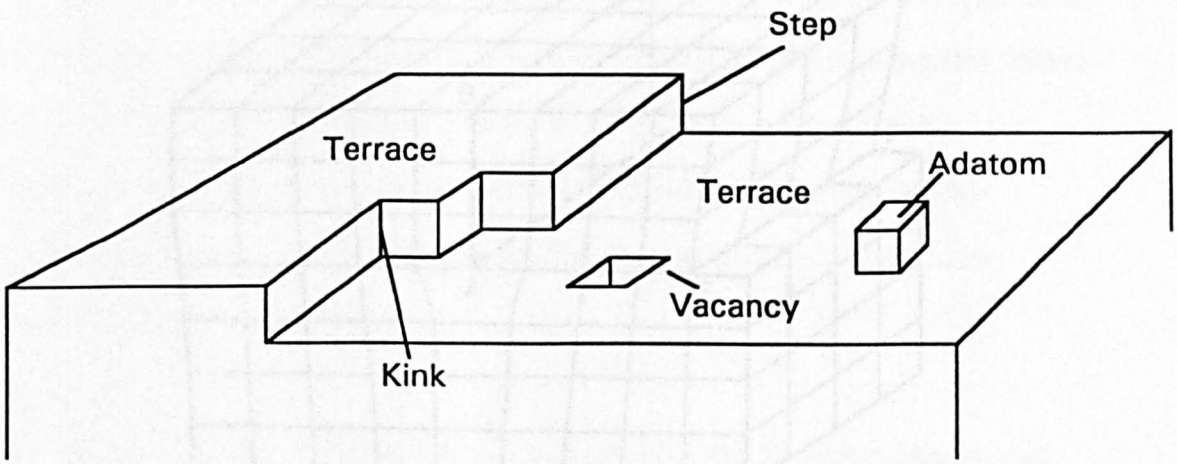

Figure 1.2. Schematic of the typical sites found on the (100) surface of a simple cubic crystal.

(a)

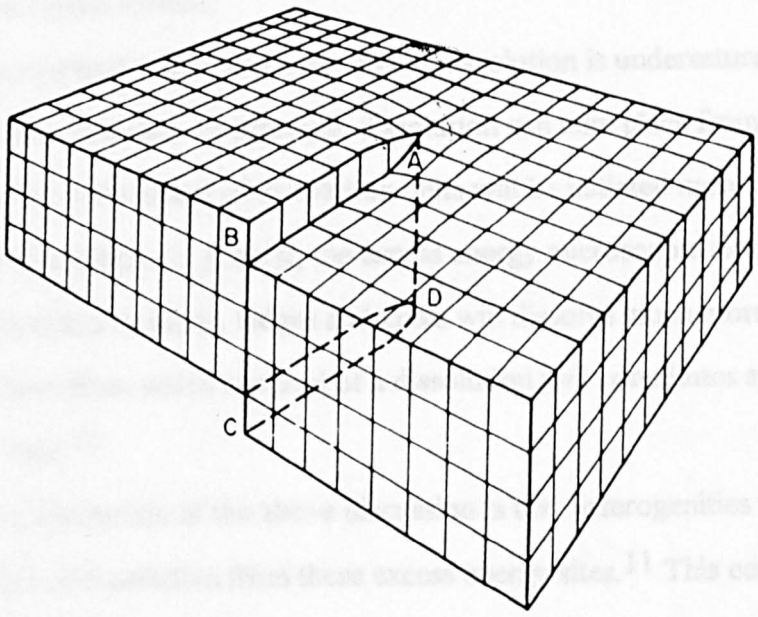

(b)

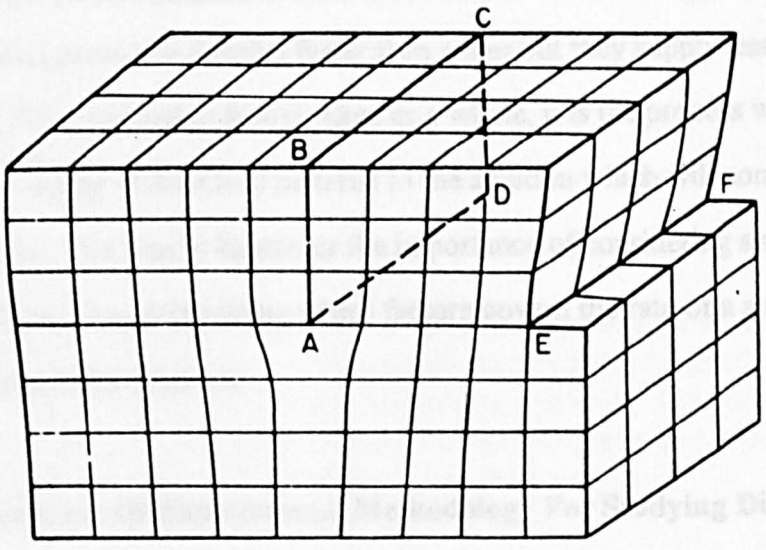

Figure 1.3. Dislocations in a simple cubic lattice: (a) screw-type and (b) edge type.

In both cases the effect is the distortion of lattice layers resulting in the production of steps on the crystal surface.

The thermodynamic force for crystal dissolution is undersaturation at the crystal/solution interface. In principle, dissolution can take place from any site on the crystal, but the detachment of dissolution units will be initiated more quickly from some sites than others. In general, the excess energy microscopic sites, varying from screw dislocations to edges, ledges and kinks will dissolve much more readily than planar surfaces from which removal of a dissolution unit constitutes a very high energy process.[10]

The implication of the above discussion is that heterogenities will exist in the relative rates of dissolution from these excess energy sites.[11] This concept is illustrated in Figure 1.4, which shows a highly schematic representation of the parallel processes involved in crystal dissolution. Even though dissolution proceeds simultaneously from all sites, each of the parallel processes contributes dissolved material to the aqueous solution at different rates and in different quantities. For example, dislocations may dissolve faster than edges but they supply less material to the solution. If the dissolving face is taken as a whole, it is the process which delivers the greatest quantity of dissolved material to the solution which will control the surface kinetics. This clearly illustrates the importance of considering surface structure effects when determining which factors govern the rate of a surface-controlled dissolution reaction.

1.2 An Assessment Of Experimental Methodology For Studying Dissolution Kinetics

In order to evaluate critically the various techniques available for studying dissolution kinetics, it is first necessary to consider the general requirements which must be met by any experimental investigation. It follows from the preceding section

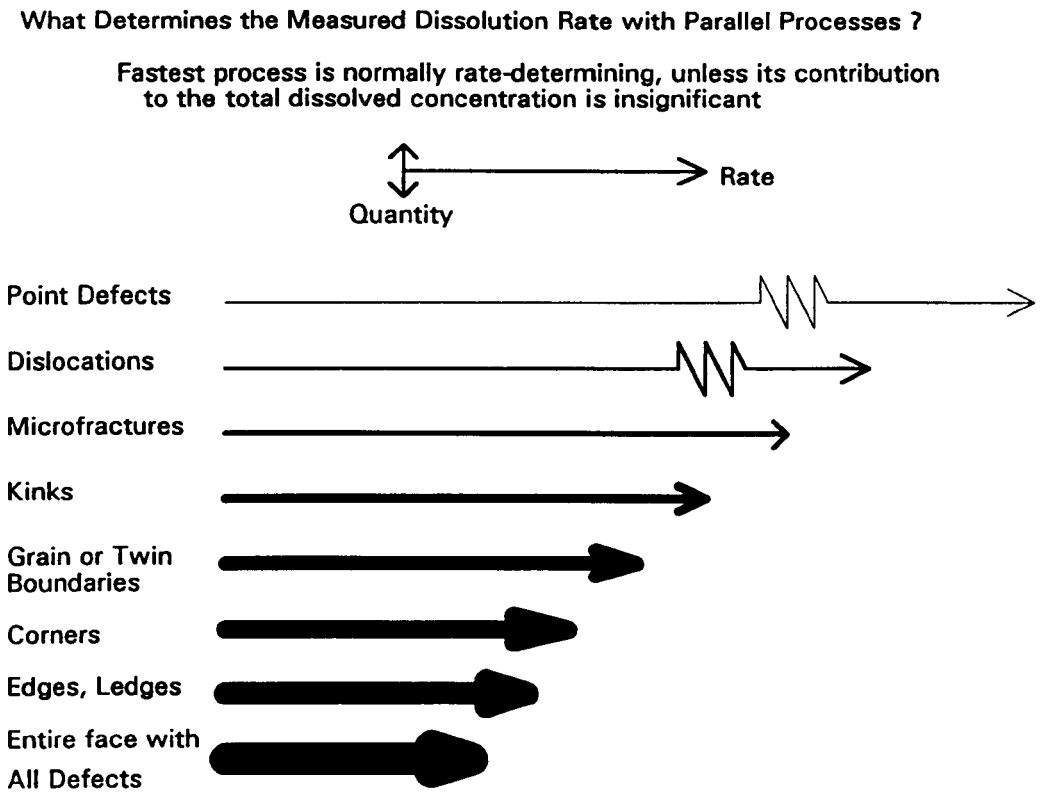

Figure 1.4. Highly schematic illustration of the parallel processes involved in crystal dissolution. The horizontal length of each arrow indicates the relative rate of each process (actual rates can differ by many orders of magnitude). The vertical thickness of each arrow represents the relative quantity of material dissolved and delivered to aqueous solution by that process. Redrawn from reference 11.

that the following questions require answers.

(i) *What is the relationship between surface structure and reactivity?* This includes the ability to study the reactivity of both an individual crystal face and a particular structural feature on a face.

(ii) *What role does local mass transport play in controlling the dissolution rate?* For a particular face (or preferably a specific feature on a crystal face) is the rate controlled by mass transport in solution, or a surface process, or does it proceed under mixed kinetic control? If there are surface kinetic limitations, which surface process limits the rate? It also follows that if fast surface processes are to be characterised, techniques must be able to deliver sufficiently high mass transfer rates to compete with the kinetics of the surface reactions.

(iii) *How does the rate and mechanism depend on local undersaturation at the solid/liquid interface*? This question recognises that the level of undersaturation at the crystal/solution interface provides the driving force for dissolution.

Although there have been a large number of experimental studies of crystal dissolution kinetics, the conventional experimental techniques are: (i) unable to quantitatively address all of the above questions simultaneously and (ii) usually only applicable to sparingly soluble materials. The following section in this introduction provides a comparative critical assessment of the most important techniques currently in use in the dissolution field in order to identify their strengths and weaknesses and to highlight the need for new experimental approaches.

1.2.1 Dissolution methods involving powders

The majority of dissolution studies have employed suspensions of powdered materials.[1,2,12-30] Experimentally, the powder is stirred in an undersaturated solution and the resulting concentration change of the bulk solution, measured as a function of time, enables kinetic and mechanistic information on the dissolution rate

to be inferred. Although this approach allows average dissolution rates to be measured, there are several inherent drawbacks which lead to difficulties in the accurate interpretation of the interfacial kinetics, as discussed below.

Several methods have been used to monitor the dissolution of powders. The two most commonly employed are the free drift method[2] and the constant composition method.[2] In the case of the free drift method, the concentration changes are continuously recorded until the system reaches equilibrium. Both *in-situ* and *ex-situ* detection methods have been used. In the former case these include conductometric,[14,15] pH monitoring[16,17] or radioactive labelling[18] methods. In *ex-situ* detection, aliquots of the solution are removed at periodic intervals, from a batch reactor, and analysed using conventional analytical methods, for example, titrametric methods,[19,20] atomic absorption spectroscopy,[19, 21] photometry[22] or radioactive monitoring.[23] This general approach suffers from the possibility that the composition of the extracted solution may change, with the result that the determination of solution compositions with an accuracy of better than ± 10% is difficult.[24] Other methods have also been utilised in the batch procedure but are not as common, *e.g.* weight loss of the solid material.[25,26] For the constant composition method the activity of a single ion species is controlled and kept constant by titrant addition, while the concentration of other lattice ions are allowed to vary with time. An example of this is the pH stat method,[27-30] pioneered by Nancollas.[31]

The rate of mass transport in particulate systems is varied using stirrers. Stirring has the effect of decreasing the boundary layer thickness surrounding the particles and hence increasing the rate of mass transport. Unfortunately, modelling the relationship between the stirring frequency and the rate of mass transport is difficult in this type of system as mass transport depends on many parameters,[32] including (i) the geometry of the reaction vessel; (ii) type of baffles and stirrer; (iii) speed of stirrer; (iv) slurry density; (v) liquid density and viscosity; (vi) molecular

diffusivity of the diffusing solute; (vii) particle size distribution and geometry and (viii) density of the particles. Consequently, "there is no reliable general correlation of mass transfer coefficients for such systems"[32] and investigating the extent to which mass transfer controls even the average dissolution rates of particles has proved to be difficult.

The importance of mass transport in the rate of heterogeneous reactions has often been determined by investigating the effect of the stirring rate on the reaction rate. A lack of stirring dependence has been taken to imply a lack of transport control in the reaction, *i.e.* that the rate is controlled by a surface process. However, for particulate systems, with poorly defined hydrodynamics, it has been demonstrated that a lack of stirring dependence of the reaction rate may simply mean that the hydrodynamic environment around a particle does not change with stirring speed,[33] as opposed to the dissolution process becoming surface-controlled.

In addition to poorly defined mass transfer, particulate-based experiments suffer from further drawbacks. The concentration of the dissolving species is measured in bulk solution and not at the crystal/solution interface. Under these conditions, the level of undersaturation in the bulk of the solution is often considered to be the driving force for dissolution, rather than at the crystal/solution interface, which is clearly inappropriate. Furthermore, for some types of investigations the batch nature of particulate systems dictates that kinetic measurements are restricted to short times to avoid significant changes in the solution composition. Finally, the use of particles makes it difficult to investigate the effect of surface structure on the dissolution rate and mechanism. In particular, with this approach, it is impossible to study dissolution from a single crystal face or from an individual surface feature.

1.2.2 Techniques incorporating well-defined hydrodynamics

To overcome the problem of ill-defined mass transport, workers have turned to methods which possess well-defined hydrodynamics. These techniques allow mass transport to be varied in a controlled and calculable manner over a wide dynamic range. The advantages and disadvantages of two of the most popular techniques of this type, the rotating disc method[33-53] and the channel flow method with electrochemical detection,[54-63] are assessed in this section.

1.2.2.1 The rotating disc method (RDM)

Although the use of the RDM can be traced back a long way,[64] early experimental work was hampered by a lack of theoretical treatments for convective-diffusive mass transport to a rotating disc. The publication of the solution of the convective-diffusion equation for a transport-controlled process by Levich in 1942,[65,66] has led to the widespread use of the RDM. This is particularly true in the electrochemistry field, where the rotating disc electrode has proved to be a valuable tool for the study of electrode reaction mechanisms and kinetics.[67]

For dissolution experiments, the material of interest is cast flush in the end of a cylinder of inert material (*e.g.* epoxy resin) so that a disc of the solid is exposed in the centre of the cylinder end. The cylinder is attached to a motor which is used to rotate the solid disc about its cylindrical axis of symmetry in a solution. The rate of mass transport of solution species to and from the disc can be controlled by varying the rotation speed. A schematic of the experimental set-up is shown in Figure 1.5.

The dissolution reaction is followed by monitoring the resulting concentration change in bulk solution, which is detected by methods such as those discussed in section 1.2.1 for studies involving powders. Two factors contribute to the increased accuracy of the RDM for elucidating the dissolution kinetics of ionic

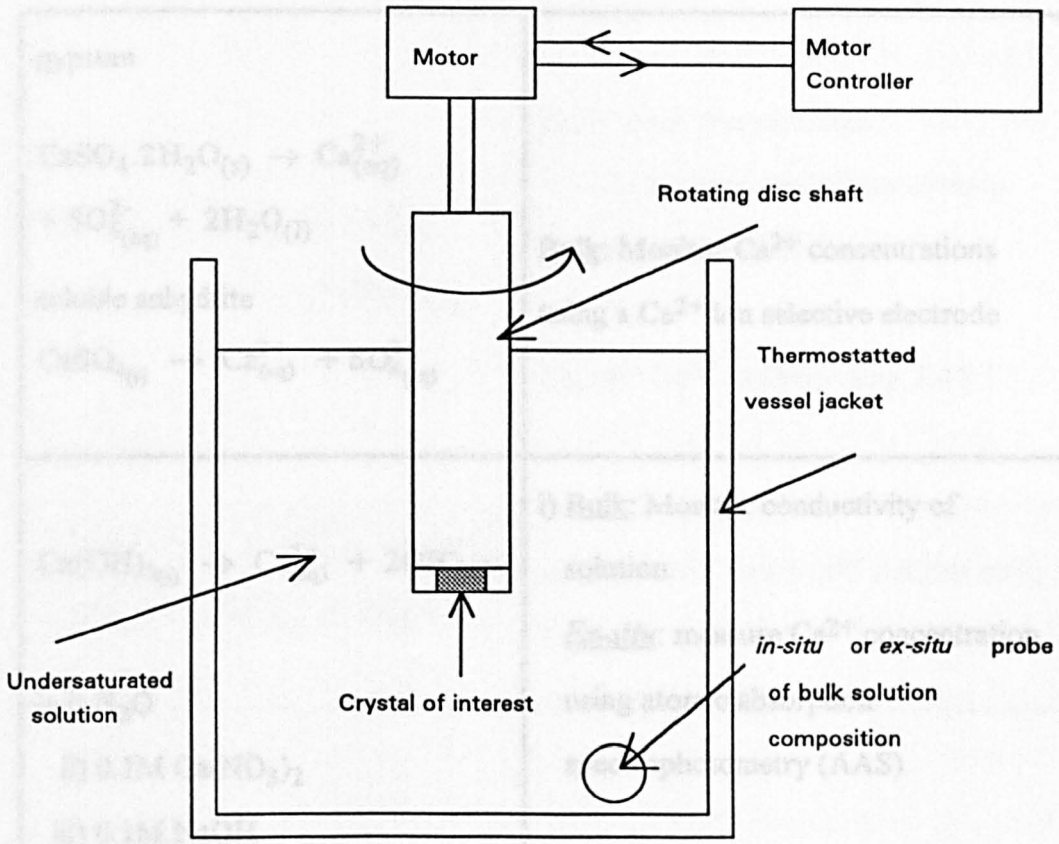

Figure 1.5. Schematic of the rotating disc experimental set-up for investigating dissolution kinetics.

Table 1.1. Dissolution systems studied using the RDM

Chemical system	**Monitoring of reaction**	**Reference**
$KCl_{(s)} \rightarrow K_{(aq)}^{+} + Cl_{(aq)}^{-}$	Bulk: Monitor conductivity of solution	45

gypsum $CaSO_4.2H_2O_{(s)} \rightarrow Ca^{2+}_{(aq)}$ $+ SO^{2-}_{4(aq)} + 2H_2O_{(l)}$ soluble anhydrite $CaSO_{4(s)} \rightarrow Ca^{2+}_{(aq)} + SO^{2-}_{4(aq)}$	Bulk: Monitor Ca^{2+} concentrations using a Ca^{2+} ion selective electrode	68
$Ca(OH)_{2(s)} \rightarrow Ca^{2+}_{(aq)} + 2OH^{-}_{(aq)}$ in i) H_2O ii) 0.1M $Ca(NO_3)_2$ iii) 0.1M NaOH	i) Bulk: Monitor conductivity of solution. *Ex-situ*: measure Ca^{2+} concentration using atomic absorption spectrophotometry (AAS) ii) Bulk: Monitor OH^- concentration using a pH electrode iii) *Ex-situ*: measure Ca^{2+} concentration using AAS	42
$Na_2CO_3.NaHCO_3.2H_2O_{(s)} \rightarrow$ $3Na^{+}_{(aq)} + CO^{2-}_{3(aq)} + HCO^{-}_{3(aq)}$ $+ 2H_2O_{(l)}$	Bulk: Monitor conductivity of solution	69

$CaCO_{3(s)} + H^{+}_{(aq)} \rightarrow Ca^{2+}_{(aq)} + HCO^{-}_{3(aq)}$	Bulk: i) pH stat technique ii) Ca^{2+} ion selective electrode iii) evolution of CO_2 *Ex-situ*: Ca^{2+} analysis using AAS	43, 47, 48 49, 50 70 39
$CaMg(CO_3)_{2(s)} + 4H^{+}_{(aq)} \rightarrow Ca^{2+}_{(aq)} + Mg^{2+}_{(aq)} + 2CO_{2(g)} + 2H_2O_{(l)}$	*Ex-situ*: Ca^{2+} and Mg^{2+} analysis using AAS	37
$BaSO_{4(s)} \rightarrow Ba^{2+}_{(aq)} + SO^{2-}_{4(aq)}$	Bulk: Monitor conductivity of solution	40
$Ca(H_2PO_4)_2.H_2O / CaSO_{4(s)} \rightarrow 2Ca^{2+}_{(aq)} + SO^{2-}_{4(aq)} + 2H_2PO^{-}_{4(aq)} + H_2O_{(l)}$	Bulk: Monitor Ca^{2+} concentrations using a Ca^{2+} ion selective electrode. *Ex-situ*: SO_4^{2-} and PO_4^{3-} analysis using spectrophotometry	71
Dental enamel dissolution at pH 4-5	Bulk: Monitor pH of solution	72

crystals. First, and most crucially, is the fact that the hydrodynamics of the system are well-defined, which allows accurate modelling of mass transport, and second is the ability to study the dissolution kinetics of well-defined crystal surfaces. Table 1.1 provides a summary of some of the dissolution systems which have been studied using rotating disc methodology.

The RDM represents a significant improvement on particulate based methods, in that it allows questions (i) to (iii), outlined in section 1.2, to be addressed at the level of a single crystal face. Moreover, there is the possibility of correlating average rate data with changes in the microtopography of the surface.[53] Disadvantages of this method arise when the detection methods used to probe the temporal changes in chemical composition are considered. As for studies involving particulates, probing concentration changes in bulk solution does not allow interfacial fluxes to be measured directly, and due to the inherent mixing time of the rotating disc system, moderate to high frequency dynamic changes in the interfacial rate are not registered. Moreover, measurements with the rotating disc are often restricted to short times to avoid the build up of dissolution products in the reaction medium.[38,42,47]

Finally, it is useful to identify the range of interfacial kinetics which may be characterised with this technique. In principle, the maximum mass transport rate which can be achieved is limited by one of two factors: (i) the maximum practical rotation speed of the disc (typically 50-100 Hz) and (ii) the critical Reynolds number (Re_{crit}),[73] below which flow is laminar. For practical discs (where the diameter is of the order of 1 cm) the first factor usually limits the mass transport rate. The maximum mass transfer coefficient for the RDM can be estimated from the following equation:[73]

$$k_t = 1.554 D^{2/3} W^{1/2} \upsilon^{-1/6} \qquad (1.2)$$

where k_t is the mass transport coefficient, D is the diffusion coefficient of the species of interest, W is the rotation frequency and υ is the solution viscosity. Assuming a

maximum rotation speed of 100 Hz and typical values of D and υ of 1 x 10^{-5} cm^2 s^{-1} and 1 x 10^{-2} cm^{-2} s^{-1}, respectively, this results in k_t (max.) $\approx$ 1.5 x 10^{-2} cm s^{-1}.

1.2.2.2 Channel flow method with electrochemical detection (CFMED)

1.2.2.2.1 Basic principles

In this method the solid of interest, typically in crystalline form, is located in one wall of a channel (rectangular duct), as shown schematically in Figure 1.6, through which a solution is flowed under laminar conditions. A detector electrode is located immediately downstream of, and adjacent to, the crystal surface. Both amperometric[54-59,63] and potentiometric[60-62] electrodes have been employed. In the former case, the detector is the working electrode in a three-electrode arrangement employed for conventional dynamic electrochemical studies. The electrode is used to measure the concentration of reactant(s) or dissolution products reaching the electrode surface which, in turn, is governed by the kinetics of the dissolution reaction.[54-63] A variation of this geometry incorporates a second (generator) electrode upstream of the solid surface, which can be used to generate reactants which are subsequently collected at the downstream (collector) electrode after passing over the reactive interface of interest. This type of experiment has been used to obtain dynamic information on the adsorption of dissolution inhibitors on crystal surfaces.[74] Mass transport in the CFMED geometry is easily varied by changing the solution velocity, the height of the channel or the length of the reactive interface.

1.2.2.2.2 Applications

The CFMED retains the attractive features of the RDM in that studies may be carried out on a single crystal face[54-63] under conditions where the transport of species to and from the reactive interface (and the detector electrode) is well-

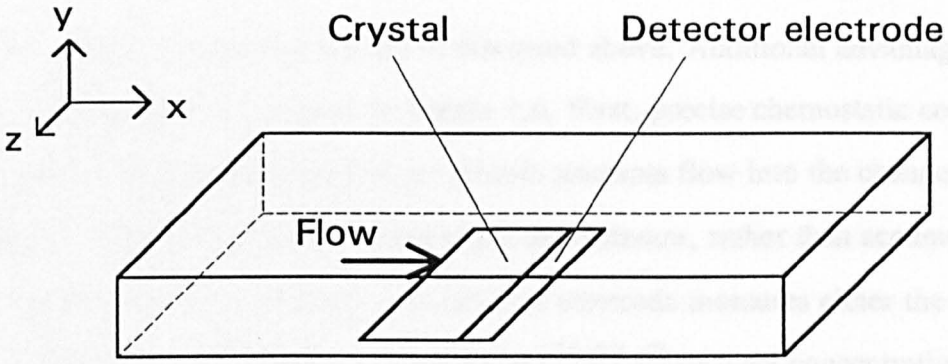

Figure 1.6. Schematic of the channel geometry for dissolution studies using the CFMED.

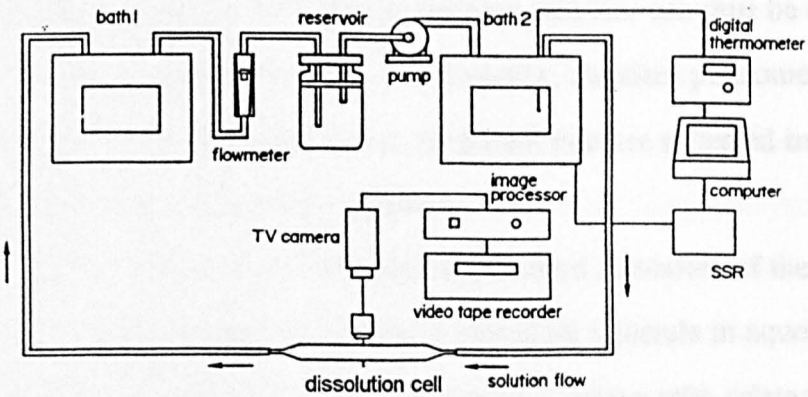

Figure 1.7. Block diagram of the apparatus used by Sunagawa and co-workers, in which the mass transport and surface kinetics can be investigated simultaneously.

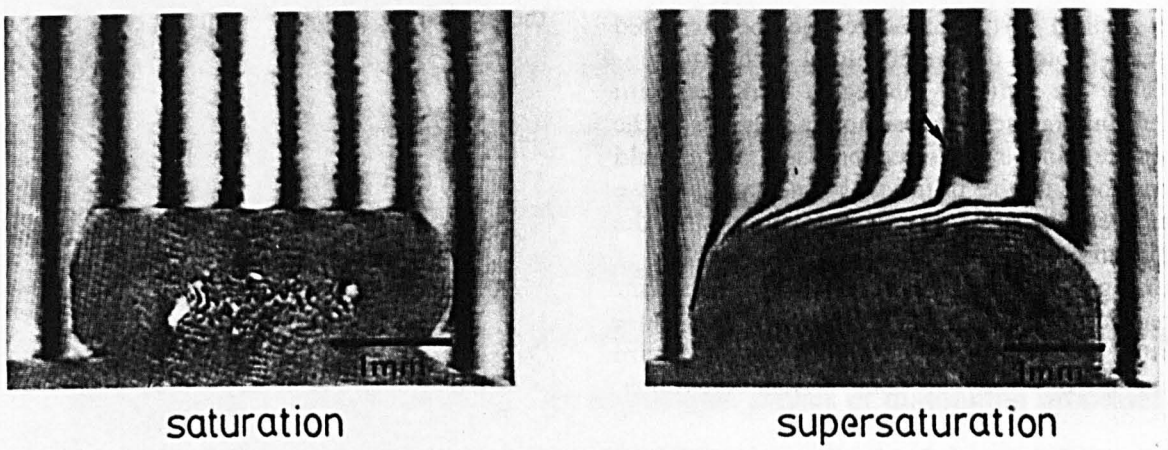

Figure 1.8. Interferometric fringes produced by Mach-Zender interferometry around: left, a crystal surface in a saturated solution; right, a crystal surface in a supersaturated solution.

defined, calculable and controllable, as discussed above. Additional advantages accrue from the geometry shown in Figure 1.6. First, precise chemostatic control of the reaction environment may be exercised: reactants flow into the channel at the upstream end and products flow to waste downstream, rather than accumulate in the reaction medium. Secondly, the detector electrode measures either the local flux (in the case of an amperometric electrode)[54-59,63] or local concentration (in the case of a potentiometric electrode)[60-62] of a target solution species, which can be described in terms of the corresponding flux (and concentration) distribution at the crystal/solution interface.[54-63] The dissolution rate law can thus be deduced in terms of the interfacial undersaturation. Additionally, transient phenomena can readily be identified, since changes in the interfacial rate are reflected in the time-dependence of the detector electrode response.

The CFMED has found considerable application in studies of the kinetics and mechanisms of the dissolution of natural carbonate minerals in aqueous solutions, such as calcite[54,60,61,63] and dolomite,[58] along with related limestones and chalks.[59] The effect of several potential inhibitors, including a range of dicarboxylate anions[55-57] and divalent metal ions[62] has also received attention.

Although CFMED and RDM enable dissolution processes to be characterised under conditions of well-defined hydrodynamics at single crystal surfaces, *ex-situ* microscopy techniques, post experiment, demonstrate that dissolution rates can vary dramatically at the local level,[53,58] but these methodologies are only able to measure the effective (average) dissolution rate of a surface. In this situation, direct *in-situ* microscopic probes of dissolution processes are proving to be extremely valuable, as described in sections 1.2.3 and 1.2.4.

1.2.3 Flow method with *in-situ* interferometry and microscopy

One approach to probing dissolution rates *in-situ* at the microscopic level has been the recent development of an apparatus which can determine directly the concentration gradient at a dissolving crystal surface and monitor, in real time, dissolution (or growth) of a particular surface feature under well-defined transport conditions *i.e.* as an undersaturated solution is flowed over the crystal. Pioneering work in this area has primarily been due to Chernov and co-workers[75-77] and Sunagawa and co-workers.[24,78-84]

The system, as shown schematically in Figure 1.7, consists of a dissolution cell, a reservoir of the solution, a circulation pump, a flowmeter and two thermostatted water baths. The solution runs through the coils of the glass tubes immersed in the water baths so that the temperature of the solution can be easily and precisely controlled. Control of the temperature of the solution is vital as this is used to determine and vary the level of solution undersaturation. A thermistor placed next to the crystal gives an accurate measurement of solution temperature in the dissolution cell. A centrifugal type pump is used to circulate the solution through the cell, with typical mean velocities employed in the range 5 - 40 cm s^{-1}. The dissolution cell is made of rectangular glass tubing (typically 3 x 12 x 250 mm), with two windows so that both reflected and transmitted microscopies can be used. The crystal is glued to the lower window, with the required face exposed to the flowing solution.

In-situ monitoring of the dissolution process is effected through a range of microscopies, typically Mach-Zehnder (MZ) interferometry, polarising light microscopy (PM), differential interference contrast microscopy (DICM), phase contrast microscopy (PCM), phase shift microscopy (PSM), and Michelson interferometry (MI). The images are usually obtained via a CCD camera and are displayed on a TV screen and recorded on a video recorder.

MZ interferometry[85] is used to determine the concentration gradient in the diffusion layer surrounding the dissolving crystal. The concentration gradient results in a refractive index gradient, which is detected as a shift in the spacing between interferometric fringes on moving from the crystal/solution interface to bulk. A typical representative MZ fringe pattern surrounding a growing crystal is shown in Figure 1.8. In this case, the concentration at the crystal surface is lower than in the bulk of the solution, and the corresponding refractive index change causes the optical path of the light to deviate such that the interference fringes bend sharply near the growing face. A similar effect is observed for dissolution, except that because the concentration close to the crystal surface is higher than that in the bulk of the solution, the fringes become wider at the interface. In the MZ system the horizontal light beam passes through the cell in one direction only. This avoids fringe broadening complications, which would arise in this application if alternative interferometric techniques, based on the light beam traversing the cell in two directions, were employed.

Birefringence patterns from PM can be used to locate and characterise dislocations on the crystal surface *in-situ*, provided that the crystal has the appropriate chemical and optical properties. Once these imperfections have been detected and characterised, DICM, PCM, PSM, or MI, can be used to visualise and quantify the *in-situ* development of etch pits, originating from the dislocations of interest, with nanometre vertical resolution. To increase the visibility of these microscopic techniques, an objective lens has been specially designed to reduce the aberration in the observation of a solid surface through a solution layer.[86]

These techniques have recently been used to monitor the formation and expansion of an etch pit, nucleated at a dislocation characterised by a <110> Burgers vector, emerging on the (111) face of potassium aluminium sulfate.[83] As deduced from *ex-situ* microscopy studies of crystal faces dissolved using the RDM,[53] pits

were only nucleated at dislocation sites when the undersaturation in bulk solution, σ_b exceeded a critical value. Below the critical value of the bulk solution undersaturation, the surface undersaturation, σ_s was found to be in close agreement with σ_b, since under these conditions the crystal was effectively inert to dissolution. However, once the critical bulk undersaturation was exceeded, dissolution of material away from the crystal surface resulted in $\sigma_s<\sigma_b$, demonstrating that, in the interpretation of crystal dissolution kinetics, σ_s should never be assumed to be equal to σ_b.

A major question in crystal dissolution and growth is whether the two processes are symmetrically related at the same point on the surface. Both Sunagawa and co-workers[83] and Chernov and co-workers[75,77] have addressed this problem, using the flow system technique which enables both growth and dissolution processes originating from the same dislocation to be observed and quantified. This is achieved by making adjustments to the temperature (and hence under/supersaturation) of the solution flowing through the cell.

The results of these studies confirmed the earlier theoretical predictions of several groups[87-89] which proposed that although the velocity of step propagation should be the same for dissolution and growth, the rate of dissolution normal to the crystal would be much faster than the growth rate, given the same relative interfacial undersaturation/supersaturation. This is because the removal of material from the zone of a stress field around the apex of an emerging dislocation releases strain energy which provides an additional driving force for dissolution. This mechanism does not apply to crystal growth.

The flow method with *in-situ* interferometry and microscopy clearly has a number of attributes which allow questions (i) to (iii) posed in section 1.2, to be directly assessed at the microscopic level. It should be recognised, however, that the surface undersaturation measured by MZ interferometry represents an average value

across the crystal in the direction of the optical light path. In practice, a heterogeneously reactive surface (under conditions of surface control) would lead to a non-uniform interfacial undersaturation, and therefore introduce some error in the estimation of the undersaturation at the part of the interface of interest.

1.2.4 Scanned probe microscopy techniques

The development of scanned probe microscopy (SPM) methods has yielded a wealth of new information on the structure, reactivity and many other properties of surfaces and interfaces at high spatial resolution.[90-94] In the dissolution field, atomic force microscopy,[95,96] is proving to be particularly useful as a direct *in-situ* probe of microscopic kinetics at the micrometre to nanometre level.

1.2.4.1 Atomic force microscopy (AFM)

1.2.4.1.1 Basic principles and applications

AFM[95,96] maps the topography of a surface through a sharp tip (1 - 4 μm in length), typically composed of Si_3N_4 (less commonly used materials include SiO_2 and Si), attached to the end of a cantilever which is approximately 100-200 μm long. The tip is held in close proximity to the surface of a sample (distances range from 100 Å to touching, depending on the mode of operation[97,98]), which is scanned underneath the tip, in a raster pattern, in the *x*, *y* plane. The attractive or repulsive forces experienced by the tip results in a deflection of the cantilever, which can be used to provide a topographical map of the surface. In order to achieve measurable deflections for small force deflections, the material and dimensions of the fabricated cantilever are such that its spring constant is typically less than 1 N/m, compared to the force between atoms which is typically of the order of 10 N/m.[95]

The cantilever deflections are usually detected by a laser beam reflected from the back of the mirrored surface of the cantilever into a position sensing diode

(although several other detection modes[95,99] are available, *e.g.* the interferometric mode[95]). In the constant force imaging mode, a feedback loop is used to keep the force between the tip and the sample constant, and the *z*-element of the piezoelectric positioner adjusts to maintain the reflected beam position constant. Relative displacements of the *z*-axis then trace changes in the height of the surface, which are measured as a function of the relative tip/sample position in the *x*, *y* plane.

The advent of AFM has opened up the possibility of studying topographical changes on dissolving surfaces, in real time, with nanometre resolution. In particular, AFM studies are able to assess directly the validity of classical dissolution models on the atomic scale, such as the Burton, Cabrera and Frank (BCF) model[4] and that developed by Hirth and Pound,[100] which treat the process in terms of the retreat of monatomic steps across a dissolving surface. Although the theories were developed specifically for the growth of metal crystals from the vapour phase, they have been widely applied in the analysis of ionic crystal dissolution and growth.[2,3]

Initial work in this area concentrated on the *ex-situ* imaging of dissolved surfaces.[101] Although sub-nanometre resolution of the structure of these etched surfaces was achieved, in order to obtain *in-situ* dynamic information on dissolution mechanisms, various types of AFM fluid flow cells[102,103] have recently been introduced, such as the one shown schematically in Figure 1.9, which was developed by Hansma and co-workers.[103,104] Imaging a surface under a fluid layer also has the advantage of increasing the resolution capabilities of the AFM, as it reduces the action of capillary forces and screens the effect of van der Waals forces by an order of magnitude.[97] Both factors contribute to strong attractive background forces between the tip and the sample, resulting in uncontrollable tip movements.

The ability to control the rate of fluid flow through the system, either through the use of gravity feed or a pump system, enables the process of crystal dissolution to be observed under surface limiting conditions where local dissolution rates have been

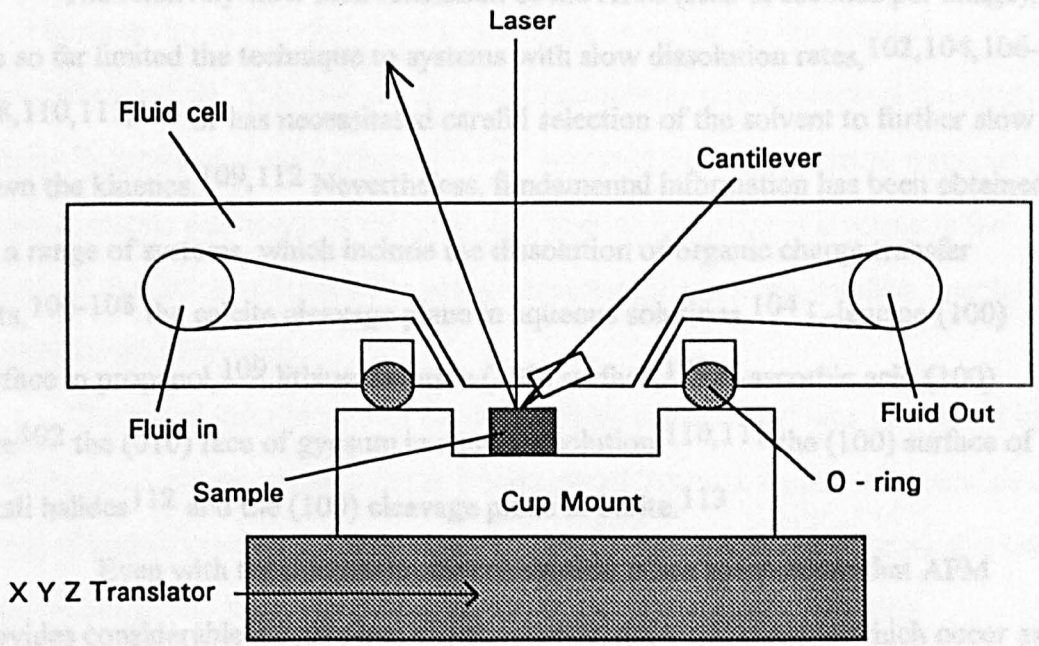

Figure 1.9. Schematic of the AFM fluid flow cell, developed by Hansma and co-workers.[129,132] The fluid volume enclosed by the O-ring is ~ 120 µl.

deduced by measuring the velocity of individual or groups of steps. Distortion of the AFM image, due to the effect of fluid flow in the vicinity of the AFM tip, can limit the values of the flow rate which can be employed. A recent study[105] demonstrated that flow rates up to a maximum of 0.032 cm^3 s^{-1} could be successfully employed to image features on a scale of 10 to 200 nm, without excessive noise, in a typical fluid cell with a diameter of 0.32 cm and a height of 0.11 cm.

The relatively slow time resolution of the AFM (tens of seconds per image), has so far limited the technique to systems with slow dissolution rates,[102,104,106-108,110,111,113] or has necessitated careful selection of the solvent to further slow down the kinetics.[109,112] Nevertheless, fundamental information has been obtained on a range of systems, which include the dissolution of organic charge transfer salts,[106-108] the calcite cleavage plane in aqueous solutions,[104] L-leucine (100) surface in propanol,[109] lithium fluoride (100) surface,[102] L-ascorbic acid (100) face[102] the (010) face of gypsum in aqueous solution,[110,111] the (100) surface of alkali halides[112] and the (100) cleavage plane of barite.[113]

Even with the limited number of studies, it has been shown that AFM provides considerable insights into the nanometre structural changes which occur as a result of dissolution processes. The ability to observe directly step retreat on crystal surfaces, *in-situ*, using flow through techniques, has been invaluable in assessing classical theoretical models which describe dissolution processes, but the nature of mass transport in the vicinity of the tip has not yet been fully studied. In order for AFM to probe dissolution under conditions where local mass transport is well-defined, further work is required on the design of AFM cells and the modelling of mass transport within them. As with all SPM methods, the range of dynamic surface phenomena accessible is governed by the image acquisition time, and the study of faster processes will require developments in instrumentation and imaging techniques.

1.3 The Scanning Electrochemical Microscope

The scanning electrochemical microscope (SECM)[114-118] is one of the new breeds of scanned probe microscopes. Its response is dependent on mass transport between a very small electrode and a sample which, in turn, is governed by chemical reactions occurring at the sample surface. Although the spatial resolution is not as advanced as for AFM[95,96] and scanning tunnelling microscopy (STM),[91-94] crucially the technique can probe both the topography and the reactivity of a surface with a resolution governed by the dimensions of the electrochemical tip. The first use of such electrodes to monitor surface reactivity was by Engstrom and co-workers[119,120] who used the amperometric response of a tiny electrode positioned at different tip/substrate distances to investigate the nature of the diffusion layer at an active macroscopic electrode/solution interface, largely in one dimension.

The actual term 'scanning electrochemical microscopy' was introduced in 1989 by Bard and co-workers at the University of Texas at Austin who published a series of papers describing the instrumentation,[121] theory,[121,122] principles and applications of the technique.[114] Since its introduction, it has provided considerable insights into, and an understanding of, localised surface reactivity at a variety of solid/liquid interfaces ranging from biomaterials,[123-125] polymers[126-131] and minerals[132,133] to electrode surfaces.[119,120,134-136] Ion and electron transfer processes occurring at the liquid/liquid interface[137-139] have also been studied recently.

1.3.1 Basic Principles

The tip employed in the SECM is an ultramicroelectrode (UME)[140-143] *i.e.* one characteristic dimension of the electrode is in the micrometre or sub-micrometre range. Usually the tip is an amperometric electrode,[114-117] although

potentiometric electrodes have also been employed,[116,117] as discussed later in section 1.3.3.7. An amperometric tip acts as the working electrode in a conventional dynamic electrochemical circuit which includes a reference electrode and sometimes an auxiliary electrode, if large currents are to be passed. The probe UME is usually a metal (such as platinum or gold) disc shaped electrode, of typical diameter dimensions 0.1 to 25 μm, which is embedded in an insulating glass sheath. The geometry of the tip (electrode plus insulating glass sheath) is characterised by the value *RG*, where:

$$RG = r_s / a \qquad (1.3)$$

and r_s is the radius of the glass sheath plus the electrode and a is the radius of the electrode. The tip is attached to piezoelectric elements which allow it to be moved and positioned relative to the sample surface in all three cartesian axial directions, with a resolution down to the nanometre level. If the sample to be studied is a conductor or a semiconductor it can be connected as a second electrode through the use of a bipotentiostat.[134-136] Insulating samples are not part of the electrochemical cell circuit and are simply positioned underneath the tip. A schematic diagram of the SECM and the probe UME utilised is shown in Figure 1.10.

The cell must contain an electroactive species (which is termed the mediator) which can be reduced or oxidised at the tip depending on the nature of the experiment. The corresponding current which flows upon electrolysis of the mediator is amplified by a current to voltage converter and measured via a data acquisition card in a personal computer as a function of tip/substrate position and time.[114,121,122]

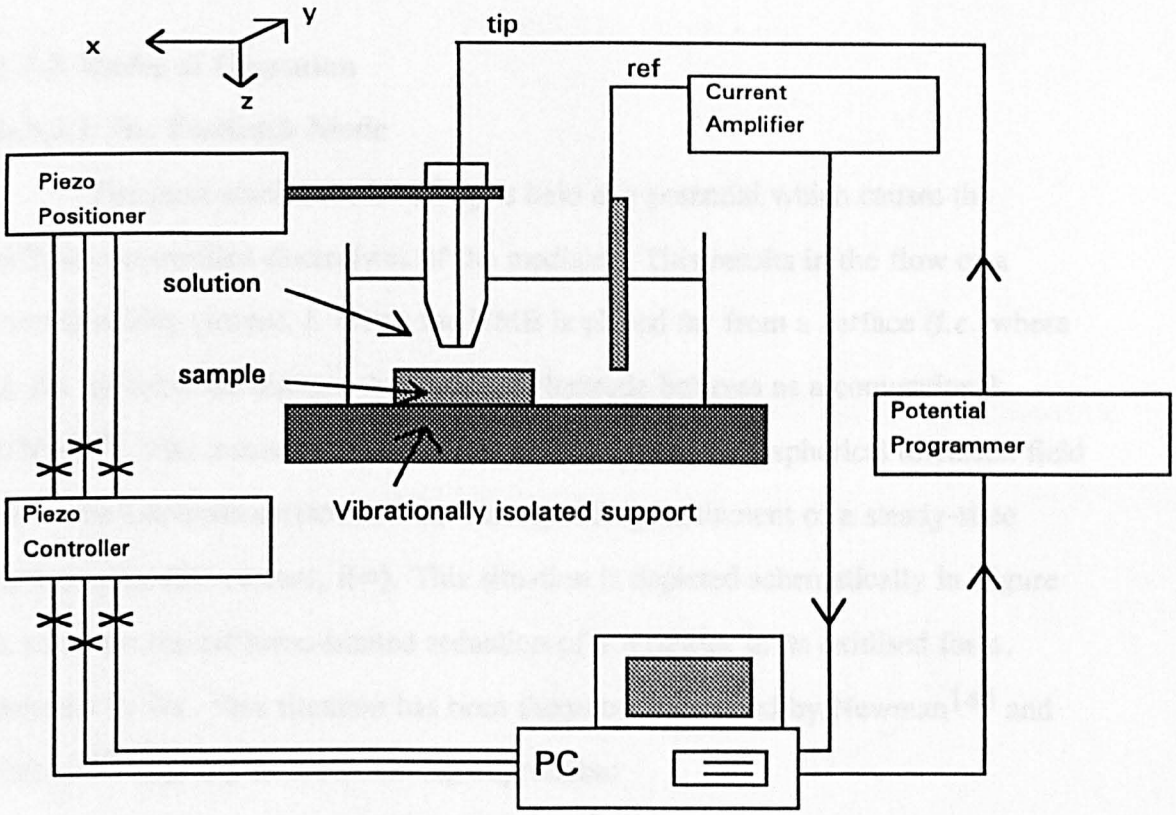

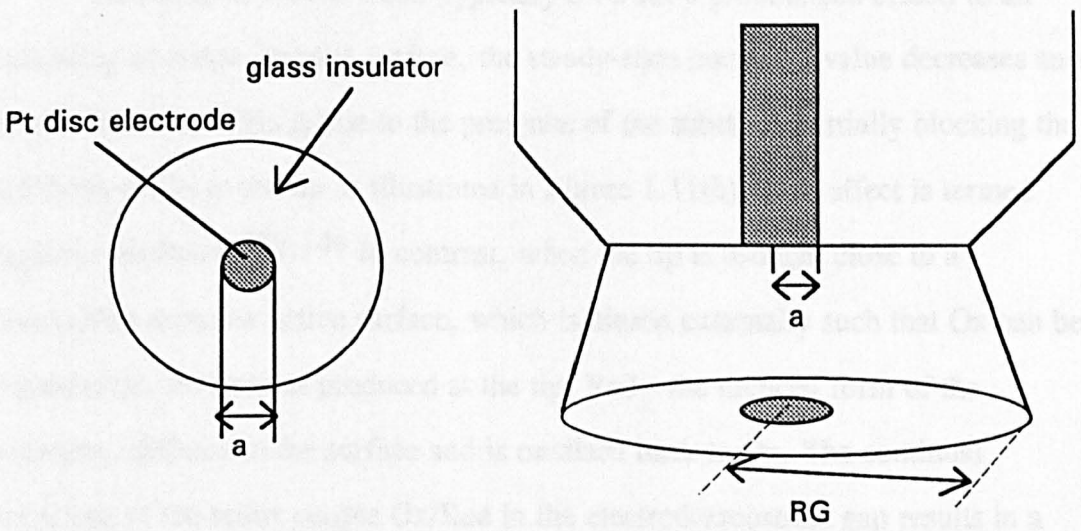

Figure 1.10. Block diagram of the SECM and schematic representation of an UME.

1.3.2 Modes of Operation

1.3.2.1 The Feedback Mode

For most studies the UME tip is held at a potential which causes the diffusion-controlled electrolysis of the mediator. This results in the flow of a corresponding current, i. When the UME is placed far from a surface (*i.e.* where d, the tip/substrate distance $\geq 10\ a$), the electrode behaves as a conventional UME.[144] This results in the establishment of a quasi-hemispherical diffusion field about the electrode surface and the corresponding attainment of a steady-state diffusion-limited current, $i(\infty)$. This situation is depicted schematically in Figure 1.11(a) for the diffusion-limited reduction of a mediator in its oxidised form, denoted by Ox. This situation has been theoretically treated by Newman[144] and Saito,[145] resulting in the following expression:

$$i(\infty) = 4n_eFDac^* \qquad (1.4)$$

where n_e is the number of electrons transferred, F is Faraday's constant and c^* is the bulk concentration of the mediator.

As the tip is moved close (typically $d < a$ for a pronounced effect) to an insulating or redox inactive surface, the steady-state current, i value decreases and is less than $i(\infty)$. This is due to the presence of the substrate partially blocking the diffusion of Ox to the tip as illustrated in Figure 1.11(b). This effect is termed negative feedback.[122,146] In contrast, when the tip is brought close to a conducting or redox active surface, which is biased externally such that Ox can be regenerated, the species produced at the tip, Red - the reduced form of the mediator, diffuses to the surface and is oxidised back to Ox. The continual recycling of the redox couple Ox/Red in the electrode/substrate gap results in a greater flux of Ox to the tip and hence the steady-state current, i is greater than $i(\infty)$. This effect is termed positive feedback[122,146] and is illustrated in Figure 1.11(c). It should be noted that biasing of the conducting surface is not required if

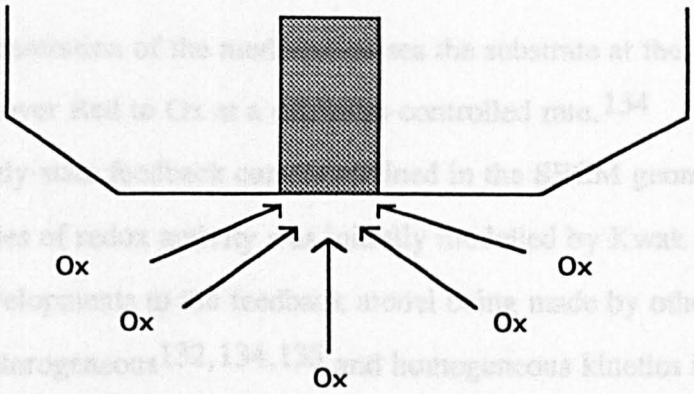

Figure 1.11(a). Hemispherical diffusion to the UME when the tip is positioned far from the substrate's surface.

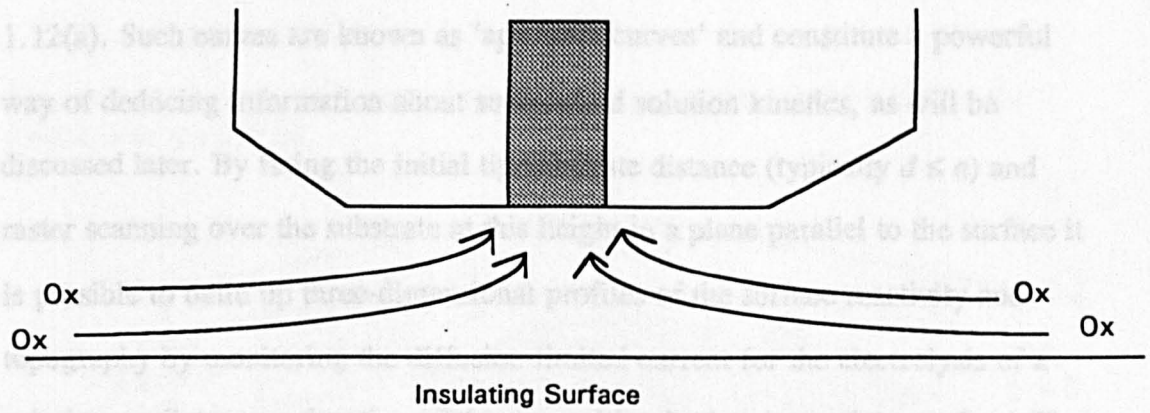

Figure 1.11(b). Hindered diffusion to the UME.

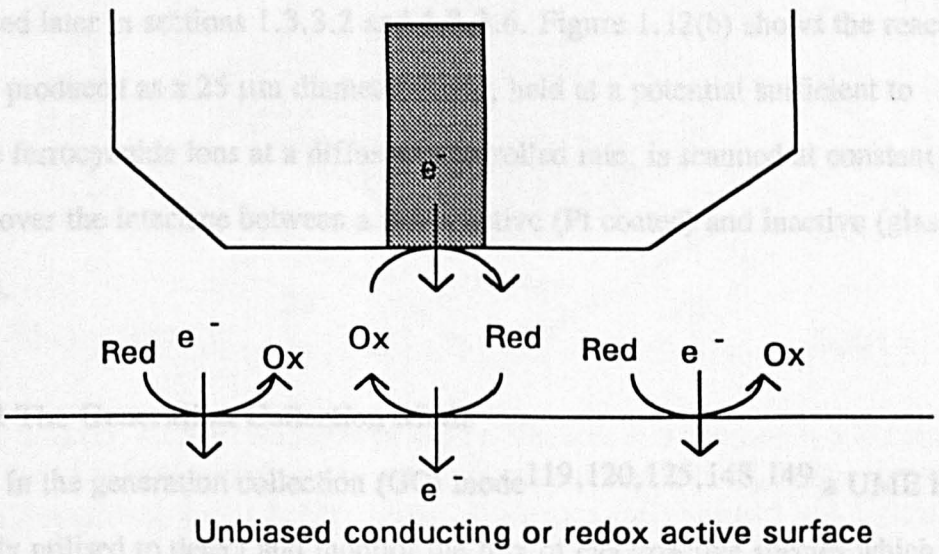

Figure 1.11(c). Feedback diffusion to the UME.

the relative concentration of the mediator poises the substrate at the required potential to turnover Red to Ox at a diffusion-controlled rate.[134]

The steady-state feedback current attained in the SECM geometry for the two extreme cases of redox activity was initially modelled by Kwak *et al*[121,122] with further developments to the feedback model being made by others to include the effects of heterogeneous[132,134,135] and homogeneous kinetics in the system.[147]

At the simplest level, curves of the ratio $i/i(\infty)$ against d, provide a way of distinguishing between conducting and insulating surfaces as illustrated in Figure 1.12(a). Such curves are known as 'approach curves' and constitute a powerful way of deducing information about surface and solution kinetics, as will be discussed later. By fixing the initial tip/substrate distance (typically $d \leq a$) and raster scanning over the substrate at this height in a plane parallel to the surface it is possible to build up three-dimensional profiles of the surface reactivity and topography by monitoring the diffusion-limited current for the electrolysis of a solution mediator as a function of the tip position in the plane of the surface. The use of this technique as a reaction rate or topographical imaging method will be discussed later in sections 1.3.3.2 and 1.3.3.6. Figure 1.12(b) shows the reactivity profile produced as a 25 μm diameter Pt tip, held at a potential sufficient to oxidise ferrocyanide ions at a diffusion-controlled rate, is scanned at constant height over the interface between a redox active (Pt coated) and inactive (glass) surface.

1.3.2.2 The Generation Collection Mode

In the generation collection (GC) mode[119,120,125,148,149] a UME is typically utilised to detect and monitor the flux of electroactive species which have been generated at a much larger substrate positioned directly underneath the tip

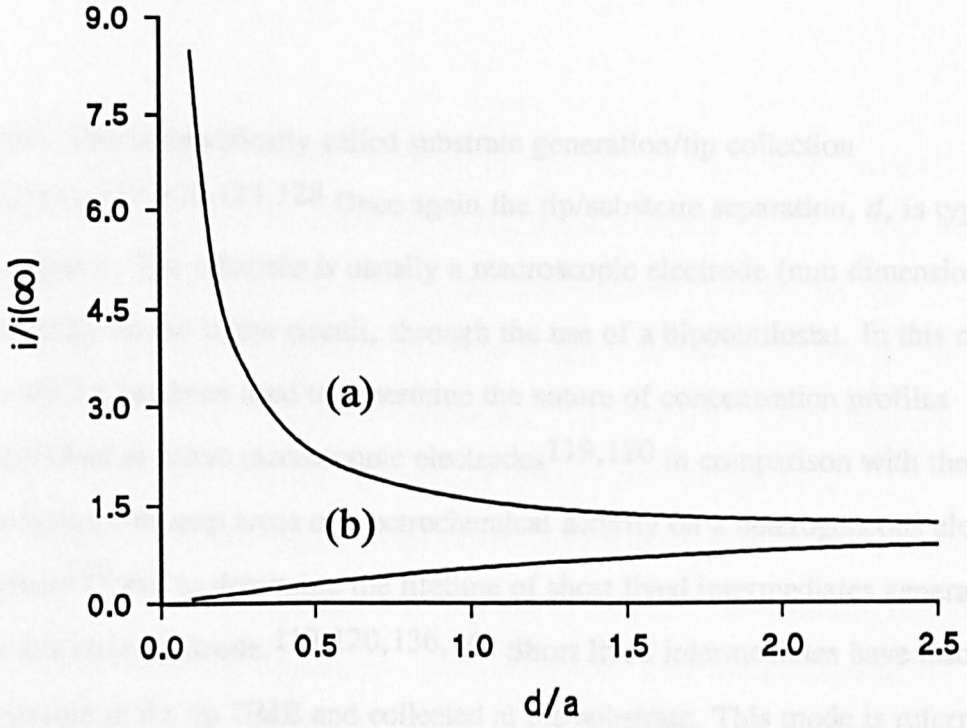

Figure 1.12(a). Approach curves demonstrating positive (a) and negative (b) feedback of the SECM.

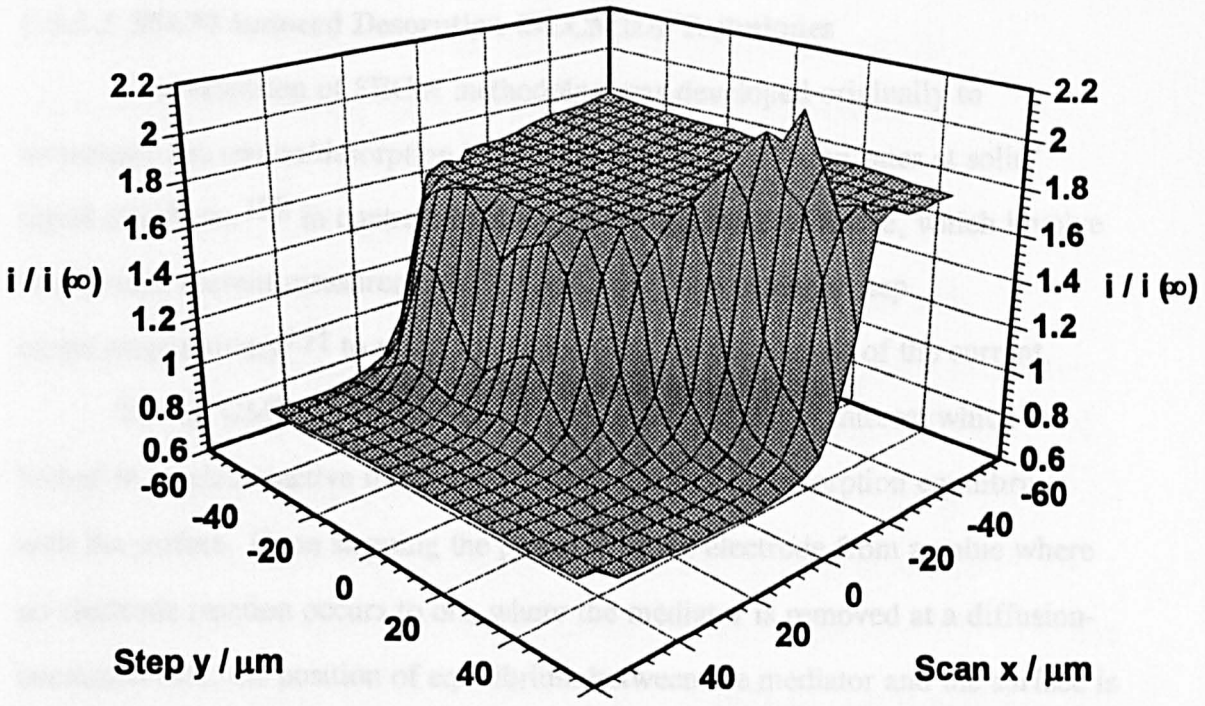

Figure 1.12(b). Current response of the tip UME as it is scanned in a constant *x*, *y* plane, (parallel to the substrate) at a tip/substrate distance of 12.5 µm, across a surface comprising a thin Pt film (redox active area-high current) and a glass film (redox inactive area-low current). Macpherson and Unwin, unpublished results.

UME. This is specifically called substrate generation/tip collection (SG/TC).[119,120,125,128] Once again the tip/substrate separation, d, is typically less than a. The substrate is usually a macroscopic electrode (mm dimensions) externally biased in the circuit, through the use of a bipotentiostat. In this mode, the SECM has been used to determine the nature of concentration profiles established at active macroscopic electrodes[119,120] in comparison with theoretical predictions, to map areas of electrochemical activity on a heterogeneous electrode surface[119] and to determine the lifetime of short lived intermediates generated at the substrate electrode.[119,120,136,141] Short lived intermediates have also been generated at the tip UME and collected at the substrate. This mode is referred to as tip generation/substrate collection (TG/SC).[149,150]

1.3.2.3 SECM Induced Desorption (SECMID) Techniques

This extension of SECM methodolgy was developed originally to investigate adsorption/desorption kinetics and surface diffusion rates at solid/liquid interfaces.[132] In contrast to many of the applications above, which involve steady-state current measurements SECMID employs potential step chronoamperometry[151] to make time dependent measurements of the current.

The tip UME is placed close ($d < a$) to the surface of interest which is bathed in an electroactive mediator which establishes an adsorption equilibrium with the surface. Upon stepping the potential at the electrode from a value where no electrode reaction occurs to one where the mediator is removed at a diffusion-controlled rate, the position of equilibrium between the mediator and the surface is perturbed. In order to requilibrate, desorption from the solid/liquid interface must occur, which is reflected in an enhanced diffusion-controlled tip current, chronoamperometrically monitored at the UME.

This concept can be illustrated by considering the adsorption of H^+ on TiO_2,[132] the principles of which are illustrated in Figure 1.13. A potential step is applied to the tip electrode which is positioned above the substrate, at a fixed distance, such that the electrolysis of the solution component of the adsorbate, in this case H^+ to H_2 is diffusion-controlled. The consequent decrease in the concentration of H^+ in the tip/substrate domain both perturbs the adsorption/desorption equilibrium, which induces desorption of H^+ from the TiO_2 surface, and promotes diffusion of H^+ through solution into the gap region. Moreover because the desorption process depletes the concentration of H^+ on the substrate surface directly under the tip, surface diffusion can also provide a path for the transport of H^+ into the gap domain if the surface diffusion coefficient is sufficiently high. The flux of protons at the tip UME, and hence resulting current-time behaviour, is a measure of the rates of these three processes: (i) adsorption/desorption; (ii) surface diffusion and (iii) solution diffusion.

1.3.3 Applications of SECM Methodology

Through the use of these different modes of operation, and both potentiometric and amperometric UMEs, the SECM has been applied extensively to (i) the determination of surface[123,134,135,152-154] and solution[120,147-150] kinetics (ii) the fabrication[155-158] and modification[159-165] of metallic and semiconductor surfaces (iii) imaging and quantifying transport processes[166-172] across porous surfaces and biomaterials and (iv) the topographical[114,173-175] and reactivity rate imaging[119,124,125,133,176,177] of surfaces. These studies (i) - (iv) involve processes which occur at or across the solid/liquid interface for a wide range of surfaces, ranging from electrodes to biological materials.

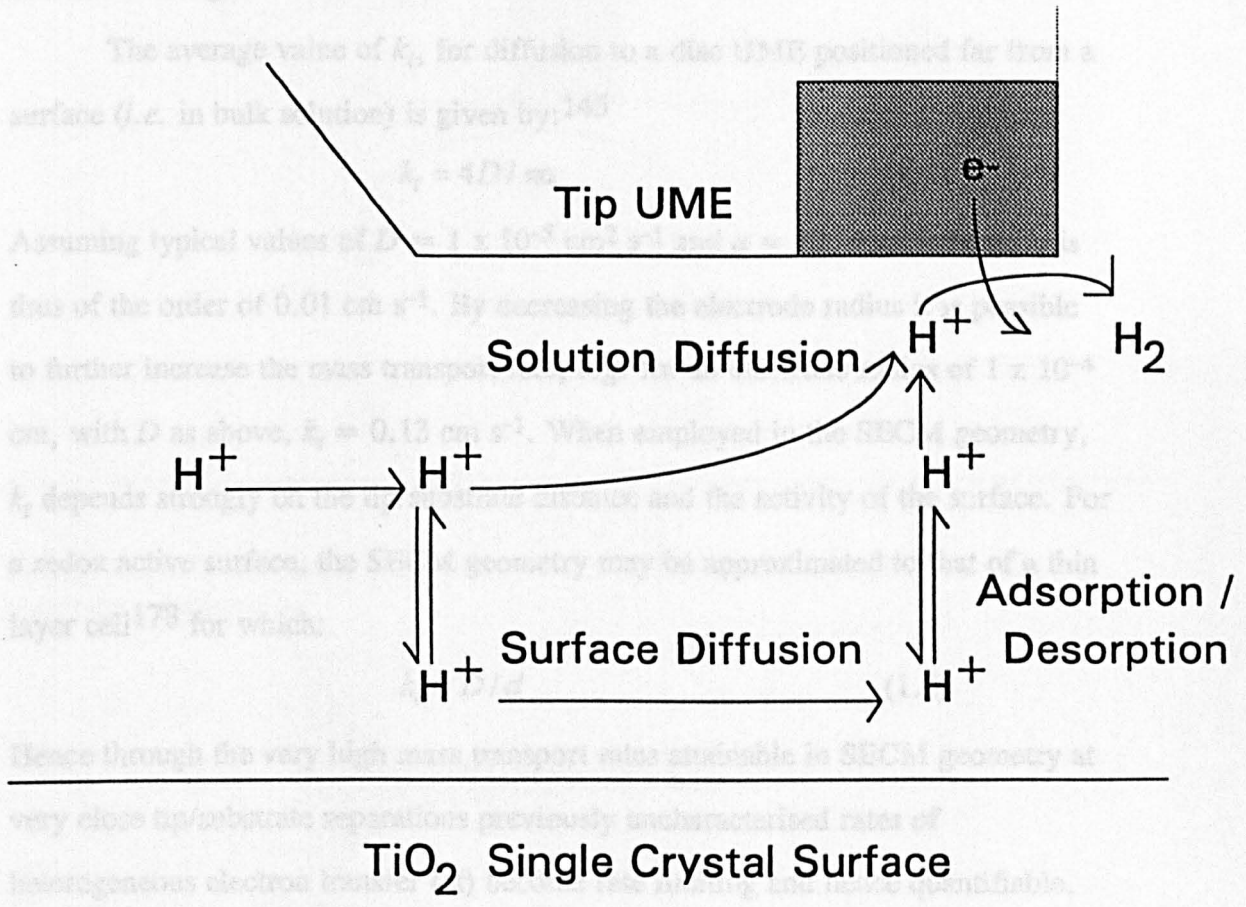

Figure 1.13. Principles of SECMID, showing schematically transport processes in the tip/substrate domain.

1.3.3.1 The Study and Quantification of Heterogeneous Electron Transfer Processes using SECM

The average value of k_t, for diffusion to a disc UME positioned far from a surface (*i.e.* in bulk solution) is given by:[145]

$$k_t = 4D / \pi a \qquad (1.5)$$

Assuming typical values of D = 1 x 10^{-5} cm^2 s^{-1} and a = 12. 5 x 10^{-4} cm, k_t is thus of the order of 0.01 cm s^{-1}. By decreasing the electrode radius it is possible to further increase the mass transport rate, *e.g.* for an electrode radius of 1 x 10^{-4} cm, with D as above, k_t = 0.13 cm s^{-1}. When employed in the SECM geometry, k_t depends strongly on the tip/substrate distance and the activity of the surface. For a redox active surface, the SECM geometry may be approximated to that of a thin layer cell[178] for which:

$$k_t \approx D / d \qquad (1.6)$$

Hence through the very high mass transport rates attainable in SECM geometry at very close tip/substrate separations previously uncharacterised rates of heterogeneous electron transfer (et) become rate limiting and hence quantifiable.

Initial work in this area was initiated by Wipf and Bard[134] who investigated the effect of the heterogeneous et rate at a substrate on the tip current using the feedback mode. A schematic model defining this system is given in Figure 1.14(a). In this application the substrate is generally a second working electrode, $k_{f,t}$ is a potential dependent rate constant for the tip reaction, $k_{b,s}$ is a rate constant for electrolysis (in the schematic: oxidation) at the substrate and $k_{f,s}$ is a rate constant for reduction at the substrate. The magnitude of the rate constant for the tip electrode reaction $k_{f,t}$ is such that the reduction of Ox to Red occurs at a diffusion-controlled rate. $k_{b,s}$ and $k_{f,s}$ are equated to the standard rate constant of the et process and the substrate potential by the Butler-Volmer equation.[134]

The above system was illustrated experimentally through studies in which

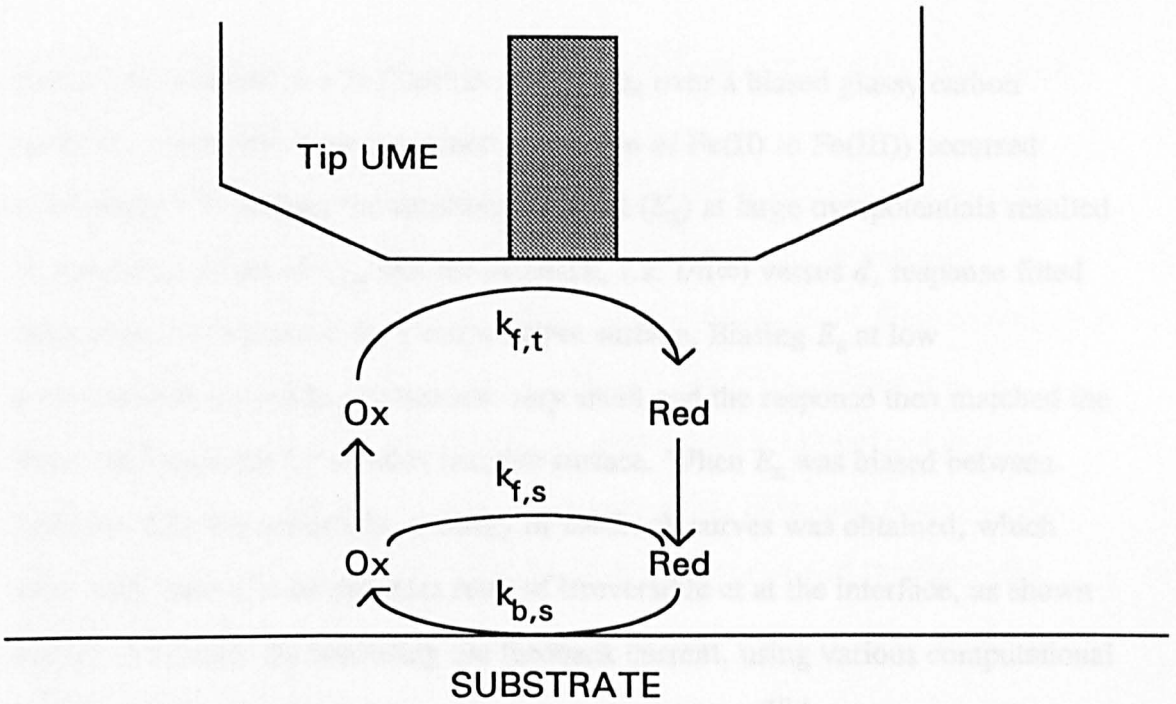

Figure 1.14(a). Schematic illustration of the SECM feedback mode with finite heterogeneous kinetics.

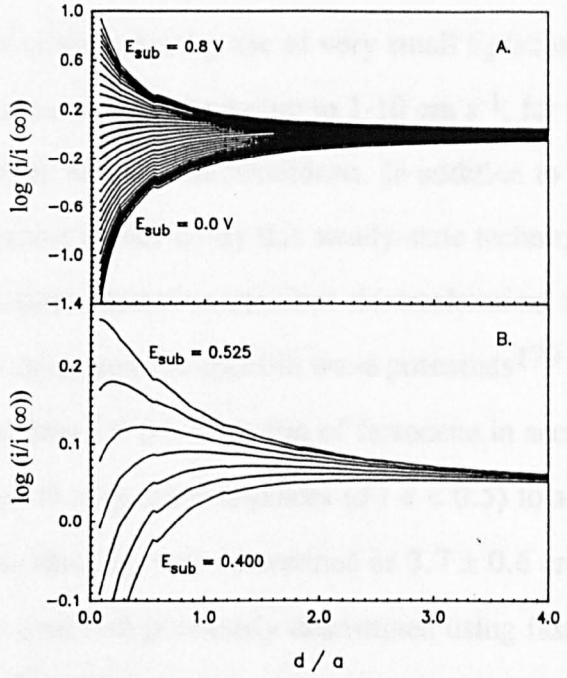

Figure 1.14(b). SECM log current-distance curves for a 2.1 mM Fe(III) solution in 1 M H_2SO_4/water. The tip UME is a 11 μm diameter carbon fibre at a potential of -0.6V versus a Hg/Hg_2SO_4 reference electrode; the substrate electrode is glassy carbon. (A) Curves for different substrate potentials at 25 mV increments between +0.8 and +0.0 V. (B) Region of (A) between +0.525 and +0.400 V. Reproduced from reference 134.

Fe(III) was reduced at a Pt UME in 1M H_2SO_4 over a biased glassy carbon substrate, where the reverse reaction (oxidation of Fe(II) to Fe(III)) occurred irreversibly.[134] Biasing the substrate potential (E_S) at large overpotentials resulted in very large values of $k_{b,s}$ and the feedback, *i.e.* $i/i(\infty)$ versus d, response fitted the theoretical behaviour for a redox active surface. Biasing E_s at low overpotentials caused $k_{b,s}$ to become very small and the response then matched the theoretical response for a redox inactive surface. When E_s was biased between these two limiting potentials, a family of feedback curves was obtained, which were each indicative of different rates of irreversible et at the interface, as shown in Figure 1.14(b). By modelling the feedback current, using various computational methods, values for the rate constant $k_{b,s}$ were obtained.[134]

This technique not only has the advantage that a large range of rate constants can be studied, but by use of very small tip/substrate distances, very large heterogeneous rate constants (up to 1-10 cm s^{-1}, for a first-order process) can be quantified under steady-state conditions. In addition to accessing large rate constants, the values measured by this steady-state technique are often higher than those reported using alternative transient electrochemical techniques.[153,154,179] For example by analysing the quartile wave potentials[179] obtained from steady-state voltammograms for the oxidation of ferrocene in acetonitrile, at a 2 μm Pt disc UME placed at very close distances (d / a < 0.5) to a conducting surface, the standard rate constant, k_o, was determined as 3.7 ± 0.6 cm s^{-1}.[153] This value was 2-4 times larger than that previously determined using fast scan cyclic voltammetry at a UME.[180-182] Using the same analysis but a slightly different experimental approach k_o for electron transfer to C_{60} in dichlorobenzene, containing 0.1 M tetra-*n*-butyl ammonium fluoroborate, at a Pt electrode, was determined to be 0.46 ± 0.08 cm s^{-1}.[154] In this case, the tip/substrate geometry was established as the thin layer of electrolyte solution trapped between a UME and a Hg surface (typical

thickness of the layer was 0.5 μm[183]) as the UME penetrated a Hg pool which served as the substrate.

The SECM methodology has also been extended to investigate et under several other conditions: (i) quasi-reversible et;[135] (ii) et at an unbiased substrate;[134] (iii) where a biased finite substrate is employed of dimensions either similar to, or less than, those of the tip UME[135] and (iv) et reactions at immobilised enzymes.[123] In the latter case, the et kinetics associated with the redox behaviour of immobilised glucose oxidase (GO) were determined. In this case the thermodynamic force for regenerating the tip produced mediator was through chemical reactivity at the enzyme surface rather than surface conductivity.

1.3.3.2 Reaction Rate Imaging

As discussed in section 1.3.2.1, it is possible to map surface reactivity by monitoring the reaction rate, from the variation in current, as the tip UME is scanned in a constant *x, y* plane parallel to the surface of interest. In order to selectively discriminate between surface reactivity and topography, it is essential that the surface topography is already known and characterised. In cases where this is not known, alternative imaging techniques can be used which distinguish between the two, as discussed later in section 1.3.3.6.

This technique in the feedback mode has been utilised to image catalytic sites on a electrode,[176] locate active oxidising sites on a thin (~ 20Å) semiconducting oxide layer (Ti / TiO_2),[133] image the active catalytic sites of redox enzymes[124] and investigate areas of active oxygen reduction at the surface of metallic biomaterials.[177] Using the SG/TC mode, SECM has been utilised to map areas of electrode surface activity[119] and image the density of active antigen binding sites in an immobilised antibody layer.[125] In the latter case, the immobilised antibody layer was treated with a enzyme labelled antigen which was

able to generate the redox active form of an enzyme substrate from a redox inactive form. This was subsequently detected at the tip electrode as a function of lateral position, thereby providing information on the spatial distribution of the antigen binding sites. For imaging purposes the feedback mode provides better lateral resolution as the generated electroactive product will only diffuse a short distance before it is collected by the tip UME. In the SG/TC mode the electroactive product is generated over the entire surface leading to the overlap of neighbouring diffusion fields from areas of differing reactivity.[123,124]

1.3.3.3 The Study and Quantification of Homogeneous Electron Transfer Processes using SECM

SECM has proven to be very useful in the studies of first and second-order homogeneous reactions associated with electrode processes.[119-120,147-150,184,185] The principle of such measurements is shown in Figure 1.15. The tip UME is positioned in close proximity to a conductive substrate. The solution contains an electroactive species which, upon electrolysis, produces a product which will undergo chemical decomposition. This is referred to as an EC mechanism.[73] Both tip and substrate are externally biased through the use of a bipotentiostat such that the following electrochemical reactions occur at diffusion-controlled rates:

$$\text{Red} \rightarrow \text{Ox} + ne^- \qquad \text{(tip)} \qquad (1.7)$$

$$\text{Ox} + ne^- \rightarrow \text{Red} \qquad \text{(substrate)} \qquad (1.8)$$

The above scheme assumes that the initial species is in the reduced form, but would also apply to a species in the oxidised form.

In the absence of decomposition of the tip generated species, Ox, the reduced form of the species is regenerated at the substrate and fed back to the tip UME and consequently $i > i(\infty)$, as expected for positive feedback. When Ox is

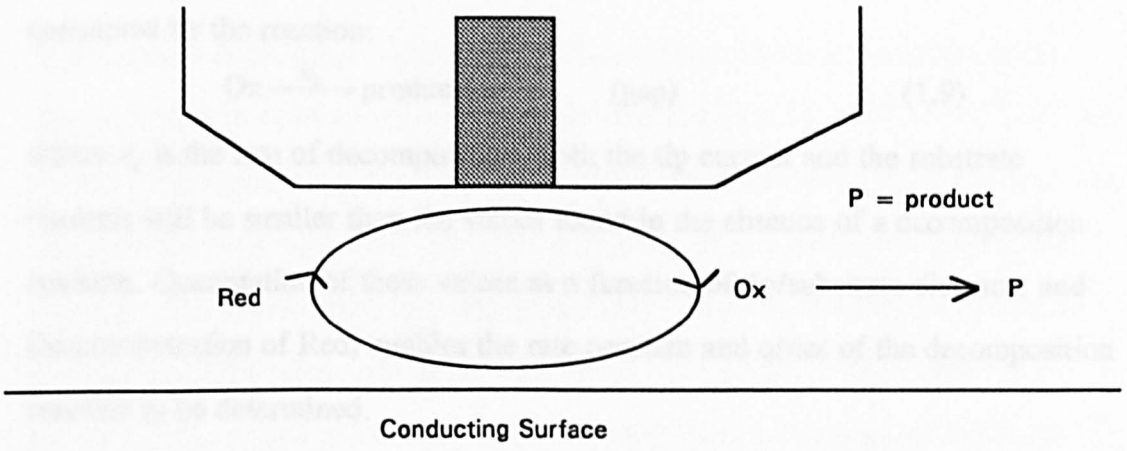

Figure 1.15(a). Homogeneous kinetics investigated with the feedback mode.

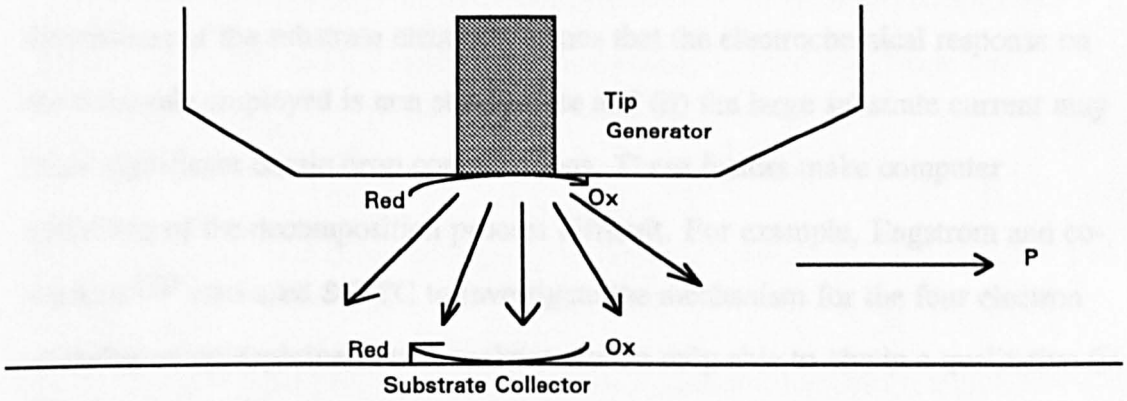

Figure 1.15(b). The TG/SC mode.

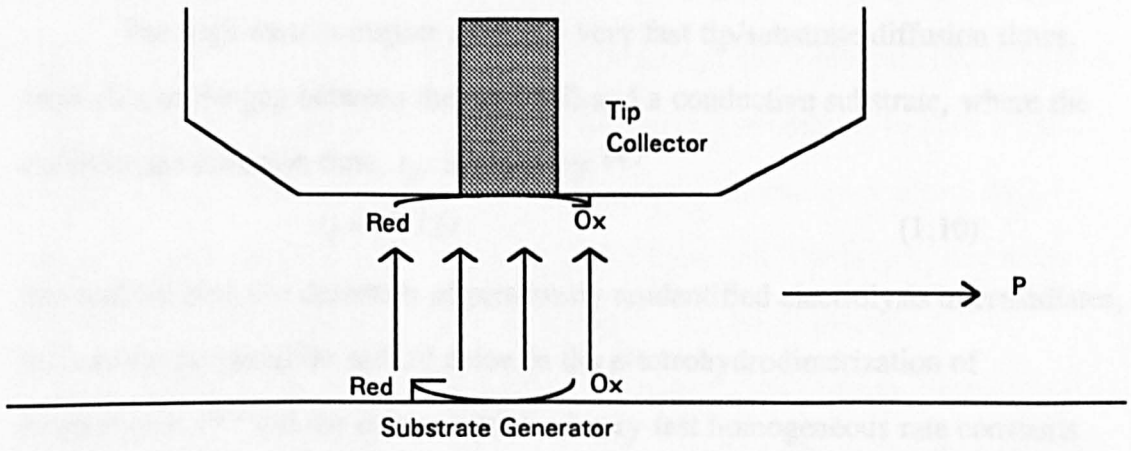

Figure 1.15(c). The SG/TC mode.

consumed by the reaction:

$$Ox \xrightarrow{k_c} \text{products} \qquad \text{(gap)} \qquad (1.9)$$

where k_c is the rate of decomposition, both the tip current and the substrate currents will be smaller than the values found in the absence of a decomposition reaction. Quantitation of these values as a function of tip/substrate distance, and the concentration of Red, enables the rate constant and order of the decomposition reaction to be determined.

The SG/TC mode has also found use in the study of homogeneous reactions[119,120,136,148] but due to the following drawbacks associated with the technique, the results obtained are usually not quantitative. (i) The large dimensions of the substrate electrode means that the electrochemical response on the timescale employed is non steady-state and (ii) the large substrate current may cause significant ohmic drop complications. These factors make computer modelling of the decomposition process difficult. For example, Engstrom and co-workers[120] who used SG/TC to investigate the mechanism for the four electron oxidation of epinephrine to adrenochrome were only able to obtain a qualitative fit between the experimental and theoretical data as the simulations were not powerful enough to distinguish between first- and second-order chemical reactions and an ECE mechanism.

The high mass transport rates and very fast tip/substrate diffusion times, attainable in the gap between the tip UME and a conductive substrate, where the tip/substrate diffusion time, t_d, is given by;[147]

$$t_d = d^2 / D \qquad (1.10)$$

has enabled both the detection of previously unidentified electrolysis intermediates, such as the acrylonitrile radical anion in the electrohydrodimerization of acrylonitrile,[185] and the determination of very fast homogeneous rate constants under steady-state conditions. For example using TG/SC a second-order radical

dimerization constant for the phenoxyl radical produced from the oxidation of 4-nitrophenolate in acetonitrile was determined as 1.2 (± 0.3) x 10^8 M^{-1} s^{-1},[150] the first study demonstrating the capabilities of SECM in measuring homogeneous rate constants in excess of 1 x 10^8 M^{-1} s^{-1}. In general, it is possible to measure rate constants with greater precision and access faster kinetics domains using SECM compared to alternative techniques such as fast scan cyclic voltammetry[186] and hydrodynamic double electrodes, *e.g.*, the rotating ring disc electrode (RRDE)[187] and the double channel electrode (DCE).[188] In the latter two cases, lower mass transfer rates limit the techniques to slower rate constants, and in the former case, although fast rate constants are accessible significant background charging and interference from adsorbed products or intermediates, may complicate the interpretation of data.

1.3.3.4 Imaging and Quantifying Local Transport through Porous Solids and Membranes

The transport of species between two solutions separated by a membrane or porous material is a general phenomenon underpinning a number of major processes, particularly in biochemical systems.[115] The transport of material across a separator can be promoted in several ways: an applied electric field will lead to the migration of charged species; a concentration gradient will promote diffusion and a pressure difference will result in transport by convection. In each situation the key questions to address are: (i) is the rate of mass transport across the separator uniform or spatially localised, (ii) if transport is localised, where are the active transport sites and can the local transport rate be quantified?

SECM is ideally suited to addressing these questions since, under conditions where the UME is held at a potential to drive the diffusion-controlled electrolysis of a target solution species, the size of the current flowing at the tip

depends only on the local rate of mass transport. By measuring the tip current as a function of position in the x, y plane as the tip is scanned over the target interface, permeable or regions of localised transport activity are identifiable from an enhancement in the current compared with the response when the tip sits above an area through which there is no transport. This principle is shown schematically in Figure 1.16. The resolution of the technique depends on the size of the electrode employed.

The first studies in this area were undertaken by White and co-workers[166-169] who utilised the SECM to identify active transport sites in excised hairless mouse skin under the application of an electric field to induce the migration of charged species. These studies were aimed at providing a better understanding of the processes involved in iontophoretic transdermal drug delivery - the electrically enhanced administration of ionic drugs across skin. The major objective of the study was to identify the extent to which the transport of the species occurred via appendages such as hair follicles and sweat ducts in the epidermis, the outer layer of skin. Previous studies, based on the staining of pores during the iontophoresis of charged dyes and the use of potentiometric microelectrodes to measure potential gradients had shown that these appendages were associated with areas of high current, but unfortunately, due to the low spatial resolution of these techniques, no information had been obtained on the contribution of individual pores to the overall iontophoretic current. White demonstrated that, upon application of an electric field, the hair follicles (pore diameter typically 15 μm, density 760 cm^{-2}), after an initial period of inactivity,[168] provided the dominant transport pathway. Moreover, this approach enabled the transport rate of ions moving through individual pores to be determined quantitatively for the first time.[166]

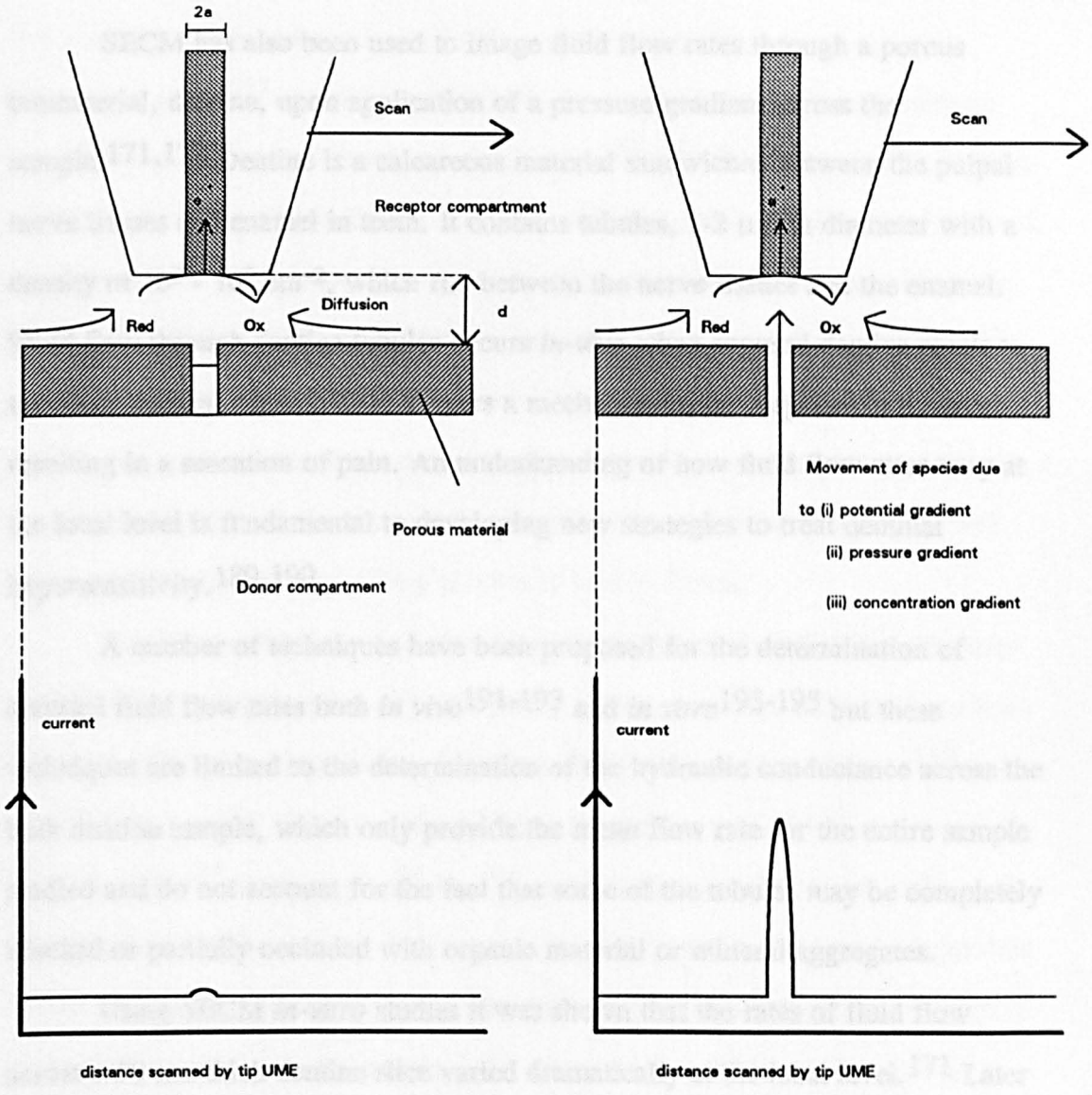

Figure 1.16. Schematic of the SECM arrangement used to probe local transport through porous materials. Two distinct transport situations arise: (a) when there is no potential/pressure/concentration gradient across the porous material, transport of species Red to the tip UME occurs by diffusion only and the tip current response is a function of the distance between the tip and the sample. (b) When a gradient is applied across the sample and the tip is in the vicinity of an open pore, transport across the sample enhances mass transport of Red to the UME, resulting in a larger transport-limited current.

SECM has also been used to image fluid flow rates through a porous biomaterial, dentine, upon application of a pressure gradient across the sample.[171,172] Dentine is a calcareous material sandwiched between the pulpal nerve tissues and enamel in teeth. It contains tubules, 1-2 μm in diameter with a density of 10^6 - 10^7 cm^{-2}, which run between the nerve tissues and the enamel. Fluid flow through dentine tubules occurs *in-vivo* when exposed dentine reacts to tactile or thermal stimuli. This triggers a mechanoreceptor response in the tooth resulting in a sensation of pain. An understanding of how fluid flow rates vary at the local level is fundamental to developing new strategies to treat dentinal hypersensitivity.[189,190]

A number of techniques have been proposed for the determination of dentinal fluid flow rates both *in vivo*[191-193] and *in vitro*[193-195] but these techniques are limited to the determination of the hydraulic conductance across the bulk dentine sample, which only provide the mean flow rate for the entire sample studied and do not account for the fact that some of the tubules may be completely blocked or partially occluded with organic material or mineral aggregates.

Using SECM *in-vitro* studies it was shown that the rates of fluid flow across a 50 μm thick dentine slice varied dramatically at the local level.[171] Later SECM studies on dentine, where transport was by diffusion due to a concentration difference, reached similar conclusions.[170] By using a 2 μm diameter Pt UME as the tip UME it was possible to quantify the rate of convection through a single dentine tubule, for the first time.[171]

1.3.3.5 Modification and Fabrication of Surfaces using SECM

1.3.3.5.1 Etching and Corrosion Studies

The high resolution etching of metals and semiconductors is of vital technological importance in the fabrication of microelectronic devices.[196] Usually

the operation is carried out by photolithography which involves several time consuming steps.[197] By utilising SECM in the feedback mode, submicrometre level etching can be performed in a single step.[158,161-163] The principles of this approach are illustrated in Figure 1.17. The solution contains the reduced form of an electroactive mediator which, upon oxidation at the tip UME, placed in close proximity to the appropriate conducting or semiconducting surface, locally generates an oxidant at the conductor/solution interface which is capable of causing the surface to undergo oxidative dissolution. As a consequence of this Ox is converted back to Red in the feedback cycle and a measure of the tip current enables the kinetics of the etching process to be elucidated.

The tip generated oxidant must be carefully selected so that it is powerful enough to initiate dissolution. The following locally generated oxidants have been utilised in SECM etching studies. Br_2 (from Br^-) in the etching of GaAs[162] and Si,[158] $Ru(phen)_3^{3+}$ (from $Ru(phen)_3^{2+}$) in the etching of GaP[161] and $Fe(phen)_3^{3+}$,[163] $Os(byp)_3^{3+}$,[56] Br_2[198] and $Ru(bipy)_3^{3+}$,[198] in the etching of Cu. In all studies the etch pit depth and shape was found to be strongly dependent on the tip/substrate distance, the tip electrode diameter and the dissolution period. In the latter study, whereby $Ru(bipy)_3^{3+}$ was used to oxidatively dissolve an unbiased Cu substrate, a minimum heterogeneous rate constant of 0.4 cm s^{-1} was determined for the etching process.[198] In this case in order to suppress regeneration of Red at the metallic surface by electron transfer due to positive feedback (as shown schematically in Figure 1.2(c)) a Cu UME of the same dimensions as the tip UME was employed as the substrate.

The extent of dissolution at the surface of doped semiconductors was found to be strongly dependent on the dopant.[162] For example, the production of $Fe(phen)_3^{3+}$, at the surface of p- doped GaAs resulted only in positive feedback whereas for undoped and n- doped GaAs, oxidative dissolution was observed. This

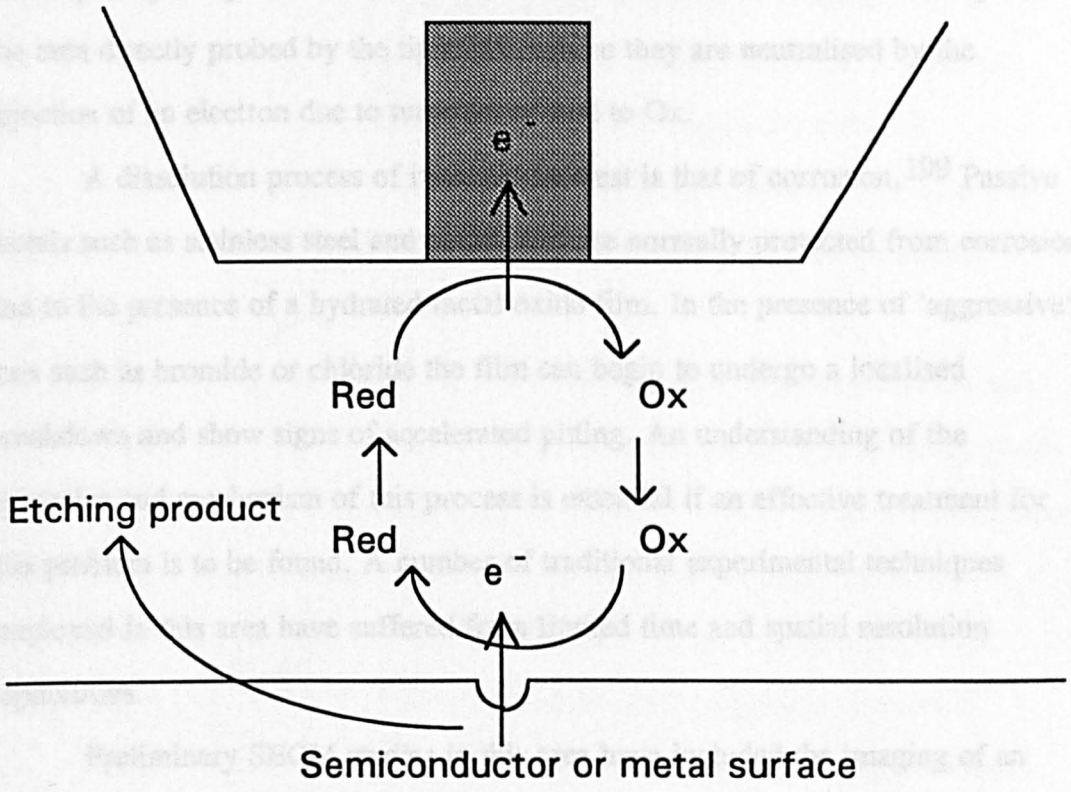

Figure 1.17. Overall scheme for the etching of metals or semiconductors utilising the SECM. The oxidising species which have been locally generated in SECM etching methodology are Br_2, $Ru(phen)_3^{3+}$and $Fe(phen)_3^{3+}$.

was attributed to the differences in the position of the locally produced positive hole due to valency band differences. For n- doped and undoped GaAs the holes remain at the surface and etching occurs whereas for p- doped GaAs the holes can move quickly away into the bulk of the solid and/or across the surface away from the area directly probed by the tip UME, where they are neutralised by the injection of an electron due to turnover of Red to Ox.

A dissolution process of immense interest is that of corrosion.[199] Passive metals such as stainless steel and aluminium are normally protected from corrosion due to the presence of a hydrated metal oxide film. In the presence of 'aggressive' ions such as bromide or chloride the film can begin to undergo a localised breakdown and show signs of accelerated pitting. An understanding of the dynamics and mechanism of this process is essential if an effective treatment for this problem is to be found. A number of traditional experimental techniques employed in this area have suffered from limited time and spatial resolution capabilities.

Preliminary SECM studies in this area have included the imaging of an active corrosion pit on the surface of stainless steel in the presence of Cl^- using the SG/TC mode of operation,[200] the initiation of pit formation on aluminium and stainless steel by locally generating Cl^- at the tip UME[200] and the location of active areas for Br^- oxidation on the oxide covered surface of a Ti substrate.[201,202] In the latter case the Br_2 produced was detected by a tip UME scanned above the TiO_2 sample in the SG/TC mode. Subsequent investigations showed a direct correlation between these electroactive sites and corrosion pits, indicating that the oxide breakdown is associated with areas of high electrical conductivity.

1.3.3.5.2 Deposition

In the SECM feedback mode for oxidative etching, the oxidant is generated locally in the vicinity of the solid/liquid interface by the tip UME. By altering the mediator so that a reduced species is formed at the tip, local production of Red in the close vicinity of a conducting or redox active surface will result in electron donation across the interface. If the surface contains a species capable of undergoing reduction to form a solid structure, localised deposition can also take place at the micrometre[155,203] and submicrometre level.[164] This process is shown schematically in Figure 1.18.

The SECM feedback mode has been used to electrodeposit palladium and gold by reduction of the metal precursors, $PdCl_4^-$ and $AuCl_4^-$, which were dopants in a polymer film, by the reducing agent $Ru(NH_3)_6^{2+}$.[155,203] The size and shape of the deposits formed were determined by the length of electrolysis, the tip/substrate separation, the *RG* value of the tip UME and the composition of the metal complex used.[155] In a slight modification of this approach, the metal complex, $AuBr_4^-$, was produced by a Au UME tip held at a oxidising potential in the presence of Br^-. Au was locally deposited[158] by approaching the tip (maintained at its oxidising potential) to a substrate surface (indium-tin-oxide) which was biased at a potential sufficient enough to reduce $AuBr_4^-$.

Deposition has also been initiated by employing SECM in the direct mode,[164] the principles of which are illustrated in Figure 1.19. In this approach, a bare etched tungsten (tip) electrode and a metal substrate electrode (silver, gold or copper) were connected in an electrochemical cell. The electrodes were separated from each other by a ionically conducting polymer (Nafion or protonated poly(vinylpyridine)) which contained mobile metal ions. Upon application of a negative potential to the tip electrode, the metal ions were reduced at the tip electrode/polymer interface while at the substrate electrode, complementary

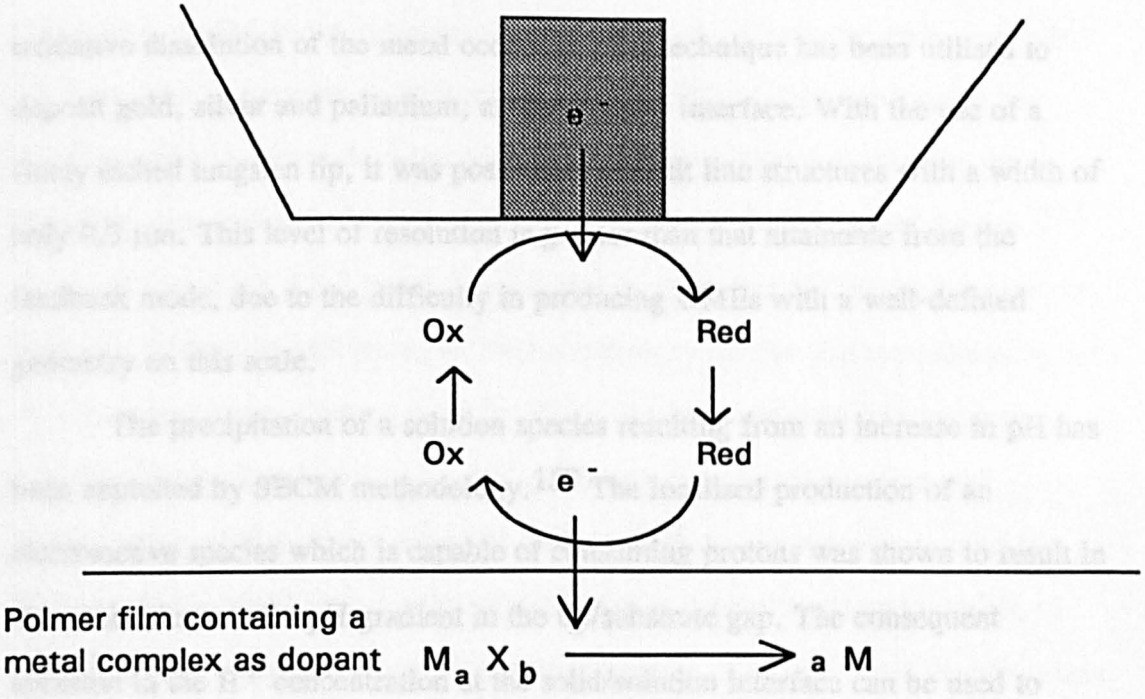

Figure 1.18. Deposition using the SECM in the feedback mode. M_aX_b is a metal precursor such as $PdCl_4^-$ or $AuCl_4^-$ which can be reduced to the metallic form by the reducing species $Ru(NH)_3^{2+}$.

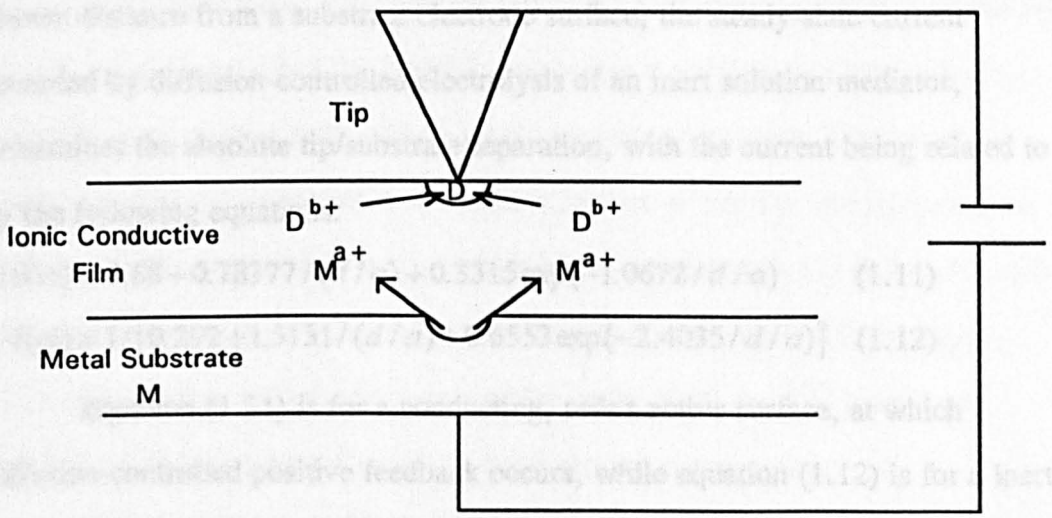

Figure 1.19. Direct mode deposition of a metal species D, from a film containing mobile D^{b+} ions, coupled with etching of the substrate metal, M.

oxidative dissolution of the metal occurred. This technique has been utilised to deposit gold, silver and palladium, at the polymer interface. With the use of a finely etched tungsten tip, it was possible to deposit line structures with a width of only 0.3 μm. This level of resolution is greater than that attainable from the feedback mode, due to the difficulty in producing UMEs with a well-defined geometry on this scale.

The precipitation of a solution species resulting from an increase in pH has been exploited by SECM methodology.[157] The localised production of an electroactive species which is capable of consuming protons was shown to result in the establishment of a pH gradient in the tip/substrate gap. The consequent decrease in the H^+ concentration at the solid/solution interface can be used to precipitate metal hydroxide structures, such as $Ni(OH)_2$, at a Pt substrate.[157]

The process of deposition on a substrate invariably results in an increase in surface height. SECM operating in either the negative or positive feedback mode (depending on the conductivity of the surface under study) has been used to measure the dynamic growth of surface films.[160] By positioning the tip UME at a known distance from a substrate electrode surface, the steady-state current recorded by diffusion-controlled electrolysis of an inert solution mediator, determines the absolute tip/substrate separation, with the current being related to d by the following equations:

$$i/i(\infty) = 0.68 + 0.78377/(d/a) + 0.3315\exp(-1.0672/d/a) \qquad (1.11)$$

$$i/i(\infty) = 1/[0.292 + 1.5151/(d/a) + 0.6553\exp(-2.4035/d/a)] \qquad (1.12)$$

Equation (1.11) is for a conducting, redox active surface, at which diffusion-controlled positive feedback occurs, while equation (1.12) is for a inert redox inactive surface, which promotes diffusion-controlled negative feedback. With the tip UME maintained at this position, monitoring the change in the steady-state current, supplies information on the decrease in tip/substrate distance when a

potential is applied to the substrate to drive a deposition process. This approach has been used to monitor AgBr formation on Ag[160] and TiO_2 production on Ti.[160] A similar approach in the scanning mode was utilised to monitor the thickness of a precipitated layer of calcium oxalate on the surface of dentine.[172]

Sections 1.3.3.5.1 and 1.3.3.5.2 clearly show that SECM can be used not only as a fabrication tool but as an *in-situ* technique for the characterisation of the modification process. Recent work by Shiku and co-workers in this area has extended the work to biological samples through the microfabrication and quantification of diaphorase-patterned surfaces.[204] By generating a species (Br_2) at the tip UME which was capable of deactivating diaphorase it was possible to microfabricate selected regions of enzyme inactivity. The active and inactive areas were subsequently imaged by monitoring the catalytic current for oxidation of NADH, as the tip UME was scanned above the enzyme treated surface.

1.3.3.6 Topographical Imaging utilising SECM

SECM has found use as a topographical imaging tool but the applications have been rather limited. This may be due to the following drawbacks: (i) the tip current which flows when the UME is scanned in a constant x, y plane above a sample surface reflects both surface reactivity and topography. It is therefore essential that the reactivity of the surface is known so that the true tip/substrate distance can be evaluated through application of equations (1.11) and (1.12). (ii) The spatial resolution is governed by the diameter of the tip UME employed. Although nanodes, with tip diameters of the order of 10 nm,[205] have been constructed, they are very difficult to fabricate and characterise.

SECM has been used in the negative feedback mode to image the surface topography of several biological redox inactive materials. In this case SECM has advantages over conventional techniques, such as electron microscopy (EM), in

that the samples can be imaged *in-situ* non invasively, as they do not need to be made conducting via application of a metallic film. SECM has successfully imaged dentine,[171,172] enzymes,[118] filaments of algae[114] and open stomata on the lower surface of a leaf.[173] The limit of resolution in all cases was *ca.* 2 μm. Recently, Fan and Bard imaged supercoiled DNA on mica with a resolution comparable to that obtained by AFM. They achieved this by monitoring the tip displacement of an uninsulated Pt-Ir electrode, etched to a very fine tip, as it was scanned in a constant current mode, in a thin layer of water on the sample surface, under conditions of high humidity.[175]

Several workers have tried to address the problems of image resolution and unknown surface reactivity associated with SECM imaging. Through the employment of digital image processing[206] and signal processing techniques[207] the quality of the SECM images of rough surfaces can be improved. The constant current mode,[208,209] in which a closed loop electronic circuit maintains a constant tip current by adjusting the tip/substrate distance, eliminates the likelihood of tip crash onto the surface when there are large sample height changes or surface tilt, which would impede the constant height mode. This advance is particularly significant for smaller diameter electrodes which have to be positioned very close to a surface.

Wipf *et al* used the constant current mode in conjunction with small amplitude tip-position modulation (TPM)[209] to distinguish selectively between conductive and insulating areas on a substrate surface. Although this provided the first method of imaging topographical changes on a surface containing areas of extreme reactivity it still did not address the problem of topographically imaging surfaces of intermediate reactivity.

Heinze[210,211] used SECM operating in the constant distance mode to overcome this. By bringing a tip UME normal to a surface to within fractions of a

micron, very quickly (>50 μm s^{-1}), the convective current recorded at the tip was found to be relatively independent of the surface reactivity but sensitive to the tip/substrate separation. By monitoring the tip displacement in the *z* direction upon reaching a threshold current at various lateral positions, the topography of the surface was elucidated. Unfortunately this approach was time consuming and suffered from limited lateral resolution.

1.3.3.7 Potentiometric Probes in SECM

All the above applications of SECM methodology have employed the use of amperometric electrodes. For the quantitative measurement of the local concentration of a specific species, potentiometric tips are more favoured since they do not significantly change the concentration of the detected species and they exhibit higher chemical specificity. In addition, for investigations into important biological processes, where the ability to monitor the alkali and alkaline earth metals is essential, potentiometric electrodes are only appropriate since the potential window of electrolytic probes is not sufficient to enable detection of these ions.

To date several potentiometric SECM tips have been fabricated and utilised, such as Ag/AgCl microelectrodes,[212-214] antimony based pH electrodes[215] and ion selective neutral carrier based microelectrodes (ISME's).[216] They are shown schematically in Figure 1.20. The Ag/AgCl electrode can be used to investigate Ag^+ and Cl^- ion fluxes. This type of probe has been employed to monitor the flux of Cl^- at a polyaniline modified electrode,[212] to determine one-dimensional Cl^- ion profiles in corrosion pits on metals[213] and to measure the rate at which aqueous 2,4 -dichlorophenol is photomineralised at the TiO_2 / aqueous interface, by monitoring the production of Cl^-.[214] Antimony microelectrodes have been utilised to spatially map the developing pH profiles of different systems,[215]

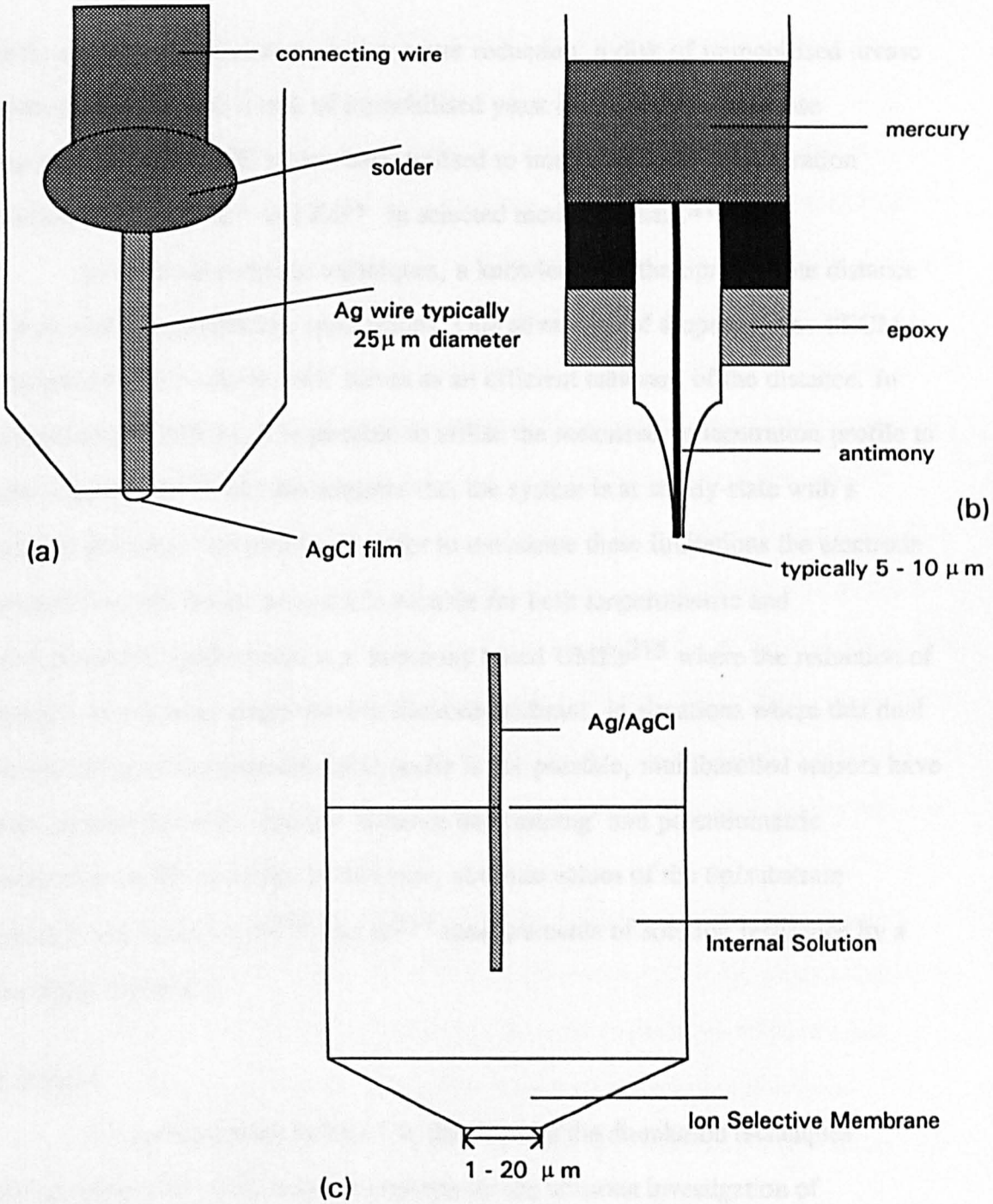

Figure 1.20. Three types of SECM potentiometric electrodes: (a) Ag/AgCl UME; (b) antimony disc UME and (c) ion selective neutral carrier based UME.

such as a platinum electrode during water reduction, a disk of immobilised urease hydrolysing urea and a disk of immobilised yeast cells catalysing glucose metabolism. The ISME's have been utilised to image the local concentration profiles of NH_4^+, K^+ and Zn^{2+} in selected model systems.[216]

As for amperometric techniques, a knowledge of the tip/substrate distance is essential for quantitative applications. One advantage of amperometric SECM is that the current response itself serves as an efficient calibrant of the distance. In potentiometric SECM, it is possible to utilise the measured concentration profile to also establish d,[216] but this assumes that the system is at steady-state with a defined concentration profile. In order to overcome these limitations the electrode material can be chosen so that it is suitable for both amperometric and potentiometric applications, *e.g.* antimony based UMEs[215] where the reduction of oxygen serves as an amperometric distance calibrant. In situations where this dual functionality of the potentiometric probe is not possible, multibarelled sensors have been constructed with separate 'distance determining' and potentiometric electrodes on the same tip. In this case, absolute values of the tip/substrate distance are based on dc[216] and ac[217] measurements of solution resistance by a Ag/AgCl electrode.

1.4 Aims

It is apparent from section 1.2, that none of the dissolution techniques discussed fulfil all of the necessary criteria for the accurate investigation of dissolution kinetics, as delineated in section 1.2. The review of SECM, in section 1.3, highlights many salient features of the methodology which, in principle, make it attractive for studying dissolution kinetics. The ability to define, vary and calculate mass transport rates in the tip/substrate gap while probing interfacial reactivity, with a spatial resolution which approaches the tip diameter, should enable the SECM to

simultaneously address all the criteria outlined, making it a powerful device for investigating interfacial dissolution kinetics of a wide range of materials.

The proposed method of measuring dissolution rates from the surface of an ionic material, is shown schematically in Figure 1.21; it is based upon the SECM equilibrium perturbation mode discussed in section 1.3.2.3. The role of the UME is to induce and monitor dissolution from a specific region of the crystal surface. This is achieved by stepping the electrode potential from a value at which no electrochemical reactions occur, and the solution is saturated with respect to the crystalline material, to a value at which the electrolysis of one of the lattice ion types in the solution occurs at a diffusion-controlled rate (the reduction of M^{z+} to M in Figure 1.21). The electrode process depletes the concentration of lattice ions in the solution between the tip and the crystal surface and the resulting undersaturation at the crystal/solution interface, located under the tip, provides the thermodynamic force for the dissolution reaction. Dissolving ions move from the crystal across the gap and are detected at the tip UME producing a current flow, the magnitude of which depends on the rate and mechanism of the dissolution process.

Very preliminary work of this kind, was carried out by the author as an undergraduate project in 1993.[218-220] Through studies of the dissolution reactivity in highly dislocated areas on the (100) face of copper sulfate pentahydrate, the validity of this technique as a method of inducing and monitoring interfacial dissolution reactions under very high and well-defined mass transfer conditions with high spatial resolution, was confirmed.[218-220]

This thesis significantly extends the SECM dissolution mode to specific systems, with the dual aim of developing the methodology and addressing many fundamental questions on dissolution kinetics and mechanisms.

The kinetics and mechanisms controlling the dissolution of unsymmetric salts are largely unresolved.[1] Chapter 4 addresses this problem by determining the

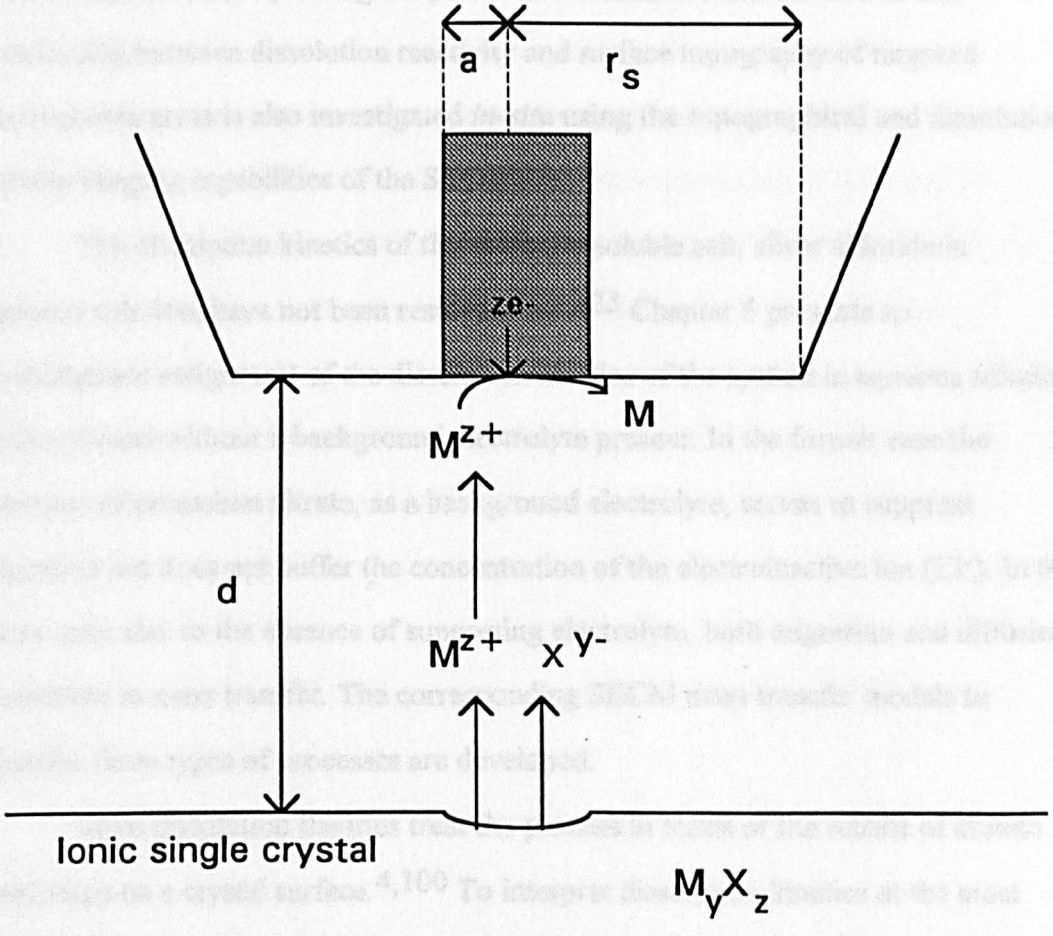

Figure 1.21. Schematic showing the principles of SECM induced dissolution.

dissolution characteristics from the (010) face of the highly soluble crystal, potassium ferrocyanide trihydrate in aqueous potassium chloride solutions. Under these conditions the theoretical treatment of mass transport in the system is reduced to the consideration of diffusion of only the electroactive ions ($Fe(CN)_6^{4-}$ and $Fe(CN)_6^{3-}$) as the supporting electrolyte (KCl) serves to buffer the concentration of the electroinactive ion (K^+) during the period of a dissolution measurement. The relationship between dissolution reactivity and surface topography of targeted macroscopic areas is also investigated *in-situ* using the topographical and dissolution activity imaging capabilities of the SECM.

The dissolution kinetics of the sparingly soluble salt, silver chloride in aqueous solution, have not been resolved.[221-223] Chapter 5 presents an unambiguous assignment of the dissolution kinetics of the system in aqueous solution both with and without a background electrolyte present. In the former case the presence of potassium nitrate, as a background electrolyte, serves to suppress migration but does not buffer the concentration of the electroinactive ion (Cl^-). In the latter case, due to the absence of supporting electrolyte, both migration and diffusion contribute to mass transfer. The corresponding SECM mass transfer models to describe these types of processes are developed.

Most dissolution theories treat the process in terms of the retreat of atomic level steps on a crystal surface.[4,100] To interpret dissolution kinetics at the most fundamental level a methodology is required which can measure reaction rates under well-defined conditions and provide complementary topographical images at high resolution. Chapter 6 describes the development of an integrated electrochemical-AFM to determine, at the elementary level, the dissolution kinetics and mechanism of dissolution from the (100) face of potassium bromide in acetonitrile solutions containing lithium perchlorate as the supporting electrolyte.

The effect of surface structure on dissolution activity is an important question. Chapter 7 addresses this point by considering the effect of dislocation density on the dissolution characteristics from the (100) face of copper sulfate pentahydrate in aqueous sulfuric acid solutions. SECM mass transfer models are developed to theoretically describe dissolution from a dislocation-free area, to support the observed behaviour.

Chapter 8 describes a microjet electrode which is capable of delivering very high, well-defined rates of mass transfer to an interface. The mass transfer rates for flow from a capillary (typically 100 μm in diameter) containing an electroactive species at a 25 μm diameter UME, are characterised and the resulting laminar flow profile imaged, by monitoring the limiting steady-state current as a function of capillary position as it is scanned above the electrode surface. The possibility of using this methodology as a means of investigating very fast dissolution processes under the well-defined conditions is discussed.

CHAPTER 2

THEORETICAL TREATMENT OF MASS TRANSFER IN THE SECM GEOMETRY

This chapter provides a theoretical foundation for the treatment of mass transfer in the SECM geometry. An overview of the numerical methods which have been utilised to address this problem is given. The alternating-direction implicit (ADI) finite-difference method, which is specific to the numerical simulations in this thesis, is described in detail.

2.1 Numerical methods employed to solve mass transport in the SECM geometry

The theoretical formulation and treatment of mass transfer is of crucial importance for the quantitative interpretation of dynamic electrochemical processes. For simple electrochemical reactions (such as kinetically uncomplicated electron transfer) occurring at uniformly accessible electrodes, it is often possible to obtain analytical solutions.[224] For more complicated processes occurring at non-uniformly accessible electrodes, semi-analytical[225-228] and digital (numerical) techniques[229,230] are required.

The first treatment of mass transfer in the two-dimensional axisymmetric geometry of the SECM was by Kwak and Bard[122] who used the numerical finite element method (FEM)[231,232] with an exponentially expanding grid,[233-235] to calculate the steady-state diffusion-controlled current that flowed at the tip UME located close to a conducting or insulating substrate, with the SECM operating in the feedback mode.[122] This method, typically employed for engineering simulations,[231,232] enabled the calculation of both the steady-state current and

concentration profiles, for the electroactive species of interest, in the tip/substrate gap, as a function of *d/a*, the normalised tip/substrate separation. By using a novel integrator based on a Krylov algorithm,[236] it was possible to simulate numerically SECM transients for the feedback case,[146] although the method presented was limited to the study of the current response in the absence of homogeneous and heterogeneous kinetic complications.

The use of semi-analytical multidimensional integral equations (MIE) to treat numerically diffusion in the SECM geometry was introduced by Mirkin and Bard.[237,238] This approach was used to simulate the transient and steady-state response of an SECM tip for irreversible, quasi-reversible and reversible kinetics at a substrate of finite size.[135]

The ADI finite-difference method,[239-241] is a well-known, efficient digital technique for solving two-dimensional time-dependent problems. It was first introduced as a method for modelling diffusion at a UME[242-244] by Heinze and has since proved to be the most widely used method of simulating mass transport in the SECM geometry. It has been applied to a variety of SECM problems, in particular the formulation of the transient response for systems where homogeneous[147,245] and heterogeneous complications[124,132,135] are apparent, under both finite[135] and infinite substrate conditions. Advantages of the methodology include: (i) the efficiency in computer time required for simulations, particularly when including exponentially expanding space grids and variable time steps; (ii) ease of use and (iii) the applicability to many different systems, requiring only limited changes to computer codes.

2.2 Mass Transfer and the ADI Finite-Difference Method in the SECM Geometry

For the work presented in this thesis, the ADI simulation method was chosen to simulate theoretically mass transport in the tip/substrate gap during electrochemical induction of a dissolution process using the SECM. The following section will outline the steps involved in the time-dependent treatment of mass transfer in the SECM geometry and subsequent application of ADI methodology to solve the problem numerically. The approach will be illustrated at the simplest level, by considering SECM diffusion-controlled electrolysis of an electroactive species above an infinitely large insulating substrate,[121] *i.e.* negative feedback, illustrated schematically in Figure 1.11(b) for the reduction of a solution containing only Ox to Red. It will then be shown how the model can be adapted to treat the various dissolution cases.

2.2.1 SECM Mass Transfer

Under conditions where migration of the species of interest can be neglected, mass transfer in the gap between the tip and the inert substrate occurs by diffusion alone, which is well-defined.[147] Fick's second law, describing the transport of Ox in the axisymmetric cylindrical SECM geometry,[246] defined in Figure 2.1, is:

$$\frac{\partial c_{Ox}}{\partial t} = D_{Ox}\left(\frac{\partial^2 c_{Ox}}{\partial r^2} + \frac{1}{r}\frac{\partial c_{Ox}}{\partial r} + \frac{\partial^2 c_{Ox}}{\partial z^2}\right) \qquad (2.1)$$

where c_{Ox} is the concentration of Ox, D_{Ox} is the diffusion coefficient of Ox, t is time and r and z are, respectively, the cylindrical co-ordinates in the directions radial and normal to the electrode surface starting at its centre. In order to determine how the tip current depends on mass transfer and surface reactivity, it is necessary to define the boundary conditions at the electrode and the substrate, which reflect the experimental and geometrical conditions of the system under study.

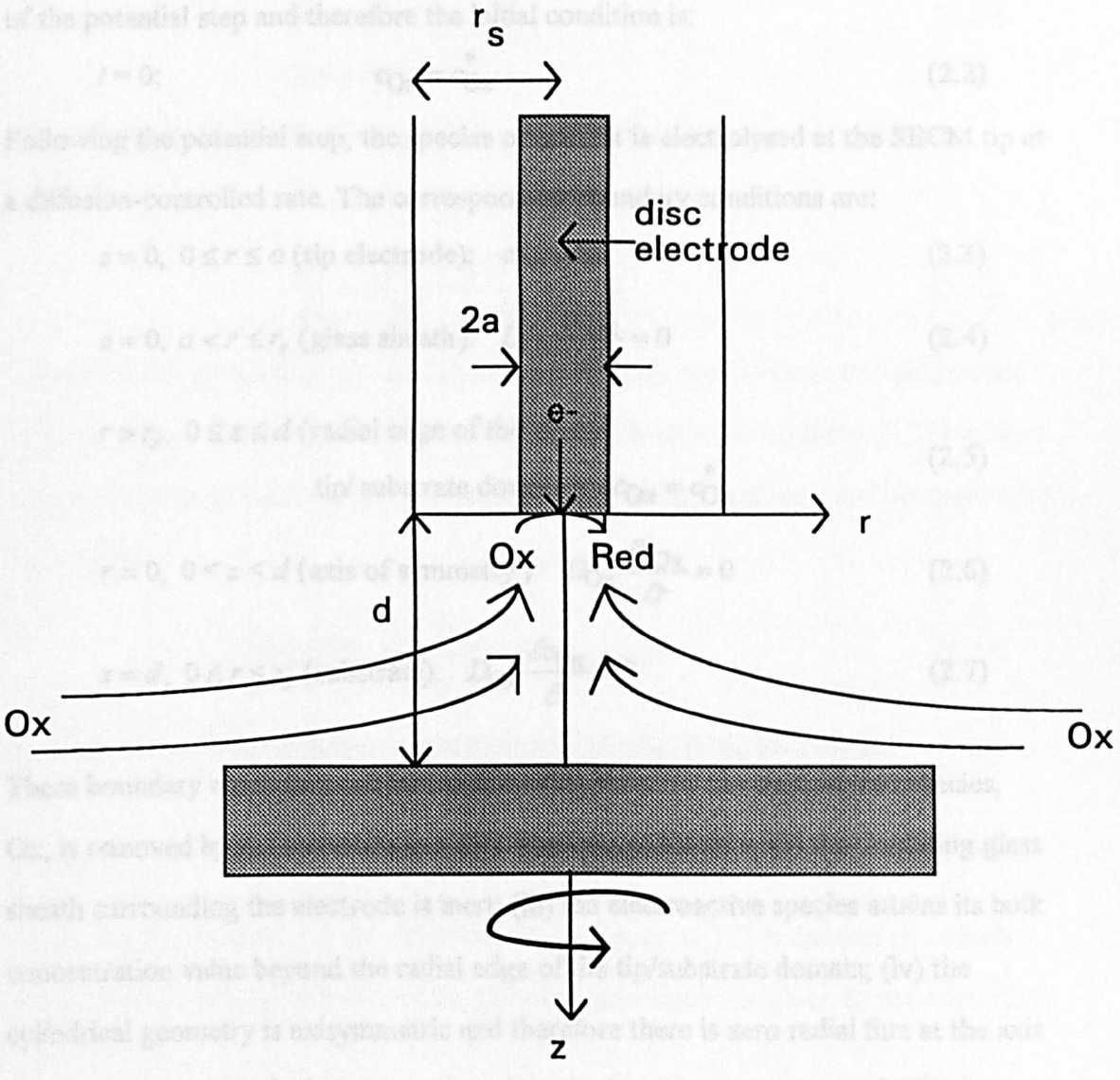

Figure 2.1. The co-ordinate system and notation used to describe the tip/substrate domain with the SECM operating in the negative feedback mode.[122]

For the chronoamperometric negative feedback experiment, it is assumed that only Ox is present in solution at the bulk concentration c_{Ox}^* prior to the application of the potential step and therefore the initial condition is:

$$t = 0: \qquad c_{Ox} = c_{Ox}^* \tag{2.2}$$

Following the potential step, the species of interest is electrolysed at the SECM tip at a diffusion-controlled rate. The corresponding boundary conditions are:

$$z = 0,\ 0 \le r \le a \text{ (tip electrode)}: \quad c_{Ox} = 0 \tag{2.3}$$

$$z = 0,\ a < r \le r_s \text{ (glass sheath)}: \quad D_{Ox}\frac{\partial c_{Ox}}{\partial z} = 0 \tag{2.4}$$

$$r > r_s,\ 0 \le z \le d \text{ (radial edge of the tip/ substrate domain)}: \quad c_{Ox} = c_{Ox}^* \tag{2.5}$$

$$r = 0,\ 0 < z < d \text{ (axis of symmetry)}: \quad D_{Ox}\frac{\partial c_{Ox}}{\partial r} = 0 \tag{2.6}$$

$$z = d,\ 0 \le r \le r_s \text{ (substrate)}: \quad D_{Ox}\frac{\partial c_{Ox}}{\partial z} = 0 \tag{2.7}$$

These boundary conditions reflect the following facts: (i) the electrolysed species, Ox, is removed by the electrode at a diffusion-controlled rate; (ii) the insulating glass sheath surrounding the electrode is inert; (iii) the electroactive species attains its bulk concentration value beyond the radial edge of the tip/substrate domain; (iv) the cylindrical geometry is axisymmetric and therefore there is zero radial flux at the axis of symmetry and (v) Ox is inert on the substrate. Previous treatments of diffusion to UMEs[144,145,247] and models of SECM under steady-state conditions[121] dictate that equation (2.5) is valid only when $RG \ge 10$. For SECM tips with smaller RG values, diffusion outside the probe/substrate domain may need to be considered.

In order to achieve a general solution to the SECM problem, the diffusion equation and boundary conditions are cast into a dimensionless form through the introduction of the following normalised terms:

$$\tau = tD_{Ox}/a^2 \tag{2.8}$$

$$C = c_{Ox}/c^*_{Ox} \tag{2.9}$$

$$R = r/a \tag{2.10}$$

$$Z = z/a \tag{2.11}$$

The time-dependent diffusion equation, subject to the above normalised terms, becomes:

$$\frac{\partial C}{\partial \tau} = \left(\frac{\partial^2 C}{\partial R^2} + \frac{1}{R}\frac{\partial C}{\partial R} + \frac{\partial^2 C}{\partial Z^2}\right) \tag{2.12}$$

The effect of equations (2.8) - (2.11) on the boundary conditions is straightforward and should be evident. The aim of the calculations is to solve equation (2.12) subject to both the dimensionless initial condition and boundary conditions and determine the tip current

$$i = 2\pi n_e a F D_{Ox} c^*_{Ox} \int_0^1 (\partial C/\partial Z)_{Z=0} R dR \tag{2.13}$$

as a function of time. In dimensionless form, equation (2.13) becomes;

$$i/i(\infty) = (\pi/2) \int_0^1 (\partial C/\partial Z)_{Z=0} R dR \tag{2.14}$$

where the denominator on the left-hand side of equation (2.14) denotes the steady-state diffusion-limited current at a simple microdisc electrode given by equation (1.4).

2.2.2 Numerical Simulation using the ADI finite-difference method

The problem, as set out in Section 2.2.1, can be solved numerically using the ADI finite-difference method. The principle of the numerical technique involves calculating concentrations at nodes on a finite-difference grid covering the

tip/substrate domain, as a function of time. The resulting current, at a particular time, is obtained by evaluating the surface concentration flux over the whole electrode area, in accordance with equation (2.14).

2.2.2.1 Definition of the grid system

The two-dimensional grid appropriate to the SECM geometry, is displayed in Figure 2.2. Only the cross section shown is considered, as the system is axisymmetric. Points in the R and Z directions are denoted j and k respectively. The number of points in the radial direction over the electrode and the glass sheath are denoted NE and NG respectively, where NE + NG is the total number of points in the radial direction. The number of points in the Z direction is given by NZ.

To account for the regions of interest in the grid and effect an efficient numerical solution, the spacing in the radial direction is compressed so that there are more points where the steepest change of concentration with R is expected. For the situation of interest, this occurs at the edge of the electrode where radial diffusion dominates. For the radial direction, appropriate expressions to describe this compression are:[234,248]

$$\rho = -\ln(1 + f[1 - R]) \quad (0 \le R \le 1) \tag{2.15}$$

$$\rho = \ln(1 + g[R - 1]) \quad (1 < R \le RG) \tag{2.16}$$

where f and g are constants. This type of function was originally introduced into electrochemical numerical simulations by Feldberg.[234]

For this system the Z direction is left untransformed and the concentration points are therefore of equal separation, although a function of a type similar to that above can be introduced when needed.[147]

The time-dependent diffusion equation must be re-written in ρ space. The first two terms on the right hand side of the mass transfer equation (2.12) can be expressed in terms of ρ as:

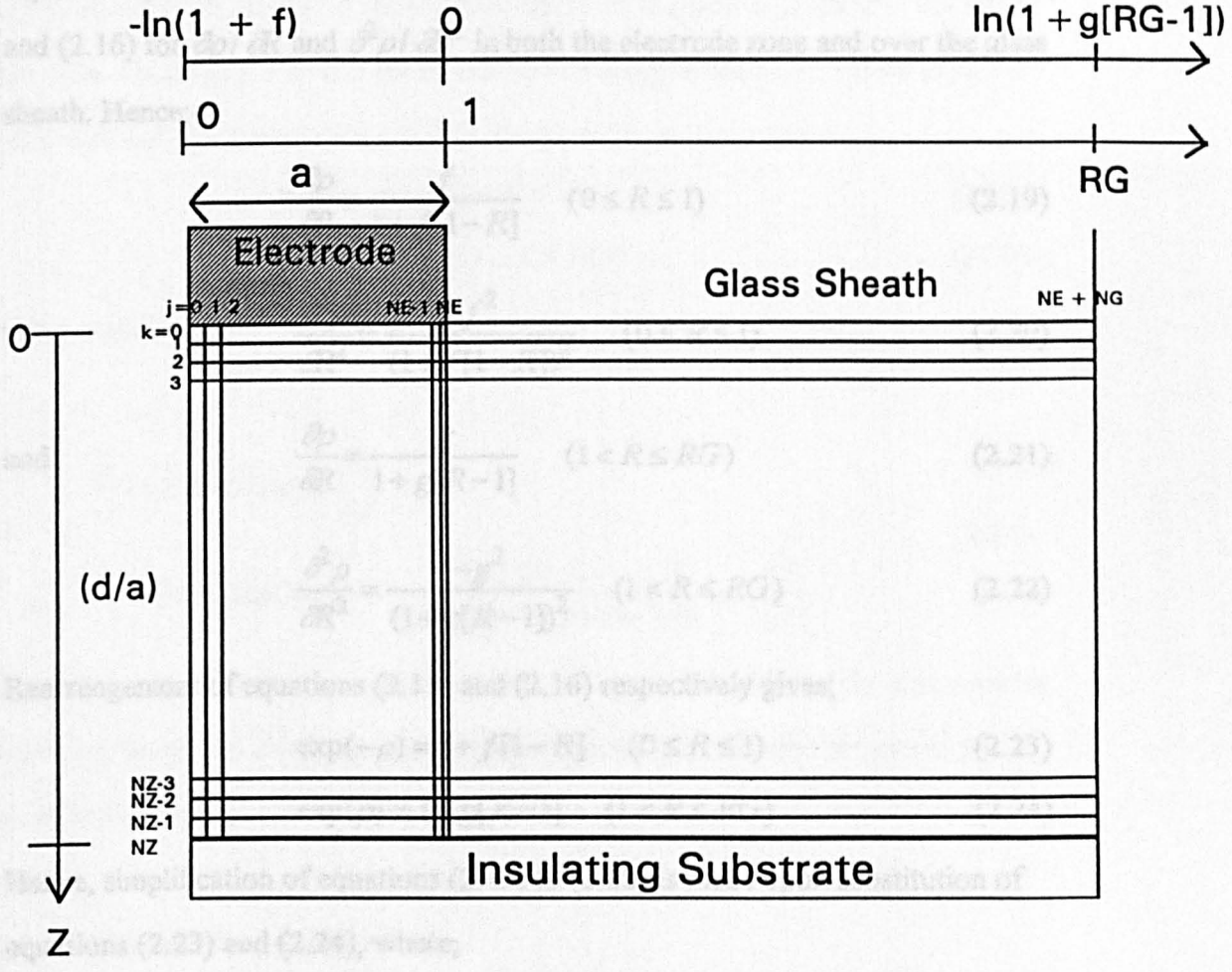

Figure 2.2. SECM finite-difference mesh for the ADI calculations.

$$\frac{\partial^2 C}{\partial R^2} = \frac{\partial}{\partial R}\left(\frac{\partial \rho}{\partial R}\cdot\frac{\partial C}{\partial \rho}\right) = \left(\frac{\partial \rho}{\partial R}\right)^2 \cdot \frac{\partial^2 C}{\partial \rho^2} + \frac{\partial^2 \rho}{\partial R^2}\cdot\frac{\partial C}{\partial \rho} \tag{2.17}$$

$$\frac{\partial C}{\partial R} = \left(\frac{\partial \rho}{\partial R}\cdot\frac{\partial C}{\partial \rho}\right) \tag{2.18}$$

Equations (2.17) and (2.18) can be partially discretised by solving equations (2.15) and (2.16) for $\partial\rho/\partial R$ and $\partial^2\rho/\partial R^2$ in both the electrode zone and over the glass sheath. Hence;

$$\frac{\partial \rho}{\partial R} = \frac{f}{1+f[1-R]} \quad (0 \le R \le 1) \tag{2.19}$$

$$\frac{\partial^2 \rho}{\partial R^2} = \frac{f^2}{(1+f[1-R])^2} \quad (0 \le R \le 1) \tag{2.20}$$

and:

$$\frac{\partial \rho}{\partial R} = \frac{g}{1+g[R-1]} \quad (1 < R \le RG) \tag{2.21}$$

$$\frac{\partial^2 \rho}{\partial R^2} = \frac{-g^2}{(1+g[R-1])^2} \quad (1 < R \le RG) \tag{2.22}$$

Rearrangement of equations (2.15) and (2.16) respectively gives;

$$\exp(-\rho) = 1+f[1-R] \quad (0 \le R \le 1) \tag{2.23}$$

$$\exp(\rho) = 1+g[R-1] \quad (1 < R \le RG) \tag{2.24}$$

Hence, simplification of equations (2.19) to (2.22) is made upon substitution of equations (2.23) and (2.24), where;

$$\frac{\partial \rho}{\partial R} = \frac{f}{\exp(-\rho)} \quad (0 \le R \le 1) \tag{2.25}$$

$$\frac{\partial^2 \rho}{\partial R^2} = \frac{f^2}{(\exp(-\rho))^2} = f^2\exp(2\rho) \quad (0 \le R \le 1) \tag{2.26}$$

and:

$$\frac{\partial \rho}{\partial R} = \frac{g}{\exp(\rho)} \quad (1 < R \le RG) \tag{2.27}$$

$$\frac{\partial^2 \rho}{\partial R^2} = \frac{-g^2}{(\exp(\rho))^2} = -g^2 \exp(-2\rho) \quad (1 < R \leq RG) \tag{2.28}$$

Substitution of equations (2.25) to (2.28), together with equations (2.17) and (2.18) into the time-dependent dimensionless diffusion equation (2.12) gives the mass transport equation subject to the transformation of R space to ρ space in the radial direction. To make the final form of this equation applicable to all values of R, *i.e.* $0 \leq R \leq RG$, f and g are represented as the constants m and s where;

$$m = 1; \quad s = f \; (0 \leq R \leq 1) \tag{2.29}$$

$$m = -1; \quad s = g (1 < R \leq RG) \tag{2.30}$$

Hence equation (2.12) now becomes:

$$\frac{\partial C}{\partial \tau} = s^2 \exp(2m\rho) \frac{\partial^2 C}{\partial \rho^2} + \left[ms^2 \exp(2m\rho) + \frac{s^2 \exp(m\rho)}{s - m\exp(-m\rho) + m}\right] \frac{\partial C}{\partial \rho} + \frac{\partial^2 C}{\partial Z^2} \tag{2.31}$$

In order to calculate the theoretical current response at the SECM tip, this equation must now be solved using the ADI finite-difference method, with respect to the boundary conditions representing the reactions of interest.

2.2.2.2 Finite-Difference Methods

The ADI method is an example of a finite-difference method (FDM). FDMs are widely used to solve differential equations arithmetically by discretising them into a series of finite-difference equations. The basic finite-difference concept may be illustrated simply by considering the case of three equidistant points on an x-y plot represented as (x_{i-1}, y_{i-1}), (x_i, y_i) and (x_{i+1}, y_{i+1}), as shown in Figure 2.3(a), where Δx is the distance $x_{i+1} - x_i = x_i - x_{i-1}$. The first derivative is equal to the slope of the graph and can be represented in three ways:

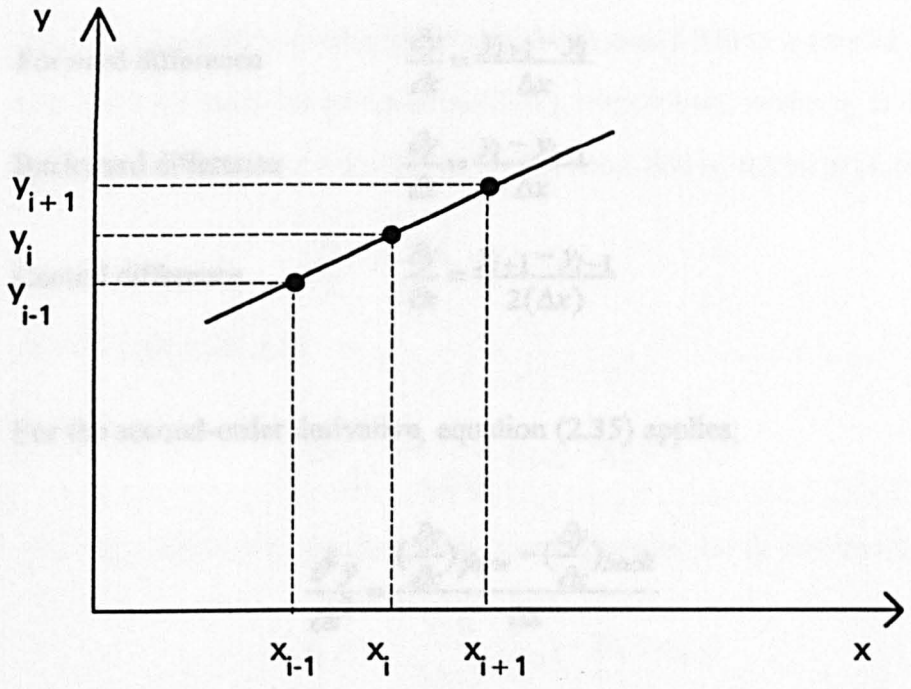

Figure 2.3(a). Point-wise discretisation.

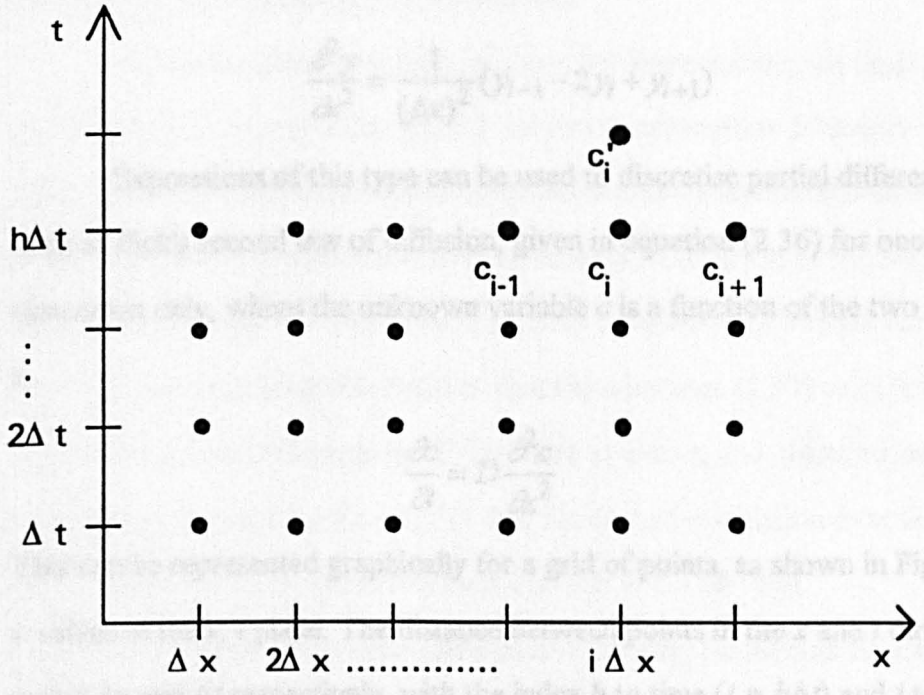

Figure 2.3(b). Space-time point discretisation.

Forward difference $$\frac{\partial y}{\partial x} = \frac{y_{i+1} - y_i}{\Delta x} \tag{2.32}$$

Backward difference $$\frac{\partial y}{\partial x} = \frac{y_i - y_{i-1}}{\Delta x} \tag{2.33}$$

Central difference $$\frac{\partial y}{\partial x} = \frac{y_{i+1} - y_{i-1}}{2(\Delta x)} \tag{2.34}$$

For the second-order derivative, equation (2.35) applies;

$$\frac{\partial^2 y}{\partial x^2} = \frac{(\frac{\partial y}{\partial x})_{forw} - (\frac{\partial y}{\partial x})_{back}}{\Delta x}$$

$$\frac{\partial^2 y}{\partial x^2} = \frac{1}{\Delta x}(\frac{y_{i+1} - y_i}{\Delta x} - \frac{y_i - y_{i-1}}{\Delta x})$$

Hence;

$$\frac{\partial^2 y}{\partial x^2} = \frac{1}{(\Delta x)^2}(y_{i-1} - 2y_i + y_{i+1}) \tag{2.35}$$

Expressions of this type can be used to discretise partial differential equations, such as Fick's second law of diffusion, given in equation (2.36) for one spatial dimension only, where the unknown variable c is a function of the two variables x and t.

$$\frac{\partial c}{\partial t} = D\frac{\partial^2 c}{\partial x^2} \tag{2.36}$$

This can be represented graphically for a grid of points, as shown in Figure 2.3(b) for c values in the x, t plane. The distance between points in the x and t direction are noted Δx and Δt respectively, with the index h to time ($t = h\Delta t$) and i to x ($x = i\Delta x$). Assuming that c values for all x up to time $h\Delta t$ are known, it is possible to determine c' values for the next row at $t + \Delta t = (h+1)\Delta t$. This is performed by generating c_i'

from c_{i-1}, c_i and c_{i+1} using equations (2.32) and (2.35) to discretise the left hand side and right hand side of equation (2.37), respectively, where c_i' is the new concentration at time $t + \Delta t$. Hence the left hand side of equation (2.36) becomes:

$$\frac{\partial c}{\partial t} = \frac{c_i' - c_i}{\Delta t} \tag{2.37}$$

and the right hand side:

$$D\frac{\partial^2 c}{\partial x^2} = \frac{D}{(\Delta x)^2}(c_{i-1} - 2c_i + c_{i+1}) \tag{2.38}$$

combining these two equations to give an expression for c_i' results in:

$$c_i' = c_i + \frac{D\Delta t}{(\Delta x)^2}(c_{i-1} - 2c_i + c_{i+1}) \tag{2.39}$$

This approach is termed the simple explicit method.[242]

2.2.2.3 The ADI finite-difference method

The basis of this method is to solve, by discretisation, the time-dependent form of the diffusion equation (2.31), subject to appropriate boundary conditions, using two finite-difference equations formulated at successive half-time intervals. Considering the first calculation over an interval of time τ to $(\tau + \Delta\tau/2)$, the derivatives $\partial C / \partial \rho$, $\partial^2 C / \partial \rho^2$ and $\partial^2 C / \partial Z^2$ in equation (2.31) are replaced by finite-difference terms, of a similar form to those in equations (2.32) to (2.35) formulated for known concentrations in the Z direction, at time τ, and unknown concentrations in the ρ direction at time $(\tau + \Delta\tau/2)$. For the second calculation over the time interval $(\tau + \Delta\tau/2)$ to $(\tau + \Delta\tau)$, the derivatives $\partial C / \partial \rho$, $\partial^2 C / \partial \rho^2$ and $\partial^2 C / \partial Z^2$ are replaced by finite-difference equations, formulated for known concentrations in the ρ direction at $(\tau + \Delta\tau/2)$ and unknown concentrations in the Z direction at $(\tau + \Delta\tau)$.

The equation for the first half-time step is of the form;

$$\frac{C^*_{j,k}-C_{j,k}}{\Delta\tau/2}=\frac{s^2\exp(2ml\Delta\rho)}{(\Delta\rho)^2}[C^*_{j+1,k}-2C^*_{j,k}+C^*_{j-1,k}]+$$
$$[\frac{C^*_{j+1,k}-C^*_{j-1,k}}{2(\Delta\rho)}][\frac{s^2\exp(ml\Delta\rho)}{s-m\exp(-ml\Delta\rho)+m}+s^2\exp(2ml\Delta\rho)]+ \qquad (2.40)$$
$$\frac{C_{j,k+1}-2C_{j,k}+C_{j,k-1}}{(\Delta Z)^2}$$

where $C_{j,k}$ denotes the normalised concentration of Ox at point j, k. The grid spacings, $\Delta\rho$ and ΔZ, for the radial and Z direction, respectively, are denoted by:

$$\Delta\rho=\ln(1+f)/\mathrm{NE} \quad \text{(electrode vicinity)} \qquad (2.41)$$

$$\Delta\rho=\ln(1+g[RG-1])/\mathrm{NG} \quad \text{(glass sheath)} \qquad (2.42)$$

$$\Delta Z=(d/a)/\mathrm{NZ} \qquad (2.43)$$

In equation (2.40), the integer l = NE - j in the vicinity of the electrode, while $l = j$ - NE in the domain of the glass sheath. An asterisk on the quantity $C_{j,k}$ identifies those concentrations which are to be evaluated at the (new) time, ($\tau + \Delta\tau/2$), from known (old) concentrations evolved at the previous time, τ. This equation applies to all j values, and corresponding k values, subject to boundary conditions.

For the second half-time step the equation is:

$$\frac{C^{**}_{j,k}-C^{*}_{j,k}}{\Delta\tau/2}=\frac{s^2\exp(2ml\Delta\rho)}{(\Delta\rho)^2}[C^{*}_{j+1,k}-2C^{*}_{j,k}+C^{*}_{j-1,k}]+$$

$$[\frac{C^{*}_{j+1,k}-C^{*}_{j-1,k}}{2(\Delta\rho)}][\frac{s^2\exp(ml\Delta\rho)}{s-m\exp(-ml\Delta\rho)+m}+s^2\exp(2ml\Delta\rho)]+ \qquad (2.44)$$

$$\frac{C^{**}_{j,k+1}-2C^{**}_{j,k}+C^{**}_{j,k-1}}{(\Delta Z)^2}$$

where $C^{**}_{j,k}$ are now the new concentrations in the Z direction at time, $(\tau + \Delta\tau)$ to be calculated from the old concentrations in the radial direction calculated at time, $(\tau + \Delta\tau/2)$. The equation applies to all k values and corresponding j values, again subject to the boundary conditions.

For the purpose of the calculation, equations (2.40) and (2.44) are rearranged. For the first-time step (equation (2.40)) the following applies:

$$-\lambda_\rho(j)\{1-\frac{\Delta\rho}{2}[1+\frac{\exp(-ml\Delta\rho)}{s+m-m\exp(-ml\Delta\rho)}]\}C^{*}_{j-1,k}$$

$$+\ [1+2\lambda_\rho(j)]C^{*}_{j,k}$$

$$-\lambda_\rho(j)\{1+\frac{\Delta\rho}{2}[1+\frac{\exp(-ml\Delta\rho)}{s+m-m\exp(-ml\Delta\rho)}]\}C^{*}_{j+1,k} \qquad (2.45)$$

$$=\lambda_z C_{j,k+1}+(1-2\lambda_z)C_{j,k}+\lambda_z C_{j,k-1}$$

where:

$$\lambda_\rho(j)=\frac{(\Delta\tau/2)s^2\exp(2ml\Delta\rho)}{(\Delta\rho)^2} \qquad (2.46)$$

$$\lambda_z=(\Delta\tau/2)/(\Delta Z)^2 \qquad (2.47)$$

For the second-time step, the following applies:

$$-\lambda_z C^{**}_{j,k-1} + (1+2\lambda_z) C^{**}_{j,k} - \lambda_z C^{**}_{j,k+1} =$$

$$+\lambda_\rho(j)\{1-\frac{\Delta\rho}{2}[1+\frac{\exp(-ml\Delta\rho)}{s+m-m\exp(-ml\Delta\rho)}]\}C^{*}_{j-1,k} \qquad (2.48)$$

$$+[1-2\lambda_\rho(j)]C^{*}_{j,k}$$

$$+\lambda_\rho(j)\{1+\frac{\Delta\rho}{2}[1+\frac{\exp(-ml\Delta\rho)}{s+m-m\exp(-ml\Delta\rho)}]\}C^{*}_{j+1,k}$$

After subjecting equation (2.45) to the appropriate boundary conditions (equations (2.4) and (2.6)), it can be condensed into the form of a matrix, consisting of {NE +NG-1}simultaneous equations in {NE+NG-1} unknowns, running successively for each value of k from $k = 1$ to $k = NZ - 1$ ($j = 1$ to $j = NE + NG - 1$). To simplify the matrix terminology, identities are given to the terms found in equation (2.45), as follows:

$$a^{*}_{j} = -\lambda_p(j)\{1-\frac{\Delta\rho}{2}[1+\frac{\exp(-ml\Delta\rho)}{s+m-m\exp(-ml\Delta\rho)}]\} \quad (2 \le j \le (NE+NG-1)) \quad (2.49)$$

$$b^{*}_{j} = 1-\lambda_\rho(j)+\left(\frac{\lambda_\rho\Delta\rho}{2}[1+\frac{\exp(-ml\Delta\rho)}{s+m-m\exp(-ml\Delta\rho)}]\right) \quad (j=1) \qquad (2.50)$$

$$b^{*}_{j} = [1+2\lambda_\rho(j)] \quad (2 \le j \le (NE+NG-1)) \qquad (2.51)$$

$$c^{*}_{j} = -\lambda_p(j)\{1+\frac{\Delta\rho}{2}[1+\frac{\exp(-ml\Delta\rho)}{s+m-m\exp(-ml\Delta\rho)}]\} \quad (1 \le j \le (NE+NG-2)) \quad (2.52)$$

The corresponding known concentrations in the Z direction are represented as follows:

$$\lambda_z C_{j,k+1} + [1-2\lambda_z]C_{j,k} + \lambda_z C_{j,k-1} = d_j \quad (1 \le j \le (NE+NG-2)) \qquad (2.53)$$

$$d_{NE+NG-1} = \lambda_z C_{NE+NG-1,k+1} + [1-2\lambda_z] C_{NE+NG-1,k} + \lambda_z C_{NE+NG-1,k+1} + \lambda_\rho \{1 + \frac{\Delta\rho}{2}[1 + \frac{\exp(-ml\Delta\rho)}{s+m-m\exp(-ml\Delta\rho)}]\} \quad (j = NE+NG-1) \quad (2.54)$$

Equation (2.45) can now be written as:

$$\begin{array}{ll} j=1 & b_1^* C_1^* + c_1^* C_2^* = d_1 \\ j=2,\ 3\ \ldots\ldots & \\ \rightarrow NE+NG-2 & a_j^* C_{j-1,k}^* + b_j^* C_{j,k}^* + c_j^* C_{j+1,k}^* = d_j \\ j=NE+NG-1 & a_{NE+NG-1}^* C_{NE+NG-2,k}^* + b_{NE+NG-1}^* C_{NE+NG-1,k}^* = d_{NE+NG-1} \end{array} \quad (2.55)$$

$$(1 \le k \le NZ-1)$$

which in matrix form is represented as:

$$\begin{bmatrix} b_1^* & c_1^* & & & & \\ a_2^* & b_2^* & c_2^* & & & \\ 0 & a_3^* & b_3^* & c_3^* & & \\ & \cdot & \cdot & \cdot & & \\ & & \cdot & \cdot & \cdot & \\ & & & \cdot & \cdot & \cdot \\ & & & & a_{NE+NG-1}^* & b_{NE+NG-1}^* \end{bmatrix} \begin{bmatrix} C_1^* \\ C_2^* \\ C_3^* \\ \cdot \\ \cdot \\ \cdot \\ C_{NE+NG-1}^* \end{bmatrix} = \begin{bmatrix} d_1 \\ d_2 \\ d_3 \\ \cdot \\ \cdot \\ \cdot \\ d_{NE+NG-1} \end{bmatrix}$$

$$(1 \le k \le NZ-1) \quad (2.56)$$

The initial condition, given by equation (2.2), supplies the first set of values for the vector $[d]_{1 \le j \le NE+NG-1,k}$ for each value of k, from which the corresponding values of $C^*_{1 \le j \le NE+NG-1,k}$ can be calculated. Since equation (2.56) is a tridiagonal matrix equation, the Thomas Algorithm[240,241,249] can be used to provide an efficient method of solution (see Appendix 1).

For the second half-time step, equation (2.48) is also condensed into the form of a matrix. As the concentration terms in Z are now unknown, it is the boundary conditions in this direction, for the surface of the probe and the substrate, which are applicable as given by equations (2.3) and (2.7). The latter is especially important as it represents the substrate reactivity, in this case an inert surface. Equation (2.48) is rearranged to give:

$$\begin{array}{ll} k=1 & b_1^{**}C_{j,1}^{**} + c_1^{**}C_{j,2}^{*} = d_1^{*} \\ k=2,3\ldots \rightarrow \mathrm{NZ}-2 & a_k^{**}C_{j,k-1}^{**} + b_k^{**}C_{j,k}^{**} + c_k^{**}C_{j,k+1}^{**} = d_2^{*} \\ k=\mathrm{NZ}-1 & a_{\mathrm{NZ}-1}^{**}C_{j,\mathrm{NZ}-2}^{**} + b_{\mathrm{NZ}-1}^{**}C_{j,\mathrm{NZ}-1}^{**} = d_{\mathrm{NZ}-1} \end{array} \qquad (2.57)$$

$$(1 \le j \le \mathrm{NE}+\mathrm{NG}-1)$$

which in matrix form is represented as:

$$\begin{bmatrix} b_1^{**} & c_1^{**} & & & & \\ a_2^{**} & b_2^{**} & c_2^{**} & & & \\ 0 & a_3^{**} & b_3^{**} & c_3^{**} & & \\ & \cdot & \cdot & \cdot & & \\ & & \cdot & \cdot & \cdot & \\ & & & \cdot & \cdot & \cdot \\ & & & a_{\mathrm{NZ}-1}^{**} & b_{\mathrm{NZ}-1}^{**} & \end{bmatrix} \begin{bmatrix} C_1^{**} \\ C_2^{**} \\ C_3^{**} \\ \cdot \\ \cdot \\ \cdot \\ C_{\mathrm{NZ}-1}^{*} \end{bmatrix} = \begin{bmatrix} d_1^{*} \\ d_2^{*} \\ d_3^{*} \\ \cdot \\ \cdot \\ \cdot \\ d_{\mathrm{NZ}-1}^{*} \end{bmatrix} \qquad (2.58)$$

$$(1 \le j \le \mathrm{NE}+\mathrm{NG}-1)$$

where:

$$a_k^{**} = -\lambda_z \quad (2 \le k \le \mathrm{NZ}-1)\ (1 \le j \le \mathrm{NE}+\mathrm{NG}-1) \qquad (2.59)$$

$$b_k^{**} = 1+2\lambda_z \quad (k=1)\ (1 \le j \le \mathrm{NE}) \qquad (2.60)$$

$$b_k^{**} = 1+\lambda_z \quad (k=1)\ (\mathrm{NE}+1 \le j \le \mathrm{NE}+\mathrm{NG}-1) \qquad (2.61)$$

$$b_k^{**} = 1+2\lambda_z \quad (2 \le k \le \mathrm{NZ}-2)\ (1 \le j \le \mathrm{NE}+\mathrm{NG}-1) \qquad (2.62)$$

$$b_k^{**} = 1+\lambda_z \quad (k=\mathrm{NZ}-1)\ (1 \le j \le \mathrm{NE}+\mathrm{NG}-1) \qquad (2.63)$$

$$c_k^{**} = -\lambda_z \quad (1 \le k \le \mathrm{NZ}-2)\ (1 \le j \le \mathrm{NE}+\mathrm{NG}-1) \qquad (2.64)$$

$$d_k^{*} = \text{right hand side of equation (2.45)}\ (2 \le k \le \mathrm{NZ}-2)\ (1 \le j \le \mathrm{NE}+\mathrm{NG}-1) \qquad (2.65)$$

The known values for the vector $[d^*]_{1\le k\le \mathrm{NZ}-1,j}$ for each value of j are calculated from the corresponding $C_{j,k}{}^{*}$ values evaluated from the previous time step. Values of $C_{j,k}{}^{**}$ are then calculated by solving the above matrix equation (equation 2.58) for successive j values, starting at $j = 1$ boundary and working across to the radial edge of the glass sheath, j = NE+NG-1.

At the end of the second half-time step, the current at the electrode is evaluated (equation (2.14)) by the summation of the local fluxes in the normal direction.[250]

$$\frac{i}{i(\infty)} = \frac{\pi}{4\Delta \mathrm{Z}} \sum_{j=0}^{j=\mathrm{NE}} (c_{j,1}^{**} - c_{j-1,1}^{**}) \left(\left(1 - \frac{\exp[\{\ln(1+f)\}.(1-\frac{j}{\mathrm{NE}})-1}{f} \right)^2 - \left(1 - \frac{\exp[\{\ln(1+f)\}.(1-\frac{j-1}{\mathrm{NE}})-1}{f} \right)^2 \right) \qquad (2.66)$$

The calculation proceeds to the next time step, with the values for $[d]_{1\le j\le \mathrm{NE}+\mathrm{NG}-1}$ along each row formulated from the previous $C_{j,k}{}^{**}$ This procedure continues until the system either approaches a steady-state or a particular period of time has elapsed.

2.3 Execution of the SECM problem

The above formulation, coded in Fortran 77, in double precision, is listed in Appendix 2. The program was executed on either a University of Warwick Central Sun System computer or a Hewlett Packard 735 Workstation. The typical number of points utilised in the radial direction over the electrode and glass sheath, NE and NG

respectively and in the Z direction, NZ, was 80. This ensured that there were a sufficient number of points to cover the reactive area with the required accuracy and computer time, per application, was kept to a minimum (typically 5-10 minutes CPU).

2.3.1 Theoretical Results for Negative Feedback

The problem outlined above treats the case of SECM negative feedback with an inert surface, simulating the current-time response as a function of tip/substrate distance, expressed as:

$$L = d / a \qquad (2.67)$$

Although this problem has been treated previously,[146,147] it is useful to review briefly the results since they correspond to a limit of no reactivity in all of the SECM induced dissolution studies described in this thesis.

A typical series of theoretical transients (plotted as $i/i(\infty)$ against $\tau^{-1/2}$) is shown in Figure 2.4 for L values of 0.1 (lower curve), 0.16, 0.25, 0.40 and 1.00 (upper curve). At the shortest time $\tau^{-1/2} > 30$, the UME response is identical for all values of L, since under these conditions, the diffusion field adjacent to the electrode is much smaller than the tip/substrate separation and hence the inert surface has no effect on diffusion to the electrode. At longer times, sufficient for the diffusion field to intercept the surface, the $i/i(\infty)$ versus $\tau^{-1/2}$ characteristics, reflect the degree diffusion to the electrode is hindered by the presence of the inert surface. As L decreases, diffusion to the electrode becomes more hindered resulting in the current response falling more steeply at shorter times and attaining lower values at longer times.

The ability to predict both the steady-state limiting current and the $i/i(\infty)$ versus $\tau^{-1/2}$ characteristics for a given L value illustrates the power of the ADI finite-difference method.

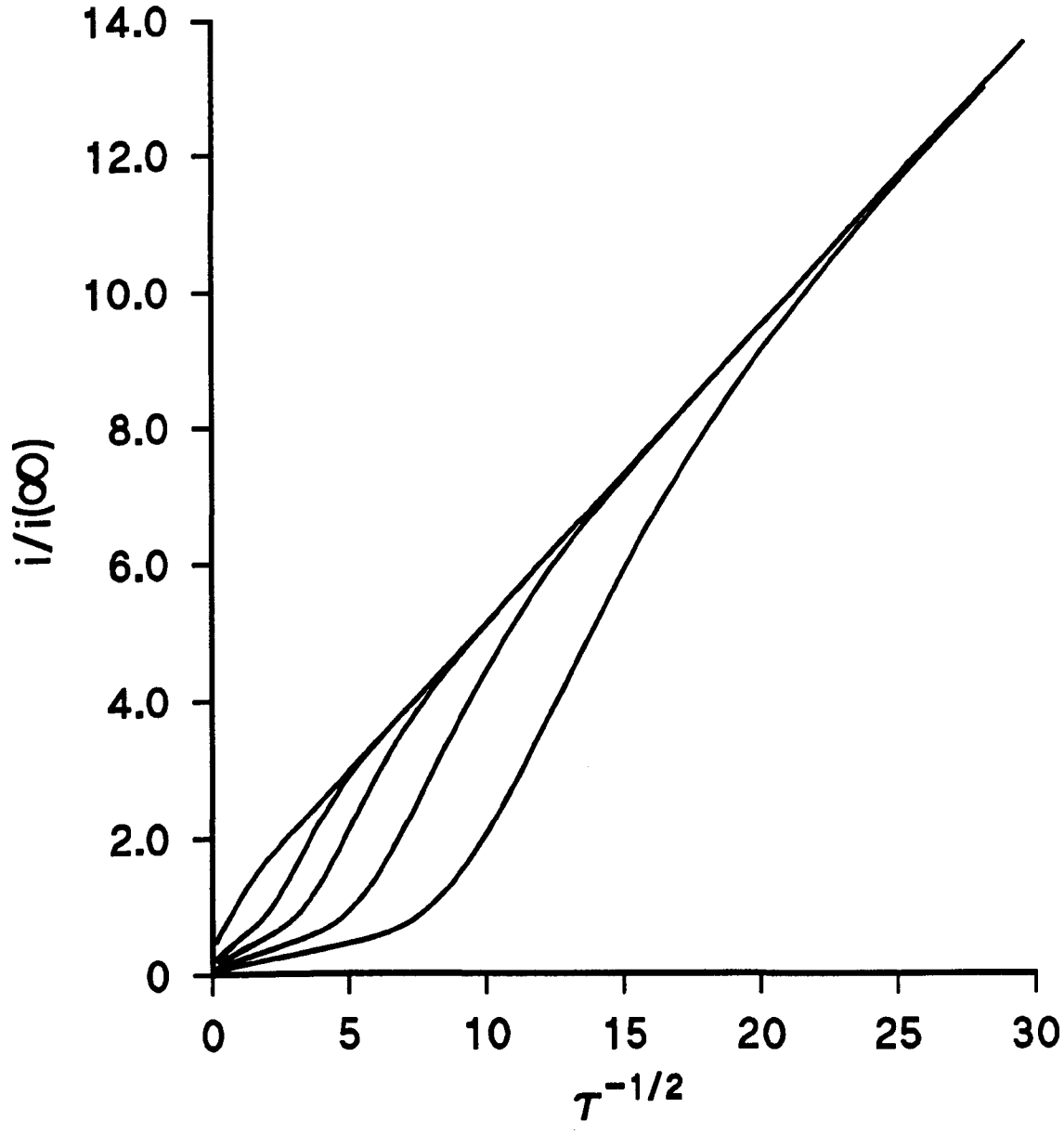

Figure 2.4. Simulated SECM negative feedback current transients, displayed as $i/i(\infty)$ versus $\tau^{-1/2}$ for $L = 0.1$ (lower curve), 0.16, 0.25, 0.40 and 1.00 (upper curve).

2.4 Application to SECM Induced Dissolution Studies

A brief outline will be given as to how the negative feedback model can be adapted to treat the case of SECM induced dissolution. The method will be illustrated with a simple case. Additional modifications to the dissolution theory, to include factors such as migration and diffusion mass transfer, will be discussed in more detail in the chapters relating to the specific dissolution systems of interest.

2.4.1 Dissolution Rate Laws

Since the process of interest is dissolution from a crystal surface, the boundary condition at the substrate/solution interface must reflect the dissolution rate law. Although a large number of rate equations, both mechanistic and empirical,[1,2,4,10] have been proposed to describe the dissolution of ionic crystals, the applicability of many of them has been questioned.[1] It is therefore instructive to use two simple well-established kinetic cases in which the dissolution rate is controlled by first- and second-order terms in the interfacial undersaturation, which also arise as limits to the spiral dislocation mechanism,[4] introduced by Burton, Cabrera and Frank. In the latter context, the first-order rate law applies at high undersaturations, when desorption is rate limiting, while the second-order rate law holds for low undersaturations when surface diffusion limits the rate.

For a crystal such as that represented in Chapter 1, equation (1.1), the rate law is therefore written as:

$$j_{M_yX_z} = j_{M^{z+}} / y = j_{X^{y-}} / z = k_n \sigma^n \qquad (2.68)$$

where j_i denotes the rate of the dissolution reaction in terms of the flux of species i (where i is M^{z+}, X^{y-} or M_yX_z), k_n is the dissolution rate constant, n represents the order of the dissolution process (n = 1 or 2) and σ is the relative undersaturation *at the crystal/solution interface* which is defined by:

$$\sigma = 1 - S \tag{2.69}$$

S is the saturation ratio and is given by equation (2.70)

$$S = (I_p / K_s)^{1/\nu} \tag{2.70}$$

where I_p is the ionic activity product, K_s is the solubility product and ν the number of ions in the formal unit of the ionic crystal. Hence for M_yX_z:

$$S = \left(\frac{a^y_{M^{z+}} a^z_{X^{y-}}}{(a^y_{M^{z+}})^* (a^z_{X^{y-}})^*} \right)^{1/y+z} \tag{2.71}$$

where a_i denotes the activity of the species i and the asterisk indicates the saturated solution value.

In the simplest case the dissolution problem is readily condensed to the consideration of only one species if conditions are set such that the concentration of the electroinactive detected ion in the experiment remains constant during a measurement. Assuming X^{y-} is the buffered electroinactive ion and M^{z+} is the electrochemically active species, equation (2.71) now becomes:

$$S = \left(\frac{a^y_{M^{z+}}}{(a^y_{M^{z+}})^*} \right)^{1/y+z} \tag{2.72}$$

2.4.2 Formulation and Solution of the SECM Dissolution Problem

In the case of SECM induced dissolution, the experimental conditions are such that the boundary conditions, given by equations (2.2) to (2.6) also apply. For a one species dissolution problem, equation (2.7) which represents the substrate reactivity, now becomes:

$$D_{M^{z+}} (\partial a_{M^{z+}} / \partial z)_{z=d} = -k_n \sigma^n \tag{2.73}$$

Assuming the concentration of X^{y-} remains constant, equation (2.73) can be written as:

$$D_{M^{z+}}\gamma_{M^{z+}}(\partial c_{M^{z+}}/\partial z)_{z=d} = -k_n[1-(c_{M^{z+}}/c^*_{M^{z+}})^{1/y+z}]^n \qquad (2.74)$$

where $\gamma_{M^{z+}}$ is the activity coefficient of M^{z+} which is treated as a constant, and $c^*_{M^{z+}}$ is the bulk concentration of M^{z+}.

The dissolution rate constant is cast into a dimensionless form through application of equation (2.75):

$$K_n = \frac{k_n a}{D_{M^{z+}} a^*_{M^{z+}}} \qquad (2.75)$$

For the limiting dissolution kinetic regimes, *i.e.* an inert crystal surface and a diffusion-controlled dissolution reaction, the boundary conditions given by equations (2.7) and (2.76) apply:

$z = d,\ 0 \le r \le r_s$: $c_{M^{z+}_{z=d}} = c^*_{M^{z+}}$ diffusion-controlled dissolution (2.76)

2.4.2.1 The ADI finite-difference method applied to the SECM dissolution problem

During the first half-time step, in which the calculation proceeds in the radial direction, the concentrations at the probe and the substrate are known (old) values and the radial boundary conditions are as defined previously. Therefore there are no dramatic changes to the ADI algorithm at this stage. During the second half-time step, the boundary conditions must be applied to the Z terms to eliminate the point $C^{**}_{j,NZ(1\le j\le NE+NG)}$ from the calculation, as discussed in section 2.2.2.3 for the case of an inert surface where a no-flux condition prevailed. The form of equation (2.48) at the substrate boundary is:

$$-\lambda_z C^{**}_{j,\mathrm{NZ}-2} + (1+2\lambda_z) C^{**}_{j,\mathrm{NZ}-1} - \lambda_z C^{**}_{j,\mathrm{NZ}} =$$

$$+\lambda_\rho(j)\{1-\frac{\Delta\rho}{2}[1+\frac{\exp(-ml\Delta\rho)}{s+m-m\exp(-ml\Delta\rho)}]\}C^{*}_{j-1,\mathrm{NZ}-1} \qquad (2.77)$$

$$+[1-2\lambda_\rho(j)]C^{*}_{j,\mathrm{NZ}-1}$$

$$+\lambda_\rho(j)\{1+\frac{\Delta\rho}{2}[1+\frac{\exp(-ml\Delta\rho)}{s+m-m\exp(-ml\Delta\rho)}]\}C^{*}_{j+1,\mathrm{NZ}-1}$$

$C^{**}_{j,\mathrm{NZ}}$ can be eliminated from equation (2.77) by consideration of the substrate boundary condition reflecting the dissolution rate law, given by equations (2.74) and (2.75), where

$$\frac{C^{**}_{j,\mathrm{NZ}-1} - C^{**}_{j,\mathrm{NZ}}}{\Delta Z} = -K_n\left[1-\left(C^{**}_{j,\mathrm{NZ}}\right)^{1/y+z}\right]^n \qquad (2.78)$$

Upon rearrangement, assuming the simplest kinetic case where $1/y+z$ and n are both unity, an expression for $C^{**}_{j,\mathrm{NZ}}$ in terms of $C^{**}_{j,\mathrm{NZ}-1}$ can be derived:

$$C^{**}_{j,\mathrm{NZ}} = \left(\frac{C^{**}_{j,\mathrm{NZ}-1} + K_n\Delta Z}{1+K_n\Delta Z}\right) \qquad (2.79)$$

Thus equation (2.77) becomes:

$$-\lambda_z C^{**}_{j,\mathrm{NZ-2}} + [1+\lambda_z\,(2-\frac{1}{1+K_n\Delta Z})]C^{**}_{j,\mathrm{NZ-1}} =$$

$$+\lambda_\rho(j)\{1-\frac{\Delta\rho}{2}[1+\frac{\exp(-ml\Delta\rho)}{s+m-m\exp(-ml\Delta\rho)}]\}C^{*}_{j-1,\mathrm{NZ-1}} \qquad (2.80)$$

$$+[1-2\lambda_\rho(j)]C^{*}_{j,\mathrm{NZ-1}}$$

$$+\lambda_\rho(j)\{1+\frac{\Delta\rho}{2}[1+\frac{\exp(-ml\Delta\rho)}{s+m-m\exp(-ml\Delta\rho)}]\}C^{*}_{j+1,\mathrm{NZ-1}}$$

$$+\frac{\lambda_z K_n\Delta Z}{1+K_n\Delta Z}$$

where $b^{**}_{\mathrm{NZ-1}}$ is expressed as:

$$b^{**}_{\mathrm{NZ-1}} = 1+\lambda_z\left(2-\frac{1}{1+K_n\Delta Z}\right) \qquad (2.81)$$

and $d^{*}_{\mathrm{NZ-1}}$ becomes:

$$d_{\mathrm{NZ-1}} = \lambda_\rho(j)\{1-\frac{\Delta\rho}{2}[1+\frac{\exp(-ml\Delta\rho)}{s+m-m\exp(-ml\Delta\rho)}]\}C^{*}_{j-1,\mathrm{NZ-1}}$$

$$+[1-2\lambda_\rho(j)]C^{*}_{j,\mathrm{NZ-1}}$$

$$+\lambda_\rho(j)\{1+\frac{\Delta\rho}{2}[1+\frac{\exp(-ml\Delta\rho)}{s+m-m\exp(-ml\Delta\rho)}]\}C^{*}_{j+1,\mathrm{NZ-1}}$$

$$+\frac{\lambda_z K_n\Delta Z}{1+K_n\Delta Z}$$

(2.82)

In this way the Thomas Algorithm is readily applied, as in the case of an inert surface. Once all the new concentrations have been obtained for the solution $C^{**}_{j,k}(1\le j\le \mathrm{NE}+\mathrm{NG}-1; 1\le k\le \mathrm{NZ}-1)$, the boundary conditions can be applied to obtain the new concentrations at the boundary. Once the current has been evaluated (equation 2.66) the new concentrations become the old concentrations and the

calculation proceeds as discussed in section 2.2.2.3. More complicated rate laws may also be treated in a similar manner, but these are discussed for the specific areas of interest in the relevant chapters of this thesis.

CHAPTER 3

EXPERIMENTAL

This chapter surveys the experimental techniques employed in the studies described in this thesis. Details are given of: (i) the fabrication of UMEs; (ii) the instrumentation for SECM and dynamic electrochemical measurements; (iii) the integrated electrochemical-AFM instrumentation; (iv) the microjet electrode instrumentation; (v) the solutions and substrates used. Due to the wide variety of experimental procedures adopted, for the systems of interest, it is not appropriate to give a detailed account of these in this chapter. Rather, detailed procedures will be given in the chapters relating to specific dissolution systems.

3.1 SECM Ultramicroelectrode Fabrication Procedures

3.1.1 SECM Electrodes (disc diameter 10 μm or greater)

The fabrication of SECM UMEs was in general accordance with the procedure adopted by Wightman and Wipf[251] and Bard and co-workers.[116] Figure 3.1(a) shows a schematic diagram of a SECM disc UME. A glass capillary (borosilicate glass, 2 mm o. d., 1.16 mm i. d., Clark Electromedical Instruments, Reading) was drawn down to a very fine point under the application of high temperatures and a fixed weight, using a micropipette puller (PB-7, Narishige Co. Ltd., Japan). The end was then sealed in the flame of a bunsen burner.

Approximately 10 mm of the wire used (Pt 99.99 % purity, 10, 25 or 50 μm diameter; Ag 99.99 % purity, 50 or 125 μm diameter, all from Goodfellow) was cut and inserted into the open end of the capillary. Gentle tapping of the glass ensured that the wire was located at the sealed end of the capillary. The capillary was then secured on the micropipette puller so that the tapered end, containing the wire, was

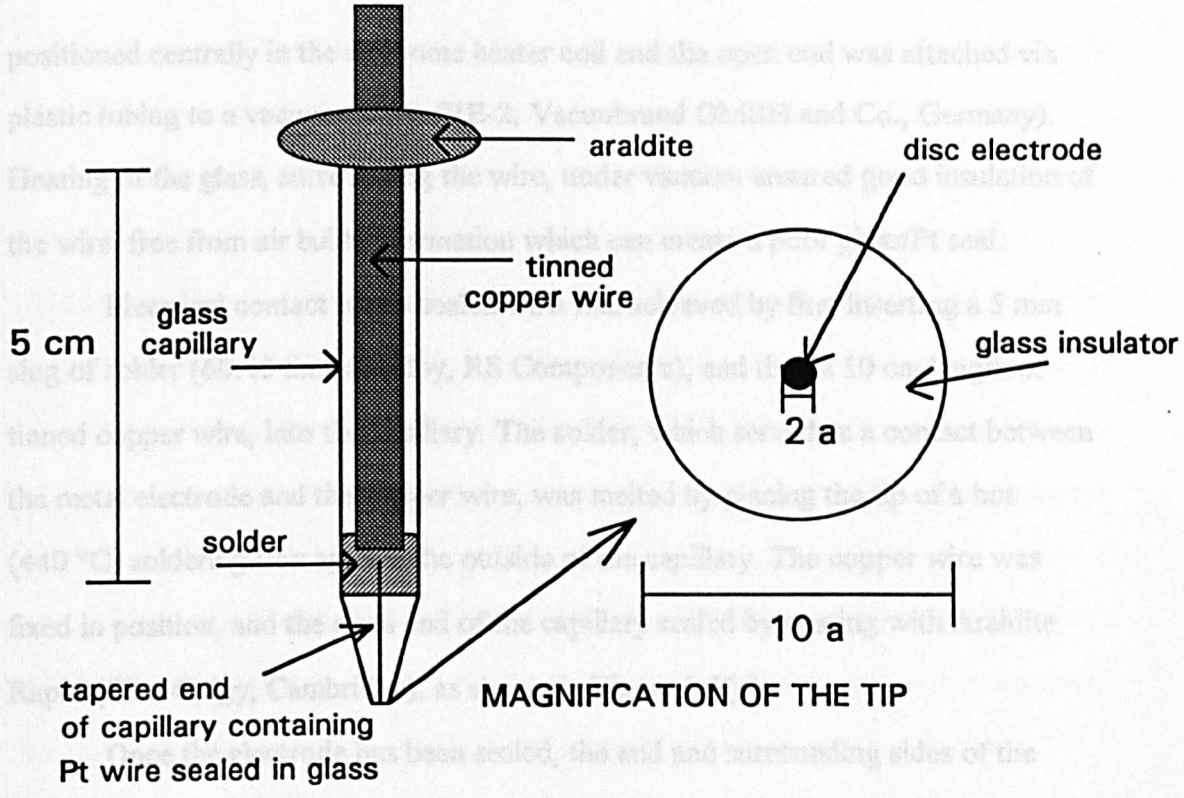

Figure 3.1(a). Schematic diagram of the components of a disc UME.

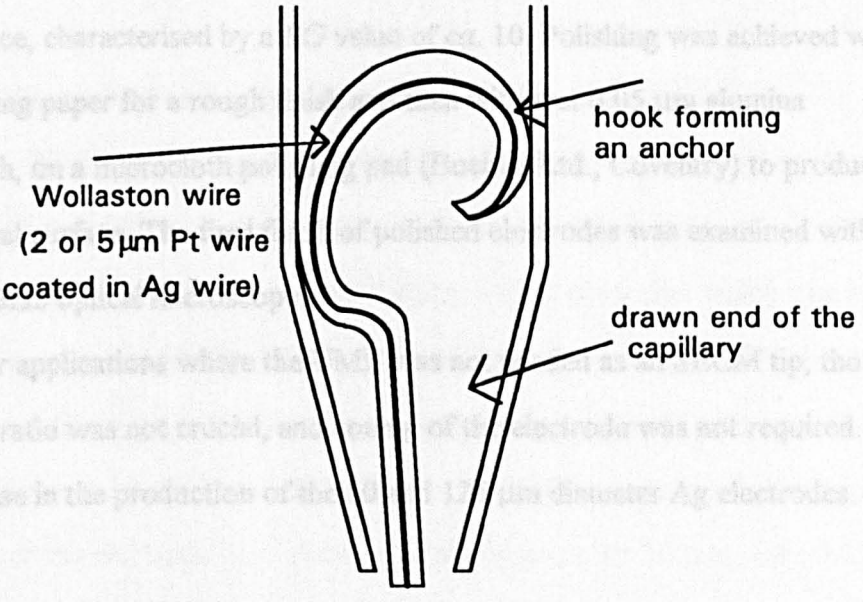

Figure 3.1(b). Schematic diagram showing the position of the hooked and straight parts of the Wollaston wire in the tapered shank of the unsealed capillary.

positioned centrally in the nichrome heater coil and the open end was attached via plastic tubing to a vacuum pump (RE-2, Vacuubrand GMBH and Co., Germany). Heating of the glass, surrounding the wire, under vacuum ensured good insulation of the wire, free from air bubble formation which can create a poor glass/Pt seal.

Electrical contact to the sealed wire was achieved by first inserting a 5 mm slug of solder (60:40 tin:lead alloy, RS Components), and then a 10 cm length of tinned copper wire, into the capillary. The solder, which served as a contact between the metal electrode and the copper wire, was melted by placing the tip of a hot (440 °C) soldering iron against the outside of the capillary. The copper wire was fixed in position, and the open end of the capillary sealed by coating with Araldite Rapid (Ciba-Geigy, Cambridge), as shown in Figure 3.1(a).

Once the electrode has been sealed, the end and surrounding sides of the probe must be polished flat and "coned", in order to expose the metal disc electrode with the desired SECM geometry. This stage is crucial in the production of SECM UMEs, requiring the fabrication of a flat, planar electrode plus surrounding insulating glass surface, characterised by a *RG* value of *ca.* 10. Polishing was achieved with 600 grit polishing paper for a rough finish and then with wet 0.05 μm alumina micropolish, on a microcloth polishing pad (Buehler Ltd., Coventry) to produce an optically flat surface. The final finish of polished electrodes was examined with an Olympus BH2 optical microscope.

For applications where the UME was not needed as an SECM tip, the value of the *RG* ratio was not crucial, and coning of the electrode was not required. This was the case in the production of the 50 and 125 μm diameter Ag electrodes.

3.1.2 SECM Electrodes (disc diameter of 2 or 5 μm)

For the manufacture of Pt disc electrodes characterised by a diameter of 2.0 or 5.0 μm, the procedure adopted was slightly different[245] as Pt wire of this size is

too small and fragile to handle and is therefore supplied in the form of Wollaston wire (Goodfellow, in which the metal of interest is coated with a 50 μm thick Ag layer).

A 15 mm length of Wollaston wire was cut using a sharp blade and 5 mm of one end was bent into a hook. The wire was then dropped down a drawn, but unsealed, capillary until the hook, acting as an anchor, secured the wire just above the tapered end of the capillary. In this way the straight part of the wire was suspended in the narrow shank as shown in Figure 3.1(b). The silver coating was removed from the Wollaston wire in this part of the glass shank by dipping the tip of the capillary into a 1:1 nitric acid/water solution.

Upon completion of the Ag layer removal, nitric acid was removed from the capillary by dipping the tip repeatedly in water (up to ten times), and then in acetone. Prior to each immersion, the liquid remaining in the shank, from the previous immersion, was removed using tissue paper. The tip of the open capillary was sealed in a bunsen burner flame and the fabrication procedure was then as outlined in section 3.1.1.

3.2 SECM Instrumentation and Apparatus

The SECM was designed such that the UME tip was mounted on three closed loop TSE-75 translation stages from Burleigh Instruments (Fischer, N. J.), in an *x*, *y*, *z* configuration. The stages were controlled by a 6200 controller which was interfaced to an IBM compatible 486DX 66MHz personal computer using a PC-Lab model 660 interface card (Burleigh). A schematic and photograph of the SECM employed are shown in Figure 1.10 and Figure 3.2 respectively. This instrumentation allowed movement of the electrode in all three axial directions, over 25 mm, with 0.05 μm maximum resolution, enabling the tip to be scanned in close proximity to, or positioned at, targeted distances from a sample surface.

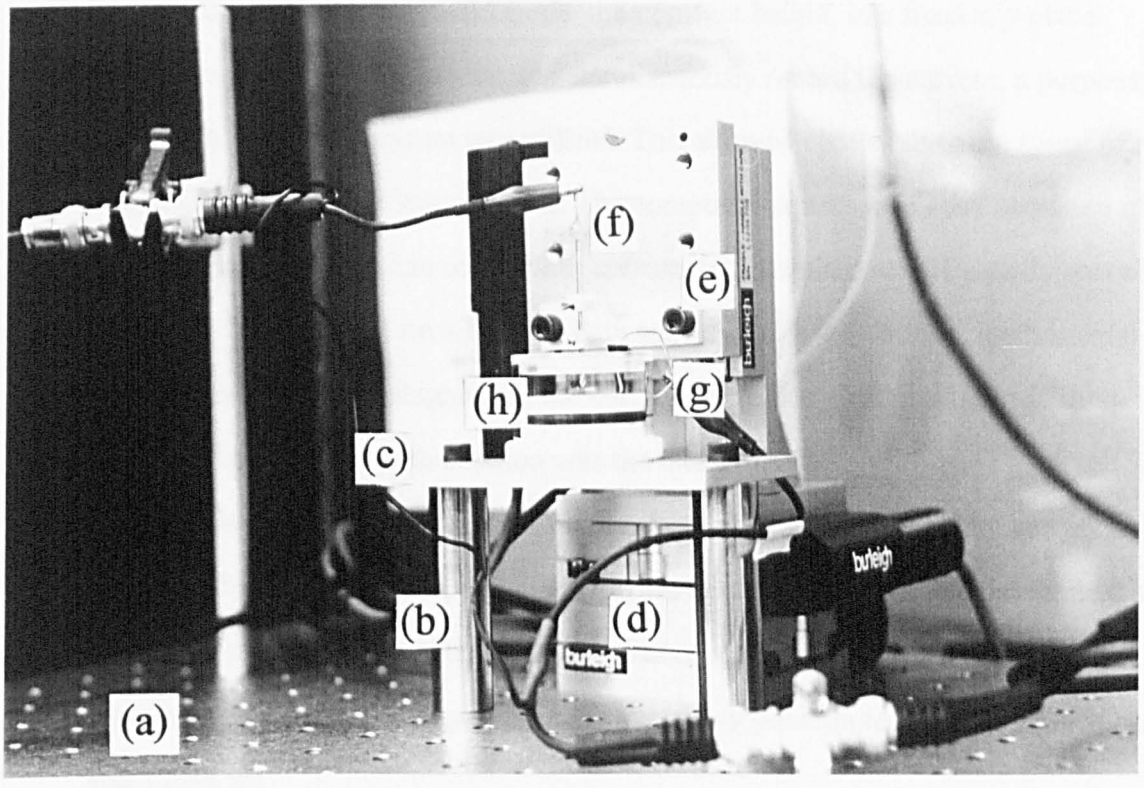

(a) breadboard

(b) stainless steel poles

(c) aluminium plate

(d) closed loop translation stages

(e) aluminium UME holder

(f) UME

(g) Ag wire

(h) SECM dissolution cell

Figure 3.2. Photograph of the SECM instrumentation.

For experiments requiring fixed tip/substrate distances, the stages were controlled either manually through the use of a joystick (Burleigh, model 6003) or via the computer, using a program supplied by Burleigh. For imaging experiments, where it was necessary to scan the electrode at a constant height, in a fixed x, y plane parallel to the surface of interest and simultaneously record the current, a purpose written QuickBasic program was utilised. This allowed control over the speed of the stages and the targeted imaging area. The composite square area scan consisted of a series of unidirectional line scans, with current data acquired at 101 equally spaced points per line recorded on a Lab-PC data acquisition card (National Instruments) after conversion to a voltage using the current transducer described later in this section. The datum at each position was the mean of 100 current readings. Each line scan was separated by a constant step size. Both values (*i.e.* scan width and step size) could be altered as required, depending on the nature of the scanning experiment and the size of the electrode utilised. The program outputted the data in the form of current (recorded as a voltage) as a function of x, y position to both the PC screen and a data file.

The stages were mounted on a Newport CSD series breadboard, which in turn was placed on a custom built marble bench incorporating vibration isolators. The piezoeletric stages and breadboard were encased in a Faraday cage (built in house) in order to eliminate stray electrical noise.

All measurements were made using a two electrode arrangement, with the Pt UME as the working electrode and a silver wire serving as a quasi-reference electrode (AgQRE) in home built electrochemical cells. The UME was secured onto the translation stages via a home built aluminium holder. With this device the electrode was held firm in two separate places, ensuring that it remained with its axis normal to the surface of the substrate of interest.

The electrochemical cells were designed to be fully detachable, consisting of a cell base, a cylindrical body and a lid as shown in Figure 3.3. The bases were constructed out of teflon or perspex, with a typical diameter of 4.0 cm. A recess was included, half way up, around the circumference of all cell bases in order to accommodate a chemically inert 'viton' O-ring (James Walker & Co. Ltd., Cumbria). This acted as a seal between the base and the cell body, preventing leakage of both aqueous and organic solvents.

Precision bore cylindrical glass (40 mm, i.d., Chance Bros., Malvern) was used to construct the cell body. This was attached to the base by pushing it gently over the O-ring. A perspex or teflon lid fitted onto the top of the cell, and contained holes for the UME (typically 2 cm in diameter in order to allow movement of the UME when utilised in the SECM imaging mode) and the reference electrode. Some lids also contained ports for degassing lines, when this facility was required.

The substrates utilised in the experiments were secured to the base of the cell so that their top face lay parallel with the base and perpendicular to the cylindrical axis of the UME probe. Due to the variety of substrates utilised, several different cell bases were constructed. For experiments with glass disc substrates, the cell base contained a recess into which the disc could be secured with teflon tape. When a UME was used as the substrate, a hole was bored out in the centre of the base so that the electrode could be accommodated securely. Copper sulfate pentahydrate crystals, potassium ferrocyanide crystals and silver chloride pellets were secured to a piece of tape, adhered to a flat cell base, and the crystal was firmly held in place using, where appropriate, double sided adhesive tape, epoxy resin or 'Superglue 4' (Bostik, Leicester, U. K.).

When using organic solvents, teflon cells were utilised to resist chemical attack. The adhesives quoted above were inefficient under these solvent conditions and the crystal was affixed to the base using teflon anchors positioned firmly over

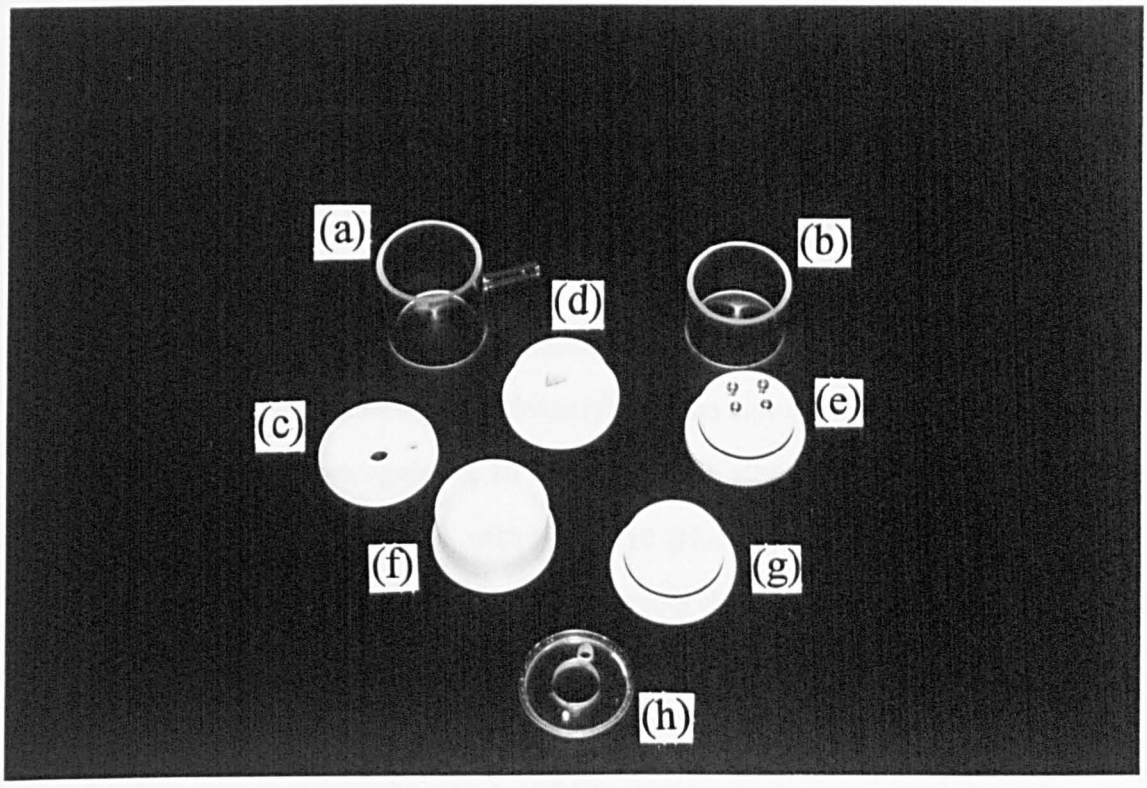

(a) MJE glass cell body

(b) typical glass cell body

(c) teflon lid

(d) teflon cell base

(e) teflon base with anchors attached for use with KBr crystals in acetonitrile solutions

(f) HDPE undetachable cell base and body

(g) teflon cell base with recess for glass disc

(h) perspex cell lid

Figure 3.3. The electrochemical cells employed in SECM experiments.

both ends of the substrate using small screws. For experiments involving the use of aqueous saturated silver chloride solutions, the electrochemical cell was prepared from high density polyethylene (HDPE), with the base and body now undetachable.

The cells were mounted either on top of a home built aluminium platform using double sided adhesive tape or in an aluminium plate which was held in position by two supporting, stainless steel poles attached to the breadboard, as schematically depicted in Figure 3.5.

The UME potential was controlled with a purpose-built triangular wave/pulse generator (Colburn Electronic, Coventry) and the current was measured with a home built current follower (gains of 10^{-5} to 10^{-9} A/V). Chronoamperometric characteristics were acquired with a NIC310 (Nicolet) digital storage oscilloscope with disc storage capabilities. Current-potential characteristics were recorded directly on an *x*, *y* recorder (PL3, Lloyd Instruments, Southampton, U. K.).

3.3 Integrated electrochemical-AFM instrumentation

AFM experiments were carried out during a visit to Professor A. J. Bard's laboratory at the University of Texas at Austin and utilised a Nanoscope III scanned probe microscope and fluid cell (Digital Instruments, Santa Barbara, CA). A schematic of the cell geometry is shown in Figure 3.4. The AFM was equipped with a scan head allowing a maximum scan range of 14 μm by 14 μm, but images were generally acquired over an area of 7 μm by 7 μm. AFM probes (Nanoprobe, Park Scientific, Sunnyvale, CA) consisted of silicon nitride cantilevers (length 200 μm, spring constant 0.06 N/m) with integrated pyramidal tips, which had a height of 2.86 μm and a base width of 4 μm. The entire cantilever and support was sputter coated first with Cr (100 Å) and then with Pt (300 Å). A thicker Pt coat would induce a bend in the cantilever and prevent the laser diode-detection system of the AFM from being properly aligned. After the Pt-coated AFM probe had been secured

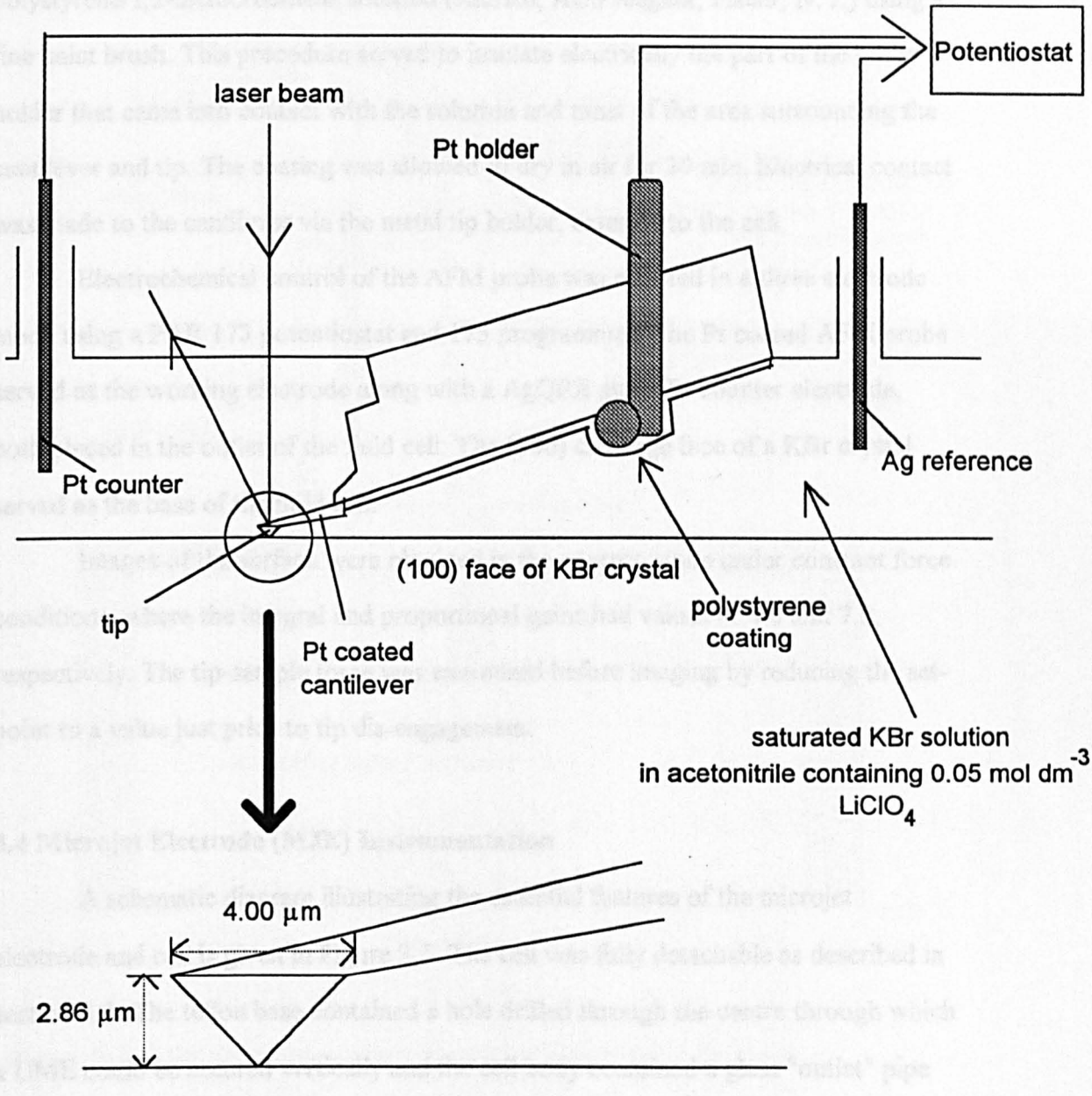

Figure 3.4. Schematic of the modified AFM probe employed in the fluid cell.

in place in the cell, the underside was coated in a 1:40 (by mass) solution of polystyrene/1,2-dichloroethane solution (Aldrich, ACS reagent, Fisher, N. J.) using a fine paint brush. This procedure served to insulate electrically the part of the probe holder that came into contact with the solution and most of the area surrounding the cantilever and tip. The coating was allowed to dry in air for 30 min. Electrical contact was made to the cantilever via the metal tip holder, external to the cell.

Electrochemical control of the AFM probe was effected in a three electrode mode using a PAR 173 potentiostat and 175 programmer. The Pt coated AFM probe served as the working electrode along with a AgQRE and a Pt counter electrode, both placed in the outlet of the fluid cell. The (100) cleavage face of a KBr crystal served as the base of the fluid cell.

Images of the surface were obtained in the contact mode under constant force conditions, where the integral and proportional gains had values of 4.0 and 7.0, respectively. The tip-sample force was minimised before imaging by reducing the set-point to a value just prior to tip dis-engagement.

3.4 Microjet Electrode (MJE) Instrumentation

A schematic diagram illustrating the essential features of the microjet electrode and cell is given in Figure 3.5. The cell was fully detachable as described in section 3.2. The teflon base contained a hole drilled through the centre through which a UME could be secured vertically and the cell body contained a glass "outlet" pipe (i.d. 3 mm) to prevent solution overflow in the cell. The UME was positioned such that it sat well below the level of the solution outlet.

The nozzle of the MJE was constructed by drawing a borosilicate capillary (2.0 mm o.d., 1.16 mm i.d.) with the aid of a Narishighe PB7 pipette puller, to produce a fine point. It was essential that the nozzle of the capillary was flat and planar in order to ensure a uniform fluid profile, upon laminar flow of electrolyte

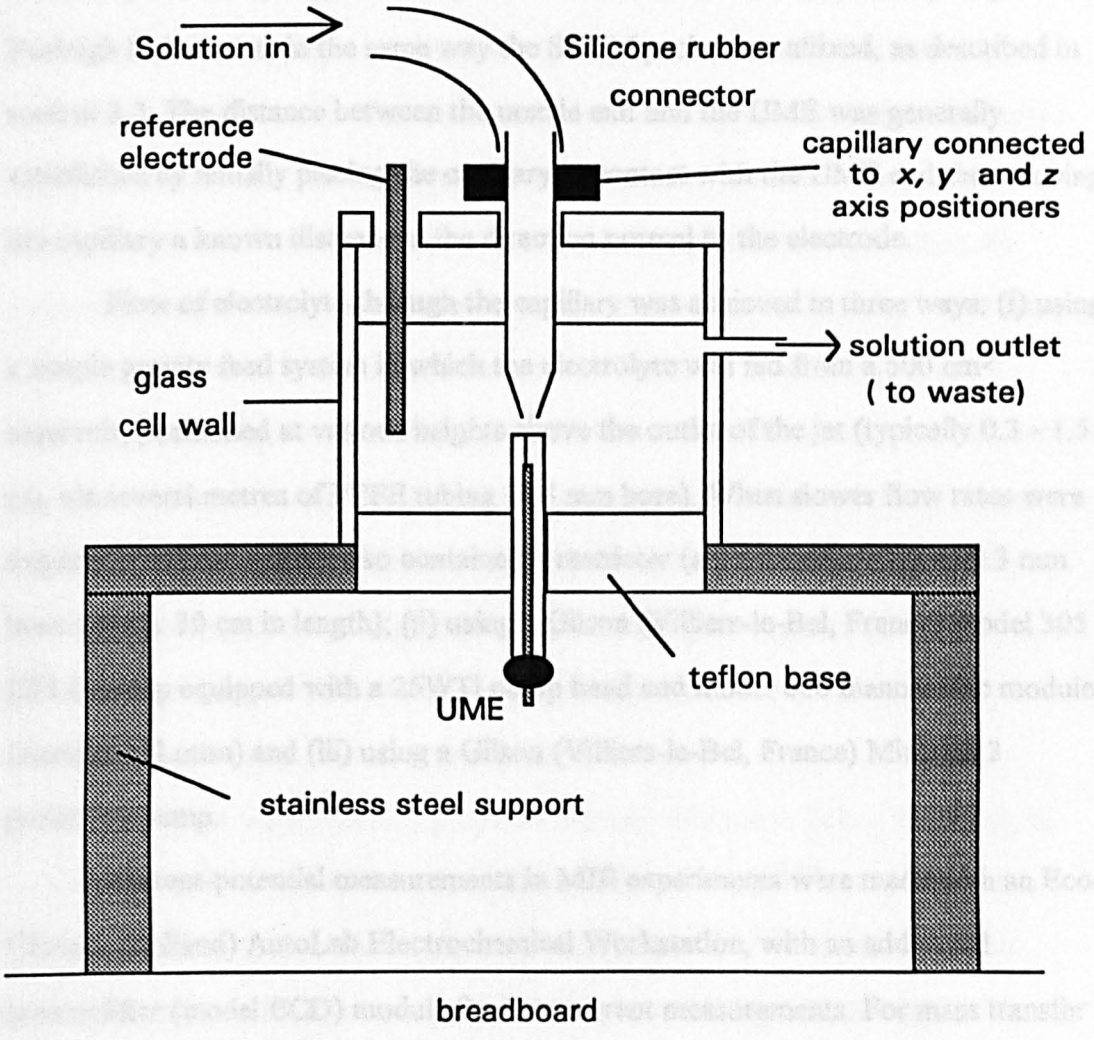

Figure 3.5. Schematic drawing (not to scale) of the microjet electrode.

through the capillary. The inner diameter of the capillary (typically in the range 60-120 μm) was measured with a precision of 1 μm, using an Olympus BH2 optical microscope. The capillary was mounted on the three TSE-75 (*x*, *y* and *z*) stages from Burleigh Instruments in the same way the SECM probe was affixed, as described in section 3.2. The distance between the nozzle exit and the UME was generally established by initially placing the capillary in contact with the UME and then moving the capillary a known distance in the direction normal to the electrode.

Flow of electrolyte through the capillary was achieved in three ways: (i) using a simple gravity feed system in which the electrolyte was fed from a 500 cm^3 reservoir, positioned at various heights above the outlet of the jet (typically 0.3 - 1.5 m), via several metres of PTFE tubing (1.5 mm bore). When slower flow rates were required, the flow system also contained a restricter (a glass tube of 0.2 or 0.3 mm bore and *ca.* 30 cm in length); (ii) using a Gilson (Villiers-le-Bel, France) model 305 HPLC pump equipped with a 25WTi pump head and model 806 manometric module (Anachem, Luton) and (iii) using a Gilson (Villiers-le-Bel, France) Miniplus 3 peristaltic pump.

Current-potential measurements in MJE experiments were made with an Eco-Chemie (Holland) AutoLab Electrochemical Workstation, with an additional preamplifier (model ECD) module for low-current measurements. For mass transfer imaging experiments, the nozzle of the capillary was scanned over the UME, with the solution flowing. Images were obtained by measuring the transport-limited current as a function of nozzle position in the *x*, *y* plane. Details on image acquisition have been described fully in section 3.2. Both a two- and three- electrode configuration were used for steady-state MJE voltammetric measurements. A saturated calomel electrode (Radiometer model K401) served as the reference electrode and, when required, a Pt gauze served as the counter electrode.

3.5 Solutions and Substrates

3.5.1 Solutions

The sources and grades of all the chemicals utilised are given in Table 3.1. Most solutions were prepared with Milli-Q reagent water (Millipore Corp. 18.2 MΩ resistivity) with exception of all the solutions containing potassium bromide, which were prepared in acetonitrile. Saturated solutions of potassium ferrocyanide trihydrate, silver chloride, potassium bromide and copper sulfate pentahydrate contained, respectively, 3.5 mol dm^{-3} potassium chloride, 0.1 mol dm^{-3} potassium nitrate, 0.05 mol dm^{-3} $LiClO_4$ and 3.6 mol dm^{-3} sulfuric acid, as background electrolytes, although some measurements on silver chloride were carried out without supporting electrolyte. All AgCl solutions were thoroughly deareated with argon for a period of *ca.* 15 min and during all measurements argon was passed over the surface of the solution. For AgCl solutions containing no supporting electrolyte, the pH of the solution, after this procedure, was typically found to be *ca.* 6.7 confirming that Ag^+ and Cl^- were the major ions present.

Solutions were generally prepared in glass volumetric flasks. However, to avoid problems from photodecomposition of silver chloride[252] and possible ion adsorption, from dilute solution, to the walls of glass[253-255] flasks, saturated solutions of silver chloride were prepared in light excluding HDPE vessels (Fisons, Loughborough).

For the MJE experiments, concentrations of *ca.* 5×10^{-4} mol dm^{-3} potassium ferrocyanide trihydrate were used in kinetic measurements, whilst concentrations of *ca.* 2×10^{-3} mol dm^{-3} potassium ferrocyanide trihydrate were employed in mass transfer imaging experiments. In all cases strontium nitrate served as the supporting electrolyte at a concentration of 0.2 mol dm^{-3}.

Chemical	Source	Grade
Acetonitrile	BDH	Far U.V.
	EM Science	HPLC
Argon	BOC	99.998 % volume
Copper sulfate pentahydrate	Fisons	A. R.
Hydrochloric acid	Fisons	A. R., specific gravity 1.18
Hydrogen	BOC	99.99 % volume
Lithium perchlorate	Aldrich	A. C. S.
Nitric acid	Aldrich	Volumetric standard, 0.996M
Potassium bromide	Fisons	A. R.
Potassium chloride	Fisons	A. R. and 99.98 % purity
Potassium ferricyanide	Aldrich	A. C. S.
Potassium ferrocyanide trihydrate	Fisons	A. R.
Potassium nitrate	Aldrich	99.99 % purity
Silver chloride	Fluka	Puriss p.a.
Silver nitrate	Aldrich	99+ % purity
Strontium nitrate	Aldrich	A. C. S.
Sulfuric acid	Fisons	A. R., specific gravity 1.84

Table 3.1. A. R. is analytical reagent grade, A. C. S. is American Chemical Society grade and HPLC is high-performance liquid chromatography.

3.5.2 Substrates

Copper sulfate pentahydrate and potassium ferrocyanide trihydrate crystals were grown from saturated aqueous solutions through slow evaporation at 20 °C in a cooled incubator (Jencons Scientific, model 303, Leighton Buzzard). Slow growth over 4 - 5 (copper sulfate pentahydrate) and 7 - 8 weeks (potassium ferrocyanide trihydrate) yielded well-defined crystals with an average dimension in the range 0.5 - 1.0 cm. The crystal morphology was verified by measuring the interfacial angles directly from photomicrographs (magnification x69 to x150) taken with the Olympus BH2 microscope fitted with an Olympus PM-10AK camera attachment. Crystals with extensive planar surfaces and devoid of macroscopic steps, as judged by Nomarski differential contrast microscopy (x50 to x1000), were selected for dissolution studies.

Prior to use, potassium bromide crystals (grown from the melt, Crystran, Poole, England) were cleaved using a sharp steel blade to provide a workable sized substrate (with typical dimensions 10 mm by 10 mm (surface area) by 5 mm (height)) and a fresh surface devoid of macroscopic defects.

Two types of silver chloride substrates were employed: (i) AgCl in the form of a pressed pellet (Crystran, Poole, England) of diameter 12.7 mm and thickness 2 mm and (ii) electrochemically grown AgCl films. The latter substrates were prepared from the oxidation of home constructed Ag disc UMEs (see section 3.1.1.), either 50 or 125 μm in diameter, in 0.1 mol dm^{-3} potassium chloride. In order to obtain complete coverage of the surface with AgCl, a current density of approximately 0.16 mA cm^{-2} was maintained at the electrode for a period of 15 min.[213] The electrochemically grown surfaces were aged by storage of the electrodes in 0.1 mol dm^{-3} potassium chloride for 24 h in the dark.

Optically flat glass disc substrates were employed for experiments where it was necessary to quantify the distance of closest approach of the SECM tip (UME) to a planar surface.

CHAPTER 4

POTASSIUM FERROCYANIDE TRIHYDRATE INDUCED DISSOLUTION IN AQUEOUS SOLUTIONS OF POTASSIUM CHLORIDE

The SECM has been used to induce and monitor dissolution from the (010) surface of (monoclinic) potassium ferrocyanide trihydrate crystals in initially saturated aqueous solutions containing 3.5 mol dm^{-3} potassium chloride. The reaction has been investigated by SECM chronoamperometry in which the potential of a disc UME tip, positioned close to the crystal surface, was stepped from a value at which no reactions occurred to a value at which the oxidation of ferrocyanide to ferricyanide occurred at a diffusion-controlled rate, thereby initiating the crystal dissolution process.

The resulting chronoamperometric characteristics, obtained with a range of tip sizes (electrode radii of 2.5, 5.0 and 12.5 μm) and tip to crystal separations, demonstrate that the dissolution reaction initially occurs at a rapid rate and quickly attains a steady-state. Quantitative analysis of this data in terms of appropriate candidate dissolution rate laws indicates that the dissolution process is second-, rather than first-order in the interfacial undersaturation at the crystal/solution interface.

At longer times in the chronoamperometric measurements, the current decreases suggesting that the crystal becomes less active to dissolution. The theoretical model demonstrates that this occurs when the concentration of ferricyanide, accumulating in the tip/crystal gap, reaches a value at which the solution becomes supersaturated with respect to potassium ferricyanide. This provides the thermodynamic force for the nucleation and growth of potassium

ferricyanide on the potassium ferrocyanide trihydrate surface, thus blocking the dissolution reaction.

Taking account of this phenomenon, the SECM has been successfully employed to image the dissolution activity of the (010) surface, particularly around pits which were electrochemically pre-etched in the surface. Additionally, by adding a small concentration (2×10^{-3} mol dm^{-3}) of potassium ferricyanide to the saturated solution, the reduction of which served as a calibrant of the tip to crystal distance, it has been possible to use the SECM to image both the topography and dissolution activity of the potassium ferrocyanide trihydrate (010) surface.

4.1 Introduction

In this chapter the proposed SECM approach to the measurement of crystal dissolution kinetics is developed by considering dissolution from the (010) face of monoclinic potassium ferrocyanide trihydrate in aqueous solutions of 3.5 mol dm^{-3} potassium chloride. This reaction is of interest for several reasons. First, under the defined conditions, the system is a good example of an unsymmetric crystal dissolving in a non-stoichiometric solution. A generally unresolved problem is explaining empirically observed dissolution rate laws for such processes.[1] The aim here is therefore to investigate a representative of this class of dissolution reactions under the well-defined conditions provided by the SECM, and assess to what extent the kinetics can be modelled in terms of rate laws which have a sound mechanistic foundation, as outlined in section 2.4.1. Second, the electrochemical oxidation of ferrocyanide to ferricyanide, by which the dissolution reaction may be induced, is well characterised.[256,257] Third, potassium ferrocyanide trihydrate is very soluble in aqueous solutions and is characterised by rapid dissolution kinetics, providing a useful test of the ability of the SECM to measure fast surface reactions. Fourth, since potassium ferricyanide, the product of the tip oxidation

reaction, is more soluble than potassium ferrocyanide trihydrate,[258] the spatial dependence of the dissolution kinetics can be investigated through SECM reaction rate imaging. This approach has been shown to be powerful in mapping redox activity at metals[136,176,201] and immobilised enzymes[124,217] at the micrometre level, but has not previously been used to image the dissolution activity of a crystal surface.

4.2 Theory

As discussed in section 2.4.1, rate laws are considered in which the dissolution kinetics show either a first- or second-order dependence on the interfacial undersaturation. These cases represent the high and low undersaturation limits of the BCF spiral dissolution model[4] and can also be derived from several other dissolution mechanisms.[2] The rate laws are defined by equation (2.69) which for potassium ferrocyanide trihydrate becomes:

$$j_{Fe(CN)_6^{4-}} = j_{K^+}/4 = k_n \sigma^n \tag{4.1}$$

where σ, for this system, in accordance with equation (2.71), is given by:

$$\sigma = 1 - \left(\frac{a_{K^+}^4 a_{Fe(CN)_6^{4-}}}{(a_{K^+}^4)^* (a_{Fe(CN)_6^{4-}})^*} \right)^{1/5} \tag{4.2}$$

The experiments reported herein have been carried out in the presence of excess potassium chloride, so that the concentration (or, strictly, activity) of potassium ions remains effectively constant during the course of a measurement, even as potassium ferrocyanide trihydrate dissolves into the solution. Under these conditions equation (4.2) can, to a good approximation, be simplified to:

$$\sigma = 1 - \left(\frac{a_{Fe(CN)_6^{4-}}}{(a_{Fe(CN)_6^{4-}})^*} \right)^{1/5} \qquad (4.3)$$

and the dissolution problem reduces to the consideration of only the ferro/ferricyanide couple.

The UME chronoamperometric response is considered following a step in the potential to a value at which ferrocyanide is oxidised at a diffusion-controlled rate, and the solution initially contains no ferricyanide ions. The general dimensionless SECM diffusion equation (given by equation (2.12)) for the species of interest is:

$$\frac{\partial C_i}{\partial \tau} = \lambda_i \left[\frac{\partial^2 C_i}{\partial R^2} + \frac{1}{R} \frac{\partial C_i}{\partial R} + \frac{\partial^2 C_i}{\partial Z^2} \right] \qquad (4.4)$$

where C_i is the concentration of ferrocyanide or ferricyanide normalised with respect to the concentration of ferrocyanide in bulk (saturated) solution. This equation has been modified, from the form given in equation (2.12), to account for the unequal diffusion coefficients of ferrocyanide and ferricyanide,[259] which is reflected in the parameter λ_i where:

$$\lambda_i = D_i / D_{Fe(CN)_6^{4-}} \qquad (4.5)$$

The subscript i refers to ferrocyanide or ferricyanide.

The corresponding boundary conditions for the experiment of interest, are:

$\tau = 0$, all R, all Z: $C_{Fe(CN)_6^{4-}} = 1, \qquad C_{Fe(CN)_6^{3-}} = 0 \qquad (4.6)$

$\tau > 0$, $Z = 0$, $0 \le R \le 1$: (tip electrode)

$$C_{Fe(CN)_6^{4-}} = 0, \qquad -\lambda_{Fe(CN)_6^{3-}} \left(\frac{\partial C_{Fe(CN)_6^{3-}}}{\partial Z} \right) = \frac{\partial C_{Fe(CN)_6^{4-}}}{\partial Z} \qquad (4.7)$$

$\tau > 0, Z = 0, 1 < R \leq RG$: (glass sheath)

$$\frac{\partial C_{Fe(CN)_6^{4-}}}{\partial Z} = 0, \quad \frac{\partial C_{Fe(CN)_6^{3-}}}{\partial Z} = 0 \tag{4.8}$$

$\tau > 0, R > RG, 0 < Z < L$: (radial edge of the tip/substrate domain)

$$C_{Fe(CN)_6^{4-}} = 1, \quad C_{Fe(CN)_6^{3-}} = 0 \tag{4.9}$$

$\tau > 0, R = 0, 0 < Z < L$: (axis of symmetry)

$$\frac{\partial C_{Fe(CN)_6^{4-}}}{\partial R} = 0, \quad \frac{\partial C_{Fe(CN)_6^{3-}}}{\partial R} = 0 \tag{4.10}$$

$\tau > 0, Z = L, 0 < R \leq RG$: (substrate)

$$\frac{\partial C_{Fe(CN)_6^{4-}}}{\partial Z} = -K_n\left[1 - C_{Fe(CN)_6^{4-}}^{1/5}\right]^n, \quad \frac{\partial C_{Fe(CN)_6^{3-}}}{\partial Z} = 0 \tag{4.11}$$

Equation (4.11) reflects the dissolution rate law. The dimensionless rate constant (equation (2.75)), in this expression is defined by:

$$K_n = \frac{k_n a}{\gamma_{Fe(CN)_6^{4-}} c^*_{Fe(CN)_6^{4-}} D_{Fe(CN)_6^{4-}}} \tag{4.12}$$

In deriving equation (4.11), it is assumed that the activity coefficient of the ferrocyanide ion remains constant during induced dissolution. This is expected to be valid under the conditions of the experiments reported herein, where potassium chloride is present in high excess.

As the solution composition is the same for all of the experiments described below, equation (4.12) can be simplified to

$$K_n = k_n' a / D_{Fe(CN)_6^{4-}} \tag{4.13}$$

where

$$k_n' = k_n / \gamma_{Fe(CN)_6^{4-}} c^*_{Fe(CN)_6^{4-}} \tag{4.14}$$

In writing equation (4.11), it has also been assumed that ferricyanide is inert with respect to the crystal surface and does not affect the dissolution process. As demonstrated later in section 4.5, this is a valid assumption provided that the concentration of potassium ferricyanide does not increase beyond the saturation ratio in the gap between the tip and crystal, causing potassium ferricyanide to precipitate. This requirement limits the above analysis to short times at close tip/substrate distances, but the treatment is generally applicable at large values of L, where ferricyanide ions can readily escape from the tip/crystal gap.

The solution to the problem outlined yields the UME current, normalised with respect to the steady-state current at infinite probe/crystal separation, as given by equation (2.14).

The problems are solved numerically using the ADI finite-difference method,[239-241] as discussed in section 2.2.2. The ADI algorithm requires some modification in order to incorporate the non-linear dissolution rate law boundary condition, defined by equation (4.15), which has been adapted from equation (2.78) to treat this specific case:

$$\frac{C^{**}_{j,\mathrm{NZ\text{-}1}} - C^{**}_{j,\mathrm{NZ}}}{\Delta Z} = -K_n\left[1-\left(C^{**}_{j,\mathrm{NZ}}\right)^{1/5}\right]^n \qquad (4.15)$$

C refers to the normalised concentration of ferrocyanide. Let:

$$\Delta Z K_n = m \qquad (4.16)$$

and

$$\left(C^{**}_{j,\mathrm{NZ}}\right)^{1/5} = x \qquad (4.17)$$

Hence, for $n = 1$, rearrangement of equation (4.15) results in the following pentic equation:

$$x^5 + mx - m - C^{**}_{j,\mathrm{NZ\text{-}1}} = 0 \qquad (4.18)$$

By letting $C^{**}_{j,NZ-1}$ equal $C^{*}_{j,NZ-1}$ (which is known), equation (4.18) can be solved for x through calls in the SECM dissolution program to the NAG routine CO2AGF.[260] Knowledge of x and hence $C^{**}_{j,NZ}$ allows equation (2.77) to be solved, using the Thomas Algorithm. If there is a greater difference than 1×10^{-4} % between the value obtained for $C^{**}_{j,NZ-1}$, upon solution of equation (2.77), and the estimated value used for $C^{**}_{j,NZ-1}$ in equation (4.18), an iterative procedure is adopted until the difference between the two values falls within the required limits, for accurate calculation of the data.

When $n = 2$, rearrangement of equation (4.15) results in the following pentic expression:

$$y^5 - my^2 + 2my - m - C^{**}_{j,NZ-1} = 0 \qquad (4.19)$$

where:

$$y = \left(C^{**}_{j,NZ}\right)^{1/5} \qquad (4.20)$$

which is solved for y as discussed above.

4.3 Theoretical Results and Discussions

The aim of this section is to present typical theoretical chronoamperometric characteristics for SECM induced dissolution with the rate laws defined by equation (4.1).

All simulations were carried out for a UME probe characterised by $RG = 10$, as this was similar to that employed in the experiments reported in section 4.5. Typical current-time curves for the dissolution problem defined by $n = 1$ are shown in Figure 4.1. These relate to $L = 0.1$ and a range of values of K_1. The data are presented as normalised current vs. $\tau^{-1/2}$ in order to emphasise the short time behaviour. The chronoamperometric characteristics are qualitatively similar to

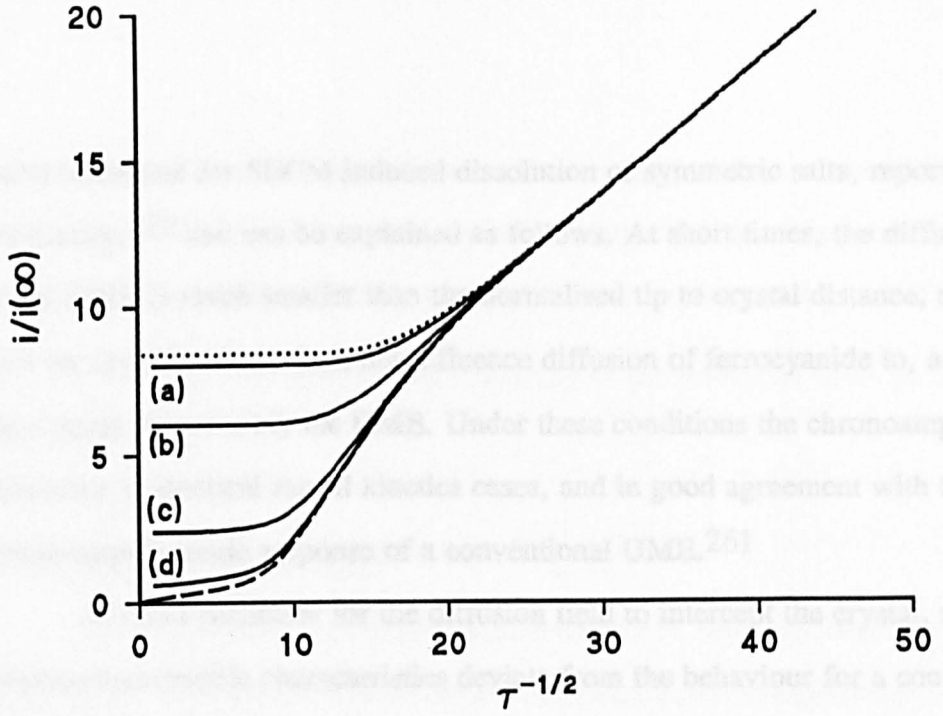

Figure 4.1. SECM chronoamperometric characteristics for an induced dissolution process governed by equation (4.11) with $n = 1$. The data were calculated using a value of $L = 0.1$. The curves shown are for the normalised rate constants, $K_1 =$ 1000 (a), 100 (b), 10 (c) and 0 (d). The behaviour is also shown for a diffusion-controlled dissolution process (···) and for an inert crystal surface (----).

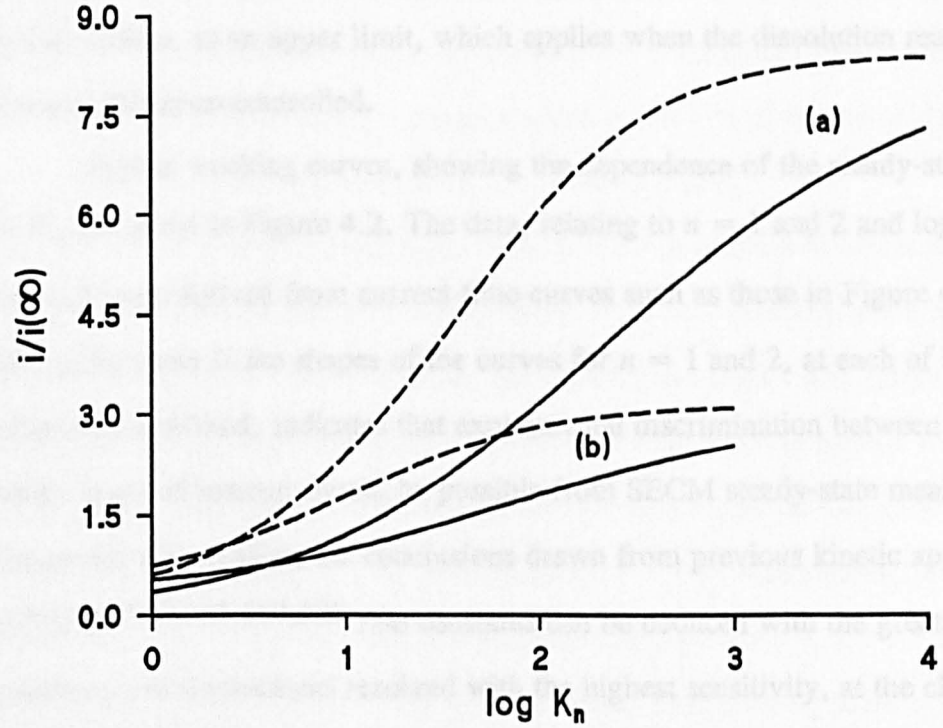

Figure 4.2. Working curves of steady-state dimensionless current, $i/i(\infty)$, vs. K_n for log L = -1.0 (a) and -0.5 (b). For each distance curves are shown for n =1 (--) and 2 (—).

those calculated for SECM induced dissolution of symmetric salts, reported previously,[220] and can be explained as follows. At short times, the diffusion field of the UME is much smaller than the normalised tip to crystal distance, and thus the crystal surface does not influence diffusion of ferrocyanide to, and hence the current response of, the UME. Under these conditions the chronoamperometric behaviour is identical for all kinetics cases, and in good agreement with the chronoamperometric response of a conventional UME.[261]

At times sufficient for the diffusion field to intercept the crystal, the chronoamperometric characteristics deviate from the behaviour for a conventional UME, and reflect the dissolution kinetics of the crystal surface. In particular, as the dissolution rate constant increases, the flux of material from the crystal surface increases, which is manifested in an increase in the long time current. This varies between a lower limit, which represents the case of negative feedback for an inert crystal surface, to an upper limit, which applies when the dissolution reaction becomes diffusion-controlled.

Typical working curves, showing the dependence of the steady-state current on K_n are given in Figure 4.2. The data, relating to $n = 1$ and 2 and $\log L = -1.0$ and -0.5 were derived from current-time curves such as those in Figure 4.1. The clear differences in the shapes of the curves for $n = 1$ and 2, at each of the distances considered, indicates that experimental discrimination between the two kinetic cases of interest should be possible from SECM steady-state measurements. The results also confirm the conclusions drawn from previous kinetic applications of SECM:[132,135,147,220] rate constants can be deduced with the greatest accuracy, and mechanisms resolved with the highest sensitivity, at the closest tip to substrate separations.

It is clear from Figure 4.2 that a wide range of normalised rate constants should be measurable using the SECM induced dissolution technique. Equation

(4.12) indicates that the range of absolute rate constants open to study depends on the activity of ferrocyanide in the saturated solution and the values of a and $D_{Fe(CN)_6^{4-}}$. Each of these parameters can be tuned to some extent (particularly the value of a) in order to enhance the sensitivity of the technique when studying a particular system.

4.4 Experimental Procedures

The alignment of the SECM tip with respect to approach measurements was checked by recording both the steady-state and current-time response of the UME as a function of the separation between the tip and a flat glass substrate for the diffusion-limited oxidation of ferrocyanide ions at a Pt UME. The glass surface is inert with respect to the species of interest and thus these experiments allowed the distance of closest approach of the UME to a surface to be determined, after comparing the experimental results with theory.[122] Typically the electrode could be reproducibly positioned within a distance which was ≤ 5 % of the electrode radius, for all of the tip sizes employed ($a = 2.5$, 5.0 and 12.5 μm).

For kinetic measurements, the UME was set at selected distances from the crystal surface, so that the separation between the tip and crystal was less than the diameter of the UME. The distance between the tip and crystal was generally established by carefully placing the electrode in contact with the surface and then moving the tip away a known distance in the direction normal to the surface. This is a general procedure which was verified previously.[218-220] Alternatively, in some experiments, a small concentration of potassium ferricyanide (*ca.* 2×10^{-3} mol dm^{-3}) was included in the saturated solution of potassium ferrocyanide, as described later in section 4.5.1, and the negative feedback current for the diffusion-limited reduction of this species was used as a distance calibrant.[122] This was added before saturating the

solution with respect to the ferrocyanide salt. Preliminary experiments demonstrated that, at this concentration, ferricyanide had no discernible effect on the SECM induced dissolution chronoamperometric characteristics and hence, by inference, the dissolution rate and mechanism.

SECM imaging experiments employed a tip of a = 5 μm, which was scanned in a raster pattern at a constant height above the crystal surface (typically of the order of a), in the x, y plane (parallel to the target surface). Scans were usually over a square area of length 200 - 300 μm, while the step size between line scans was 2 - 5 μm. Images were acquired by measuring the diffusion-limited current for the electrolysis of the target solution species, as a function of the tip position.

The crystal morphology of the solution grown potassium ferrocyanide trihydrate crystals was verified, and faces of interest identified, by measuring the interfacial angles of the exposed faces[262] directly from photomicrographs at a magnification of 150 times.

4.5 Experimental Results and Discussion

4.5.1 Ferrocyanide oxidation in saturated solutions.

The determination of heterogeneous kinetics using SECM techniques, requires that the tip electrode response is well-defined in the absence of surface kinetic complications. Preliminary experiments were thus carried out to establish the chronoamperometric characteristics for ferrocyanide oxidation at Pt electrodes in solutions containing 3.5 mol dm^{-3} potassium chloride and saturated with respect to potassium ferrocyanide trihydrate.

Typical current-time behaviour for the oxidation of ferrocyanide ions at a 25 μm diameter Pt UME is shown in Figure 4.3. The data were obtained by stepping the potential from +0.1 V vs. AgQRE, where no electrode reactions occurred, to +0.70 V, where the oxidation of ferrocyanide was diffusion-

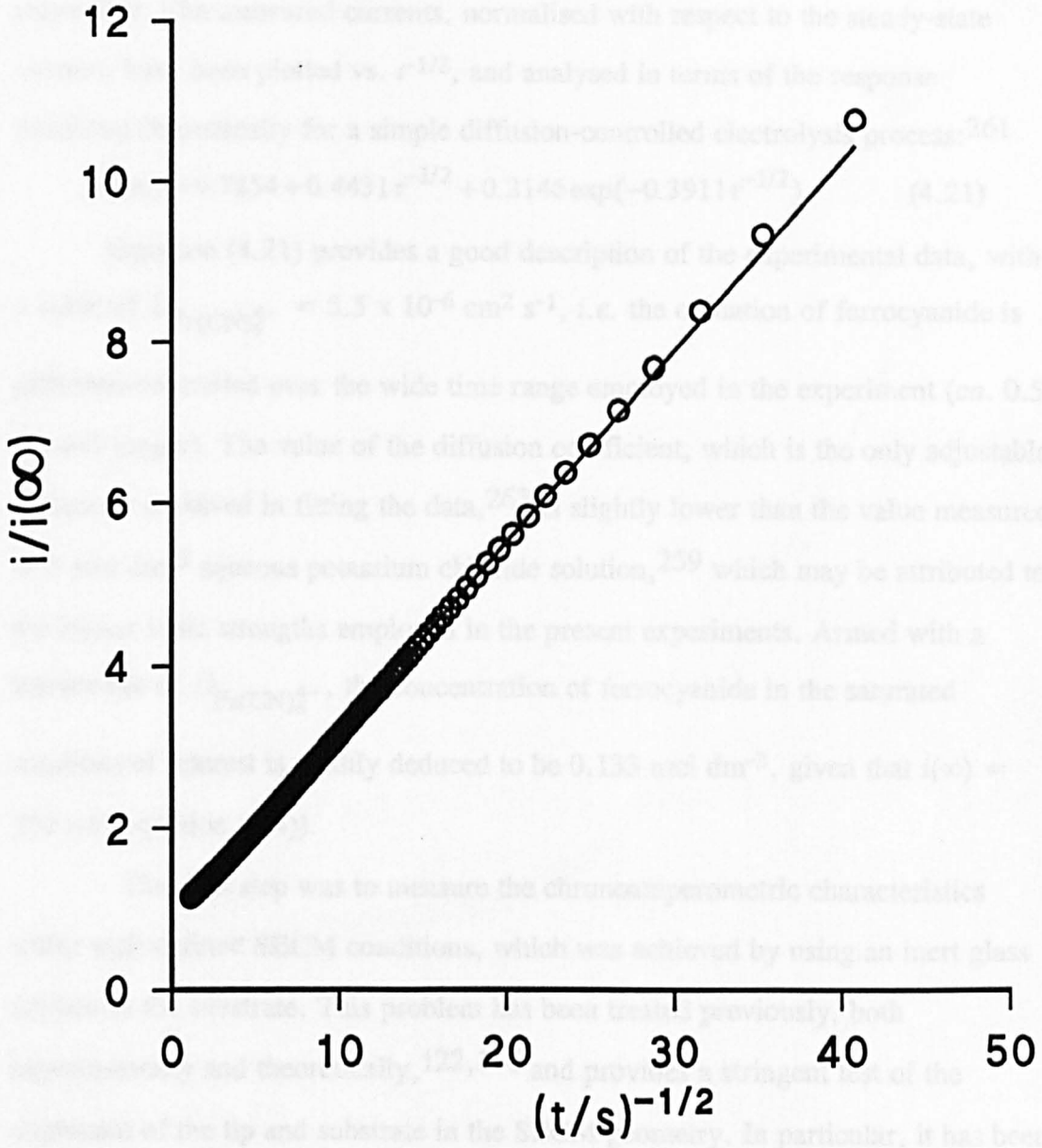

Figure 4.3. Chronoamperometric characteristics for the oxidation of ferrocyanide ions at a 25 μm diameter Pt UME in a solution containing 3.5 mol dm^{-3} KCl and saturated with respect to potassium ferrocyanide trihydrate. The solid line shows the behaviour for a simple diffusion-controlled process predicted by equation (4.21) with $D_{Fe(CN)_6^{4-}} = 5.5 \times 10^{-6}$ cm^2 s^{-1}.

controlled. The measured currents, normalised with respect to the steady-state current, have been plotted vs. $t^{-1/2}$, and analysed in terms of the response predicted theoretically for a simple diffusion-controlled electrolysis process:[261]

$$i/i(\infty) = 0.7854 + 0.4431\tau^{-1/2} + 0.2146\exp(-0.3911\tau^{-1/2}) \qquad (4.21)$$

Equation (4.21) provides a good description of the experimental data, with a value of $D_{Fe(CN)_6^{4-}} = 5.5 \times 10^{-6}$ cm^2 s^{-1}, *i.e.* the oxidation of ferrocyanide is diffusion-controlled over the wide time range employed in the experiment (*ca.* 0.5 ms and longer). The value of the diffusion coefficient, which is the only adjustable parameter involved in fitting the data,[263] is slightly lower than the value measured in 1 mol dm^{-3} aqueous potassium chloride solution,[259] which may be attributed to the higher ionic strengths employed in the present experiments. Armed with a knowledge of $D_{Fe(CN)_6^{4-}}$, the concentration of ferrocyanide in the saturated solutions of interest is readily deduced to be 0.133 mol dm^{-3}, given that $i(\infty)$ = 352 nA (equation (1.4)).

The next step was to measure the chronoamperometric characteristics under well-defined SECM conditions, which was achieved by using an inert glass surface as the substrate. This problem has been treated previously, both experimentally and theoretically,[122,146] and provides a stringent test of the alignment of the tip and substrate in the SECM geometry. In particular, it has been suggested that the experimental chronoamperometric response deviates markedly from theory if the planes formed by the substrate and the end of the tip are not aligned parallel.[146]

Figure 4.4 shows a typical series of chronoamperometric responses for the diffusion-controlled oxidation of ferrocyanide ions at a 25 μm diameter Pt UME positioned at distances of 0.8, 3.8 and 6.8 μm from a glass surface. The data are presented as normalised current vs. $\tau^{-1/2}$, using the value of $D_{Fe(CN)_6^{4-}}$ deduced

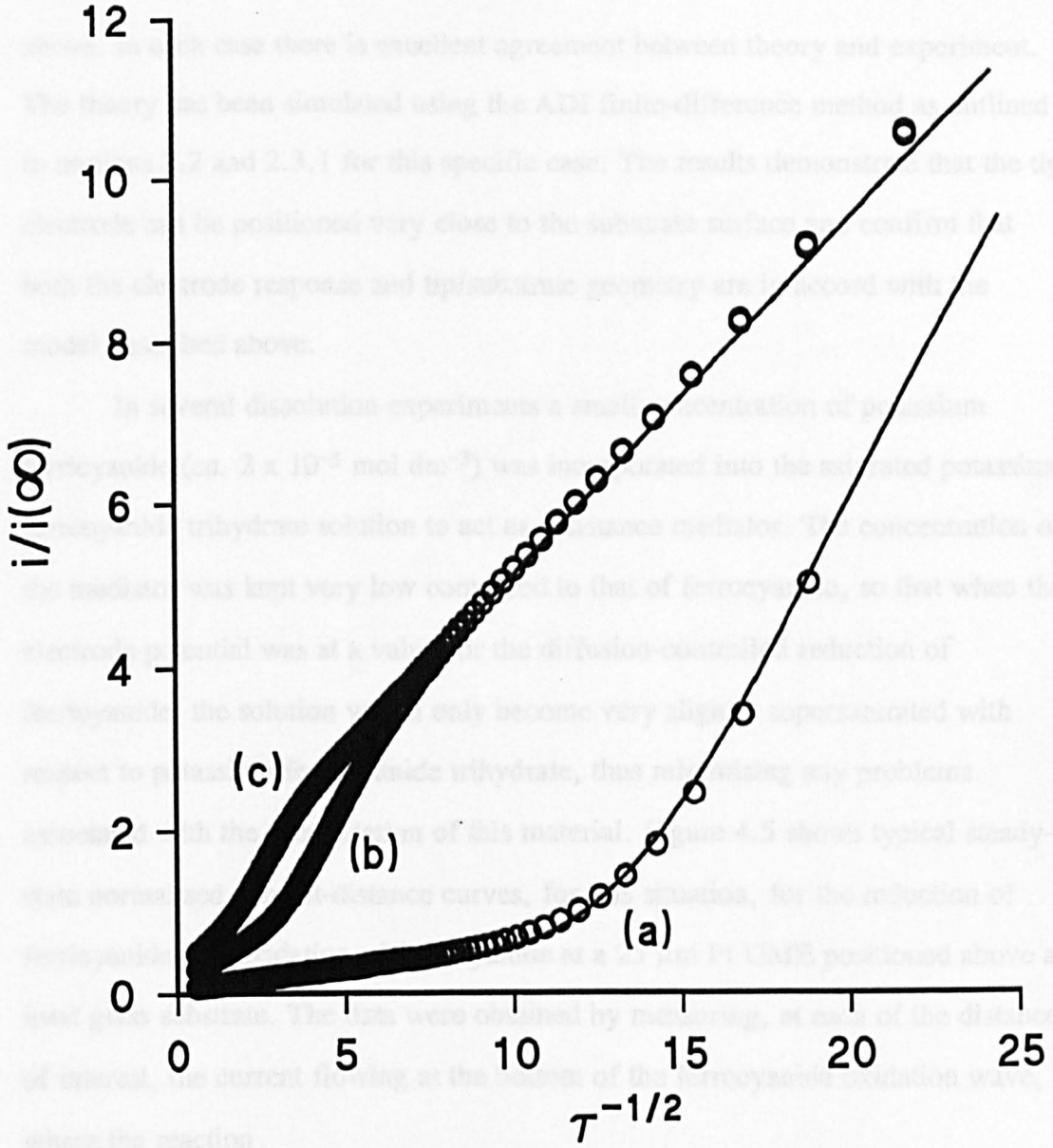

Figure 4.4. SECM chronoamperometric characteristics for the oxidation of ferrocyanide ions at a 25 μm diameter Pt UME, positioned at various distances from an inert glass substrate, in a solution containing 3.5 mol dm^{-3} KCl and saturated with respect to potassium ferrocyanide trihydrate. The data relate to tip/substrate separations of 0.8 μm (a), 3.8 μm (b) and 6.8 μm (c). Real times were converted to normalised times, to enable experiment (O) to be compared with theory (—) using the value for the diffusion coefficient of ferrocyanide deduced in the text.

above. In each case there is excellent agreement between theory and experiment. The theory has been simulated using the ADI finite-difference method as outlined in sections 2.2 and 2.3.1 for this specific case. The results demonstrate that the tip electrode can be positioned very close to the substrate surface and confirm that both the electrode response and tip/substrate geometry are in accord with the model described above.

In several dissolution experiments a small concentration of potassium ferricyanide (*ca.* 2×10^{-3} mol dm^{-3}) was incorporated into the saturated potassium ferrocyanide trihydrate solution to act as a distance mediator. The concentration of the mediator was kept very low compared to that of ferrocyanide, so that when the electrode potential was at a value for the diffusion-controlled reduction of ferricyanide, the solution would only become very slightly supersaturated with respect to potassium ferrocyanide trihydrate, thus minimising any problems associated with the precipitation of this material. Figure 4.5 shows typical steady-state normalised current-distance curves, for this situation, for the reduction of ferricyanide and oxidation of ferrocyanide at a 25 μm Pt UME positioned above an inert glass substrate. The data were obtained by measuring, at each of the distances of interest, the current flowing at the bottom of the ferrocyanide oxidation wave, where the reaction

$$Fe(CN)_6^{3-} + e^- \Leftrightarrow Fe(CN)_6^{4-} \qquad (4.22)$$

is driven to the right at a diffusion-controlled rate, and the current at the top of the wave where equation (4.22) is driven to the left at a diffusion-controlled rate. It is clear from Figure 4.5 that there is a high level of coincidence between the two sets of data and good agreement between theory[122] and experiment.

The use of the ferricyanide mediator (*ca.* 2×10^{-3} mol dm^{-3} in a saturated potassium ferrocyanide trihydrate solution) when the substrate was the (010) face of a single crystal of potassium ferrocyanide trihydrate was also checked. Typical

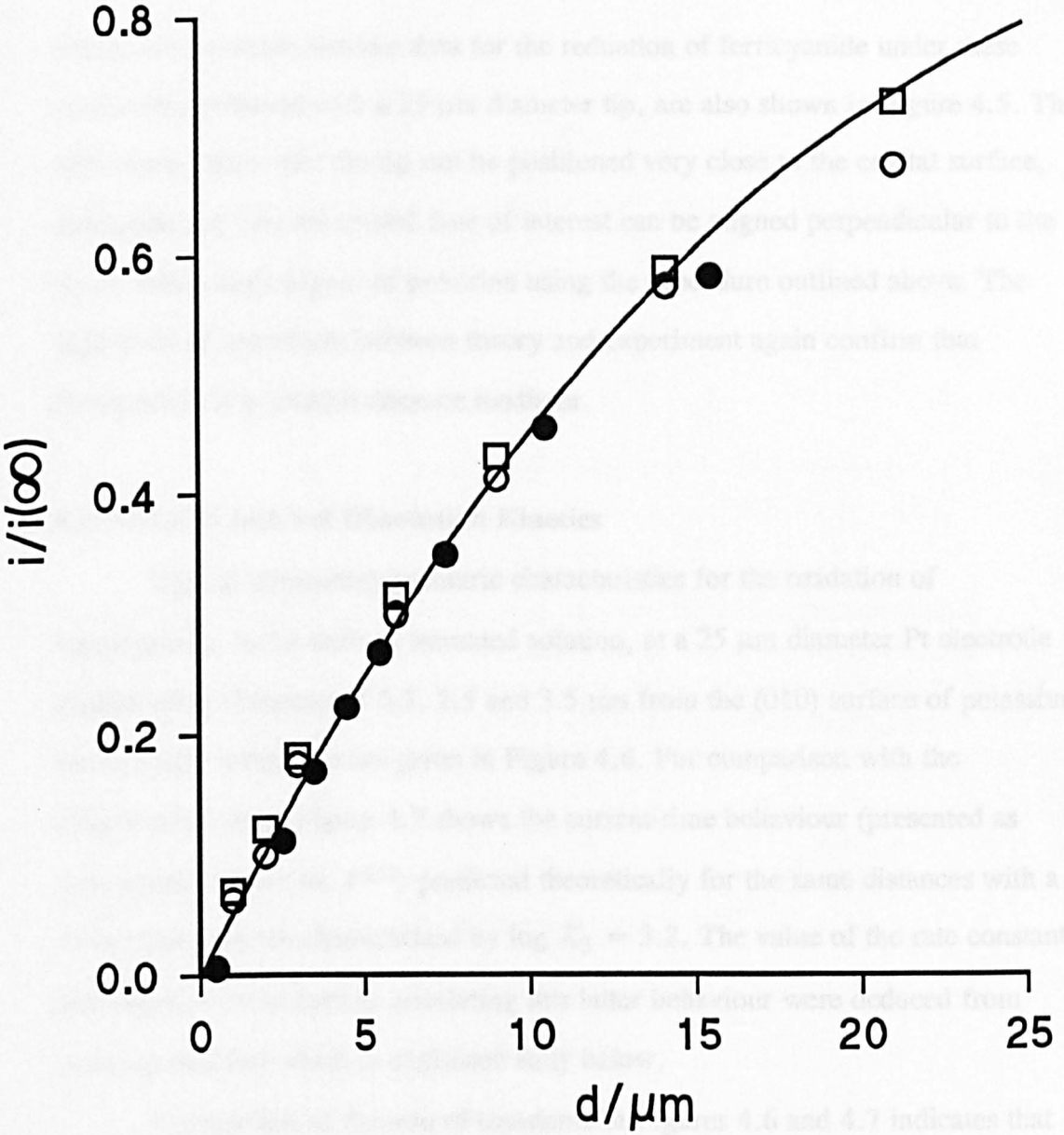

Figure 4.5. Steady-state SECM approach curves, with a 25 μm diameter Pt UME, for the oxidation of ferrocyanide ions (O) and reduction of the ferricyanide ions (□) at a tip positioned above an inert glass substrate and for the reduction of ferricyanide ions with the tip positioned above the (010) face of potassium ferrocyanide trihydrate (●). The solution contained 3.5 mol dm^{-3} KCl and 2 x 10^{-3} mol dm^{-3} potassium ferricyanide and was saturated with respect to potassium ferrocyanide trihydrate. The solid line is the theoretical behaviour for steady-state diffusion-controlled negative feedback.[122]

steady-state current-distance data for the reduction of ferricyanide under these conditions, obtained with a 25 μm diameter tip, are also shown in Figure 4.5. The data clearly show that the tip can be positioned very close to the crystal surface, demonstrating that the crystal face of interest can be aligned perpendicular to the probe with a high degree of precision using the procedure outlined above. The high level of agreement between theory and experiment again confirm that ferricyanide is a suitable distance mediator.

4.5.2 SECM Induced Dissolution Kinetics

Typical chronoamperometric characteristics for the oxidation of ferrocyanide, in the defined saturated solution, at a 25 μm diameter Pt electrode positioned at distances of 0.5, 2.5 and 3.5 μm from the (010) surface of potassium ferrocyanide trihydrate are given in Figure 4.6. For comparison with the experimental data, Figure 4.7 shows the current-time behaviour (presented as normalised current vs. $t^{-1/2}$) predicted theoretically for the same distances with a dissolution process characterised by log K_2 = 3.2. The value of the rate constant and reaction order used in simulating this latter behaviour were deduced from using an analysis which is explained fully below.

Comparison of the sets of transients in Figures 4.6 and 4.7 indicates that there is good agreement between experiment and theory at short times. At the closest distance, the current is seen to first rapidly reach a steady-state at *ca.* $t^{-1/2}$ = 50 $s^{-1/2}$, *i.e.* t = 400 μs, in agreement with the theoretical predictions for a fast dissolution process (see Figures 4.1, 4.2 and 4.7). However, at slightly longer times ($t^{-1/2}$ < 40 $s^{-1/2}$, i.e. t > 625 μs), the experimental current deviates from the response predicted by the theoretical model, by decreasing significantly with increasing time. This overall behaviour is diagnostic of the dissolution process initially attaining a steady-state, but the crystal surface then becoming less active

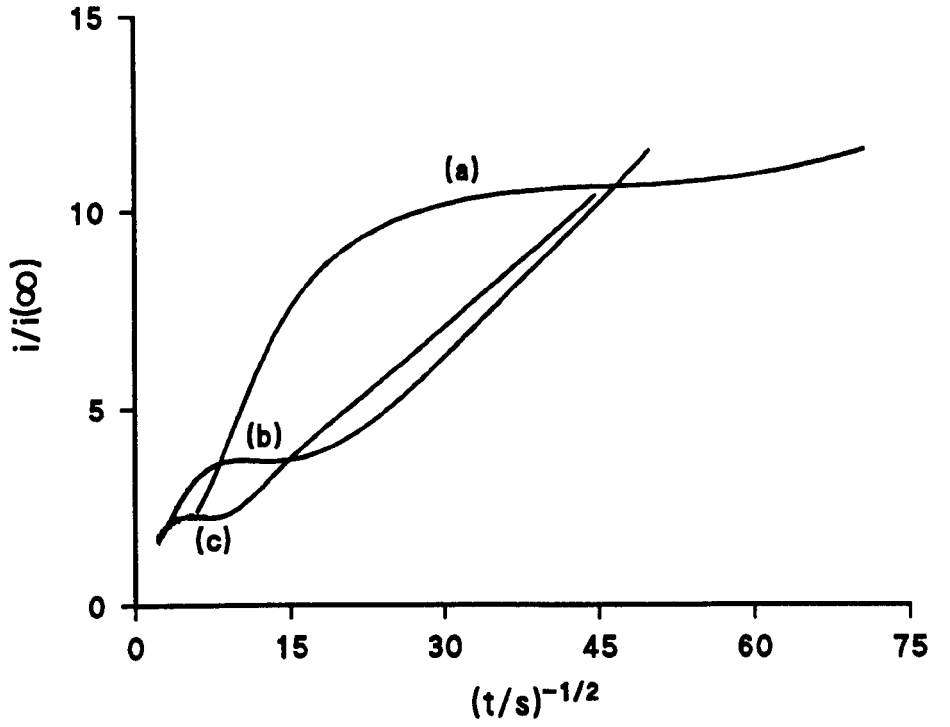

Figure 4.6. SECM chronoamperometric characteristics for the oxidation of ferrocyanide ions at a 25 μm Pt UME, positioned at various distances from the (010) face of potassium ferrocyanide trihydrate, in a solution containing 3.5 mol dm^{-3} KCl and saturated with respect to potassium ferrocyanide trihydrate. The data relate to tip/substrate separations of 0.5 (a), 2.5 (b) and 3.5 μm (c).

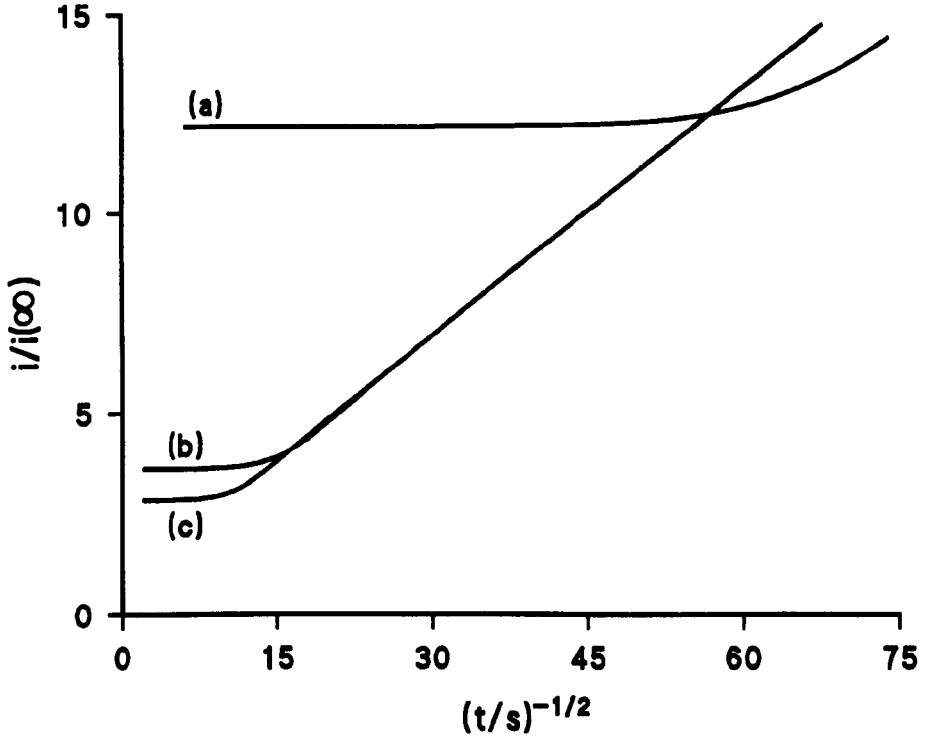

Figure 4.7. Calculated current-time characteristics for SECM induced dissolution with a rate constant log $K_2 = 3.2$. The data relate to $D_{Fe(CN)_6^{4-}} = 5.5 \times 10^{-6}$ cm^2 s^{-1} and a tip UME with $a = 12.5$ μm, positioned at various distances of 0.5 (a), 2.5 (b), and 3.5 μm (c) from the substrate surface.

to dissolution.

Similar behaviour is apparent when the tip to crystal separations are 2.5 and 3.5 μm. In these cases, the recorded chronoamperometric characteristics begin at a sufficiently short time, compared to the characteristic tip to substrate diffusion time, given by equation (1.10), so that in the initial part of the transient, the diffusion field of the UME is much smaller than the tip to crystal distance. Under these conditions, the tip response is similar to that for a conventional UME.[261] At longer times ($t^{-1/2} < 14$ s$^{-1/2}$, *i.e.* $t > 5$ ms for $d = 2.5$ μm; $t^{-1/2} < 9$ s$^{-1/2}$, *i.e.* $t > 12$ ms for $d = 3.5$ μm) the current reaches a steady-state, indicating a steady dissolution rate, but then decreases with increasing time. This behaviour again suggests that the dissolution rate decreases, having first reached a steady value.

The reason for the deviation between theory and experiment at the longest times can be explained by examining the evolution of the theoretical concentration profiles for ferrocyanide and ferricyanide following the potential step. Figure 4.8 shows the steady-state concentration profile for ferrocyanide, within the tip/crystal domain, which holds for times of 400 μs and longer. It can be seen that in the part of the crystal/solution interface directly under the UME ($Z = L$, $0 < R < 1$), the concentration of ferrocyanide is *ca.* 60 % of the bulk (saturated) solution value. This indicates that the dissolution process, although not diffusion-controlled, is fast. For a diffusion-controlled process, the ferrocyanide concentration at the crystal/solution interface would attain its bulk (saturated) solution value.

Since potassium ferrocyanide trihydrate dissolves rapidly, the oxidation of ferrocyanide at a diffusion-controlled rate (indicated by the concentration of ferrocyanide in Figure 4.8 having a value of zero at the electrode surface) leads to the rapid accumulation of ferricyanide in the gap between the tip and the crystal surface. This arises because ferrocyanide enters the solution in the gap via both the rapid dissolution of the solid crystal (predominant route) and through diffusion

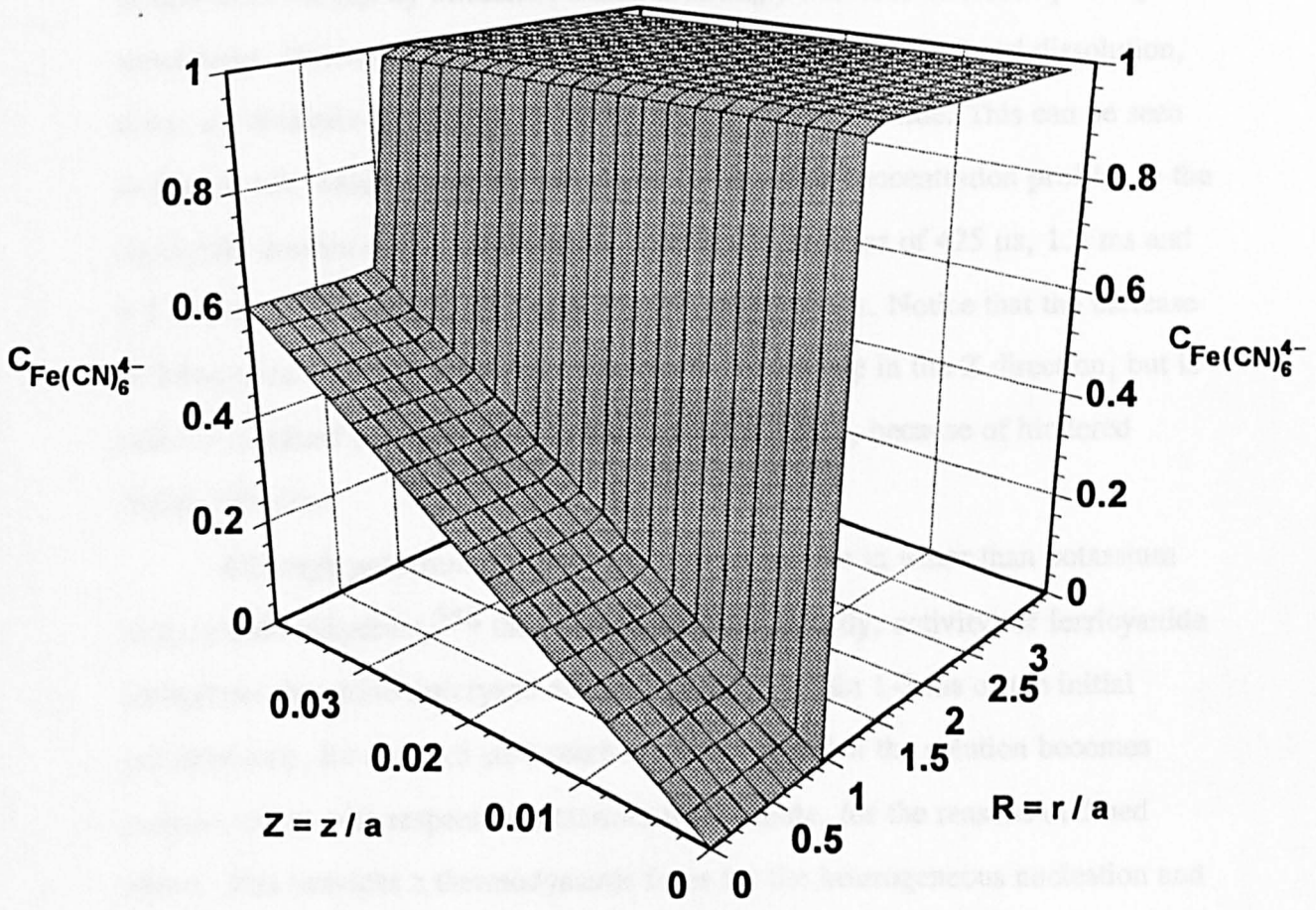

Figure 4.8. Calculated steady-state concentration profile of ferrocyanide within the tip/crystal domain for d = 0.5 μm, a = 12.5 μm and $D_{Fe(CN)_6^{4-}}$ = 5.5 x 10^{-6} cm^2 s^{-1}. The data are for log K_2 = 3.2, and the profile holds for times of 400 μs and longer.

from the edge of the tip/crystal domain (minor route), while ferricyanide can only escape from the gap by diffusion, which is strongly hindered at close tip to crystal separations. Consequently, following the initiation of SECM induced dissolution, there is a dramatic increase in the concentration of ferricyanide. This can be seen in Figure 4.9, which shows the calculated ferricyanide concentration profiles in the tip/crystal domain over a brief period, specifically at times of 425 μs, 1.3 ms and 2.5 ms, *i.e.* $t^{-1/2}$ = 48.5, 27.7 and 20 $s^{-1/2}$, respectively. Notice that the increase in ferricyanide concentration occurs across the entire gap in the Z direction, but is radially localised predominantly to the region $0 \leq R \leq 1$, because of hindered radial diffusion.

Although potassium ferricyanide is more soluble in water than potassium ferrocyanide trihydrate,[258] the concentration (or, strictly, activity) of ferricyanide throughout the entire tip/crystal domain, quickly (within 1-2 ms of the initial potential step, for d = 0.5 μm) reaches a value at which the solution becomes supersaturated with respect to potassium ferricyanide, for the reasons outlined above. This provides a thermodynamic force for the heterogeneous nucleation and growth of potassium ferricyanide on either the crystal or the electrode surface.[264] Spontaneous homogeneous nucleation of potassium ferricyanide crystals in solution can be ruled out at the relatively low supersaturations employed. Either of these processes would explain the decrease in the current at the UME. On the one hand, the precipitation of potassium ferricyanide on the crystal surface would serve to inhibit the dissolution reaction, thereby reducing the ferrocyanide flux, and hence current, at the electrode. On the other hand, the growth of potassium ferricyanide on the UME surface would block the electrode reaction itself. Since at very long times the current was found to tend towards a value for electrolysis with an insulating surface (rather than tending towards zero, as might be expected for direct inhibition of the electrode reaction), the decrease in the current is attributed

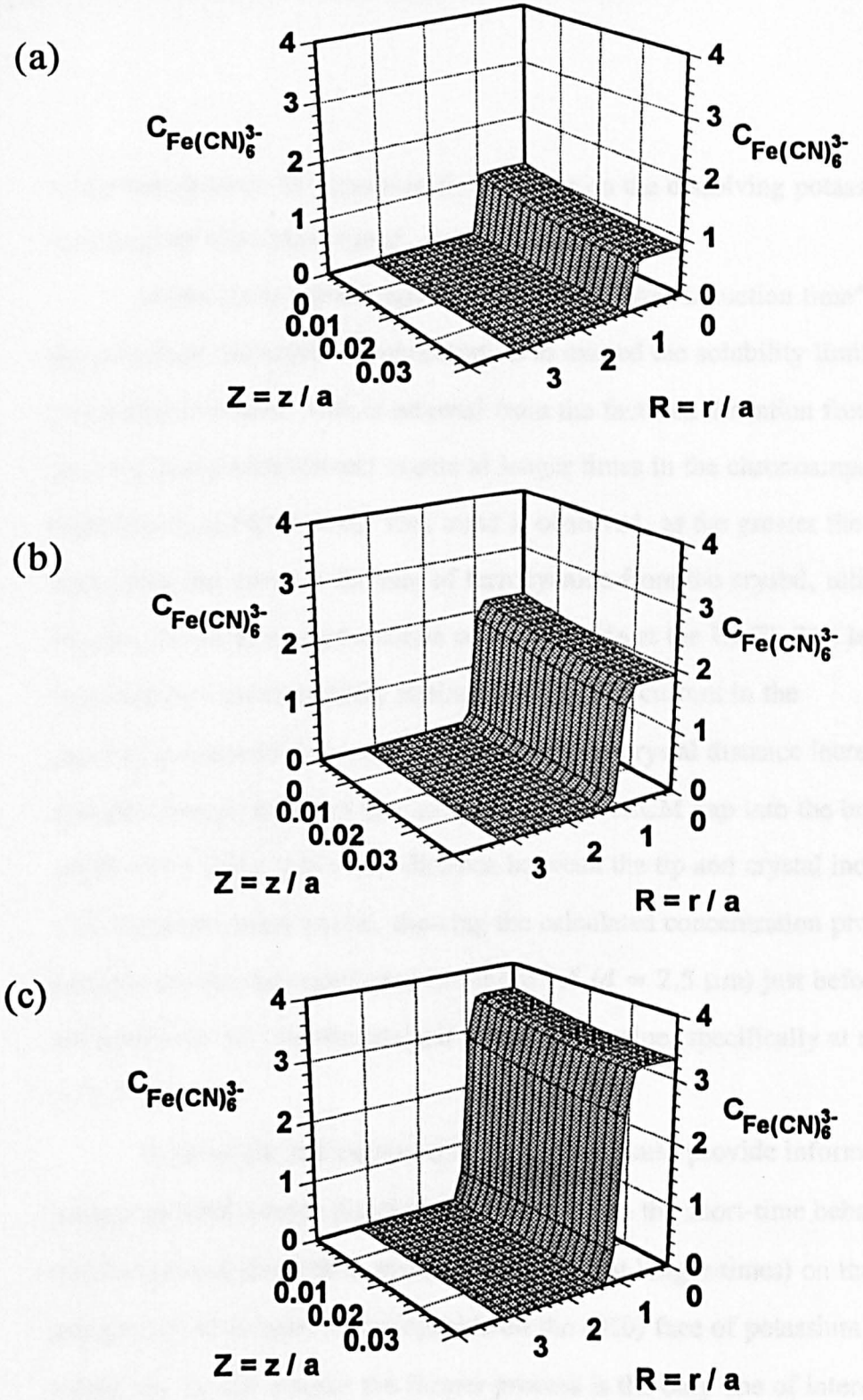

Figure 4.9. Calculated concentration profiles of ferricyanide within the tip/crystal domain for d = 0.5 μm, a = 12.5 μm, $D_{Fe(CN)_6^{4-}}$ = 5.5 x 10^{-6} cm^2 s^{-1} and log K_2 = 3.2. The profiles relate to the following times: (a, top) 425 μs; (b, middle) 1.3 ms; (c, bottom) 2.5 ms.

to the precipitation of potassium ferricyanide on the dissolving potassium ferrocyanide trihydrate crystal, at long times.

As the tip to crystal separation increases, the "induction time" required for the potassium ferricyanide concentration to exceed the solubility limit and precipitate increases. This is inferred from the fact that deviation from the initially attained steady-state current occurs at longer times in the chronoamperometric behaviour (see Figure 4.6). This trend is observed, as the greater the tip to crystal separation, the lower is the flux of ferrocyanide from the crystal, ultimately resulting in the slower production of ferricyanide at the UME. The latter is indicated by a lower initially attained steady-state current in the chronoamperometric characteristics as the tip to crystal distance increases. Note also that ferricyanide ions can escape from the SECM gap into the bulk of the solution at a faster rate as the distance between the tip and crystal increases. Figure 4.10 illustrates these points, showing the calculated concentration profile of ferricyanide for the experiment in Figure 4.6 (d = 2.5 μm) just before the current deviates from the initially attained steady-state value, specifically at t = 13 ms (d = 2.5 μm).

In principle, the current-time behaviour could provide information on both potassium ferrocyanide dissolution kinetics (from the short-time behaviour of the SECM induced dissolution measurement) and (at longer times) on the nucleation and growth of potassium ferricyanide on the (010) face of potassium ferrocyanide trihydrate. In this chapter the former process is the only one of interest and measurement times are considered which are sufficiently short for both potassium ferrocyanide trihydrate and potassium ferricyanide to be soluble, but long enough for the chronoamperometric behaviour to be influenced by the crystal dissolution kinetics.

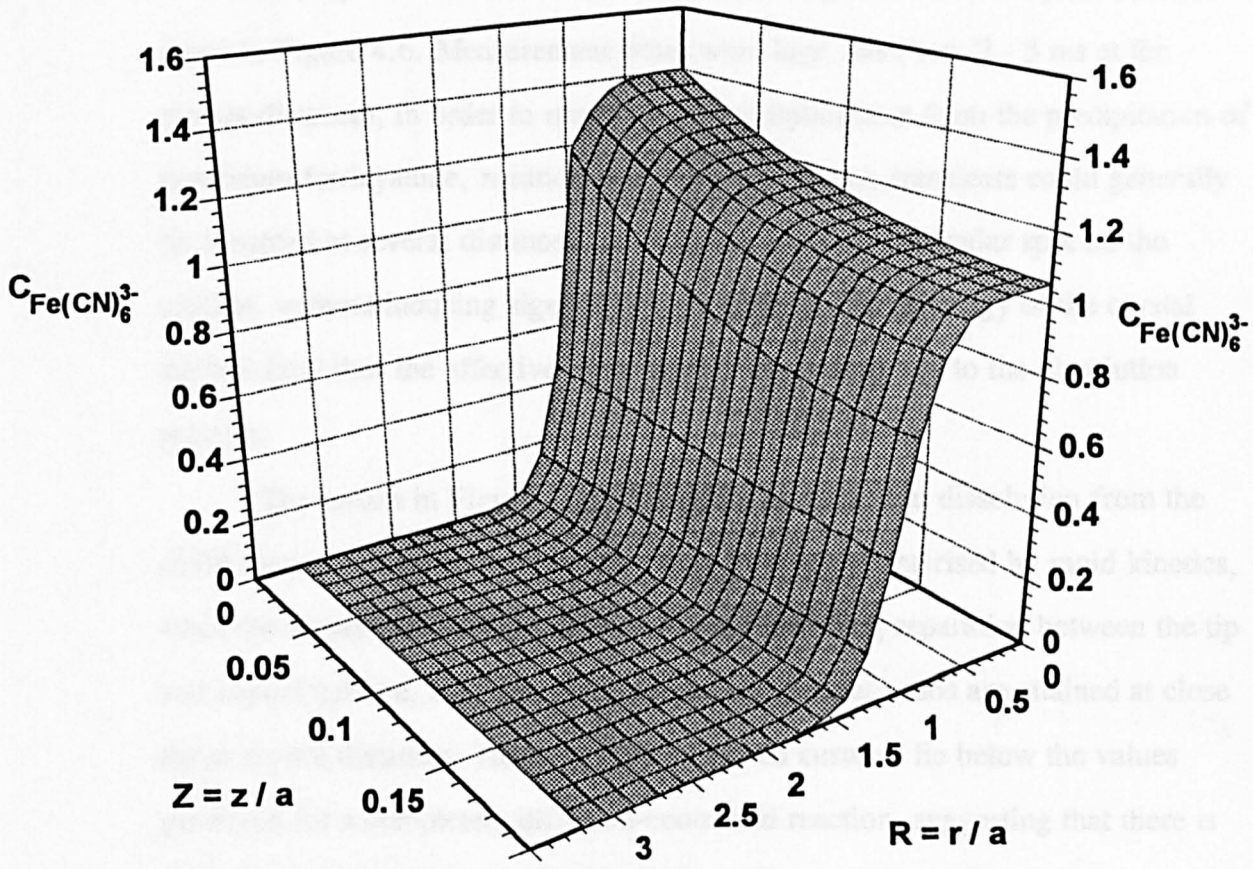

Figure 4.10. Calculated ferricyanide concentration profile within the tip/crystal domain for log $K_2 = 3.2$, $a = 12.5$ μm, $d = 2.5$ μm and $t = 13$ ms.

Figure 4.11 shows the variation of the initially attained steady-state current with distance between the tip and crystal surface. The data, obtained with a tip of a = 12.5 μm, were measured from the plateau regions of i - $t^{-1/2}$ plots such as those in Figure 4.6. Measurement times were kept short (*ca.* 2 - 3 ms at the closest distance), in order to minimise any complications from the precipitation of potassium ferricyanide, mentioned above. In this way, transients could generally be recorded at several distances for dissolution from a particular spot on the surface, without inducing significant changes in the morphology of the crystal surface (and thus the effective tip to crystal separation) due to the dissolution process.

The results in Figure 4.11 clearly demonstrate that dissolution from the (010) face of potassium ferrocyanide trihydrate is characterised by rapid kinetics, since the steady-state current increases with decreasing separation between the tip and crystal surface, and very large normalised current ratios are attained at close tip to crystal distances. However, the measured currents lie below the values predicted for a completely diffusion-controlled reaction, suggesting that there is partial surface kinetic control under the conditions of the SECM measurements. Both the first and second-order theoretical models, described above, were found to provide a good fit to the data in Figure 4.11, with log K_1 = 2.1 and log K_2 = 3.2.

It is likely that both models provide equally satisfactory fits to the experimental data because the (normalised) rate constants lie in the range where the reaction rate is only slightly slower than diffusion controlled, making mechanistic discrimination difficult (see Figure 4.2). It is clear from equation (4.12) that the reaction can be pushed towards lower values of K_n, where discrimination between the two candidate mechanisms is more likely, simply by changing the value of a employed in the tip electrode. This effectively serves to

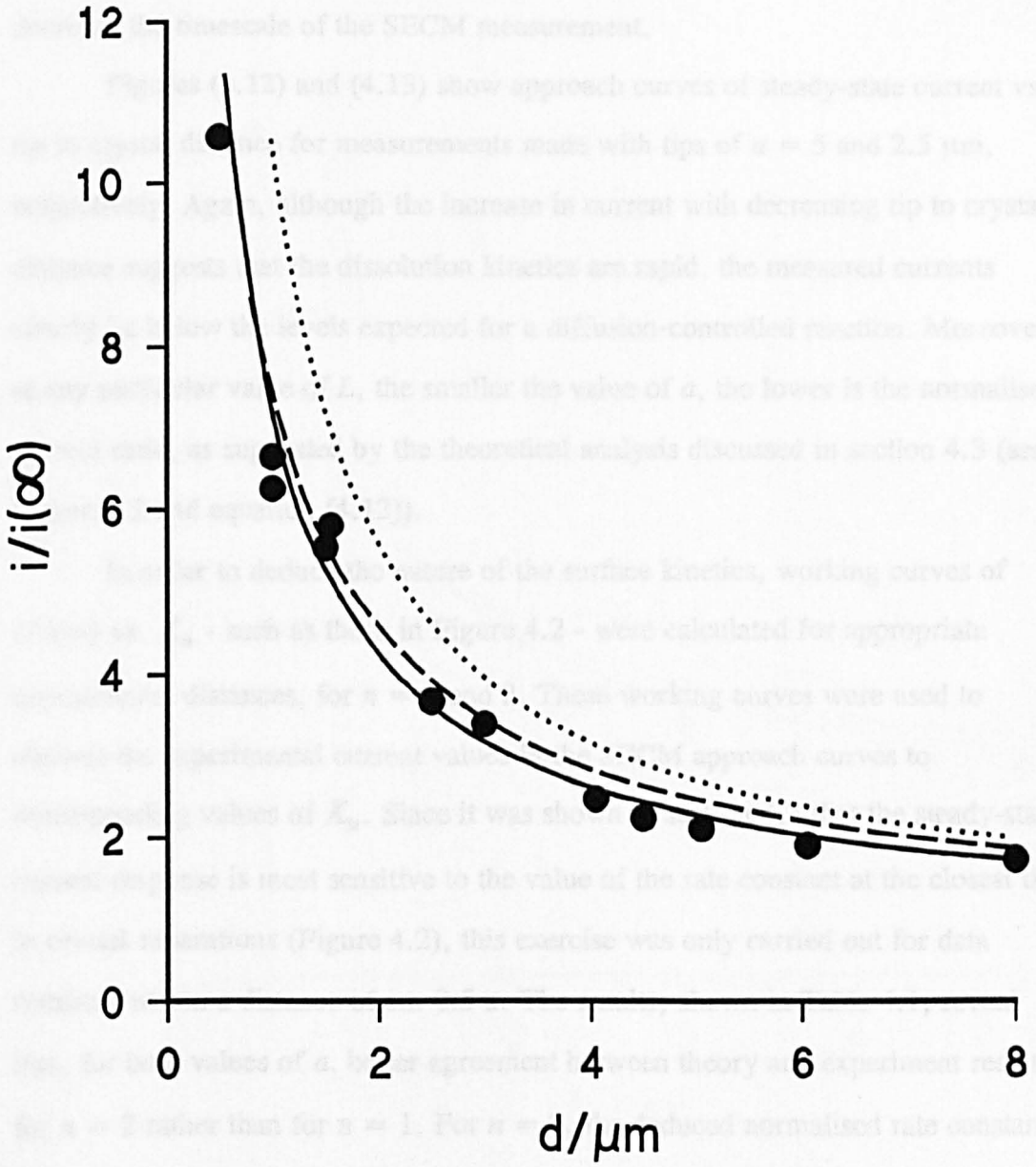

Figure 4.11. SECM experimental approach curve (●) showing the variation of the initially attained steady-state current for ferrocyanide oxidation, at a tip with a = 12.5 μm, with distance between the tip and the substrate surface. The data were derived from chronoamperometric measurements. For comparison, the theoretical behaviour for a diffusion-controlled dissolution process is also shown (···) along with the best fits to the experimental data for the first- and second-order dissolution models, obtained with $\log K_1 = 2.1$ (----) and $\log K_2 = 3.2$ (_).

decrease the timescale of the SECM measurement.

Figures (4.12) and (4.13) show approach curves of steady-state current vs. tip to crystal distance for measurements made with tips of a = 5 and 2.5 μm, respectively. Again, although the increase in current with decreasing tip to crystal distance suggests that the dissolution kinetics are rapid, the measured currents clearly lie below the levels expected for a diffusion-controlled reaction. Moreover, at any particular value of L, the smaller the value of a, the lower is the normalised current ratio, as suggested by the theoretical analysis discussed in section 4.3 (see Figure 4.2 and equation (4.12)).

In order to deduce the nature of the surface kinetics, working curves of $i/i(\infty)$ vs. K_n - such as those in Figure 4.2 - were calculated for appropriate experimental distances, for n = 1 and 2. These working curves were used to convert the experimental current values in the SECM approach curves to corresponding values of K_n. Since it was shown in section 4.3 that the steady-state current response is most sensitive to the value of the rate constant at the closest tip to crystal separations (Figure 4.2), this exercise was only carried out for data obtained within a distance of *ca.* 0.5 a. The results, shown in Table 4.1, reveal that, for both values of a, better agreement between theory and experiment results for n = 2 rather than for n = 1. For n = 2, the deduced normalised rate constant is seen to be reasonably constant over the distances considered, for each value of a, whereas there is a monotonic decrease in K_1 with increasing distance.

The second-order assignment was further confirmed by theoretically simulating the complete current-distance profiles, for comparison with the data in Figures 4.12 and 4.13, using the mean normalised rate constants deduced in Table 4.1. In both cases it is clear that the best fit to the data is obtained for n = 2. Finally, best fit analysis to the data in Figures 4.11 - 4.13 yields fairly constant values of the ratio k_2' of 7.0 cm s^{-1} (a = 12.5 μm), 6.5 cm s^{-1} (a = 5.0 μm) and

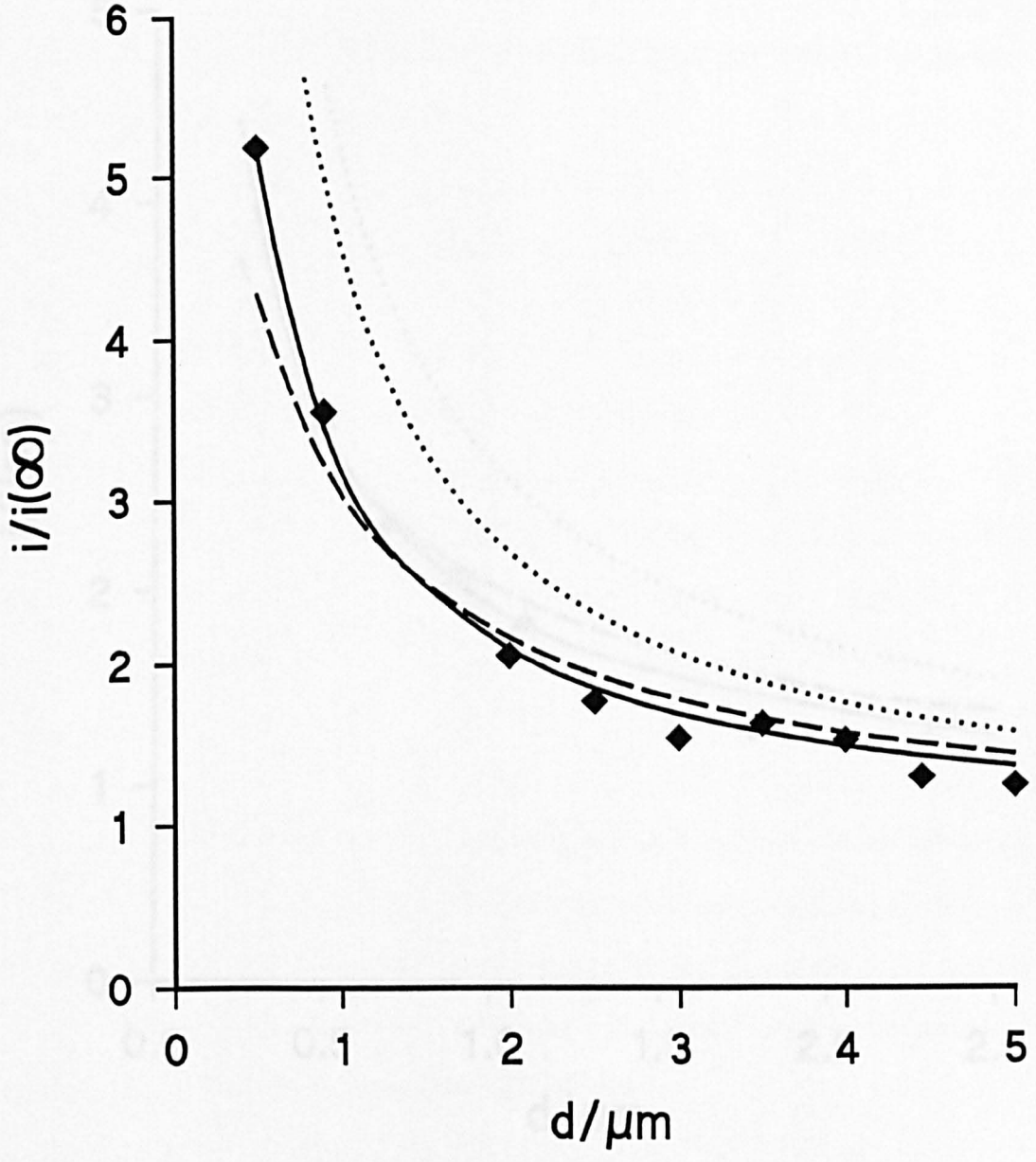

Figure 4.12. SECM experimental approach curve (◆) showing the variation of the initially attained steady-state current for ferrocyanide oxidation, at a tip with a = 5.0 μm, with distance between the tip and the substrate surface. For comparison, the theoretical behaviour for a diffusion-controlled dissolution process is also shown (···) along with the best fits to the experimental data for the first- and second-order dissolution models, obtained with log K_1 = 1.54 (----) and log K_2 = 2.77 (–).

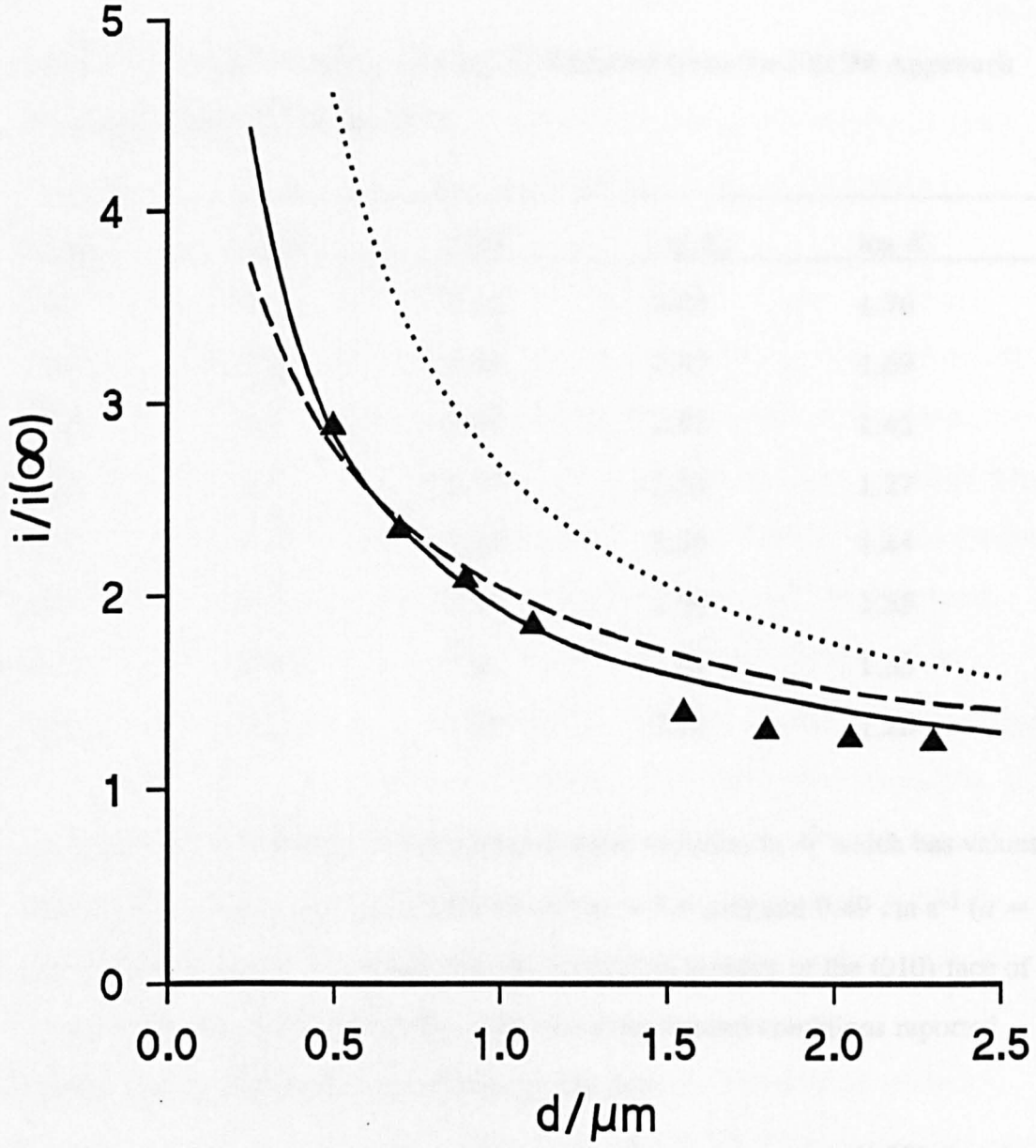

Figure 4.13. SECM experimental approach curve (▲) showing the variation of the initially attained steady-state current for ferrocyanide oxidation, at a tip with a = 2.5 μm, with distance between the tip and the substrate surface. The data were derived from chronoamperometric measurements. For comparison, the theoretical behaviour for a diffusion-controlled dissolution process is also shown (···) along with the best fits to the experimental data for the first- and second-order dissolution models, obtained with $\log K_1 = 1.35$ (----) and $\log K_2 = 2.51$ (—).

Table 4.1: Values of log K_1 and log K_2 Deduced from the SECM Approach Curves in Figures 4.12 and 4.13

$a/\mu m$	$d/\mu m$	$i/i(\infty)$	log K_2	log K_1
5.0	0.5	5.18	2.80	1.76
5.0	0.9	3.55	2.87	1.69
5.0	2.0	2.05	2.81	1.45
5.0	2.5	1.77	2.58	1.27
2.5	0.5	2.88	2.50	1.44
2.5	0.7	2.34	2.50	1.35
2.5	0.9	2.08	2.54	1.33
2.5	1.1	1.85	2.50	1.26

7.1 cm s^{-1} (a = 2.5 μm), whereas there is more variation in k_1' which has values of 0.55 cm s^{-1} (a = 12.5 μm), 0.38 cm s^{-1} (a = 5.0 μm) and 0.49 cm s^{-1} (a = 2.5 μm). This evidence suggests that the dissolution kinetics of the (010) face of potassium ferrocyanide trihydrate, under the experimental conditions reported herein, can be described by the following rate law:

$$j_{Fe(CN)_6^{4-}} = k_2' a_{Fe(CN)_6^{4-}} \sigma^2 \qquad (4.23)$$

where k_2' = 6.9 cm s^{-1}.

The above analysis demonstrates that the rate of dissolution of potassium ferrocyanide trihydrate in an aqueous solution containing 3.5 mol dm^{-3} potassium chloride (an example of an unsymmetric salt dissolving in a non-stoichiometric solution of the lattice ions), can be successfully interpreted in terms of one of the limiting laws arising from the BCF spiral dissolution model.[2,4] The observation of a second-order dependence of the dissolution rate on the interfacial undersaturation

is consistent with the BCF model at low interfacial undersaturation (which prevailed under the conditions of the experiments reported above) and suggests that the rate limiting step in the dissolution process is surface diffusion.

4.5.3 Dissolution rate imaging

In order to obtain a true spatial map of the dissolution activity of the (010) surface of potassium ferrocyanide trihydrate, it was important to carry out imaging experiments under conditions where the tip response would (i) not be affected by the precipitation of potassium ferricyanide on the crystal surface (discussed above) but (ii) be influenced by the dissolution kinetics. These considerations placed lower and upper limits on the tip scan speeds which could be employed in imaging, the values of which depended on the size of the tip and its distance from the crystal surface. In particular, although the theoretical results indicate that SECM is more sensitive to surface kinetics at close tip to crystal separations, practically this has the effect of shortening the induction time before inhibition of the dissolution reaction occurs through potassium ferricyanide precipitation, thus dramatically increasing the tip scan speeds required for imaging.

The minimum scan speed required for imaging experiments can be estimated by noting that the probe has to move through a distance of at least one electrode diameter in the critical "induction time" for ferricyanide precipitation, t_{ind}, suggesting a scan speed of:

$$v_{scan} = 2a / t_{ind} \qquad (4.24)$$

In order to illustrate this point, consider a 25 μm electrode positioned 0.5 μm from the crystal surface. It follows from Figure 4.6, that $t_{ind} \approx 3$ ms for this case, which suggests that a scan speed in excess of 8000 μm s^{-1} is required. As noted above, increasing the tip to substrate separation, increases the induction time, thereby allowing the use of more reasonable raster scan speeds. In this study, all

images were recorded with a tip of a = 5 μm which was positioned *ca.* 5 μm from the crystal surface. Experiments with a static probe at this distance indicated that no decrease in the current, from the initially attained steady-state value, occurred in periods as long as 500 ms. Thus a raster scan speed of 50 μm s^{-1} was employed to ensure that problems due to potassium ferricyanide precipitation were not encountered.

Preliminary imaging studies of the dissolution activity of the crystal surface, obtained by monitoring the diffusion-limited current for the oxidation of ferrocyanide as the tip was scanned over square areas up to 400 μm in length, indicated that the surface was uniformly reactive, as judged by the fact that a constant current was measured (deviation from the mean *ca.* ± 5 %). Thus to test the imaging capabilities of the technique, features (in particular, etch pits) were created in the surface and the corresponding activity was mapped using the SECM in the tip scanning mode.

A typical dissolution rate image is shown in Figure 4.14(a). For the purposes of this image, a pit was first electrochemically etched in the surface of the crystal, using a 50 μm diameter electrode positioned *ca.* 40 μm from the surface and held at a potential of +0.75 V for a *ca.* 1 second, so as to oxidise ferrocyanide at a diffusion-controlled rate. The 50 μm diameter tip was then replaced with a tip of a = 5 μm, positioned 5.3 μm from the surface, which was used to record an image of the dissolution activity across the pit and the surrounding area over a square region of 300 μm by 300 μm. The raster scan in Figure 4.14(a) begins at the position x = 150 μm, y = 150 μm. The current at this point is much lower than for the rest of the scan, because the tip pauses at this position for 3 s, with the potential at +0.75 V, before the scan begins, which is a sufficiently long period for the dissolution process to become inhibited by ferricyanide ions produced at the electrode. Over the remaining area surrounding

(a)

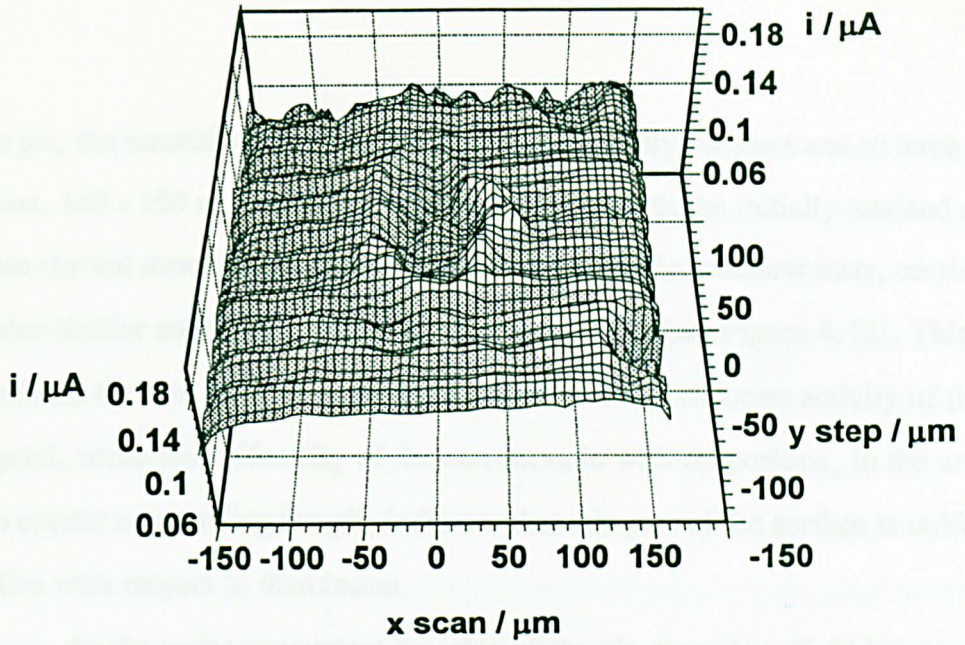

(b)

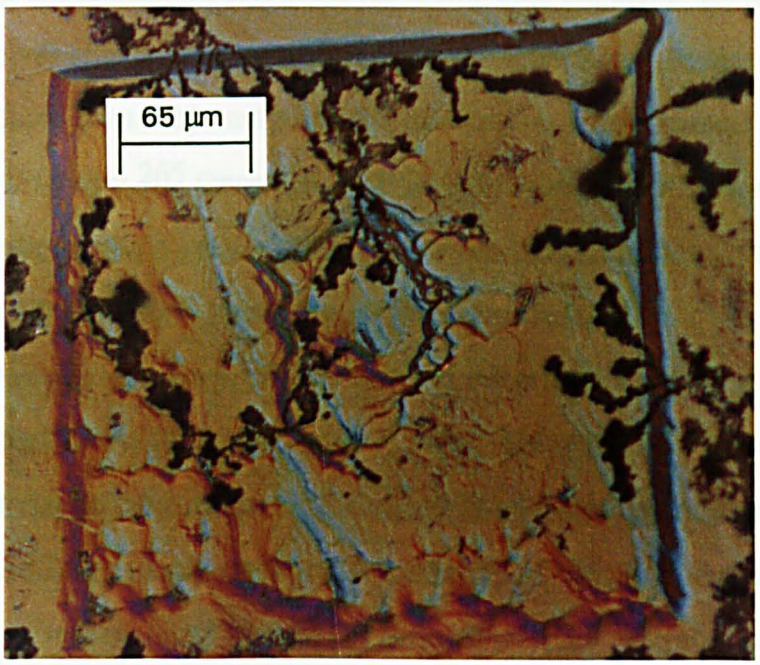

Figure 14.4. (a, top) Dissolution rate image of a single pit on the (010) surface of potassium ferrocyanide trihydrate. The 300 μm x 300 μm image was recorded by scanning a probe UME (a = 5.0 μm) at a height of 5.3 μm above the crystal surface and recording the diffusion-limited current for the oxidation of ferrocyanide as a function of tip position, with the tip potential held at +0.75 V. The step size between line scans employed in the raster scan was 5 μm. (b, bottom) DIC optical micrograph of the area of the crystal surface in which part (a) was recorded. An etched square of 300 μm length, resulting from induced dissolution during the reaction rate imaging process, is clearly evident.

the pit, the normalised current is seen to be relatively constant and to have a value of *ca.* 140 - 150 nA which is in good agreement with the initially attained steady-state current measured in chronoamperometric kinetic measurements, carried out under similar conditions, described in section 4.5.2 (see Figure 4.12). This confirms that the imaging experiment monitors the dissolution activity of the crystal, while the uniformity of the current ratio with tip position, in the area of the crystal surrounding the pit, indicates that this part of the surface is uniformly active with respect to dissolution.

As the probe encounters the edge of the pit, there is a slight increase in the current. This indicates that there is an increase in the dissolution rate, suggesting that macroscopic edges dissolve at a more rapid rate than the planar surface. Similar (qualitative) effects have been seen in *ex-situ* microscopy studies on powders which have been subjected to partial dissolution, where corners and edges show enhanced reactivity.[265] Once the UME is within the pit itself, the current falls, because there is now a greater distance between the tip and the crystal surface, and thus the tip sees a lower flux of ferrocyanide ions.

A DIC optical micrograph of the region of the crystal in which the above SECM image was taken is shown in Figure 4.14(b). Although there is some precipitated material on the surface, which results from evaporation when the crystal is removed from the saturated solution, the image clearly shows a square etched region, where the crystal surface has been dissolved during the course of the scan. The etched region is the same size as the scan employed to record the dissolution rate image in Figure 4.14(a). The outline of the pit imaged in Figure 4.14(a) is clearly evident in the centre of the scanned region in Figure 4.14(b). Moreover, comparison of Figures 4.14(a) and (b) establishes that the location and dimensions of the pit, measured by reaction rate imaging and optical microscopy correlate well.

It was shown earlier in section 4.5.1 that the diffusion-limited reduction of ferricyanide, added at low concentration to the saturated potassium ferrocyanide solution, acts as a calibrant of the tip to crystal distance. It follows that in imaging experiments, the reduction of ferricyanide could be used to provide an image of the surface topography, in an initial scan of the surface, while the oxidation of ferrocyanide during a second scan would serve to map the corresponding dissolution activity. In order to illustrate this concept practically, the crystal surface of interest was deliberately misorientated by *ca.* 1 °, in order to artificially create a substrate with a slope, and again electrochemically etched a pit in the surface, as described above. Topographic and dissolution rate images were then recorded over an area of 200 μm by 200 μm, with the tip positioned a distance of 5 μm away from the surface in the centre of the image. For the topographic image, the tip was held at a potential of -0.1 V, where the reduction of ferricyanide was diffusion-controlled, and scanned at a speed of 10 μm s^{-1}, with 4 μm steps between line scans. The dissolution rate image was recorded by holding the tip potential at +0.8 V, while scanning at 50 μm s^{-1}, with 2 μm steps between line scans.

Raw data for the topographic image, showing the current for the diffusion-controlled reduction of ferricyanide as a function of tip position is given in Figure 4.15(a). The current data have been normalised with respect to the steady-state current attained when the tip is effectively at an infinite distance from the surface ($i(\infty) = 2.62$ nA). It is evident that, in general, the normalised current ratio decreases as the tip is moved towards negative positions in both the x and y directions, suggesting that diffusion to the UME becomes increasingly hindered,[122] as would be expected if the separation decreased between the tip and the crystal surface. Superimposed on this slope, however, is an increase in current in the centre of the image. When the tip is in this position, diffusion is therefore

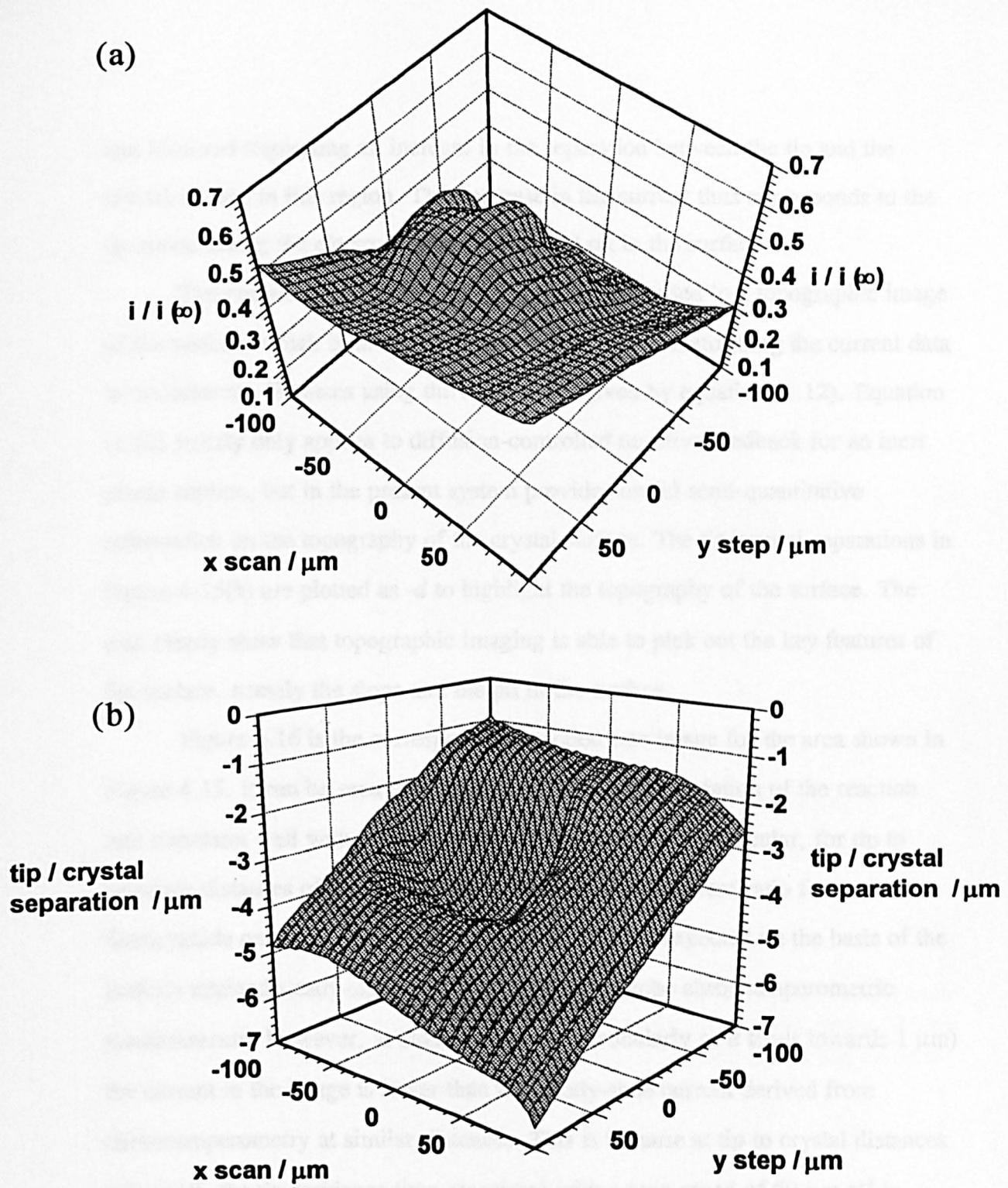

Figure 4.15. Topographic image of a pit on the surface on the (010) surface of potassium ferrocyanide trihydrate, which was misorientated by *ca.* 1 ° with respect to the base of the cell. The image is displayed in terms of $i/i(\infty)$ vs. tip position in the x, y plane (a, top) and tip to crystal separation, d, as a function of tip position in the x, y plane, obtained by transforming the raw data using equation (1.12), (b, bottom).

less hindered suggesting an increase in the separation between the tip and the crystal surface in this region. This increase in the current thus corresponds to the tip encountering the electrochemically induced pit in the surface.

The current image in Figure 4.15(a) was converted to a topographic image of the surface, which is shown in Figure 4.15(b), by transforming the current data to tip/substrate distances using the relation[266] given by equation (1.12). Equation (1.12) strictly only applies to diffusion-controlled negative feedback for an inert planar surface, but in the present system provides useful semi-quantitative information on the topography of the crystal surface. The tip/crystal separations in Figure 4.15(b) are plotted as $-d$ to highlight the topography of the surface. The data clearly show that topographic imaging is able to pick out the key features of the surface, namely the slope and the pit in the surface.

Figure 4.16 is the corresponding reaction rate image for the area shown in Figure 4.15. It can be seen that, in general, the spatial variation of the reaction rate correlates well with the topography of the surface. In particular, for tip to substrate distances of 5 μm or greater, the normalised current ratio for ferrocyanide oxidation is in close agreement with that expected on the basis of the initially attained steady-state current in stationary probe chronoamperometric measurements. However, at closer distances (particularly as d tends towards 1 μm) the current in the image is lower than the steady-state current derived from chronoamperometry at similar distances. This is because at tip to crystal distances this small, the tip residence time associated with a scan speed of 50 μm s^{-1} is sufficiently long for ferricyanide to build up in the gap between the tip and substrate beyond the saturation limit for potassium ferricyanide and block the potassium ferrocyanide trihydrate crystal surface via a precipitation process.

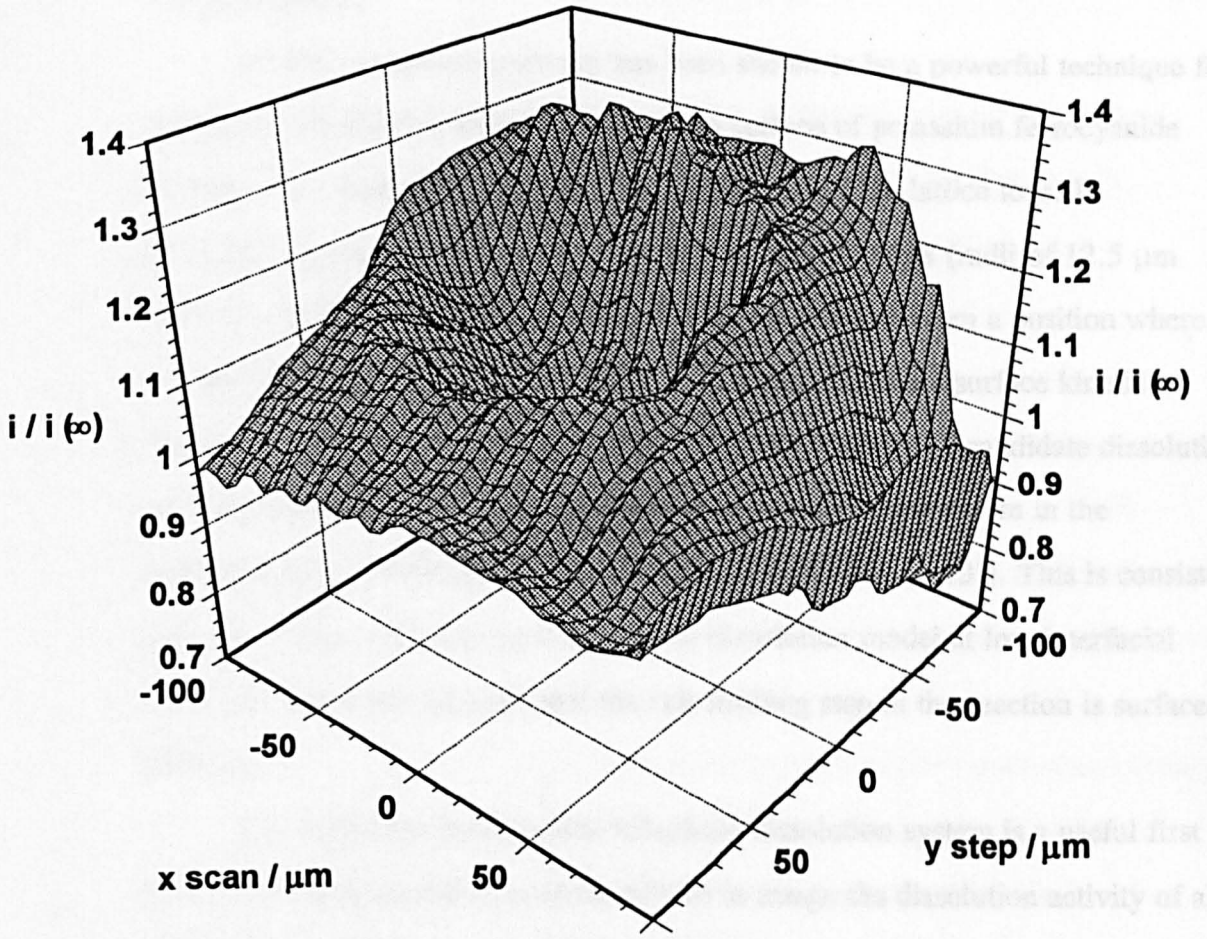

Figure 4.16. Dissolution rate image of the (010) surface of potassium ferrocyanide trihydrate recorded in the same area of the crystal as the topographic image shown in Figure 4.15. The tip was held at a potential of +0.8 V and scanned at a speed of 50 μm s^{-1} with 2 μm steps between the line scans.

4.6 Conclusions

SECM chronoamperometry has been shown to be a powerful technique for probing the dissolution kinetics of the (010) surface of potassium ferrocyanide trihydrate in a non-stoichiometric aqueous solution of the lattice ions. In particular, by using a series of increasingly smaller tip sizes (radii of 12.5 μm down to 2.5 μm) it has been possible to push the reaction from a position where the rate is close to diffusion-controlled, to a timescale where surface kinetic limitations are apparent. Interpretation of the data in terms of candidate dissolution rate laws suggests that the rate is governed by a second-order term in the undersaturation at the crystal/solution interface (equation (4.23)). This is consistent with the Burton, Cabrera and Frank spiral dissolution model at low interfacial undersaturations and suggests that the rate limiting step in the reaction is surface diffusion.[4]

The potassium ferrocyanide trihydrate dissolution system is a useful first model for testing the abilities of the SECM to image the dissolution activity of a single crystal surface. In particular, the (010) surface has been shown to be uniformly active to dissolution at spatial level of *ca.* 10 μm. Additionally, by using ferricyanide reduction as a calibrant of the tip to crystal separation it has been demonstrated that the topography and activity of a single crystal surface can be mapped at the micrometre level in sequential scans.

CHAPTER 5

SILVER CHLORIDE DISSOLUTION KINETICS IN AQUEOUS SOLUTIONS WITH AND WITHOUT SUPPORTING ELECTROLYTE

The kinetics of silver chloride dissolution in aqueous solutions with and without supporting electrolyte, have been investigated using the well-defined and high mass transport properties of the SECM. In this application a probe UME, positioned close to a silver chloride surface (pressed pellet or electrochemically grown film), is used to induce and monitor the dissolution process via the reduction of Ag^+, from an initially saturated solution.

In the presence of a supporting electrolyte (0.1 mol dm^{-3} potassium nitrate), the dissolution reaction was found to be diffusion-controlled under all of the conditions utilised. In parallel with the experiments, theory for SECM induced dissolution has been developed for the case where dissolution of a binary salt occurs in a solution in which none of the lattice ions are buffered. Under these conditions, theoretical and experimental results demonstrate that when only one of the lattice ions is removed from the tip/substrate gap by electrolysis, the electroinactive counter ion becomes trapped in the gap between the tip and substrate by hindered diffusion. Consequently the attainment of high interfacial undersaturations becomes difficult and the crystal/solution interface becomes saturated even with moderate dissolution rate constants, providing an explanation for the experimental results observed under these conditions.

For the situation where there is no supporting electrolyte, theory relating the current flow to rate laws in which dissolution is governed by either a first- or second-order dependence on the interfacial undersaturation has been developed numerically,

using the ADI finite-difference method to solve the mass transport equation appropriate to the system of interest. It is shown that the two rate laws may readily be distinguished from steady-state approach (current-distance) measurements. Experiments covering a range of mass transport rates, through the use of probe UMEs with radii of 5, 12.5 and 25 μm, demonstrate, for the first time, that the dissolution of silver chloride, in the forms of interest, occurs via a second-order rate law in *interfacial* undersaturation.

5.1 Introduction

In this chapter SECM induced dissolution studies are significantly developed by consideration of the dissolution kinetics of electrochemically grown films and pressed pellets of silver chloride, in aqueous solutions with and without supporting electrolyte. This system is of interest for several reasons. First, the kinetics and mechanisms controlling the dissolution of silver chloride in aqueous solutions is currently unresolved despite a number of studies.[221-223] The study of this process thus provides a useful test of the capabilities of the SECM to characterise, unambiguously, the dissolution kinetics of a sparingly soluble material.

Second, when supporting electrolyte is present but does not contain a common ion with the material of interest, the independent diffusion of all of the dissolving ions has to be considered. The treatment of this problem thus significantly diversifies the theory for SECM dissolution. One of the main consequences of induced dissolution under these conditions is that the solution concentration of the components of the crystalline material which are not electrolysed (ions which are electroinactive at the electrode potential of interest) will increase in the tip/substrate gap during the period of a measurement. This results in dissolution into an environment which is a spatially and temporally non-stoichiometric with respect to the lattice ions of the solid material and therefore presents an opportunity to examine,

both theoretically and experimentally, dissolution theories under these conditions.

Third, dissolution under conditions where there is no deliberately added supporting electrolyte diversifies the range of systems which can be studied electrochemically to include conditions where the use of a supporting electrolyte may be inappropriate. The electroneutrality principle which applies to the solution ensures that, for the system of interest, the local concentrations of the electroactive and electroinactive ions must remain equal, even when the concentration of the former ion type (Ag^+ for the system of interest) is depleted by electrolysis at the tip. The beneficial consequences of induced dissolution under these conditions are that mass transport can be reduced to a one species problem and both high undersaturations and mass transport rates can be attained, thus facilitating the study of rapid heterogeneous kinetics. The behaviour of UMEs under conditions where supporting electrolyte is excluded has been well-characterised, see for example references 267-270 for a selection of appropriate papers. However, there have been no previous SECM studies under these conditions.

Although the use of well-defined surfaces in the study of dissolution kinetics has been advocated (see section 1.1 and references 271 and 272) the measurements reported herein are with pressed pellets and electrochemically grown films of silver chloride to allow a comparison of the SECM results with those obtained in earlier work[221-223] which employed similar surfaces.

5.2 Theory

5.2.1 Formulation of the Problem for the Case of an Inert Supporting Electrolyte which does not Contain a Common Ion with the Dissolving Material

For the dissolution of AgCl, the rate law is:

$$j_{Ag^+} = j_{Cl^-} = k_n \sigma^n \qquad (5.1)$$

From equations (2.69) and (2.71) σ is:

$$\sigma = 1 - \left(\frac{a_{Ag^+} a_{Cl^-}}{(a_{Ag^+})^* (a_{Cl^-})^*} \right)^{1/2} \tag{5.2}$$

As the experiments were carried out in the presence of excess potassium nitrate, the electroinactive Cl^- ion concentration cannot be assumed to be constant during the course of an SECM dissolution measurement. In contrast to the problem in Chapter 4 equation (5.2) cannot be simplified further and the problem requires the consideration of two species, Ag^+ and Cl^-. The UME chronoamperometric response is considered, following a step in the potential to a value where Ag^+ is reduced at a diffusion-controlled rate. The general dimensionless SECM diffusion equation, for both Ag^+ and Cl^- is given by equation (4.4) where the parameter λ_i,

$$\lambda_i = \frac{D_i}{D_{Ag^+}} \tag{5.3}$$

reflects the fact that, under the conditions of the experiment, Ag^+ and Cl^- have unequal diffusion coefficients.

The initial and boundary conditions are:

$\tau = 0$, all R, all Z: $\quad C_{Cl^-} = 1, \; C_{Ag^+} = 1$ (5.4)

$\tau > 0$, $Z = 0$, $0 \le R \le 1$ (tip electrode):

$$C_{Ag^+} = 0, \; \frac{\partial C_{Cl^-}}{\partial Z} = 0 \tag{5.5}$$

$\tau > 0$, $Z = 0$, $1 < R \le RG$ (glass sheath):

$$\frac{\partial C_{Ag^+}}{\partial Z} = 0, \; \frac{\partial C_{Cl^-}}{\partial Z} = 0 \tag{5.6}$$

$\tau > 0$, $R > RG$, $0 < Z < L$ (radial edge of the tip/substrate domain):

$$C_{Cl^-} = 1, \; C_{Ag^+} = 1 \tag{5.7}$$

$\tau > 0, R = 0, 0<Z<L$ (axis of symmetry):

$$\frac{\partial C_{Ag^+}}{\partial R} = 0, \quad \frac{\partial C_{Cl^-}}{\partial R} = 0 \tag{5.8}$$

$\tau > 0, Z = L, 0 \leq R \leq RG$ (substrate):

$$\frac{\partial C_{Ag^+}}{\partial Z} = \frac{\partial C_{Cl^-}}{\partial Z} = -\frac{K_n}{\lambda_i}[1-(C_{Ag^+}C_{Cl^-})^{1/2}]^n \tag{5.9}$$

In equations (5.4) - (5.9), C_i is the concentration of species i (Ag^+ or Cl^-) normalised with respect to the saturated concentration of AgCl, c^*_{AgCl}. The dimensionless dissolution rate constant in equation (5.9) is given by:

$$K_n = \frac{k_n a}{c^*_{AgCl} D_{Ag^+}} \tag{5.10}$$

where k_n is the dissolution rate constant.

The problem was solved numerically using the ADI finite-difference method[239-241] to calculate the normalised tip current response, as given by equation (2.14), where C now represents C_{Ag^+}. In ADI finite-difference form, the substrate boundary condition for Ag^+ during the second half-time step, is given by:

$$\frac{{}^{Ag^+}C^{**}_{j,NZ} - {}^{Ag^+}C^{**}_{j,NZ-1}}{\Delta Z} = K_n\left[1-\left({}^{Ag^+}C^{**}_{j,NZ}\,{}^{Cl^-}C^{**}_{j,NZ}\right)^{1/2}\right]^n \tag{5.11}$$

For $n = 1$, and

$$x = \left({}^{Ag^+}C^{**}_{j,NZ}\right)^{1/2} \tag{5.12}$$

equation (5.11) can be rearranged to the following quadratic equation:

$$x^2 + xm\left({}^{Cl^-}C^{**}_{j,NZ}\right)^{1/2} - {}^{Ag^+}C^{**}_{j,NZ-1} - m = 0 \tag{5.13}$$

where m is as defined in equation (4.16). Hence:

$$x = \frac{\left[m^2\,{}^{Cl^-}C^{**}_{j,NZ} + 4\left({}^{Ag^+}C^{**}_{j,NZ-1} + m\right)\right]^{1/2} - m\left({}^{Cl^-}C^{**}_{j,NZ}\right)^{1/2}}{2} \qquad (5.14)$$

i.e.;

$${}^{Ag^+}C^{**}_{j,NZ} = \frac{\left(\left[m^2\,{}^{Cl^-}C^{**}_{j,NZ} + 4\left({}^{Ag^+}C^{**}_{j,NZ-1} + m\right)\right]^{1/2} - m\left({}^{Cl^-}C^{**}_{j,NZ}\right)^{1/2}\right)^2}{4} \qquad (5.15)$$

Equation (5.15) can be substituted into equation (2.77) written for Ag^+ and Cl^-, which then allows the calculation of Ag^+ concentrations. Commencing with Ag^+, ${}^{Cl^-}C^{**}_{j,NZ}$ must be known. Thus the calculation of Ag^+ and Cl^- proceeds sequentially and iteratively with ${}^{Cl^-}C^{**}_{j,NZ}$ initially approximated by ${}^{Cl^-}C^{*}_{j,NZ}$, until the new concentrations are converged to 10^{-4} % between successive iterations.

Using the Cl^- substrate boundary condition, ${}^{Cl^-}C^{**}_{j,NZ}$ is expressed as:

$${}^{Cl^-}C^{**}_{j,NZ} = \frac{\left({}^{Ag^+}C^{**}_{j,NZ} - {}^{Ag^+}C^{**}_{j,NZ-1}\right)}{\lambda_{Cl^-}} + {}^{Cl^-}C^{**}_{j,NZ-1} \qquad (5.16)$$

When $n = 2$, equation (5.13) can be rearranged to:

$$x^2 + 2m\,{}^{Cl^-}C^{**,1/2}_{j,NZ}x - {}^{Cl^-}C^{**}_{j,NZ}x - m = 0 \qquad (5.17)$$

Equation (5.16) still holds and the calculation proceeds in an analogous manner to the case for $n = 1$.

5.2.2 Formulation of the SECM Dissolution Problem for the Case where there is No Supporting Electrolyte

The aim is to calculate the tip current response when the dissolution of a sparingly soluble binary (1:1) salt, such as AgCl,[273] in a solution containing no

supporting electrolyte, is induced through the diffusion-controlled electrolysis of one of the types of ion (Ag^+) at the tip UME of the SECM. This requires the solution of the mass transport equations appropriate to these conditions, subject to initial and boundary conditions which define the experiment of interest.

An authoritative overview of mass transport in dilute electrolyte solutions has been given by Newman,[274] and is drawn upon for the initial formulation of the problem. The material balance equation for each species of interest, i (Ag^+ and Cl^-) is:

$$\frac{\partial c_i}{\partial t} = -\nabla \cdot \mathrm{N}_i \tag{5.18}$$

where N_i is the flux of the species i. Since mass transport occurs in a dilute ionic solution (given the sparingly soluble nature of AgCl in aqueous solution[273]), without supporting electrolyte and convective effects, it is reasonable to employ the Nernst-Planck equation[274] to define the ionic fluxes, which comprise contributions from diffusion and migration:

$$\mathrm{N}_i = -D_i \nabla c_i - z_i F u_i c_i \nabla \Phi \tag{5.19}$$

In equation (5.19) z_i is the charge number of species i, Φ is the electric potential in solution and u_i is the mobility of the species of interest. u_i and D_i are both treated as constants. This is a reasonable assumption given that the solution is initially dilute. Thus, although electrolysis will locally decrease the ionic strength of the solution in the vicinity of the tip, the changes involved will not significantly effect the values of D_i and u_i.

Away from the thin double charge layer near the electrode and other boundaries, the solution will be electrically neutral.[274] The characteristic thickness of the diffuse layer at the electrode/solution and substrate/solution interfaces, under the conditions of the studies described herein (at equilibrium) may be estimated to be *ca.* 80 nm (using the Gouy-Chapman model[274] together with the concentration of the

ions in the saturated solution, identified later in section 5.5.1.2). The thickness of the diffuse layer is much less than the length over which diffusion occurs in the induced dissolution measurements with the tip/substrate separations employed (2 - 12 μm). Throughout the tip/substrate gap, it is thus reasonable to define the concentration of electrolyte by:

$$c = c_+ = c_- \tag{5.20}$$

where cations and anions are denoted, respectively by the subscripts + and -. After substituting equations (5.19) and (5.20) into equation (5.18), with the assumptions outlined above, the material balance for each of the species can be written thus:

$$\frac{\partial c}{\partial t} = z_+ u_+ F \nabla \cdot (c \nabla \Phi) + D_+ \nabla^2 c \tag{5.21}$$

$$\frac{\partial c}{\partial t} = z_- u_- F \nabla \cdot (c \nabla \Phi) + D_- \nabla^2 c \tag{5.22}$$

The potential term can readily be eliminated from either of equations (5.21) or (5.22) by subtracting equation (5.22) from (5.21), rearranging and substituting the resulting expression for the potential into equation (5.21) or (5.22). This yields:[274]

$$\frac{\partial c}{\partial t} = D \nabla^2 c \tag{5.23}$$

where

$$D = \frac{z_+ u_+ D_- - z_- u_- D_+}{z_+ u_+ - z_- u_-} \tag{5.24}$$

Equation (5.23) is the time-dependent diffusion equation demonstrating that, due to the requirement of electroneutrality, electrolyte transport is a one species problem. The apparent diffusion coefficient, D, is that for the diffusion of the electroactive ion under the influence of electroinactive counter ion; its value is therefore system dependent and may be different from the diffusion coefficient measured in the presence of excess supporting electrolyte.

In the axisymmetric cylindrical geometry of the SECM, equation (5.23) can be expressed as equation (2.12). Prior to the potential step, the solution is saturated with respect to the lattice ions of the solid material, which is reflected in the initial condition for the problem, given by equation (2.2) where c_{Ox} replaced by c, is now the concentration of silver chloride.

Following the potential step, the species of interest (Ag^+) is electrolysed (reduced to Ag) at a diffusion-controlled rate at the UME tip, while the insulating sheath surrounding the electrode is inert, as given by equations (2.3) and (2.4) respectively. From a physical point of view, when migration effects are important, it is extremely difficult to achieve a concentration of zero at the electrode surface immediately after the potential step, even at large driving potentials.[267] A more comprehensive treatment of the chronoamperometric mode at very short times would employ the Butler-Volmer equation in place of equation (2.3), but since this chapter is concerned with steady-state characteristics, it is reasonable to use the boundary condition adopted in the solution of the problem. The boundary conditions given by equations (2.5) and (2.6) also apply.

Under the defined conditions, the flux of material from the substrate surface is given by equation (2.73). σ for a (1:1) electrolyte is given, strictly, by equation (5.2). For the treatment of a sparingly soluble material with no inert supporting electrolyte present, it is reasonable to replace activities by concentrations such that, under the defined conditions, the interfacial undersaturation may be written as:

$$\sigma = 1 - (c_{AgCl} / c^{*}_{AgCl}) \tag{5.25}$$

The aim of the calculations is to determine the current flowing at the UME. For the situation where the cation (Ag^+) is reduced at the electrode and the anion is electroinactive, it can readily be shown that the relationship between the current and concentration gradient normal to the electrode surface is:[274]

$$i = -\frac{2\pi z_+ FDac^*_{AgCl}}{1-t_+}\int_0^1\left(\frac{\partial C_{AgCl}}{\partial Z}\right)_{Z=0} RdR \qquad (5.26)$$

where the number of electrons transferred in the electrode process is equivalent to the charge number of the cation, z_+. The transference number of the cation, for the system in question, is given by:

$$t_+ = \frac{z_+ u_+}{z_+ u_+ - z_- u_-} \qquad (5.27)$$

In the absence of supporting electrolyte, the steady-state diffusion-limited current when the tip is positioned at an effectively infinite distance from the substrate is:[275,276]

$$i(\infty) = \frac{4z_+ FDac^*_{AgCl}}{1-t_+} \qquad (5.28)$$

and so the dimensionless current ratio is given by equation (2.14).

Numerical solutions to the SECM problems were achieved using the ADI finite-difference method.[239-241] For this particular problem, the substrate boundary condition in finite-difference form for the second half-time step in the calculation is:

$$\frac{{}^{AgCl}C^{**}_{j,NZ-1} - {}^{AgCl}C^{**}_{j,NZ}}{\Delta Z} = -K_n\left[1 - {}^{AgCl}C^{**}_{j,NZ}\right]^n \qquad (5.29)$$

When $n = 1$, ${}^{AgCl}C^{**}_{j,NZ}$ is expressed in terms of ${}^{AgCl}C^{**}_{j,NZ-1}$ as shown by equation (2.79). Thus equation (2.80) results and the Thomas algorithm is readily applied. When $n = 2$, the expression given by equation (2.79) is slightly more complicated and becomes:

$$mx^2 - (2m+1)x + m + {}^{AgCl}C^{**}_{j,NZ-1} = 0 \qquad (5.30)$$

where m is as defined in equation (4.16) and

$$x = C^{**}_{j,NZ} \qquad (5.31)$$

The quadratic is solved for x resulting in the need for an iterative procedure, as outlined in sections 4.2 and 5.2.1, for the calculation of new concentrations, through application of the Thomas Algorithm.

5.3 Theoretical Results and Discussion

All results presented in this section were, for simulations, carried out for an UME characterised by $RG = 10$, which was similar to that employed in the experiments reported below. Typical examples of the calculated chronoamperometric responses for dissolution with an inert supporting electrolyte without common ions with the dissolving material and without supporting electrolyte for a process defined by $\log K_1 = 2$ and $L = 0.16$, are shown in Figure 5.1. At this tip/substrate separation, the rate constant corresponds to an effectively diffusion-controlled dissolution process.

For both cases, the current ratio-time characteristics are the same at short times when the diffusion field thickness is smaller than the tip/substrate distance and the substrate surface does not therefore influence the diffusion field. However, at longer times, when the diffusion field has intercepted the surface, the current response, for the case where the inert supporting electrolyte contains no common ions with the dissolving material, lies below that for the situation where there is no supporting electrolyte. The reason for this difference in behaviour is explained by reference to Figures 5.2 and 5.3 which show the Cl^- and Ag^+ concentration profiles, respectively, in the tip/substrate gap at selected times during the chronoamperometric characteristics shown in Figure 5.1. It is clear that, with an inert supporting electrolyte containing no common ion with the dissolving material, the concentration of the electroinactive counter ion, Cl^-, increases in the tip/substrate gap during the period of the chronoamperometric measurement. Consequently, at the substrate/solution interface where, for a diffusion-controlled dissolution process, the

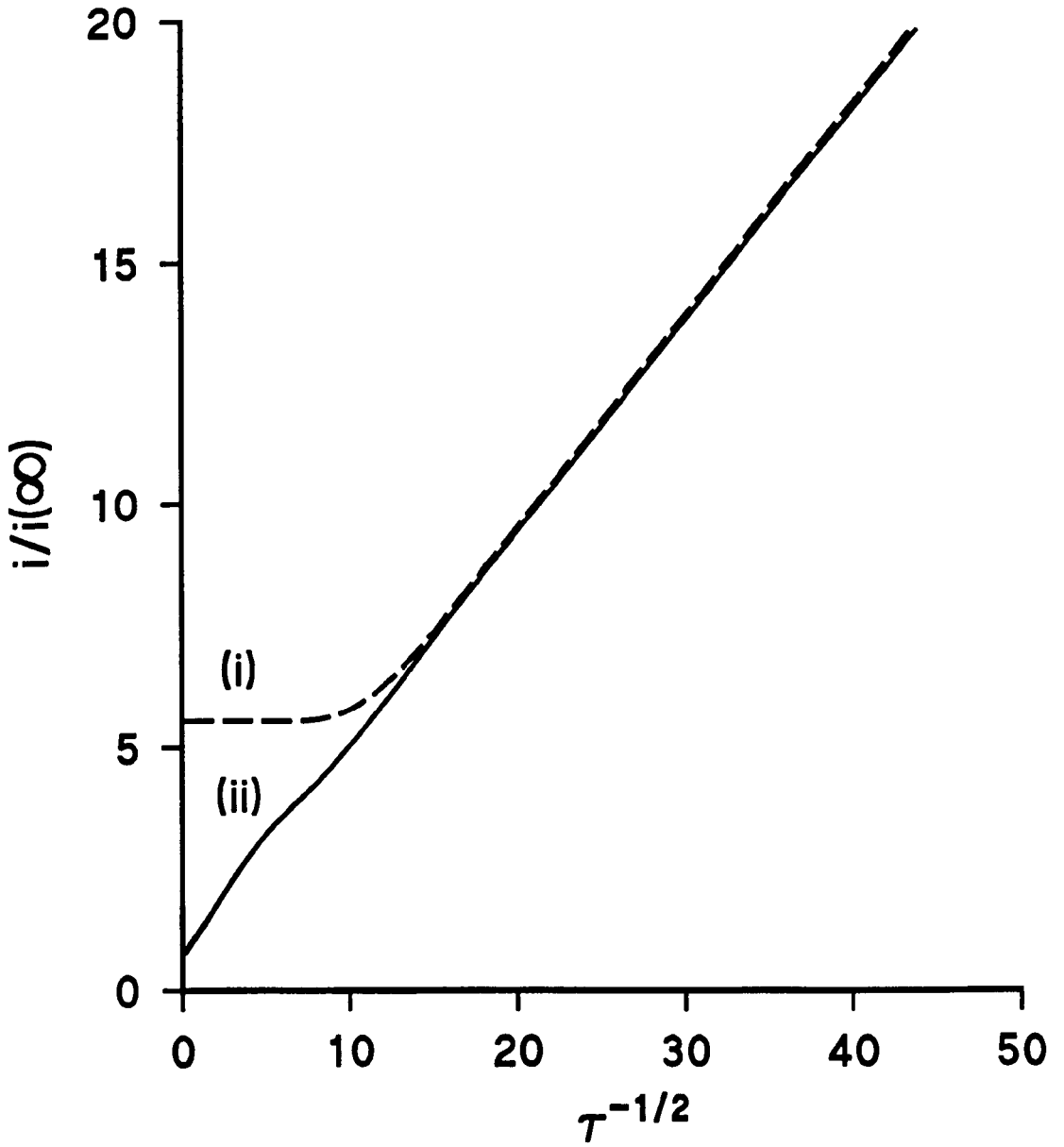

Figure 5.1 Normalised chronoamperometric characteristics for an induced dissolution process defined by the model outlined in sections 5.2.1 and 5.2.2 with K_1 = 100 and L = 0.16. The data relate to the situations (i) the absence of supporting electrolyte and (ii) where the supporting electrolyte does not contain a common ion with the dissolving material.

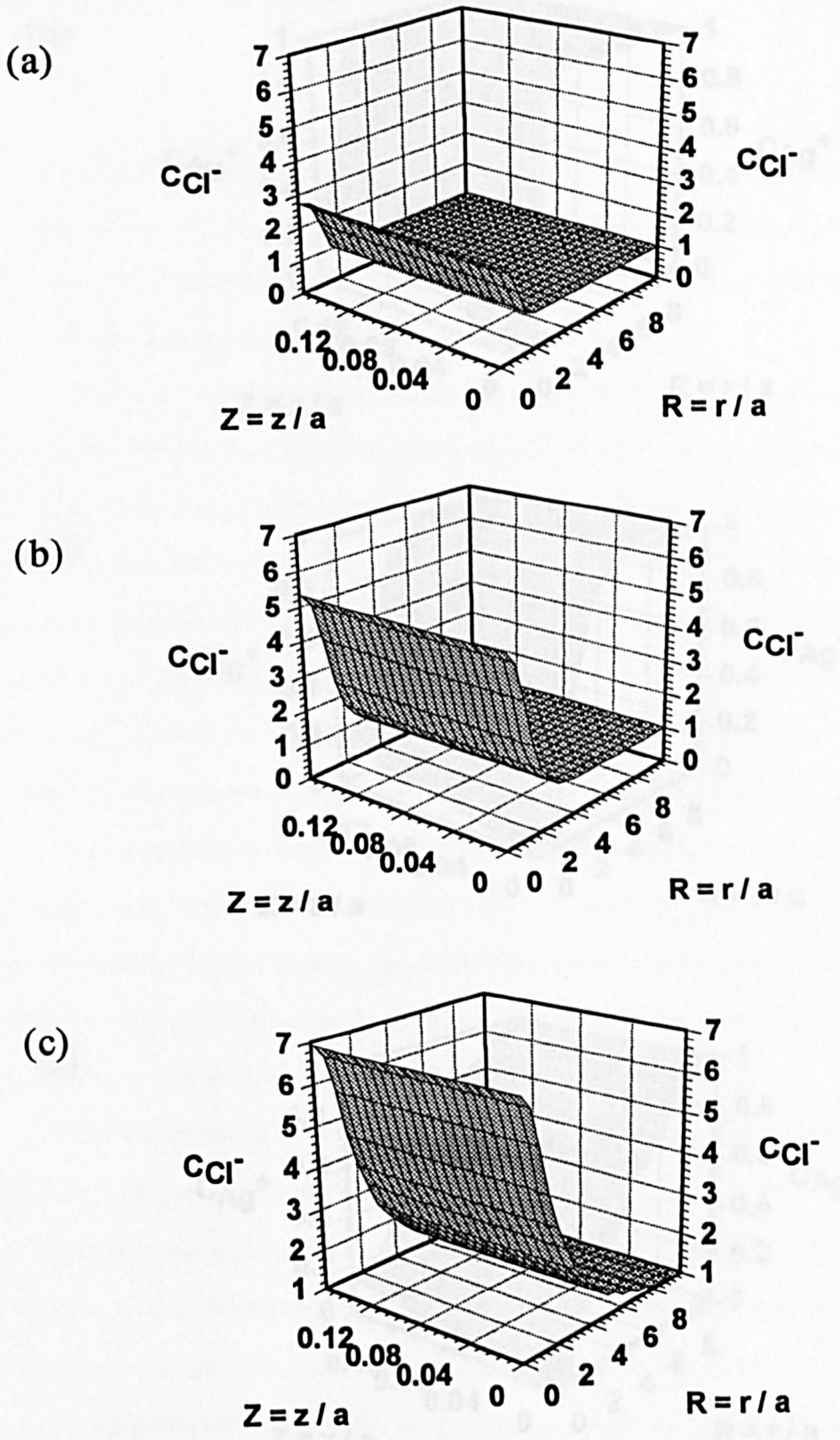

Figure 5.2. Chloride ion concentration profiles in the tip/substrate gap for various times during the chronoamperometric transient shown in Figure 5.1 (—), where the supporting electrolyte does not contain a common ion with the dissolving material. The data relate to τ = (a) 0.1 (b) 1.0 and (c) 10.0.

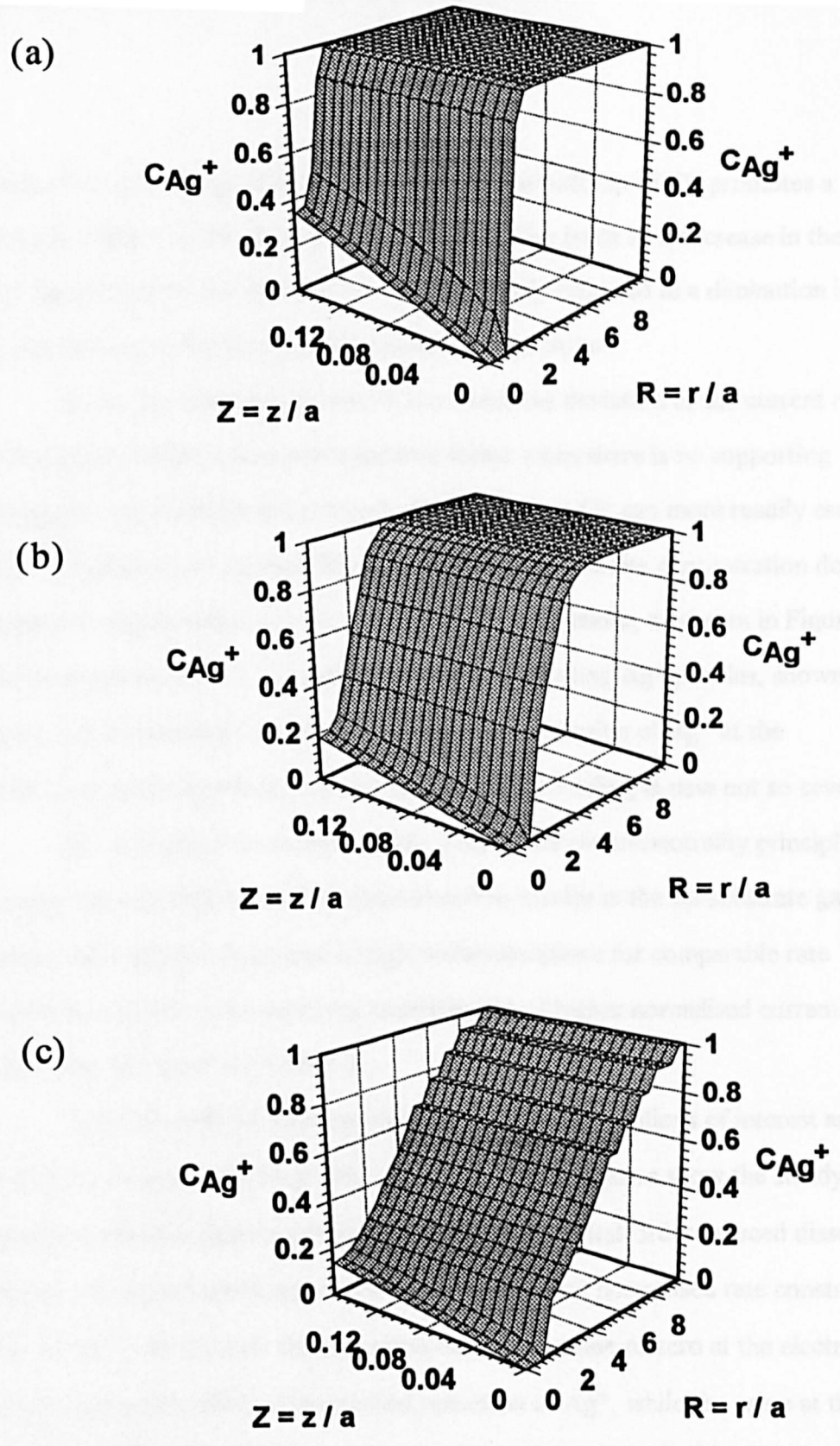

Figure 5.3. Silver ion concentration profiles in the tip/substrate gap for various times during the chronoamperometric transient shown in Figure 5.1 (—), where the supporting electrolyte does not contain a common ion with the dissolving material. The data relate to τ = (a) 0.1 (b) 1.0 and (c) 10.0.

solution remains saturated with respect to AgCl, a build up of Cl^- promotes a decrease in the concentration of Ag^+ with time. This leads to a decrease in the flux of Ag^+ (and Cl^-) from the interface which is ultimately reflected in a diminution in the current flowing at the tip electrode towards longer times.

As the tip/substrate distance is increased, the deviation of the current response for the case of interest from the behaviour found when there is no supporting electrolyte, becomes less pronounced. This is because Cl^- can more readily escape from the tip/substrate gap by diffusion with the result that its concentration does not increase as significantly as at close tip/substrate separations, as shown in Figure 5.4 for the case where $L = 1$. As expected, the corresponding Ag^+ profiles, shown in Figure 5.5, demonstrate that the depletion in concentration of Ag^+ at the substrate/solution interface, from the initial saturated value, is now not so severe.

For the case of no supporting electrolyte, the electroneutrality principle prevents the accumulation of the electroinactive species in the tip/substrate gap, thereby allowing the attainment of high undersaturations for comparable rate constants, which is reflected in the establishment of higher normalised currents at long times, as shown in Figure 5.1.

Typical interfacial undersaturations for the two situations of interest are illustrated in Figure 5.6(a) and (b) respectively. These figures show the steady-state saturation ratio throughout the tip/substrate gap for a first-order induced dissolution process, at a tip/substrate separation $\log L = -0.8$, with normalised rate constants of 100, 10 and 1. In all cases the saturation ratio has a value of zero at the electrode surface, due to the diffusion-controlled reduction of Ag^+, while the value at the substrate surface depends on the rate constant and whether or not an inert supporting electrolyte is present. It can clearly be seen that for K_1 values of 10 and 100, when supporting electrolyte containing no common ions with the dissolving material, is present, the saturation ratio at the substrate/solution interface is close to unity, even

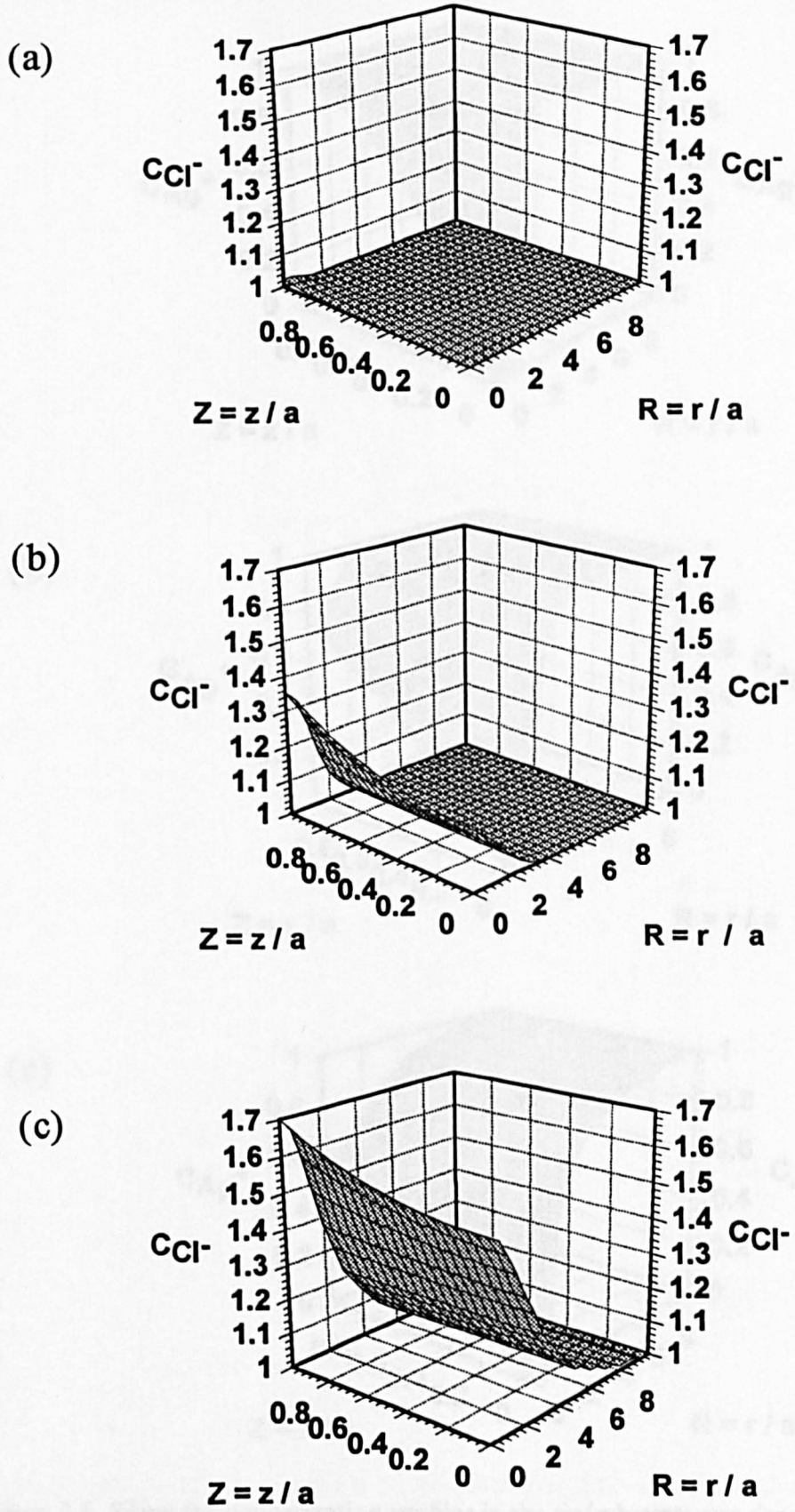

Figure 5.4. Chloride ion concentration profiles in the tip/substrate gap for various times during an induced dissolution process (K_1 = 100) where the supporting electrolyte does not contain a common ion with the dissolving material, at L = 1.0. The data relate to τ = (a) 0.1 (b) 1.0 and (c) 10.0.

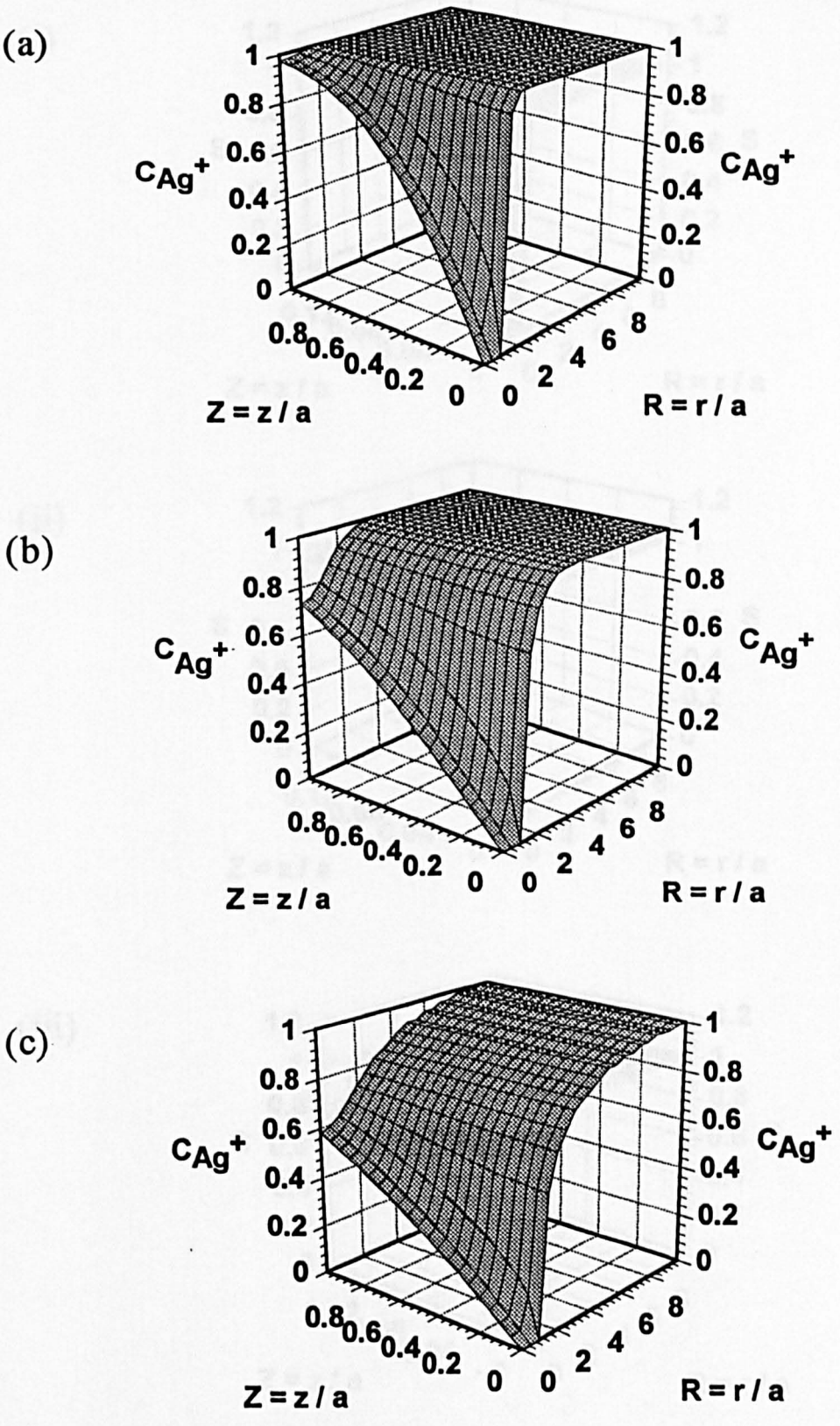

Figure 5.5. Silver ion concentration profiles in the tip/substrate gap for various times during an induced dissolution process (K_1 = 100) where the supporting electrolyte does not contain a common ion with the dissolving material, at L = 1.0. The data relate to τ = (a) 0.1 (b) 1.0 and (c) 10.0.

(i)

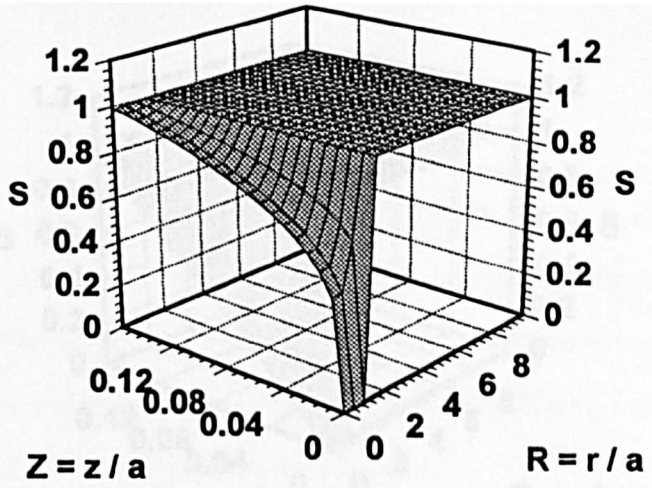

(ii)

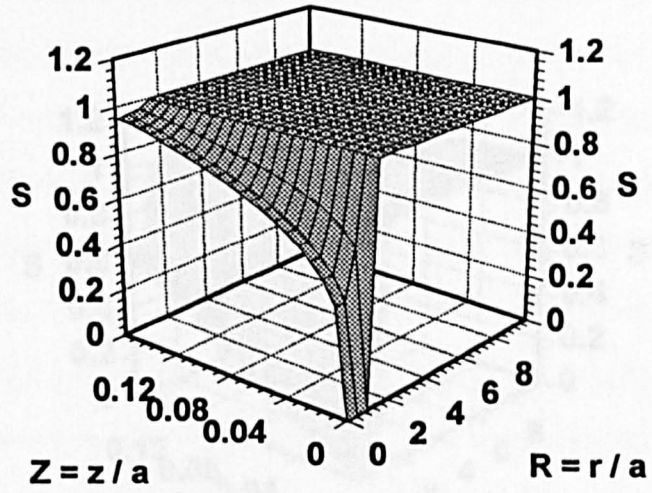

(iii)

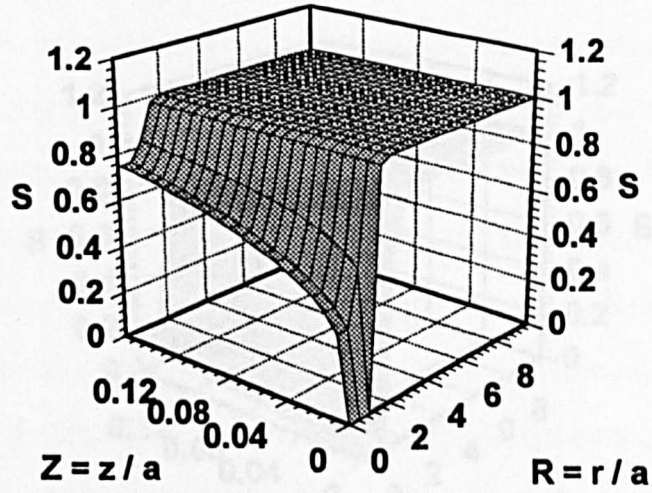

Figure 5.6(a). Steady-state profiles of the saturation ratio in the tip/substrate gap (log L = -0.8) for first-order induced dissolution processes, characterised by K_1 = (i) 100 (ii) 10 and (iii) 1. The data are for induced dissolution reactions in the presence of a supporting electrolyte which does not contain a common ion with the dissolving material.

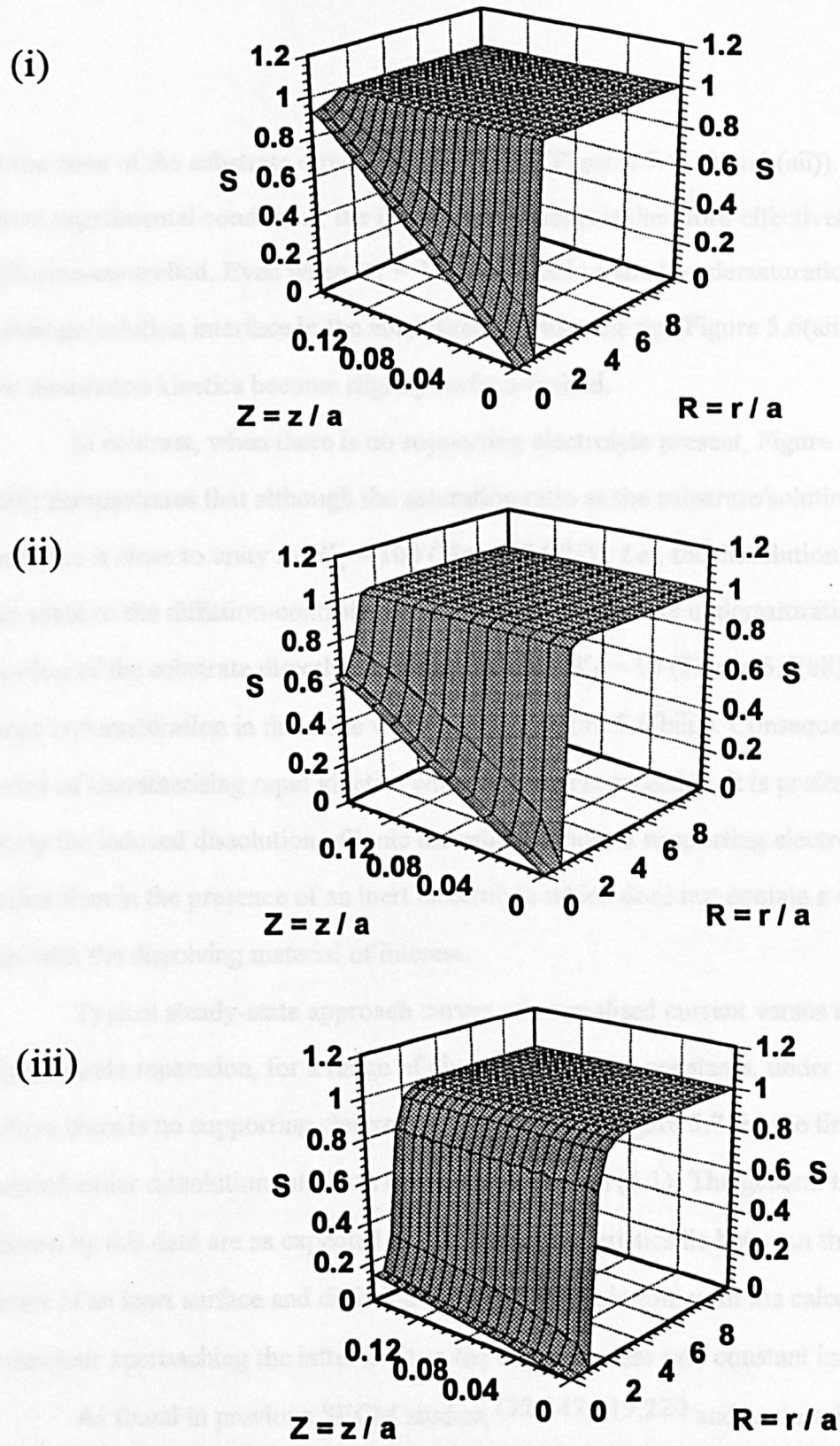

Figure 5.6(b). Steady-state profiles of the saturation ratio in the tip/substrate gap (log L = -0.8) for first-order induced dissolution processes, characterised by K_1 = (i) 100 (ii) 10 and (iii) 1. The data are for induced dissolution reactions in the absence of a supporting electrolyte.

in the zone of the substrate directly under the tip (Figures 5.6(ai) and (aii)). Under these experimental conditions, the dissolution process is therefore effectively diffusion-controlled. Even when $K_1 = 1$, there is only a small undersaturation at the substrate/solution interface in the zone directly under the tip (Figure 5.6(aiii)), and the dissolution kinetics become slightly surface-limited.

In contrast, when there is no supporting electrolyte present, Figure 5.6(bi) - (biii) demonstrates that although the saturation ratio at the substrate/solution interface is close to unity for $K_1 = 100$ (Figure 5.6(bi)), *i.e.*, the dissolution kinetics are close to the diffusion-controlled limit, there is a moderate undersaturation at the portion of the substrate directly under the tip when $K_1 = 10$ (Figure 5.6(bii)) and a large undersaturation in this zone when $K_1 = 1$ (Figure 5.6(biii)). Consequently, in terms of characterising rapid kinetics with the greatest precision, it is preferable to study the induced dissolution of ionic materials without a supporting electrolyte rather than in the presence of an inert electrolyte which does not contain a common ion with the dissolving material of interest.

Typical steady-state approach curves of normalised current versus normalised tip/substrate separation, for a range of dimensionless rate constants, under conditions where there is no supporting electrolyte, are shown in Figure 5.7 for the first- and second-order dissolution rate laws defined by equation (5.1). The general trends shown by this data are as expected in that the characteristics lie between the reactivity limits of an inert surface and diffusion-controlled dissolution, with the calculated behaviour approaching the latter limit as the dimensionless rate constant increases.

As found in previous SECM studies,[132,147,219,220] and as described in section 4.5.2, the change in current with rate constant, for a particular mechanism, is greater the closer the tip/substrate separation. In general, kinetics may therefore be characterised with the greatest sensitivity from the current response, the closer the tip/substrate separation. It is also apparent from Figure 5.7 that there are subtle

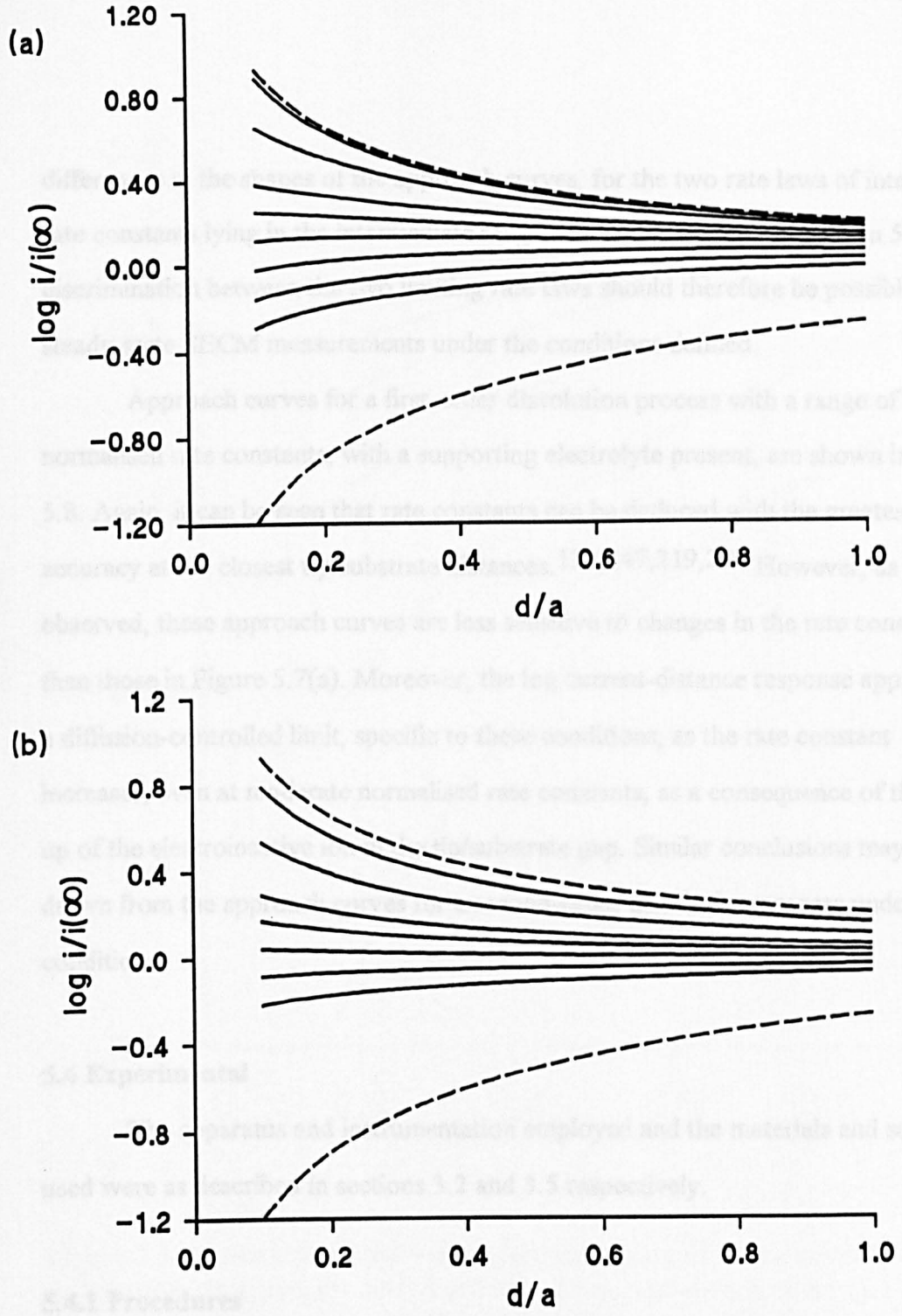

Figure 5.7. Dimensionless steady-state approach curves of tip current versus tip/substrate separation for the rate laws of interest, in the absence of a supporting electrolyte, for (a) first-order and (b) second-order dissolution processes. The data are for the following dimensionless rate constants: (a) log K_1 = 2.0 (upper solid line), 1.0, 0.5, 0.3, 0.1, -0.1, -0.3 and -0.5 (lower solid line); (b) log K_2 = 2.0 (upper solid line), 1.0, 0.5, 0.3, 0.1, -0.1 and -0.3 (lower solid line). In each case the upper and lower dashed lines represent the behaviour for a diffusion-controlled dissolution reaction and an inert surface respectively.

differences in the shapes of the approach curves, for the two rate laws of interest, for rate constants lying in the intermediate range. As confirmed later in section 5.5.2.2, discrimination between the two limiting rate laws should therefore be possible from steady-state SECM measurements under the conditions defined.

Approach curves for a first-order dissolution process with a range of normalised rate constants, with a supporting electrolyte present, are shown in Figure 5.8. Again, it can be seen that rate constants can be deduced with the greatest accuracy at the closest tip/substrate distances.[132,147,219,220] However, as observed, these approach curves are less sensitive to changes in the rate constant, than those in Figure 5.7(a). Moreover, the log current-distance response approaches a diffusion-controlled limit, specific to these conditions, as the rate constant increases, even at moderate normalised rate constants, as a consequence of the build-up of the electroinactive ion in the tip/substrate gap. Similar conclusions may be drawn from the approach curves for a second-order dissolution process under these conditions.

5.4 Experimental

The apparatus and instrumentation employed and the materials and substrates used were as described in sections 3.2 and 3.5 respectively.

5.4.1 Procedures

When the substrate was a pressed pellet of AgCl, the tip UME was placed at selected distances from the substrate surface and the current was recorded as a function of time following the reduction of Ag^+ at a diffusion-controlled rate in the chronoamperometric mode, by stepping the tip electrode potential from open circuit to -0.3 V vs. AgQRE. The tip/substrate separations of interest were selected by first carefully contacting the substrate surface with the tip and then retracting the tip a

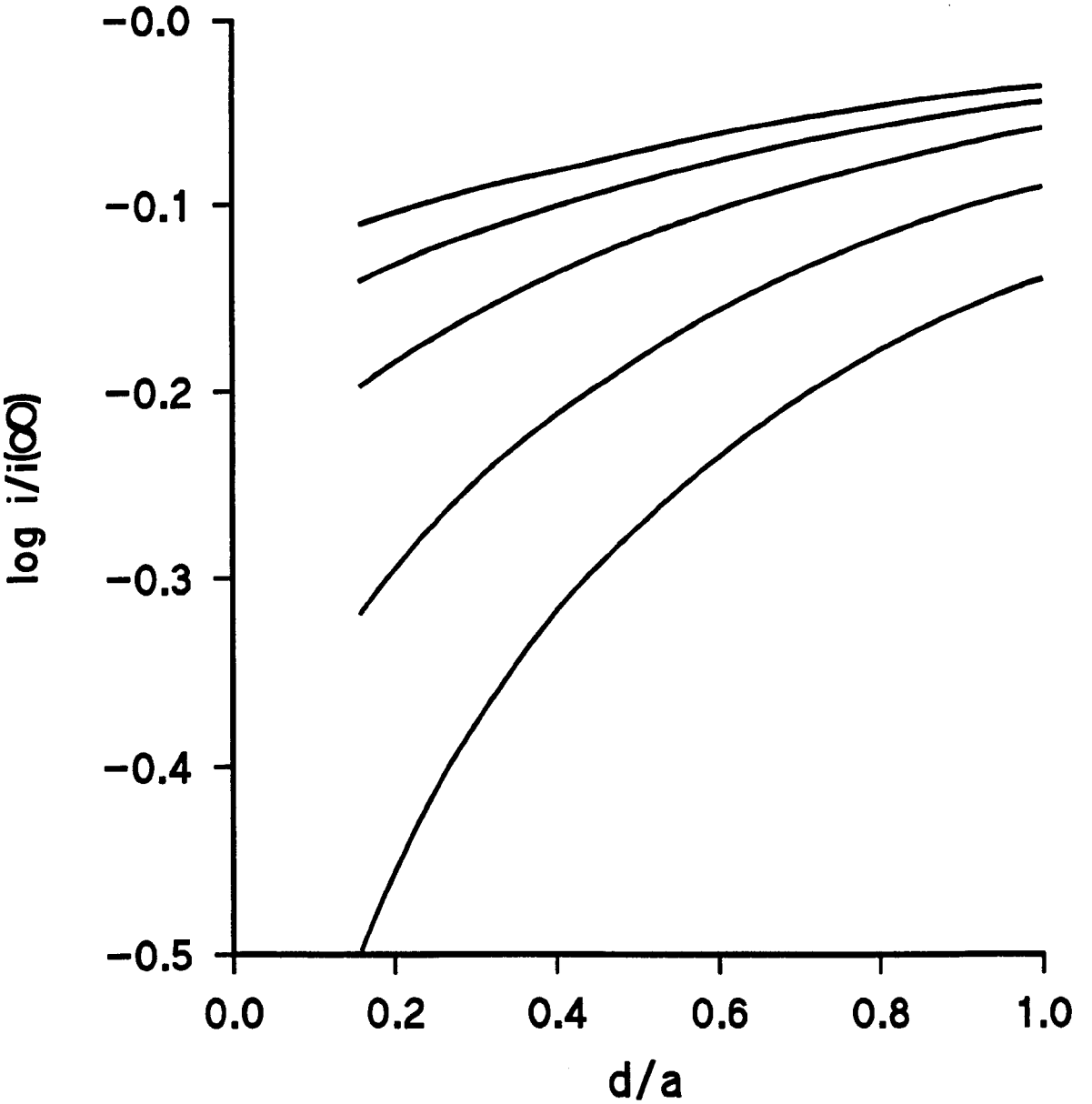

Figure 5.8. Dimensionless steady-state approach curves of log tip current versus tip/substrate separation for the induced dissolution reaction of a binary (1:1) salt in the presence of a supporting electrolyte which does not contain a common ion with the dissolving material. The data are for a first-order process characterised by dimensionless rate constants, log K_1 = 2.0 (upper curve), 1.0, 0.5, 0.0 and -0.5 (lower curve). The behaviour for log K_2 is effectively that for a diffusion-controlled process under these conditions.

known distance from the surface. The position at which the tip contacted the surface was readily established as that at which large current ratios were attained in the chronoamperometric mode.

For measurements involving the AgCl film grown on an Ag UME, it was first necessary to locate the position of the film with the tip electrode. This was achieved by using the SECM in the imaging mode, in which the tip electrode was first carefully placed on the surface of the AgCl substrate electrode and then retracted 10 μm. While held at a potential of -0.3 V vs. AgQRE, sufficient to reduce Ag^+ at a diffusion-controlled rate, the tip was then scanned at a constant height (in a fixed x, y plane) in a series of unidirectional line scans over the surface of the AgCl film and surrounding glass insulator, as described in section 3.2. By monitoring the diffusion-limited current for the reduction of Ag^+, as a function of tip position, it was possible to locate the presence of the film from the increase in the current, when the tip initiated dissolution over the AgCl surface. The tip was then repositioned so that it sat directly above the centre of the AgCl film, and a series of chronoamperometric measurements at different tip/substrate separations, were carried out as described above.

Chronoamperometric measurements were typically made over a period of time equivalent to a normalised time of *ca.* 50 to ensure that the current response was very close to the true steady-state value. Although the direct reduction of Ag^+ resulted in deposition of Ag on the tip UME and the induced dissolution of AgCl, the quantity of material deposited on the electrode and dissolved from the substrate was not sufficient to significantly alter the electrode geometry, substrate geometry or the tip/substrate distance on this timescale.

5.5 Experimental Results and Discussion

5.5.1 Voltammetric and Chronoamperometric Measurements of Ag^+ Reduction

5.5.1.1 With 0.1 mol dm^{-3} Potassium Nitrate as an Inert Supporting Electrolyte

Initial voltammetric experiments for the reduction of Ag^+ were carried out using 25 μm diameter Pt and 50 μm diameter Ag electrodes in solutions containing either 0.001 or 0.0001 mol dm^{-3} $AgNO_3$, with KNO_3 added as a supporting electrolyte at a concentration of 0.1 mol dm^{-3}. The steady-state current response was measured by scanning the potential in the range 0.0 V to -0.3 V at a scan rate of 10 mV s^{-1}. Application of equation (1.4) to the measured diffusion-limited currents yielded a value for D_{Ag+} of 1.65 x 10^{-5} cm^2 s^{-1}, which was in very good agreement with the values of 1.65 x 10^{-5} and 1.55 x 10^{-5} cm^2 s^{-1} quoted, respectively, by Newman[277] and Johnston and Spiro[278] for similar experimental conditions.

Voltammetric measurements carried out with 25 and 10 μm diameter Pt electrodes in solutions containing 0.1 mol dm^{-3} KNO_3, and saturated with respect to AgCl, yielded typical diffusion-limited currents of 103 and 45 pA, respectively. A typical voltammogram showing the steady-state voltammetric response at a 25 μm diameter Pt UME under these conditions, is shown in Figure 5.9(a). Armed with a knowledge of D_{Ag+} from above, the saturated concentration of AgCl was determined as 1.35 x 10^{-5} mol dm^{-3}, after the application of equation (1.4). This value compares favourably with the literature value measured under similar conditions.[273,279]

Chronoamperometric characteristics for Ag^+ reduction, measured after stepping the electrode potential from open circuit or 0.0 V to -0.3 V, were found to deviate markedly at short times from the theoretical predictions for a simple diffusion-controlled electrolysis process, in that much larger currents flowed, as shown in Figure 5.9(b). Crucially, however, at longer times (3 s and greater with the 25 μm diameter tip), measured current values were found to be in good agreement with the steady-state voltammetric response. All measurements were thus restricted

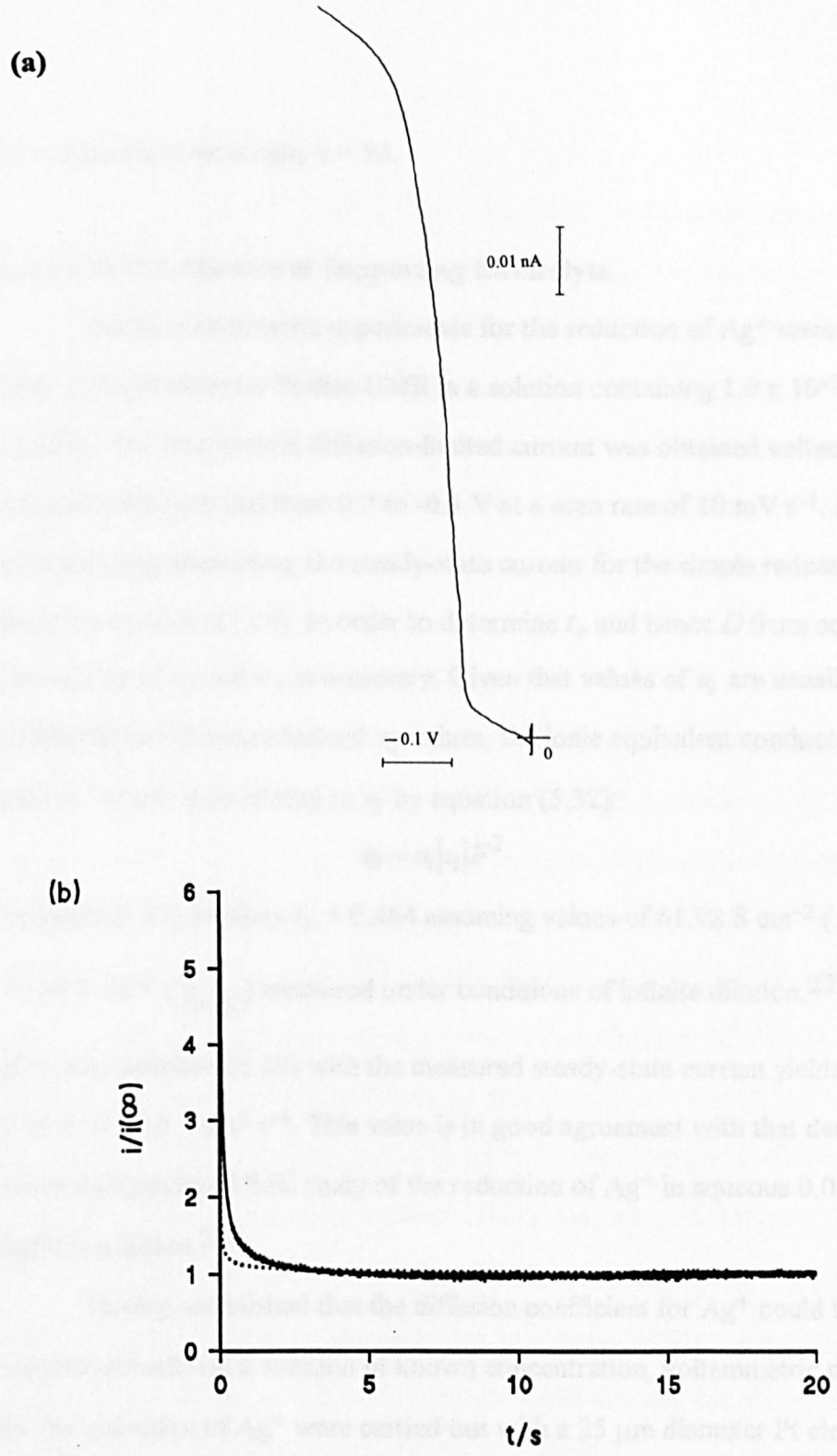

Figure 5.9. Dynamic electrochemical characteristics for the reduction of Ag^+ at a Pt UME (a = 12.5 μm) from a saturated silver chloride solution (0.1 mol dm^{-3} KNO_3): (a) steady-state voltammogram; (b) chronoamperometric behaviour. In the latter case the behaviour expected for a simple diffusion-controlled electron transfer process is also shown (· · ·).

to a normalised timescale, $\tau = 50$.

5.5.1.2 In the Absence of Supporting Electrolyte

Initial voltammetric experiments for the reduction of Ag^+ were carried out with a 25 μm diameter Pt disc UME in a solution containing 1.0×10^{-3} mol dm^{-3} $AgNO_3$. The steady-state diffusion-limited current was obtained voltammetrically by sweeping the potential from 0.0 to -0.3 V at a scan rate of 10 mV s^{-1}. In the absence of supporting electrolyte, the steady-state current for the simple reduction of Ag^+ is given by equation (5.28). In order to determine t_+ and hence D from equation (5.28), knowledge of z_+ and u_+ is necessary. Given that values of u_i are usually not found directly in the literature instead η_i values, the ionic equivalent conductance, are quoted, where η_i is related to u_i by equation (5.32):

$$\eta_i = u_i |z_i| F^2 \qquad (5.32)$$

equation (5.27) predicts $t_+ = 0.464$ assuming values of 61.92 S cm^{-2} (η_{Ag^+}) and 71.44 S cm^{-2} ($\eta_{NO_3^-}$) measured under conditions of infinite dilution.[274] Substitution of t_+ into equation (5.28) with the measured steady-state current yielded a value for D of 1.67×10^{-5} cm^2 s^{-1}. This value is in good agreement with that deduced from a recent independent UME study of the reduction of Ag^+ in aqueous 0.01 mol dm^{-3} $AgNO_3$ solution.[276]

Having established that the diffusion coefficient for Ag^+ could be measured voltammetrically on a solution of known concentration, voltammetric measurements for the reduction of Ag^+ were carried out with a 25 μm diameter Pt electrode in saturated AgCl solutions, in order to determine D for these conditions. The steady-state diffusion-limited current was typically *ca.* 180 pA. Given that the concentration of AgCl in a saturated aqueous solution[273,279] is *ca.* 1.30×10^{-5} mol dm^{-3}, coupled with a value of t_+ of 0.45 for this system,[274] D was found to be approximately

1.60×10^{-5} cm^2 s^{-1}.

As determined in section 5.5.1.1, the chronoamperometric response for the diffusion-controlled reduction of Ag^+ in saturated AgCl solutions was found to deviate at short times from the behaviour predicted theoretically for simple diffusion-controlled electrolysis[261] in that larger currents flowed. Crucially, at long times (τ = 50), the measured current values were found to be in very good agreement with the diffusion-limited values obtained from linear sweep voltammetry. All induced dissolution measurements were therefore made on this timescale.

5.5.2 SECM Induced Dissolution Kinetics

5.5.2.1 With 0.1 mol dm^{-3} Potassium Nitrate as an Inert Supporting Electrolyte

Initial studies focused on electrochemically grown films of AgCl, a substrate identical to that employed by Jones in earlier work which utilised a radioactive tracer technique to monitor the dissolution rate of radioactive labelled Ag^+ ions from a rotating AgCl rod into water.[223] For the experiments described in this thesis a 125 μm diameter AgCl film was employed as the substrate, which was located by the tip using SECM in the imaging mode, as described in section 5.4.1. A typical image, resulting from this procedure with a Pt tip of 25 μm diameter, is shown in Figure 5.10. The dark areas represent areas of low tip current, and correspond to the hindered diffusion of Ag^+ to the tip as it passes over the insulating glass sheath surrounding the AgCl film. The light area indicates a higher current, representing the position at which the tip is directly over the AgCl film and initiates dissolution. After identifying the co-ordinates of the AgCl film, the tip was repositioned so that it sat above the centre of the film and chronoamperometry for Ag^+ reduction was carried out in this area as a function of tip/substrate distance.

A typical approach curve for a tip of a = 12.5 μm, constructed by plotting the normalised long time currents from chronoamperometric measurements as a function

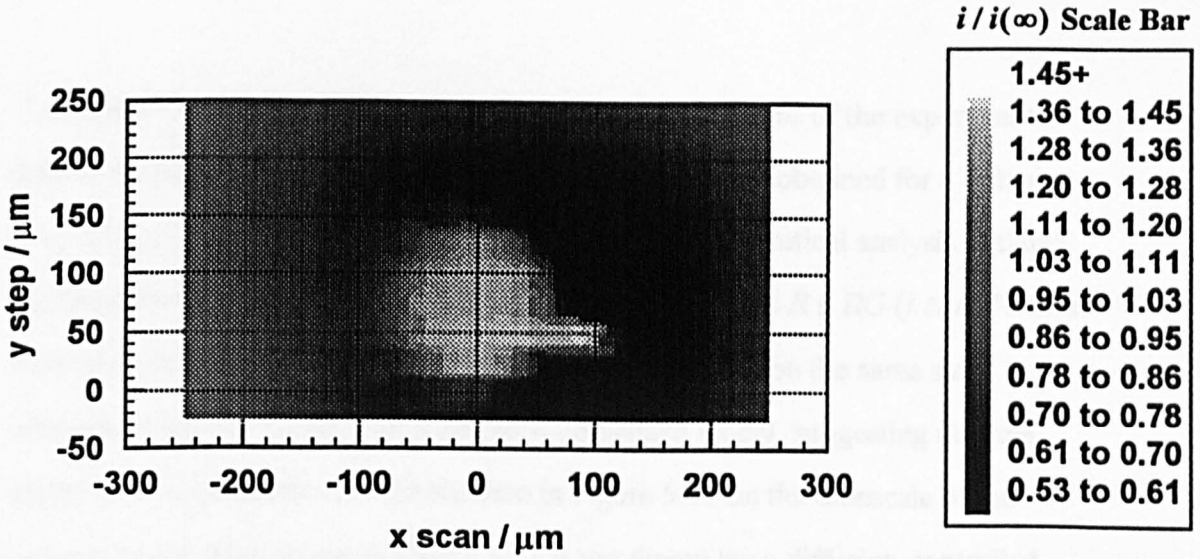

Figure 5.10. Variation of the normalised diffusion-limited current for Ag^+ reduction as a tip (a = 12.5 μm) was scanned over a AgCl disc (125 μm diameter) embedded in a glass sheath. The position of the disc is identified from the increase in the current response when the tip induces dissolution of the AgCl substrate. The tip was positioned at a height of 10 μm above the substrate and scanned at 100 μm s^{-1}. The grey scale bar represents values of $i/i(\infty)$.

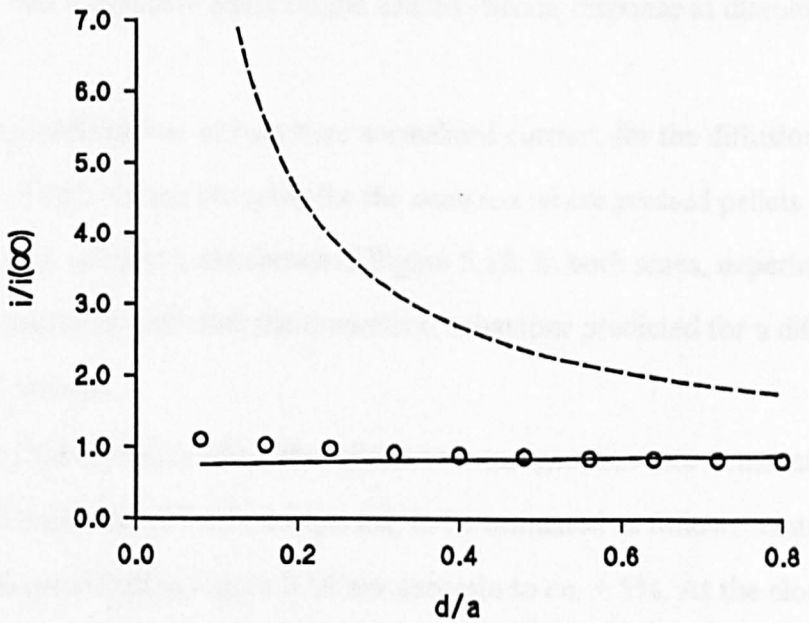

Figure 5.11. Experimental approach curve (O) of normalised long time current for Ag^+ reduction vs. tip (a = 12.5 μm) to substrate separation with a 125 μm diameter AgCl disc. Also shown is the theoretical behaviour for a diffusion-controlled process in the presence of a supporting electrolyte which does not contain a common ion with the dissolving material (___) together with the situation where the concentration of the electroinactive lattice counter ion remains constant (- - -).

of tip/AgCl film distance, is shown in Figure 5.11. The best fit of the experimental data to the theory outlined above, for these conditions, was obtained for a diffusion-controlled dissolution process (K_1 = 100). Strictly, the theoretical analysis outlined above applies to substrates which extend over a distance $0 \leq R \leq RG$ (*i.e.* an "infinite" substrate), however results obtained with a tip of a = 5 μm on the same sized substrate were also found to fit a diffusion-controlled model, suggesting that the model used is generally valid for the data in Figure 5.11 on the timescale of the measurements. Also shown in Figure 5.11 is the theory for a diffusion-controlled dissolution process where the concentration of the electroinactive lattice counter ion remains constant (due to the supporting electrolyte also containing the electroinactive ion). Comparison of this response, with that described above, clearly demonstrates that the build up in Cl^- concentration which occurs with KNO_3 as the supporting electrolyte has a dramatic effect on the SECM current response in dissolution systems.

Approach curves of long time normalised current, for the diffusion-controlled reduction of Ag^+, versus distance, for the situation where pressed pellets of AgCl were used as a substrate, are shown in Figure 5.12. In both cases, experimental data are again seen to fit well with the theoretical behaviour predicted for a diffusion-controlled process.

The above results allow the minimum heterogeneous rate constant for AgCl dissolution under the conditions imposed, to be estimated as follows, assuming that the currents measured in Figure 5.12 are accurate to *ca.* ± 5%. At the closest distance (d = 0.5 μm for a tip of a = 5 μm), it follows from a working curve of steady-state normalised current versus normalised rate constant for L = 0.1, that the observation of a diffusion-controlled dissolution process means that for a first-order process

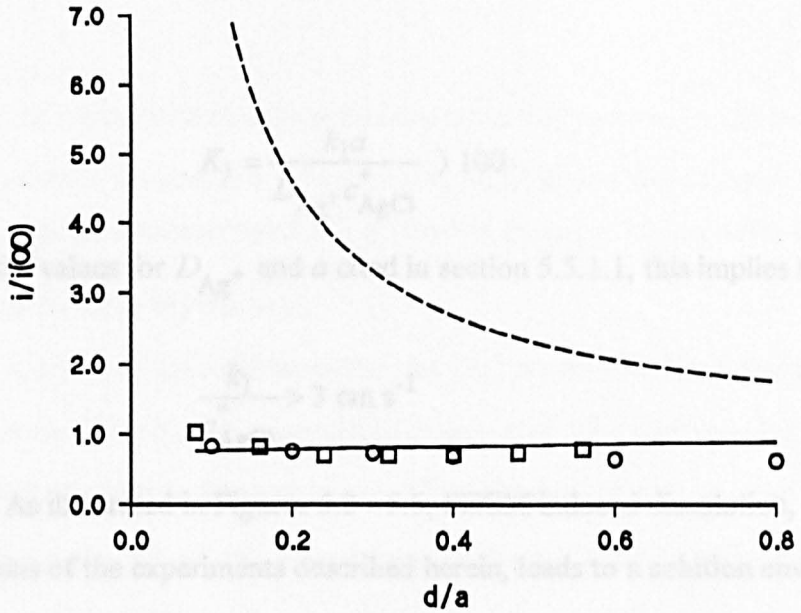

Figure 5.12. Experimental approach curves of normalised long time current for Ag^+ reduction vs. tip (a = 12.5 μm) to substrate separation measured over a AgCl pellet with tips characterised by a = 12.5 μm (□) and 5 μm (O). Also shown is the theoretical behaviour for a diffusion-controlled process in the presence of a supporting electrolyte which does not contain a common ion with the dissolving material (——) together with the situation where the concentration of the electroinactive lattice counter ion remains constant (- - -).

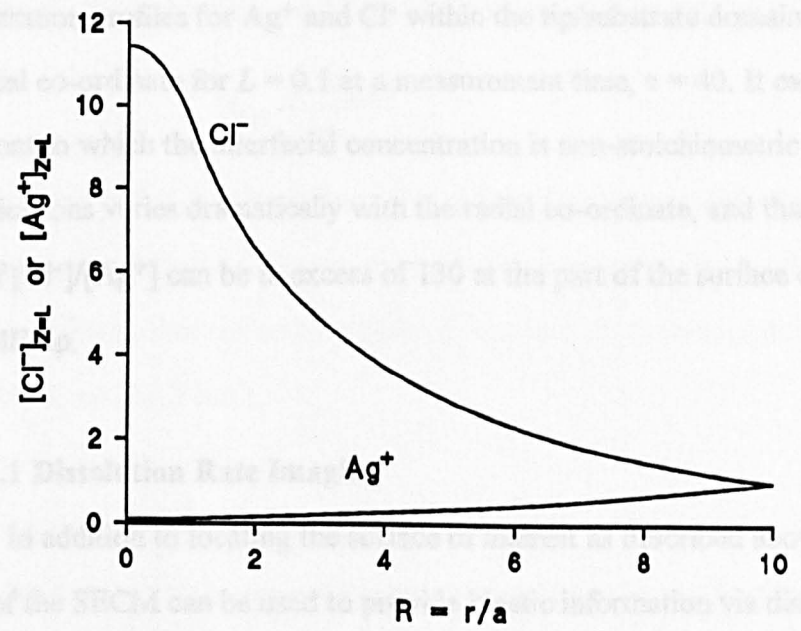

Figure 5.13. Concentration profiles of Ag^+ and Cl^- at the AgCl substrate/solution interface as a function of the radial co-ordinate for a diffusion-controlled dissolution reaction with L = 0.1, and τ = 40.

$$K_1 = \frac{k_1 a}{D_{Ag^+} c^*_{AgCl}} \rangle 100 \qquad (5.33)$$

Given the values for D_{Ag^+} and a cited in section 5.5.1.1, this implies that

$$\frac{k_1}{c^*_{AgCl}} > 3 \text{ cm s}^{-1} \qquad (5.34)$$

As illustrated in Figures 5.2 - 5.5, SECM induced dissolution, under the conditions of the experiments described herein, leads to a solution environment in the tip/substrate gap which is highly non-stoichiometric with respect to the AgCl lattice ions. In earlier work[222,223] such conditions were found to influence the dissolution rate and it is therefore useful to identify the range of interfacial concentrations which prevail during the conditions of these experiments. It follows from Figures 5.2 - 5.5 that, for a diffusion-controlled reaction, the interfacial region deviates most from stoichiometry at the closest tip/substrate separation. Figure 5.13 shows the interfacial concentration profiles for Ag^+ and Cl^- within the tip/substrate domain as a function of the radial co-ordinate for $L = 0.1$ at a measurement time, $\tau = 40$. It can be seen that the extent to which the interfacial concentration is non-stoichiometric with respect to the lattice ions varies dramatically with the radial co-ordinate, and that the interfacial ratio of $[Cl^-]/[Ag^+]$ can be in excess of 130 at the part of the surface directly under the UME tip.

5.5.2.1.1 Dissolution Rate Imaging

In addition to locating the surface of interest as described above, the scanning mode of the SECM can be used to provide kinetic information via dissolution rate imaging. In these experiments, the tip is scanned at a series of constant heights above

the surface while recording the diffusion-controlled current for the reduction of Ag^+ as a function of tip position. To avoid prolonged deposition of Ag at the electrode surface, smaller diameter Ag/AgCl electrodes, a_{AgCl} = 25 μm, were used as substrates in these experiments.

A series of typical dissolution rate images, recorded as a function of tip/substrate distance, are presented in Figure 5.14. The scan area for each image was 200 x 200 μm, with a step size between line scans of 10 μm. v_{scan} of the 25 μm diameter tip was 10 μm s^{-1}. The position of the AgCl film in each image is clearly evident as the peak in the current when the probe passes over the film and initiates dissolution, which provides an additional source of Ag^+ for reduction at the tip. By taking the maximum value of the current in each image as a function of d, an approach curve can be produced, as shown in Figure 5.15. The long time (approaching steady-state) theoretical analysis presented above is expected to be applicable to the data in Figure 5.15 since, at the slow tip scan speed employed, the characteristic residence time of the tip in the vicinity of the AgCl film,

$$t_{res} = \frac{2a_{AgCl}}{v_{scan}} \qquad (5.35)$$

is of the order of 5 s. It is clear from Figure 5.15 that the experimental data are in good agreement with the diffusion-controlled dissolution model for these conditions, which provides further support for the deductions from the transient measurements described in section 5.5.2.1.

5.5.2.2 In the Absence of Supporting Electrolyte

Dissolution measurements were made on both electrochemically grown films and pressed pellets of AgCl, with similar results. Approach curves for tips characterised by a = 5, 12.5 and 25 μm, constructed by plotting the normalised long time currents, from chronoamperometric measurements, as a function of normalised

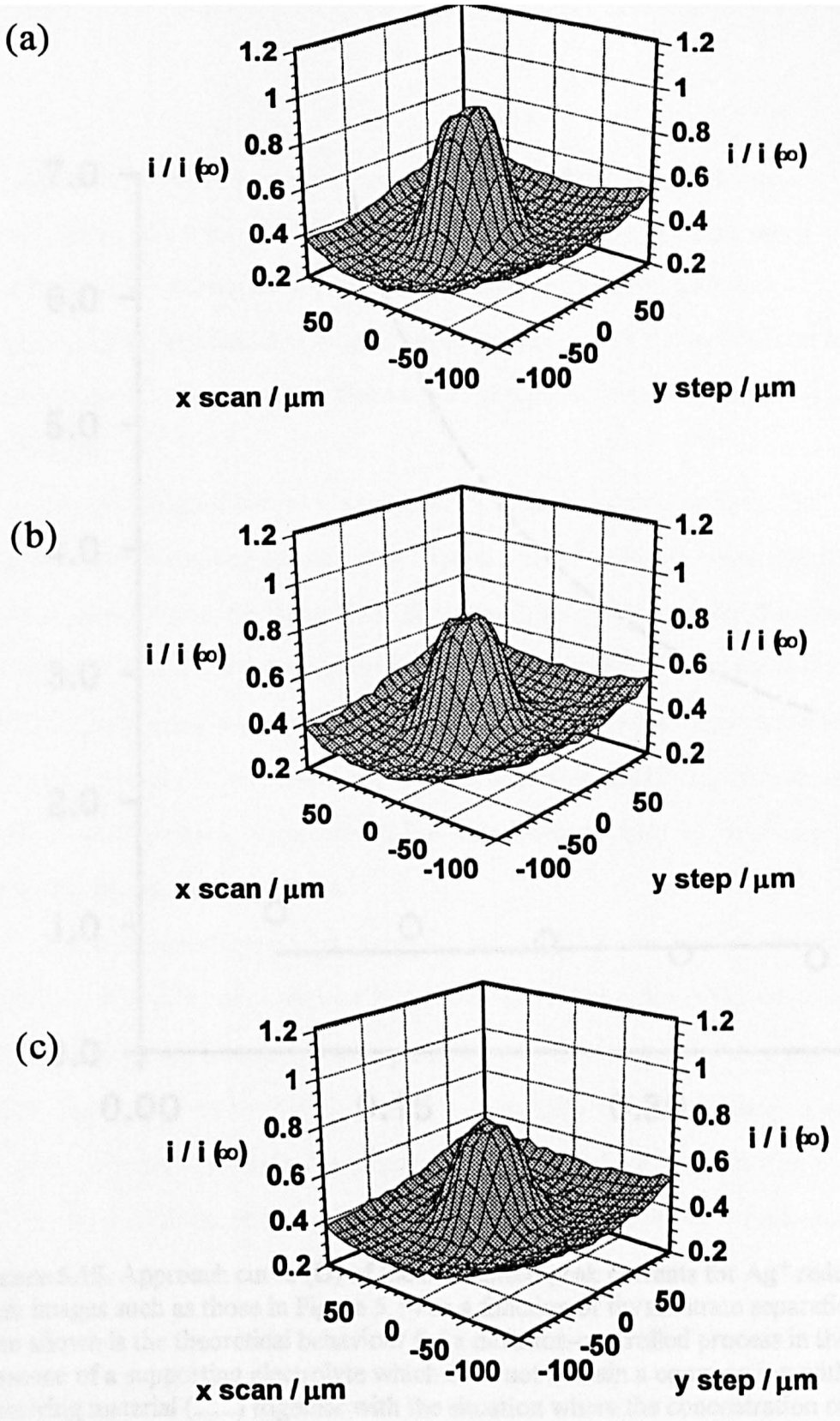

Figure 5.14. Selection of typical dissolution rate images for the diffusion-controlled reduction of Ag^+ at a tip (a = 12.5 μm) scanned at heights of (a) 3.0 μm, (b) 4.0 μm and (c) 5.0 μm over a silver chloride disc (125 μm diameter) embedded in a glass disc.

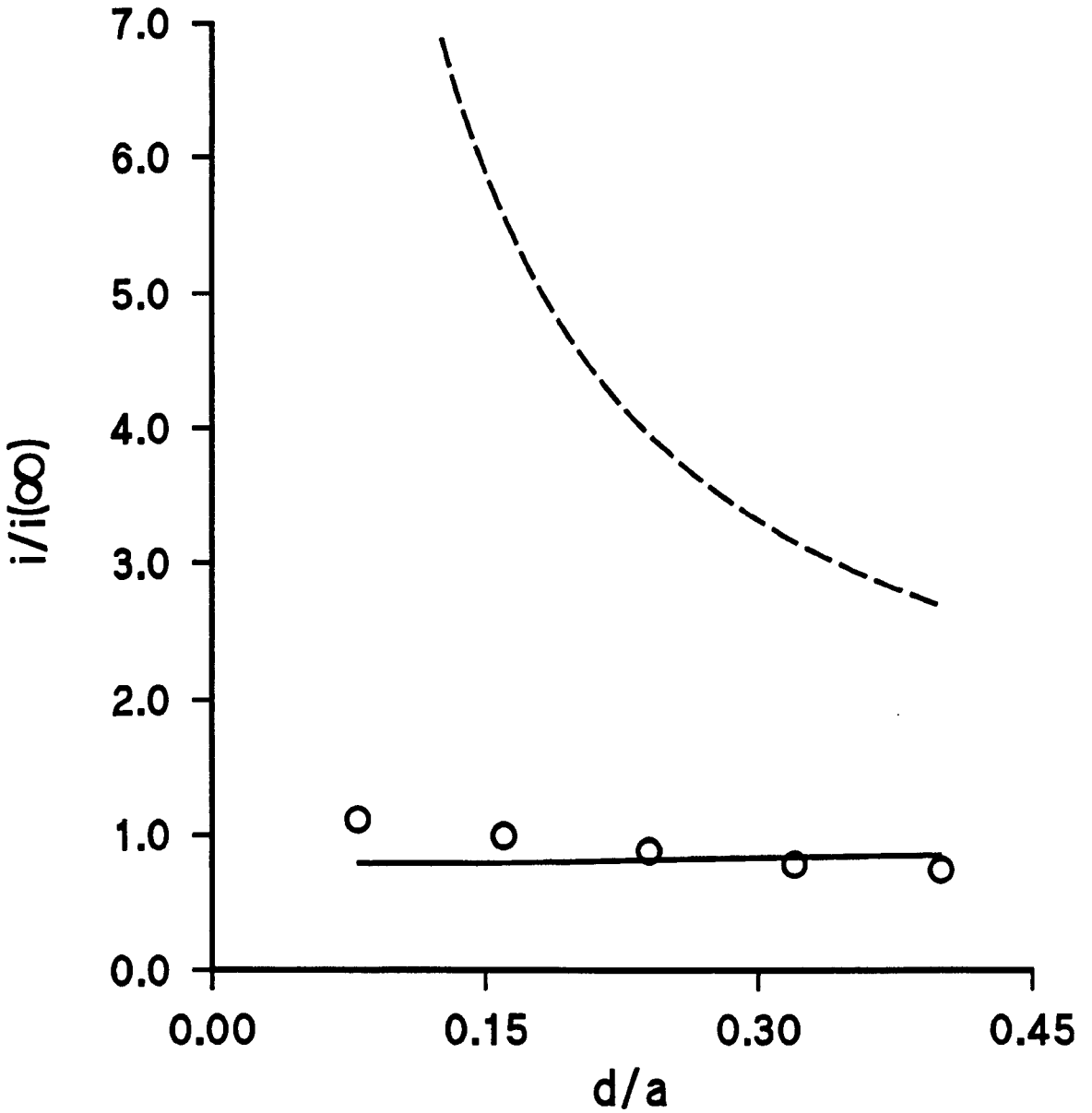

Figure 5.15. Approach curve (O) of the normalised peak currents for Ag^+ reduction from images such as those in Figure 5.14 as a function of tip/substrate separation. Also shown is the theoretical behaviour for a diffusion-controlled process in the presence of a supporting electrolyte which does not contain a common ion with the dissolving material (___) together with the situation where the concentration of the electroinactive lattice counter ion remains constant (- - -).

tip/substrate distance are shown in Figures 5.16(a) and (b). The curves cover different values of L since in each case measurements were made over a range of distances up to 2 μm from the substrate surface. For comparison with the experimental data, theoretical approach curves are also shown for second- and first-order dissolution processes with a range of rate constants (Figures 5.16(a) and (b), respectively).

The experimental curves are different for each electrode size, since the timescale of the dissolution measurement depends on the electrode radius: the larger the electrode employed, the larger is the dimensionless rate constant for dissolution (equation (5.10)), *i.e.* the faster the surface kinetics compared to mass transport. Consequently, in experiments with a range of electrode sizes, the larger the value of a, for a given value of L, the higher is the dimensionless current ratio, since these conditions serve to increase the contribution from mass transport to the overall kinetics for the dissolution process.

It is clear from Figure 5.16(a) that the second-order rate law provides an excellent fit to each set of experimental data over the entire range of tip/substrate distances employed. Moreover, the normalised rate constants employed to generate the data, $\log K_2$ = -0.3 (a = 5 μm), 0.1 (a = 12.5 μm) and 0.4 (a = 25 μm), in each case yield the same dissolution rate constant, $k_2/c^* = 0.016$ cm s^{-1}, assuming $D = 1.6 \times 10^{-5}$ cm^2 s^{-1}, as deduced in section 5.5.1.2. In contrast, the first-order dissolution theory does not provide a good description of any of the sets of experimental data, and even the most consistent fits of this theory to the data do not yield a constant value of k_1/c^* across all data sets.

The rate law observed for a dissolution process usually depends on the interfacial undersaturation. For example, under the classical BCF scheme, the first- and second-order cases in interfacial undersaturation represent the high and low undersaturation limits, respectively, where direct detachment or surface diffusion are

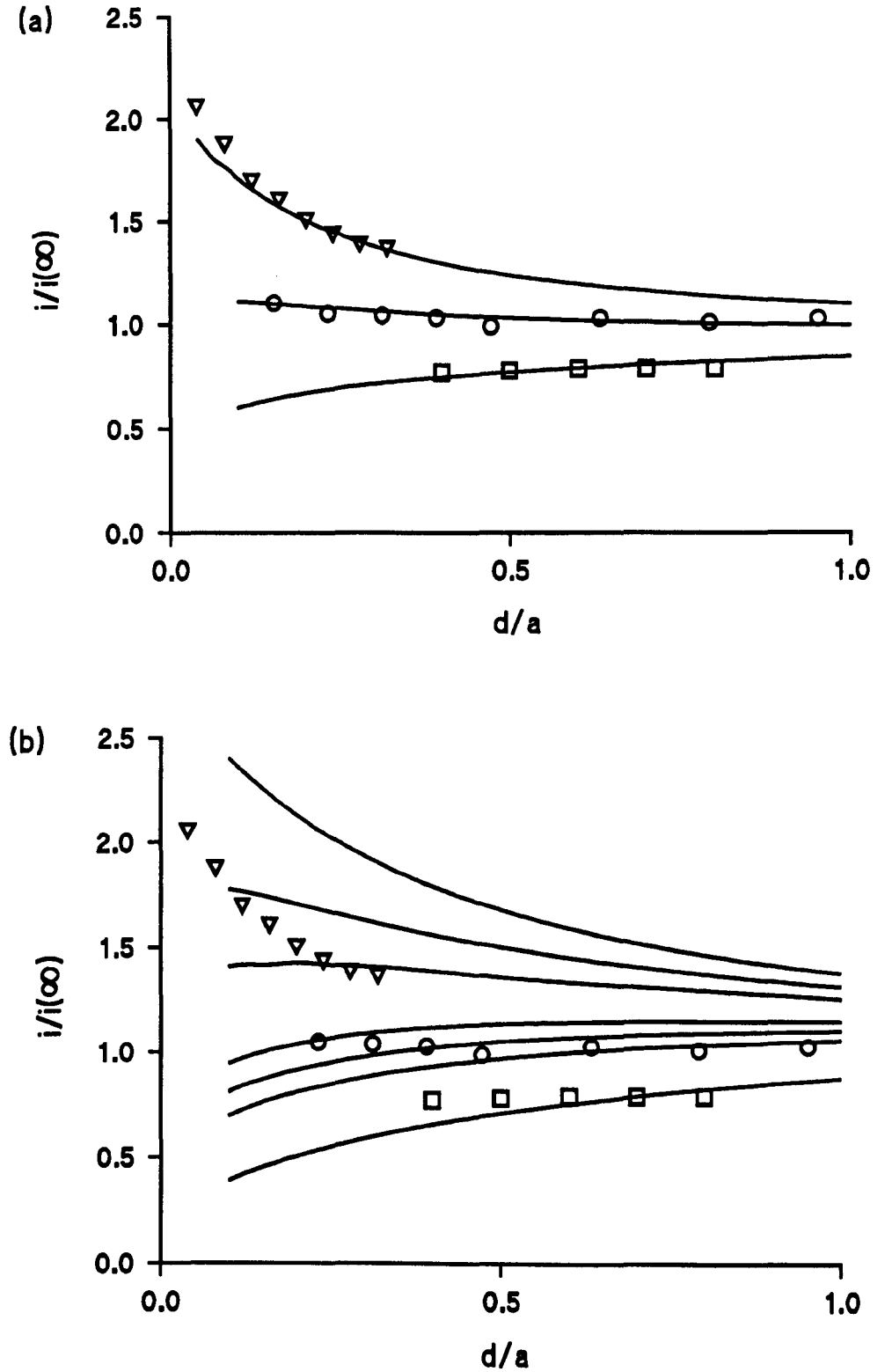

Figure 5.16. Normalised approach curves of steady-state current for Ag^+ reduction versus separation between the tip and AgCl substrate. Data relate to experiments with Pt tips with a = 5.0 μm (□), 12.5 μm (O) and 25.0 μm (∇). Corresponding theory is shown for: (a) second-order process with log K_2 = 0.4 (upper curve), 0.1 and -0.3 (lower curve); (b) a first-order process with log K_1 = 0.5 (upper curve), 0.3, 0.15, -0.1, -0.2, -0.3 and -0.7 (lower curve).

the rate limiting steps in the dissolution process.[2,4] It is therefore valuable to employ the numerical procedure to identify the interfacial undersaturations corresponding to the dissolution experiments described above. Figure 5.17 shows the steady-state normalised concentration of silver chloride at the substrate/solution interface as a function of the radial co-ordinate, R, for the five closest distances in each of the experiments described above. The simulation is for a second-order dissolution process with the rate constants deduced earlier. It can be seen that, in all cases, relatively large undersaturations prevail in the region of the substrate directly under the tip, but for $R > 1$, the interfacial concentration rapidly rises and approaches the bulk solution value. As expected, each of these sets of profiles show the trend that the closer the tip/substrate separation, the lower the interfacial concentration, *i.e.* the higher the interfacial undersaturation. This is because the mass transfer rate increases as the tip is moved towards the surface, which serves to push the dissolution process to increasing surface control. It is also clear from Figure 5.17, that as the normalised tip/substrate ratio decreases (smallest values with $a = 25$ μm and largest values with $a = 5$ μm) and the normalised rate constant increases (highest value with $a = 25$ μm and lowest value with $a = 5$ μm) the interfacial undersaturation becomes more localised to the zone of the substrate directly under the UME, *i.e.* the spatial resolution of the technique increases.

Given that the interfacial undersaturation changes quite dramatically from fairly high to very low values, as R increases, the question arises as to why a simple rate law is observed under all conditions studied. Figure 5.18, which shows the calculated normalised fluxes for the closest five distances in the experiments above, demonstrates that, in general, predominant dissolution occurs from the region directly under the active UME, which is the zone where the interfacial undersaturation is fairly constant with R for a particular tip/substrate separation (Figure 5.17). For all of the experiments carried out, the saturation ratio in this zone (at $R = 0$) varies over the

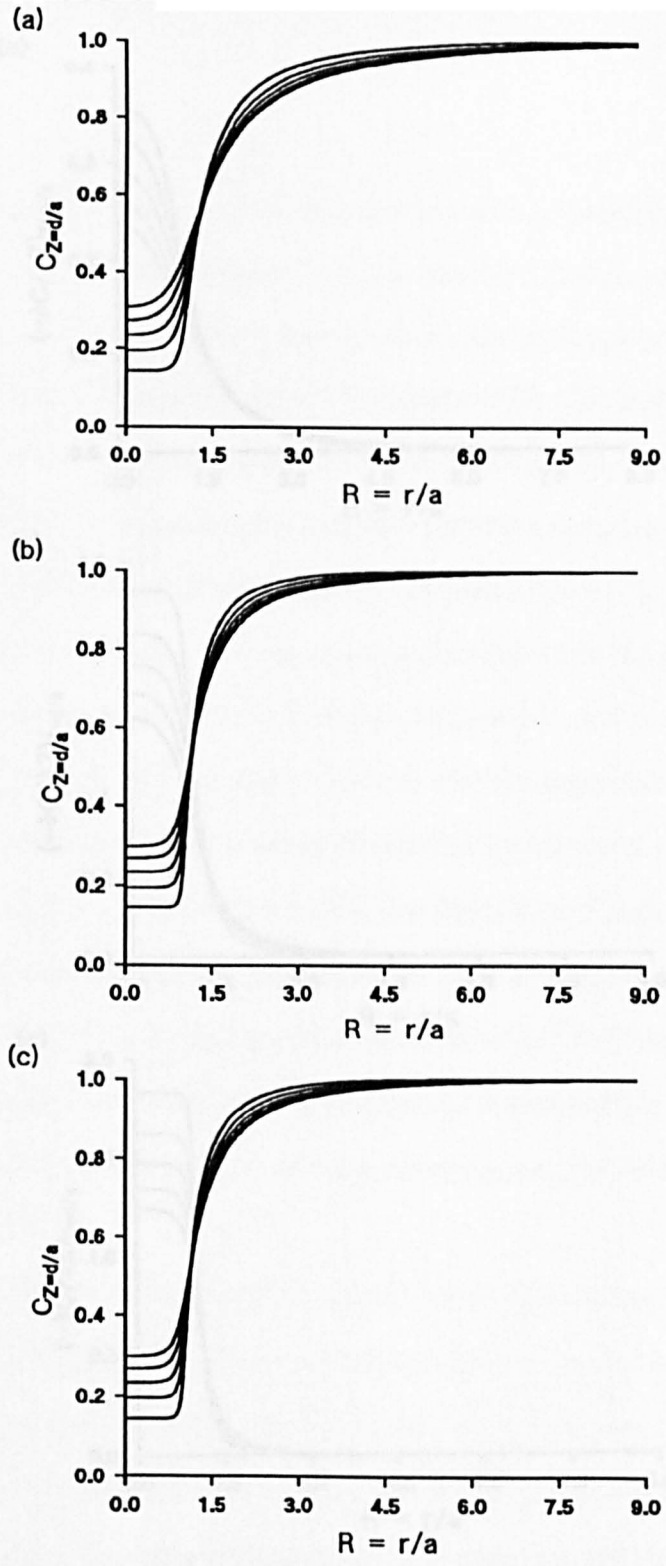

Figure 5.17. Calculated concentration of AgCl at the substrate/solution interface during induced dissolution for the five closest distances in each of the experiments in Figure 5.16. A second-order dissolution process has been considered: (a) $\log K_2 = -0.3$ (corresponding to $a = 5$ μm) with $L = 0.40$ (lowest curve at $R = 0$), 0.50, 0.60, 0.70 and 0.80 (uppermost curve at $R = 0$); (b) $\log K_2 = 0.1$ (corresponding to $a = 12.5$ μm) with $L = 0.15$ (lowest curve at $R = 0$), 0.23, 0.30, 0.39 and 0.47 (uppermost curve at $R = 0$); (c) $\log K_2 = 0.4$ (corresponding to $a = 25$ μm) with $L = 0.08$ (lowest curve at $R = 0$), 0.12, 0.16, 0.20 and 0.24 (uppermost curve at $R = 0$).

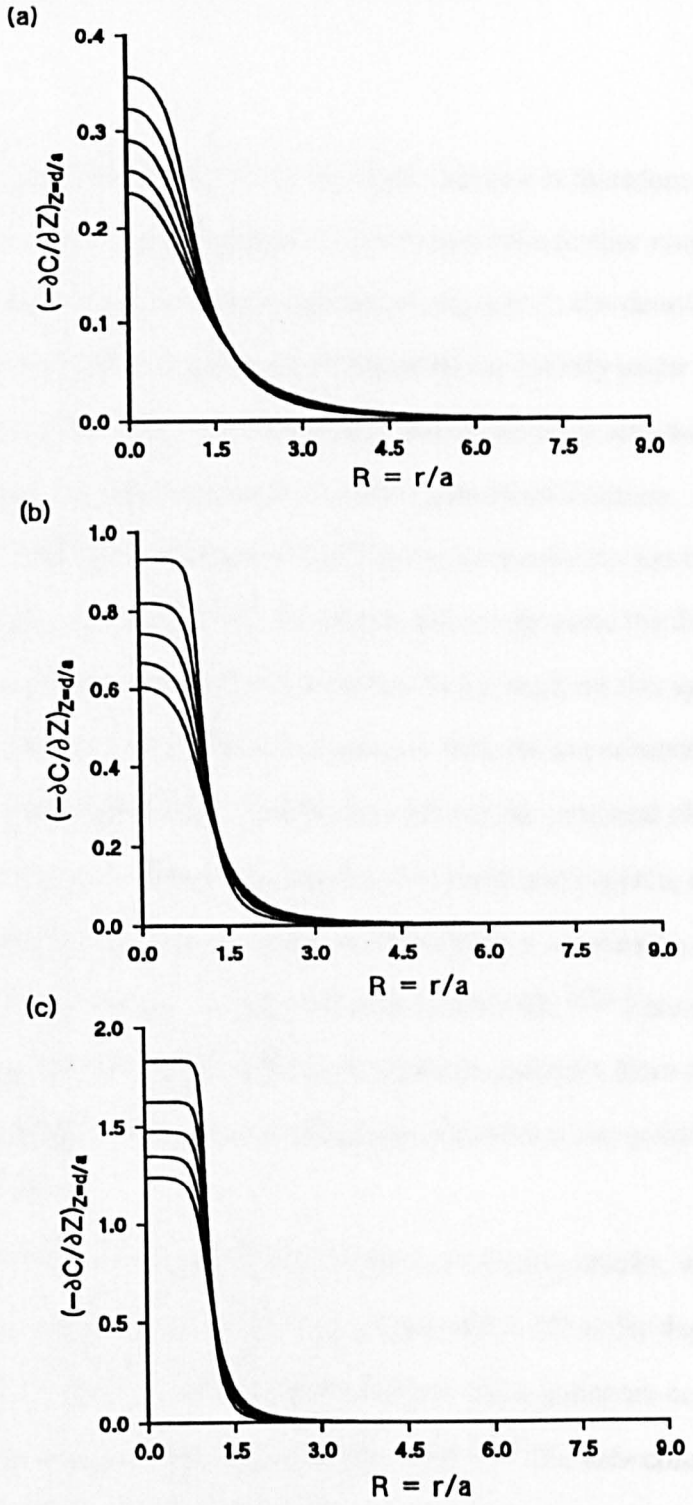

Figure 5.18. Calculated dimensionless flux of AgCl at the substrate/solution interface during induced dissolution for the five closest distances in each of the experiments in Figure 5.16. A second-order dissolution process has been considered: (a) $\log K_2 = -0.3$ (corresponding to $a = 5$ μm) with $L = 0.40$ (lowest curve at $R = 0$), 0.50, 0.60, 0.70 and 0.80 (uppermost curve at $R = 0$); (b) $\log K_2 = 0.1$ (corresponding to $a = 12.5$ μm) with $L = 0.15$ (lowest curve at $R = 0$), 0.23, 0.30, 0.39 and 0.47 (uppermost curve at $R = 0$); (c) $\log K_2 = 0.4$ (corresponding to $a = 25$ μm) with $L = 0.08$ (lowest curve at $R = 0$), 0.12, 0.16, 0.20 and 0.24 (uppermost curve at $R = 0$).

range of 0.16 to 0.30 (Figure 5.17). A simple rate law is therefore not unexpected. A comparison of the profiles in Figure 5.18 also provides further confirmation that the spatial resolution of the technique depends on K_n and L: the dissolution flux is localised predominantly to the zone of the substrate directly under the UME with the 50 μm diameter electrode at its closest normalised distance and most diffuse with the 10 μm diameter tip positioned at its furthest normalised distance.

Although the dissolution of AgCl in aqueous solution has been the subject of several previous studies,[221-223] the results above represent the first quantitative determination of the kinetics of this reaction. Early work on this system[221-223] was hampered by the inherent problems associated with the experimental methodologies employed. These experiments involved monitoring the temporal change in the chemical composition of the bulk solution, at a fixed stirring rate, as AgCl dissolved into an undersaturated aqueous solution, either from a suspension of seed crystals[221,222] or from a rotating rod of silver chloride.[223] These types of approaches make it extremely difficult to separate transport from surface rates and interpret dissolution rates in terms of undersaturations at the solid/liquid interface.[271,272]

Studies on stirred suspensions yielded conflicting results, with initial work reporting the reaction to be surface-controlled with a 3/2 order dependence on the *bulk undersaturation*,[221] while later work reported a transport-controlled reaction when the solution was more than 85% saturated.[222] The rate constants reported in these studies were first-order *homogeneous* rate constants and the deduction of corresponding heterogeneous rate constants is difficult, since the surface area of the samples employed can only be estimated from an average reported crystal size, with no information on the size distribution of the sample. The study in which dissolution occurred from a rotating rod deduced that the dissolution rate was diffusion-controlled from 0 to 90% of saturation in the bulk solution.[223] However, only one

rotation speed was used and the mass transport rate was likely to be *ca.* 0.006 cm s^{-1} which is much lower than the heterogeneous rate constant measured in this study. On the basis of the results presented in this chapter, a transport-controlled process, under the experimental conditions employed by Jones,[223] is not unexpected.

In comparison to the above studies, it has clearly been demonstrated that by employing the well-defined, calculable and high mass transport rates attainable from the SECM, the rate law for the AgCl dissolution process can be elucidated in terms of the undersaturation prevailing at the solid/liquid interface. It is interesting to compare the results reported here with those presented in section 5.5.2.1 for AgCl dissolution in a solution containing 0.1 mol dm^{-3} potassium nitrate as a supporting electrolyte. Under the latter conditions the rate was found to approach the diffusion-controlled limit which applied specifically to those conditions. Although, as pointed out in section 5.3, it may be more difficult to accurately characterise fast kinetics when induced dissolution measurements are carried out in the presence of an inert supporting electrolyte, there is clearly a difference in the rate constant for SECM induced AgCl dissolution under the contrasting conditions of supporting electrolyte vs. no supporting electrolyte.

When an inert supporting electrolyte is present in excess, induced dissolution through Ag^+ reduction leads to the build up of Cl^- and severe depletion of Ag^+ in the tip/substrate gap, an effect which does not occur when there is no supporting electrolyte due to electroneutrality considerations. Two factors result from these different conditions which need to be taken into account when comparing the apparently contrasting rate constants. First, the undersaturations for the two studies are different. In the presence of supporting electrolyte, high undersaturations (and thus dissolution driving forces) are difficult to achieve due to the build up of Cl^-. The reported rate constants are for quite different undersaturations which, in turn, may lead to different mechanisms and kinetics. Second, in the presence of supporting

electrolyte, there is a significant imbalance in the concentration of Cl^- to Ag^+ at the solid/liquid interface, leading to a surface potential which is significantly more negative than that which prevails for induced dissolution without a supporting electrolyte. Under the latter conditions the solution remains electroneutral, and the surface is likely to be slightly negative of its potential of zero charge (based on the situation in saturated solution).[280] Thus, a further explanation for the difference in rate constants may be that silver chloride dissolution is a potential dependent process, with the rate constant increasing as the surface potential becomes more negative.

5.6 Conclusions

Theory for SECM induced dissolution has been successfully extended to the case of a sparingly soluble (1:1) salt dissolving in a solution containing (i) a supporting electrolyte which does not contain a common ion with the electroinactive ion of the dissolving material (ii) no supporting electrolyte. Under the former conditions the dissolution process was found to be diffusion-controlled. This was as a direct consequence of the trapping of the electroinactive ion in the tip/substrate gap due to hindered diffusion, resulting in the suppression of the interfacial undersaturation. Under the latter conditions, a wide range of rate constants were open to study and the limiting rate laws, which consider dissolution to be controlled by first- and second-order terms in the interfacial undersaturation, were readily distinguished from steady-state current-distance measurements. The application of the technique to the study of AgCl dissolution in aqueous solution has allowed the rate law to be determined for the first time as: $j_{AgCl} = 2.1 \times 10^{-10}$ mol cm^2 s^{-1} σ^2.

CHAPTER 6

IN-SITU IMAGING OF IONIC CRYSTAL DISSOLUTION USING AN INTEGRATED ELECTROCHEMICAL-ATOMIC FORCE MICROSCOPE PROBE.

The kinetics and mechanism controlling dissolution from the (100) cleavage face of potassium bromide single crystals in acetonitrile solutions have been identified using a novel integrated electrochemical-AFM probe (IE-AFM) and the SECM. With both techniques, dissolution is induced by perturbing the dynamic dissolution/growth equilibrium at the crystal/solution interface through the electrochemical oxidation of bromide ions to either the acetonitrile stable tribromide ion or, under greater oxidising potentials, to bromine. By careful control of the oxidation potential employed it is possible to exert different thermodynamic driving forces on the process.

SECM measurements demonstrate that the dissolution reaction is diffusion-limited when bromide is electrochemically depleted by diffusion-controlled oxidation to the tribromide ion, suggesting that the surface reaction is characterised by a rate constant in excess of 5 cm s^{-1} (assuming a first-order dissolution process). Under these conditions the topography of the dissolving surface has been imaged, *in-situ*, under conditions which closely mimic those of the SECM measurements, using an electrochemically active AFM probe. These studies provide the first direct experimental evidence of the operation of the spiral mechanism in the dissolution of an ionic single crystal, in which steps of half unit cell height unwind from screw dislocations emerging on the crystal surface.

Under conditions where bromide is electrochemically depleted through diffusion-controlled oxidation to bromine, IE-AFM images show the dynamic

emergence of hollow cores at the centre of the most highly strained screw dislocations, suggesting the operation of a dissolution process which is kinetically limited, under the experimental conditions examined.

6.1 Introduction

As highlighted in chapters 4 and 5, although SECM studies can provide valuable quantitative information on local dissolution rates, important complementary topographical information is limited to microscopic studies of reacted surfaces at a resolution on the micrometre scale, either *ex-situ* using optical microscopy or *in-situ* using SECM in the negative feedback mode. Application of AFM (discussed in section 1.2.4.1.1) to the investigation of the dissolution of ionic crystals has provided important topographical information at the nanometre level. Unfortunately with present AFM methodology, the range of accessible systems is limited to those involving low interfacial dissolution fluxes, in order to avoid significant dissolution during image acquisition.[102,104,106-108,110,111,113]

In this chapter a significant advance in the measurement of dissolution kinetics is described, through the introduction of a complementary AFM technique in which a Pt-coated, electrochemically active AFM tip is used to measure the topography of a dissolving crystal surface, at the nanometre level under electrochemically induced dissolution conditions which closely mimic those for SECM kinetic measurements. This approach allows kinetic and structural information to be linked more closely.

The proposed approach is illustrated through studies of dissolution from the (100) cleavage face of KBr single crystals in acetonitrile solutions. This material has previously been imaged by AFM in air[281] and in ultra-high vacuum[282] and is characterised by flat terraces, separated by steps of unit cell height, often over a scale of micrometres. Consequently, this surface has also attracted attention as a substrate

for imaging adsorbates.[283,284] However KBr surfaces have not been examined by AFM when in contact with a solution. In the studies described herein, dissolution is induced electrochemically by perturbing the dynamic dissolution/growth equilibrium at the crystal/solution interface through the oxidation of bromide to tribromide or bromine. The current, monitored in the SECM configuration as a function of time and tip/substrate distance, provides information on the dissolution rate, while *in-situ* topographical measurements with the electrochemically active AFM tip allow the structural changes that accompany the dissolution process to be identified.

6.2 Theory

For the dissolution of KBr the rate law may be written as:

$$j_{Br^-} = j_{K^+} = k\sigma^n \tag{6.1}$$

where σ (equation (2.69)) is defined as:

$$\sigma = 1 - \left(\frac{a_{K^+} a_{Br^-}}{a^*_{K^+} a^*_{Br^-}} \right)^{1/2} \tag{6.2}$$

Under the conditions of the SECM kinetic experiments, where Br^- is oxidised to Br_3^- at a diffusion-controlled rate in the presence of excess lithium perchlorate, equation (6.2) cannot be simplified further as the K^+ concentration during the course of a dissolution measurement does not remain constant. This case is therefore analogous to AgCl dissolution into a solution where the supporting electrolyte does not contain a common ion with the dissolving material and therefore all further theoretical treatments are as described in Section 5.2.1 where λ_i is now defined as:

$$\lambda_i = \frac{D_i}{D_{Br^-}} \tag{6.3}$$

6.3 Experimental

6.3.1 SECM Procedure

For all SECM measurements, dissolution was initiated and monitored at the UME by stepping the electrode potential from open circuit to +1.3 V, where the oxidation of bromide to tribromide occurred at a diffusion-controlled rate. The resulting current-time behaviour was recorded as a function of tip/substrate separation. Care was taken in setting the final potential to ensure that further oxidation of tribromide to bromine, which occurs at a higher potential, did not take place.

6.3.2 IE-AFM Procedure

Images were acquired at set times post-application of a one second potential pulse to the working electrode from +0.5 V, where no electrode reaction occurred, to either +0.9 V, +1.1 V or +1.3 V, so as to initiate the electrolysis of bromide to tribromide at the working electrode and from +0.5 V to +1.5 V or +1.7 V to initiate the electrochemical oxidation of bromide to bromine.

6.4 Results and Discussion

6.4.1 SECM measurements

Linear sweep voltammetry (LSV) for the oxidation of bromide at a Pt UME in acetonitrile solution, recorded over the potential range +0.5 to +1.8 V vs. AgQRE at a scan rate of 0.01 V s^{-1} gave two clearly defined waves. A typical voltammogram showing the steady-state voltammetric response at a 25 μm Pt UME in a solution containing 0.05 mol dm^{-3} $LiClO_4$, saturated with respect to potassium bromide, is shown in Figure 6.1. UMEs characterised by a = 2.5 and 5.0 μm showed similar voltammetric behaviour but with an overall height which scaled with a. As is well-documented in acetonitrile solutions,[285,286] the first wave ($E_{1/2}$ = +1.05 V vs.

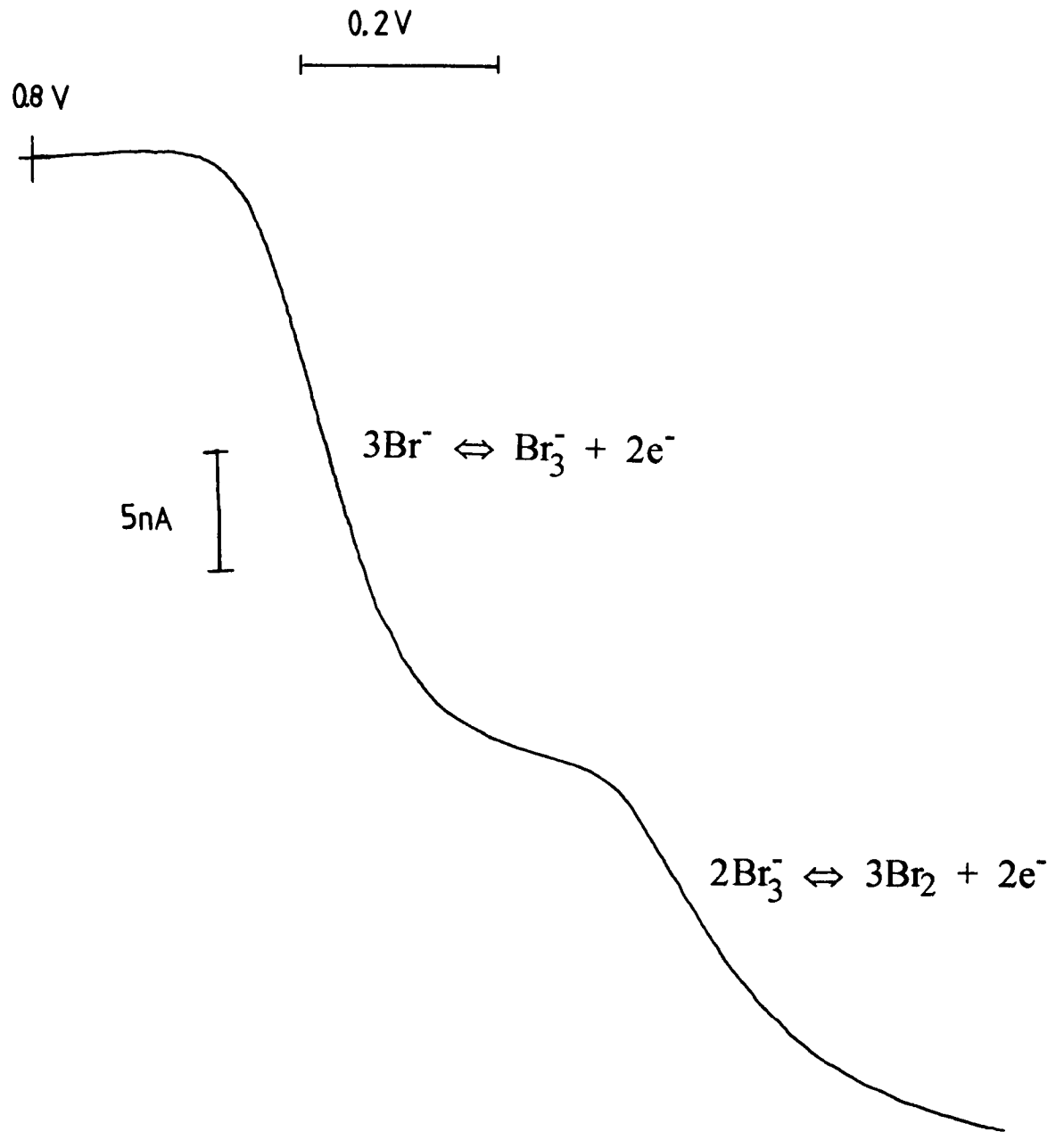

Figure 6.1. Steady-state voltammetric wave for the oxidation of bromide at a 25 μm diameter Pt UME versus AgQRE, at a scan rate of 20 mV s^{-1}, in an acetonitrile solution containing 0.05 mol dm^{-3} $LiClO_4$ and saturated with respect to potassium bromide.

AgQRE) corresponds to the oxidation of bromide to the tribromide species;

$$3Br^- \Leftrightarrow Br_3^- + 2e^- \quad (6.4)$$

while the second wave ($E_{1/2}$ = 1.42 V vs. AgQRE) is due to the oxidation of tribromide to bromine:

$$2Br_3^- \Leftrightarrow 3Br_2 + 2e^- \quad (6.5)$$

Equations (6.4) and (6.5) predict the height of the second wave is half that of the first, which is observed in Figure 6.1. During the second process, the following equilibrium becomes important:

$$Br^- + Br_2 \Leftrightarrow Br_3^- \quad (6.6)$$

due to the high equilibrium constant of 1 x 10^7 mol^{-1} dm^3, which explains the stability of the Br_3^- ion in acetonitrile solutions.[287] Both waves showed a substantial degree of irreversibility on the voltammetric timescale of these measurements, in agreement with previous work.[286]

Given the above information, it is possible to remove Br^- electrochemically from solution, in the SECM induced dissolution configuration, by two routes. Each is effected by stepping the UME potential from a value where no electrolysis occurs to one where Br^- is removed at a diffusion-controlled limit, in this case the steady-state limits of equations (6.4) and (6.5). To simplify the dissolution model, all SECM dissolution experiments reported herein were performed by stepping to a potential where Br_3^- was produced at a diffusion-controlled rate, thus eliminating complications to the model from the homogeneous depletion of Br^- by the equilibrium pathway given in equation (6.6).

6.4.1.1 Bromide Oxidation in Saturated Solutions

The determination of dissolution kinetics via SECM requires that the tip response for the electrochemical process of interest is well-defined in the absence of interfacial kinetic complications. Preliminary experiments were carried out to determine the chronoamperometric characteristics for the oxidation of bromide to tribromide at a Pt UME in an acetonitrile solution containing 0.05 mol dm^{-3} lithium perchlorate and saturated with respect to potassium bromide.

Typical current-time behaviour for the oxidation of bromide at 25, 10 and 5 μm diameter UMEs are shown in Figure 6.2. The data were obtained by stepping the potential from open circuit to +1.275V, +1.3V and +1.3 V, respectively, versus an AgQRE. The current has been normalised with respect to the steady-state current and plotted as a function of $t^{-1/2}$. Analysis of the experimental data in terms of the predicted theoretical response for simple diffusion-controlled electrolysis at a UME (as given by equation (4.21)) revealed that over the timescales employed (400 μs and longer), the oxidation of bromide to tribromide occurred at a diffusion-controlled rate[261] characterised by a value of $D_{Br^-} = 1.25 \times 10^{-5}$ cm^2 s^{-1}. This value is in good agreement with the value $D_{Br^-} = 1.17 \times 10^{-5}$ cm^2 s^{-1} obtained under similar experimental conditions.[285] Knowledge of D_{Br^-} allows the concentration of K^+ and Br^- ions present in the solution to be readily deduced as 6.3×10^{-3} mol dm^{-3} through application of equation (1.4), where the steady-state current response of a 25 μm diameter Pt UME, is 25.2 nA and $n_e = 2 / 3$.

Potential step chronoamperometry carried out in the SECM configuration with a series of tips ($a = 2.5$, 5.0 and 12.5 μm) placed at distances in the range 0.1 a to 1.3 a from an inert glass surface, in an acetonitrile solution containing 0.05 mol dm^{-3} $LiClO_4$ and saturated with respect to potassium bromide gave current-time responses which were observed to be in good agreement with theoretical predictions

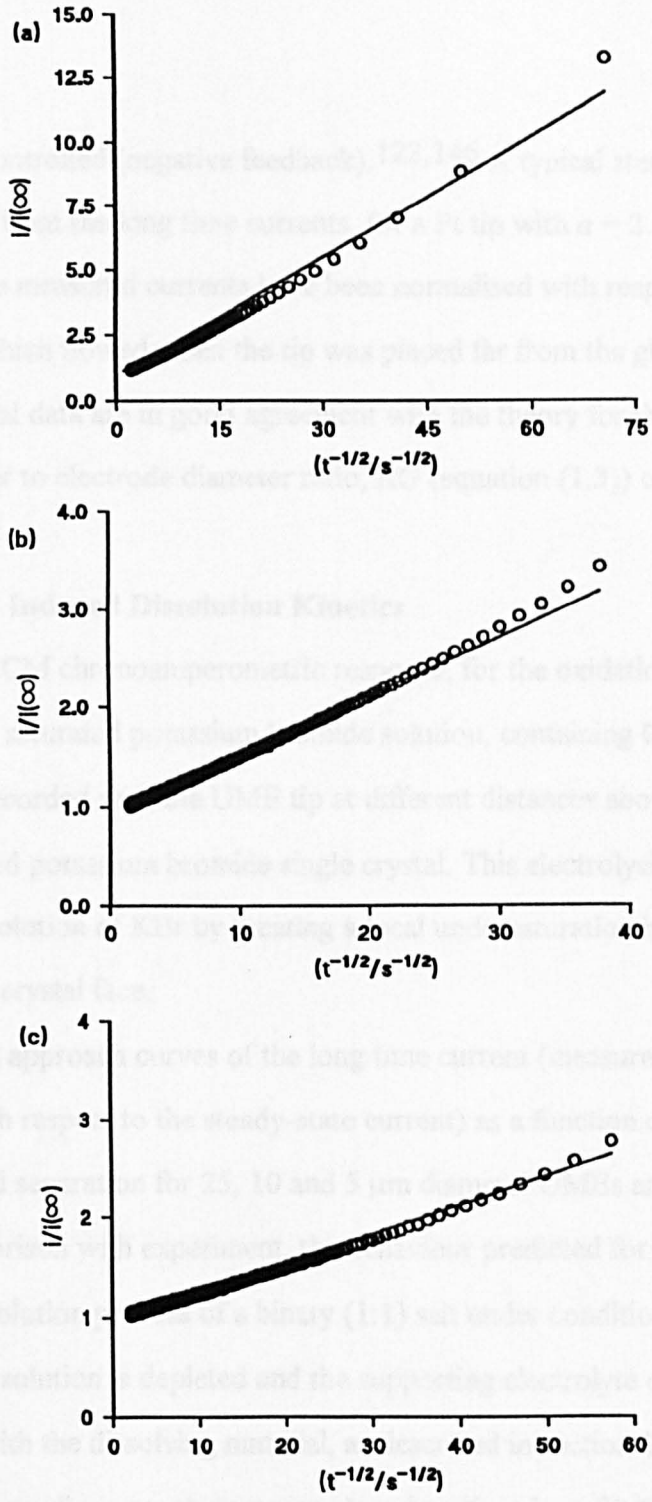

Figure 6.2. Chronoamperometric characteristics for the oxidation of bromide to tribromide in an acetonitrile solution containing 0.05 mol dm^{-3} $LiClO_4$ and saturated with respect to potassium bromide at a (a) 25 μm (b) 10 μm and (c) 5 μm diameter Pt UME. In all cases the solid line shows the theoretical response for a simple diffusion-controlled process, in accordance with equation (4.21), characterised by $D_{Br^-} = 1.25 \times 10^{-5}$ cm^2 s^{-1}.

for diffusion-controlled (negative feedback).[122,146] A typical steady-state approach curve, derived from the long time currents, for a Pt tip with $a = 2.5$ μm is shown in Figure 6.3. The measured currents have been normalised with respect to the steady-state current which flowed when the tip was placed far from the glass surface. Clearly the experimental data are in good agreement with the theory for this probe, which had an insulator to electrode diameter ratio, *RG* (equation (1.3)) of 15.

6.4.1.2 SECM Induced Dissolution Kinetics

The SECM chronoamperometric response, for the oxidation of bromide to tribromide in a saturated potassium bromide solution, containing 0.05 mol dm^{-3} $LiClO_4$, was recorded with the UME tip at different distances above the (100) face of a freshly cleaved potassium bromide single crystal. This electrolysis process serves to induce the dissolution of KBr by creating a local undersaturation in the gap between the tip and the crystal face.

Typical approach curves of the long time current (measured at $\tau = 6.4$ and normalised with respect to the steady-state current) as a function of tip/potassium bromide crystal separation for 25, 10 and 5 μm diameter UMEs are shown in Figure 6.4. For comparison with experiment, the behaviour predicted for a diffusion-controlled dissolution process of a binary (1:1) salt under conditions where only one ion type in the solution is depleted and the supporting electrolyte does not contain a common ion with the dissolving material, as described in section 5.2.1 and 6.2, is also shown. The theory lines are characterised by a log K_1 value of 2.0, which equates to an effectively diffusion-controlled dissolution process.

It is clear that, even on the fastest timescale possible, (achieved with the smallest diameter UME), the dissolution process is effectively diffusion-controlled even at a probe/crystal separation as close as 400 nm ($d/a = 0.16$). This is not unexpected, given that the K^+ concentration levels build up in the gap between the

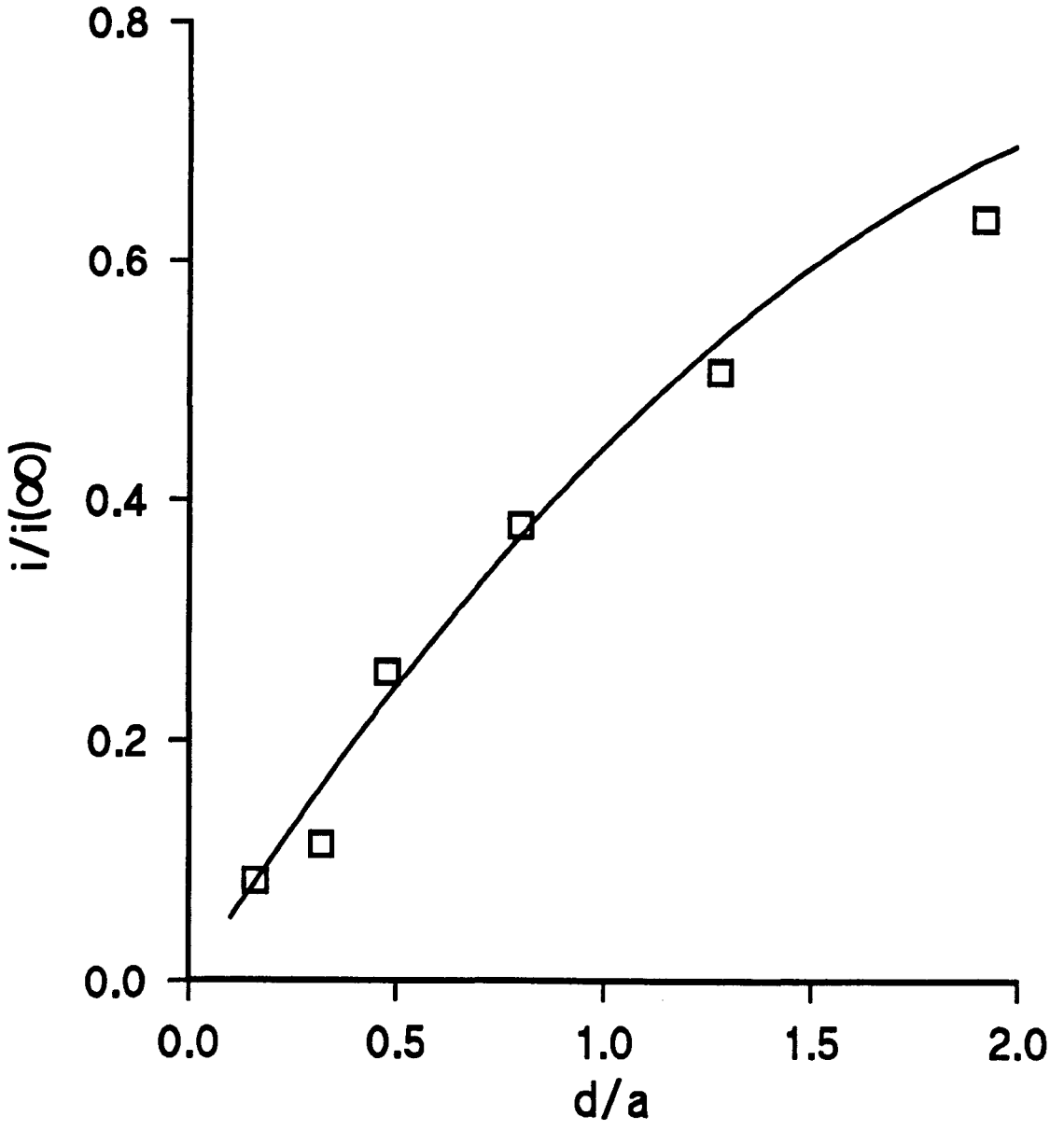

Figure 6.3. Steady-state approach curve of the diffusion-limited current for the oxidation of Br^- to Br_3^- at a Pt tip (a = 2.5 μm), as a function of distance from a glass surface (□). The theoretical behaviour for negative feedback (___) for RG = 15, under the conditions of the SECM measurements, is also shown.

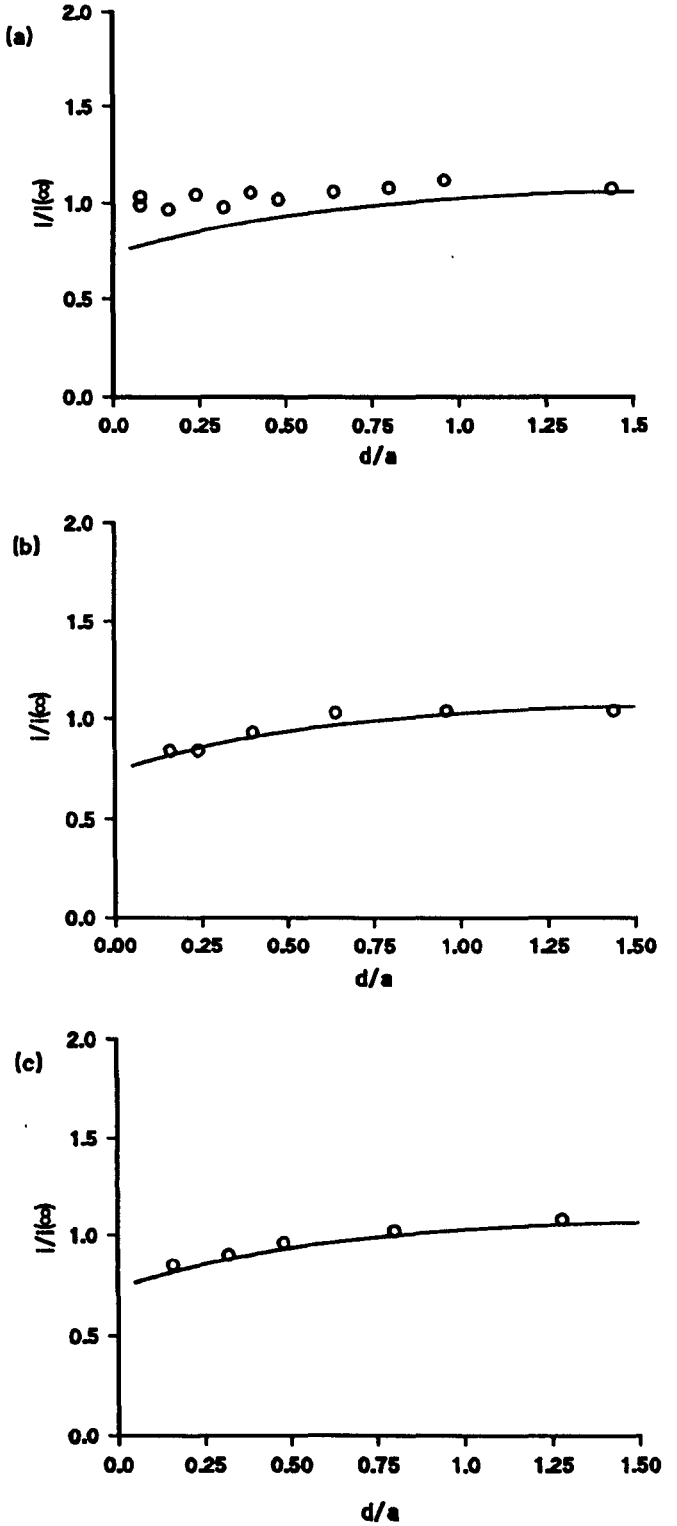

Figure 6.4. Steady-state approach curves of the diffusion-limited current (taken at measurement times of $\tau = 6.4$) for the oxidation of Br^- to Br_3^-, as a function of distance from the (100) face of a single crystal of potassium bromide, in an acetonitrile solution containing 0.05 mol dm^{-3} $LiClO_4$ and saturated with respect to potassium bromide at (a) 25 μm (b) 10 μm and (c) 5 μm diameter Pt UMEs. The theoretical behaviour (——) for a diffusion-controlled dissolution process under the conditions of the SECM measurements is also shown.

tip and the crystal surface during the course of the measurement, suppressing the attainment of high undersaturations and pushing the surface process towards mass transfer-controlled.

Under these conditions, the minimum effective heterogeneous dissolution rate constant, in terms of a first order process, can be estimated from equation (2.75), where $a = 2.5 \times 10^{-4}$ cm and $D_{Br^-} = 1.25 \times 10^{-5}$ cm^2 s^{-1} hence:

$$k' > 5 \text{ cm s}^{-1} \tag{6.7}$$

under the experimental conditions.

6.4.2 IE-AFM probe results

6.4.2.1 Electrochemical and Imaging Characteristics of the IE-AFM Probe

The sputtering technique used to create the integrated IE-AFM probe produced a tip and cantilever that were evenly coated with metal. The presence of metal at the apex of the AFM tip was verified by measuring the tip/sample resistance as the tip was brought into contact with a conductive sample.[288] A small (10-50 mV) bias was applied between the Pt-coated AFM tip and a gold or graphite surface across a current limiting resistor (5 MΩ). As the tip/sample separation was reduced, the tip deflection and the tip/sample resistance were recorded simultaneously. For most tips, the resistance dropped at contact between tip and sample, indicating the presence of conductive material at the tip apex.

The imaging ability of the Pt-coated AFM probe appeared to be unaffected by the presence of the additional metal layer. With this probe, steps with heights of atomic dimension (*vide infra*) and high resolution lattice images of the (100) face of the KBr surface, were easily resolved in an acetonitrile solution saturated with respect to KBr and containing 0.05 mol dm^{-3} $LiClO_4$. Figure 6.5(a) shows a schematic of the KBr surface lattice. The arrangement of the atoms is face centred

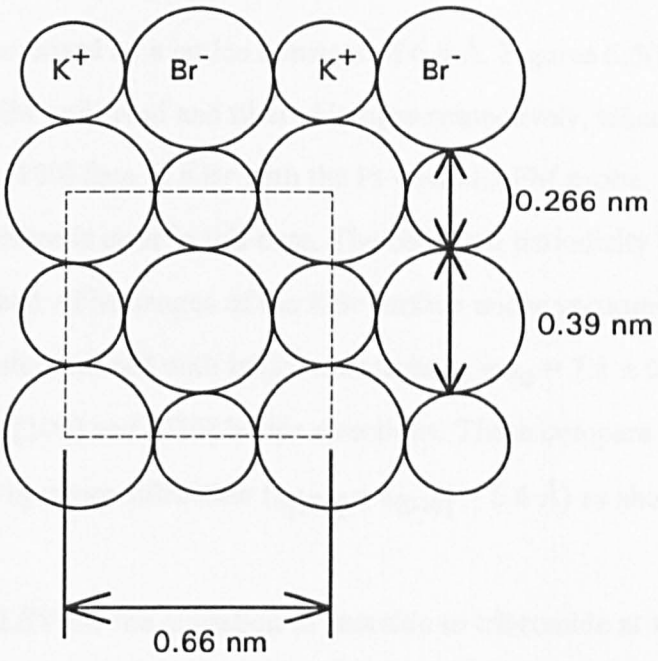

Figure 6.5(a) Schematic of the surface structure of the KBr lattice (100). The large circles represent the Br^- ions (bare ion radius is 0.195 nm) and the small circles represent the K^+ ions (bare ion radius 0.133 nm).

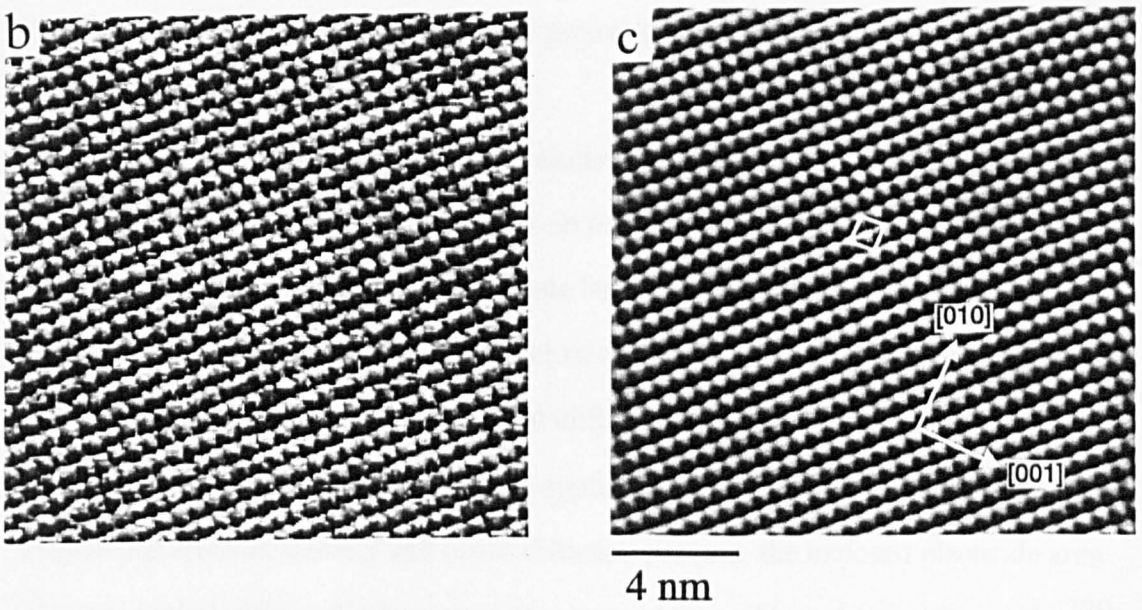

High resolution **(b)** unfiltered and **(c)** filtered AFM image of the (100) face of the KBr surface in an acetonitrile solution saturated with respect to KBr.

cubic (fcc), characterised by a lattice constant of 6.6 Å. Figures 6.5(b) and (c) show representative AFM unfiltered and filtered images respectively, taken at high resolution on the (100) face of KBr with the Pt-coated AFM probe. The periodic registry of this surface is clear in this data. The observed periodicity is typical of previously published AFM images of the KBr surface under vacuum[282] and clearly depicts a rectangular unit cell with lattice constants $a_1 = a_2 = 7.1 \pm 0.4$ Å, which correspond to the [100] and [010] lattice directions. These compare favourably to those determined by x-ray diffraction ($a_{[100]} = a_{[010]} = 6.6$ Å) as shown in Figure 6.5(a).

A typical LSV for the oxidation of bromide to tribromide at a Pt-coated AFM probe, recorded at a scan rate of 0.05 V s^{-1} between +0.5 V and +1.8 V (vs. AgQRE) in a saturated potassium bromide acetonitrile solution containing 0.05 mol dm^{-3} $LiClO_4$, is shown in Figure 6.6. This measurement was made with the KBr sample retracted far from the tip (*ca.* 100 μm), to ensure that the electrode diffusion field would not be significantly perturbed by the sample and to suppress the induction of dissolution.

The LSV shows clearly the two electrolysis waves associated with the oxidation of Br^- in acetonitrile solutions. In contrast to Figure 6.1, the voltammogram does not show steady-state behaviour for the production of Br_3^- and Br_2. This is due to the increase in the size of the exposed electrode area and therefore a switch from semi-infinite hemispherical diffusion (as shown in Figure 6.1) to predominantly linear diffusion. Through application of equation (6.8), assuming an irreversible electron transfer and linear diffusion process, the exposed electrode area can be established from the first wave for the oxidation of bromide to tribromide:[289]

$$i_p = 2.99 \times 10^5 n_e (\alpha n_a)^{1/2} A c^* D^{1/2} V^{1/2} \qquad (6.8)$$

where i_p is the peak current, which in Figure 6.6 is 7.2 μA, α is the transfer

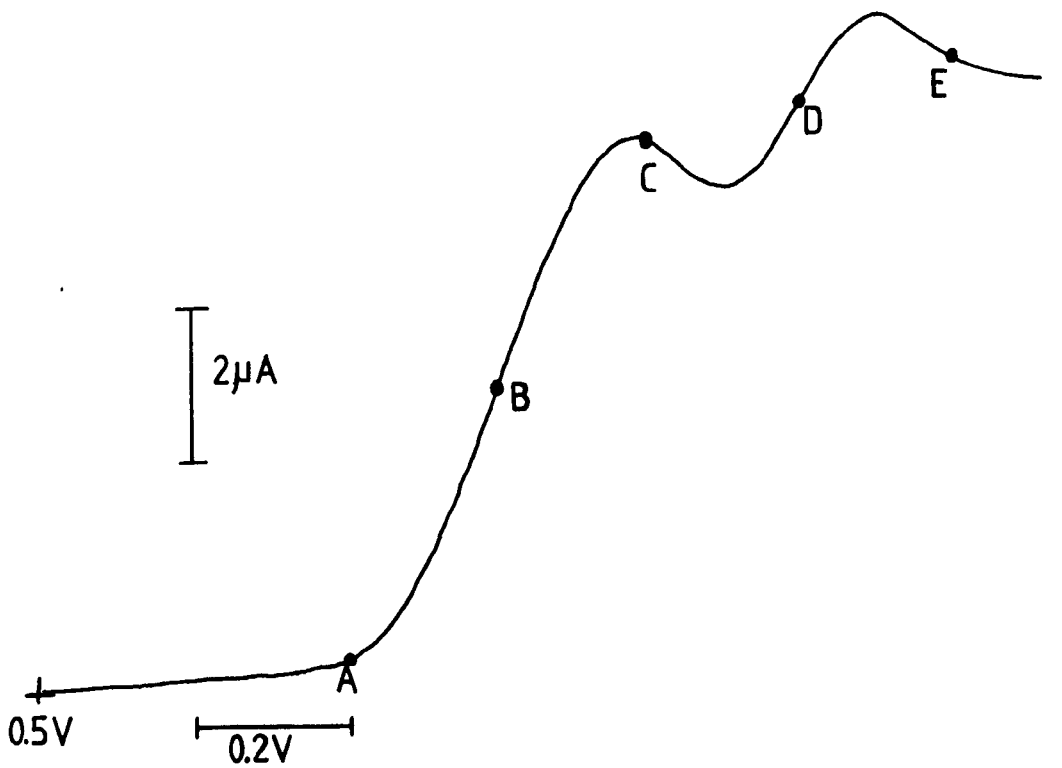

Figure 6.6. Linear sweep voltammogram at a Pt-coated AFM probe for the oxidation of Br^- to Br_3^- in an acetonitrile solution containing 0.05 mol dm^{-3} $LiClO_4$, as a supporting electrolyte, and saturated with respect to KBr. The potential scan rate was 0.05 V s^{-1}. The potentials to which the probe was pulsed during electrochemically induced AFM dissolution studies are also indicated.

coefficient, which is assumed to be 0.5, A is the electrode area, $V^{1/2}$ is the potential scan rate and n_a is the number of electrons up to and including the rate determining step (rds), which is 2/3, given the following reaction mechanism for the oxidation of bromide to tribromide in acetonitrile solutions;[285,286]

$$Br^- \underset{K_{-1}}{\overset{K_1}{\Leftrightarrow}} Br_{ads} + e^- \tag{6.9}$$

$$Br_{ads} + Br^- \underset{K_{-2}}{\overset{K_2}{\Leftrightarrow}} Br_2 + e^- \tag{6.10}$$

$$Br_2 + Br^- \underset{K_{-3}}{\overset{K_3}{\Leftrightarrow}} Br_3^- \tag{6.11}$$

where equation (6.10) is the rds and Br_{ads} corresponds to adsorbed bromide on the electrode surface. Hence A can be estimated as 1.25 mm^2, for this particular polystyrene coated AFM probe, although it was found that the electroactive area typically varied between 0.7 to 1.3 mm^2 after application of the insulating film.

Together, the results in Figures 6.5(b), 6.5(c) and 6.6 demonstrate that high resolution topographical and electrochemical measurements are feasible at the Pt-coated AFM probe.

6.4.2.2 IE-AFM Induced Dissolution

6.4.2.2.1 The Br^- to Br_3^- Oxidation Wave

As noted in section 6.4.2.1, a consequence of the procedure adopted to electrically insulate the AFM probe is that the tip and a significant fraction of the cantilever are electrochemically active. Thus, most of the electrochemically active part of the probe (apart from the apex of the tip in contact with the surface) is at a sufficiently great distance from the crystal surface (3-40 μm) to ensure that the dissolution images, reported below for oxidation of the Br^- to Br_3^- in the

probe/substrate gap, relate to effective conditions of a diffusion-controlled process.

Figure 6.7 shows a sequence of *in-situ* AFM images of an area of the KBr surface recorded prior to, and after, electrochemically inducing dissolution by pulsing the probe potential from +0.5 V to +0.9 V (point A in Figure 6.6) for 1 s and then back to +0.5 V. The step to +0.9 V (just into the bromide-tribromide oxidation wave) slightly depletes the bromide concentration, providing the thermodynamic force for dissolution, but the irreversibility of the electrochemical process dictates that tribromide is not reduced back to bromide when the potential is returned to +0.5 V.

Although the solution in contact with the crystal surface was nominally saturated with respect to KBr, before dissolution was induced, Figure 6.7(a) clearly shows the presence of a dissolution spiral, which was found to slowly rotate over a period of several minutes, consistent with a very slowly dissolving surface. The spiral comprises widely spaced steps (width in the range 400-900 nm) of *ca.* half unit cell height (3.4 ± 0.5 Å) winding down to an origin located at the lower left of Figure 6.7(a). The spiral is not of the classical archemedian type,[4,290] as a result of a number of breaks in the steps. As identified below, these breaks coincide with the cores of other dislocations which emerge at the surface.

The wide spacing of the steps far from the origin of the main spiral is diagnostic of only very slightly undersaturated solution.[87] Even though dissolution is not electrochemically induced during the recording of the image in Figure 6.7(a), a slowly dissolving surface is not unexpected, since small temperature increases in the sample chamber can arise from the diode laser in the detection unit.[291] The influence of the scanning tip may also create slightly undersaturated conditions as a result of local frictional heating. These effects were minimised by periodically injecting fresh solution into the reaction cell but, nonetheless, even small variations in temperature will lead to slightly undersaturated (or supersaturated) conditions sufficient to promote dissolution (or growth) at highly strained dislocation features. It is unlikely

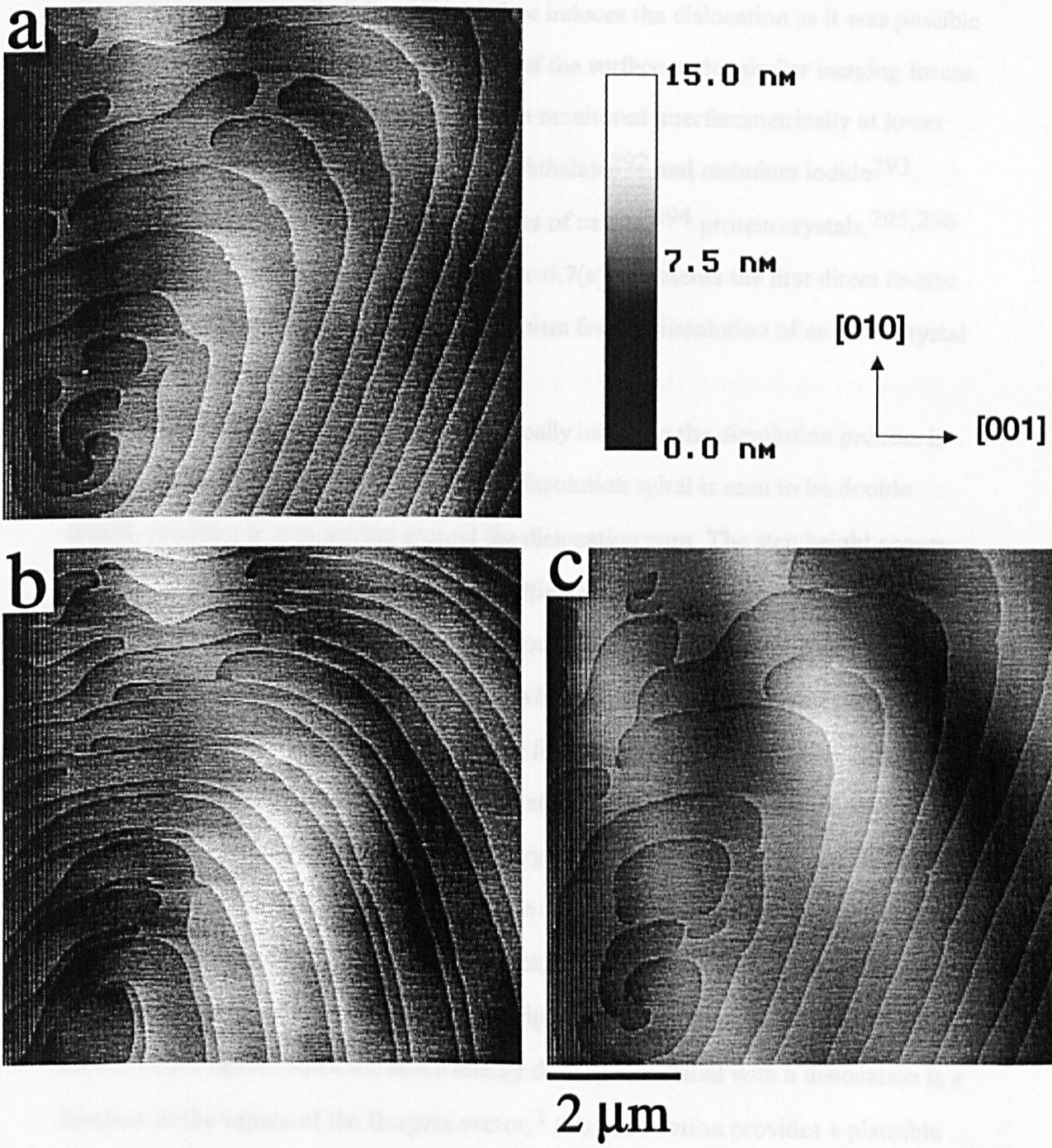

Figure 6.7. Height mode AFM images of a 7 µm by 7 µm area of the (100) face of potassium bromide in contact with a saturated KBr solution prior to (a), 60 s after (b) and eight minutes after (c), the application of a 1 s potential pulse (+0.5 V to +0.9 V) to the electrochemically active AFM probe.

that contact between the tip and the surface induces the dislocation as it was possible to obtain images of dislocation-free areas of the surface under similar imaging forces.

Although rotating spirals have been monitored interferometrically at lower resolution, *in-situ* on growing potassium phthalate[292] and cadmium iodide[293] crystal surfaces, and in AFM growth studies of calcite,[294] protein crystals,[295,296] and organic charge transfer salts,[297] Figure 6.7(a) represents the first direct *in-situ* observation of the operation of this mechanism for the dissolution of an ionic crystal surface in contact with a liquid medium.

The surface 60 s after electrochemically initiating the dissolution process is shown in Figure 6.7(b). The predominant dissolution spiral is seen to be double armed, resulting in step pairing around the dislocation core. The step height across the double arm is *ca.* 6.7 ± 0.5 Å. The resulting decrease in the distance between steps as they pair indicates that the step velocity and hence dissolution rate has increased from the initial conditions (Figure 6.7(a)), where only thermal perturbations from equilibrium provided the driving force for dissolution of the surface. Spirals with two arms which rotate together as the step advances have recently been observed by AFM during the growth of inorganic[294] and organic crystals[295] but Figure 6.7(b) is the first example of a double armed spiral imaged dynamically on a dissolving surface. For the KBr crystal lattice, the observation of such a spiral suggests that the screw dislocation at the origin is characterised by a Burgers vector of two lattice layers. Since the strain energy density associated with a dislocation is a function of the square of the Burgers vector,[3] this observation provides a plausible explanation as to why this dislocation, and no other, dominates in the imaged region when the solution is very close to saturation. Figure 6.7(c), which was recorded eight minutes after the initial 1 s potential pulse, demonstrates that, as the solution returns to equilibrium through dissolution of the crystal, the dissolution rate decreases resulting in an increase in step spacing and a return to a surface structure similar to

that depicted in Figure 6.7(a).

The evolving topography of the crystal surface following a 1 s potential pulse further into the Br^- to Br_3^- oxidation wave, from +0.5 V to +1.1 V (point B in Figure 6.6) is depicted in Figures 6.8(a) - (c). These images clearly demonstrate that, under conditions of high mass transport rates, dissolution still occurs via a spiral mechanism, but many more dislocations are activated and hence revealed. In total, nine spirals appear in the area of the surface under study (Figure 6.8(a)). Coupled with Figure 6.7, this observation is important since the spiral mechanism underpins a number of the theoretical treatments of crystal dissolution.[2,5,7,8,271,272] Although this model was originally introduced by Burton, Cabrera and Frank[4,290] to describe the growth of metals from a vapour, it has been adapted and used widely to interpret experimental dissolution kinetics,[2,5,7,8,271,272] including the rapid kinetics deduced from the SECM induced dissolution studies described in this thesis. The results herein provide the first *in-situ* evidence of the validity of this mechanism in describing fast dissolution processes of ionic single crystal surfaces.

The difference in the shape and depth of the features in Figure 6.8(a) suggests different strain energies associated with the core dislocations, with the deepest spirals associated with the largest strain energy.[3] However, the geometry of the electrochemically active AFM probe is such that there will be a variation in the probe/crystal separation, and thus slight variation of the mass transport rate, over the region of interest during dissolution which must also be taken into account when interpreting this data.

The operation of the spiral dissolution process is consistent with the SECM kinetic results (described in section 6.4.1.2), which demonstrated that the dissolution process will be predominantly transport-controlled over a wide range of mass transport rates, including those of the AFM experiments. In this regime, the spiral dissolution process is sufficiently rapid to maintain the crystal/solution interfacial

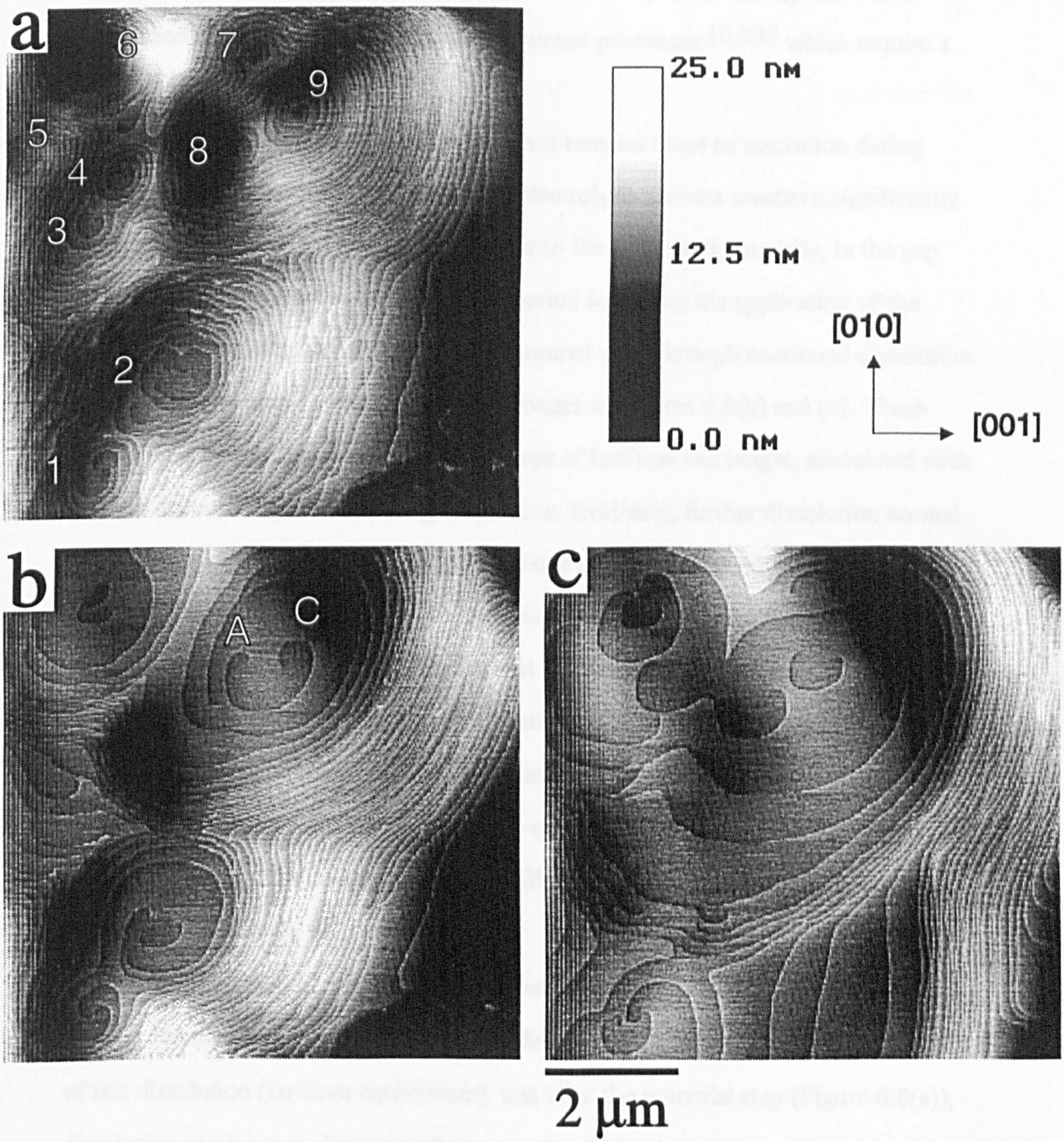

Figure 6.8. Height mode AFM images of the same area of the KBr (100) face as in Figure 6.7 immediately after the application of a 1 s potential pulse (+0.5 V to +1.1 V) to the electrochemically active probe. Images (a) to (c) were recorded sequentially at a rate of 21 s/frame.

region close to effectively saturated conditions, thereby disfavouring alternative dissolution mechanisms, such as birth and spread processes,[10,298] which require a large interfacial undersaturation.

Although the crystal/solution interface remains close to saturation during electrochemically induced dissolution, the electrolysis process creates a significantly undersaturated zone in the solution adjacent to the probe and, crucially, in the gap between the probe and the surface. In the period following the application of the potential pulse, the solution returns to a saturated state through continued dissolution of the crystal surface, as evident from the images in Figures 6.8(b) and (c). These images provide vital information on how steps of half unit cell height, associated with specific dislocations, retreat during dissolution. Evidently, further dissolution normal to the surface slows considerably and continued dissolution occurs via the motion of steps away from the dislocation core, resulting in the step spacing becoming wide towards the centre of the spiral and closer at a distance from the core. Spirals with this morphology have been predicted theoretically for dissolution processes close to saturation.[89] *Ex-situ* optical microscopy studies of the surfaces of naturally-occurring hematite crystals have also identified spirals of this type[299] on a much larger scale, but the natural dissolution conditions are difficult to predict,[300] making quantitative interpretation difficult.

The images in Figure 6.8 contain interesting information on the influence of etching conditions on step orientations for the KBr (100) surface. Under conditions of fast dissolution (far from equilibrium), just after the potential step (Figure 6.8(a)), dissolution produces surface steps that, near the dislocation core, are isotropic with no preferred orientations, as expected for a crystal dissolution or growth process controlled by solution diffusional processes. As the rate of surface etching slows and the crystal dissolution process approaches equilibrium, surface steps facet along the directions of lowest surface energy corresponding to the strongest crystallographic

bonding directions. Ideas of this type have been put forward, for example, in the periodic bond chain,[301] surface roughening[302] and attachment energy models.[303,304] Analysis of Figures 6.8(b) and (c) (see also Figure 6.7) demonstrates that the steps favour an orientation along the [010] and [001] crystallographic directions. These orientations correspond to the direction of strong Coulombic bonding between neighbouring K^+ and Br^- sites[282] in the lattice.

Figures 6.8(b) and (c) also demonstrate elegantly the interactions between closely spaced spirals at the points where they intercept. It is particularly interesting to note the step pattern that results from the interception of spirals which rotate in opposite directions, labelled A (anticlockwise rotation, moving outwards from the centre) and C (clockwise rotation) in Figure 6.8(b). The steps emerging from dislocations A and C travel towards one another and annihilate when they intersect, leaving a single step connecting the dislocation cores, the morphology of which is very similar to that predicted theoretically for this situation by Burton, Cabrera and Frank.[4]

After several minutes the surface was found to reconstruct to a form which was similar to that which prevailed prior to the induction of dissolution. A subsequent 1 s pulse of the probe potential from +0.5 V to +1.3 V (point C in Figure 6.6) and back to +0.5 V was then applied to increase the transport driving force exerted on the dissolution process. Figure 6.9(a), recorded immediately after the pulse demonstrates that the same dislocations are revealed as in Figure 6.8(a). However, the spirals penetrate deeper into the crystal surface, as expected for a diffusion-controlled process under more extensive dissolution conditions due to a faster mass transfer rate from the crystal surface. As described above, the solution returns to a saturated state via the further dissolution of the crystal surface, which can be followed over time. Figures 6.9(b) and (c) show the surface *ca.* 60 s and 180 s, respectively, after the potential pulse, demonstrating that the surface reconstructs to a morphology which is

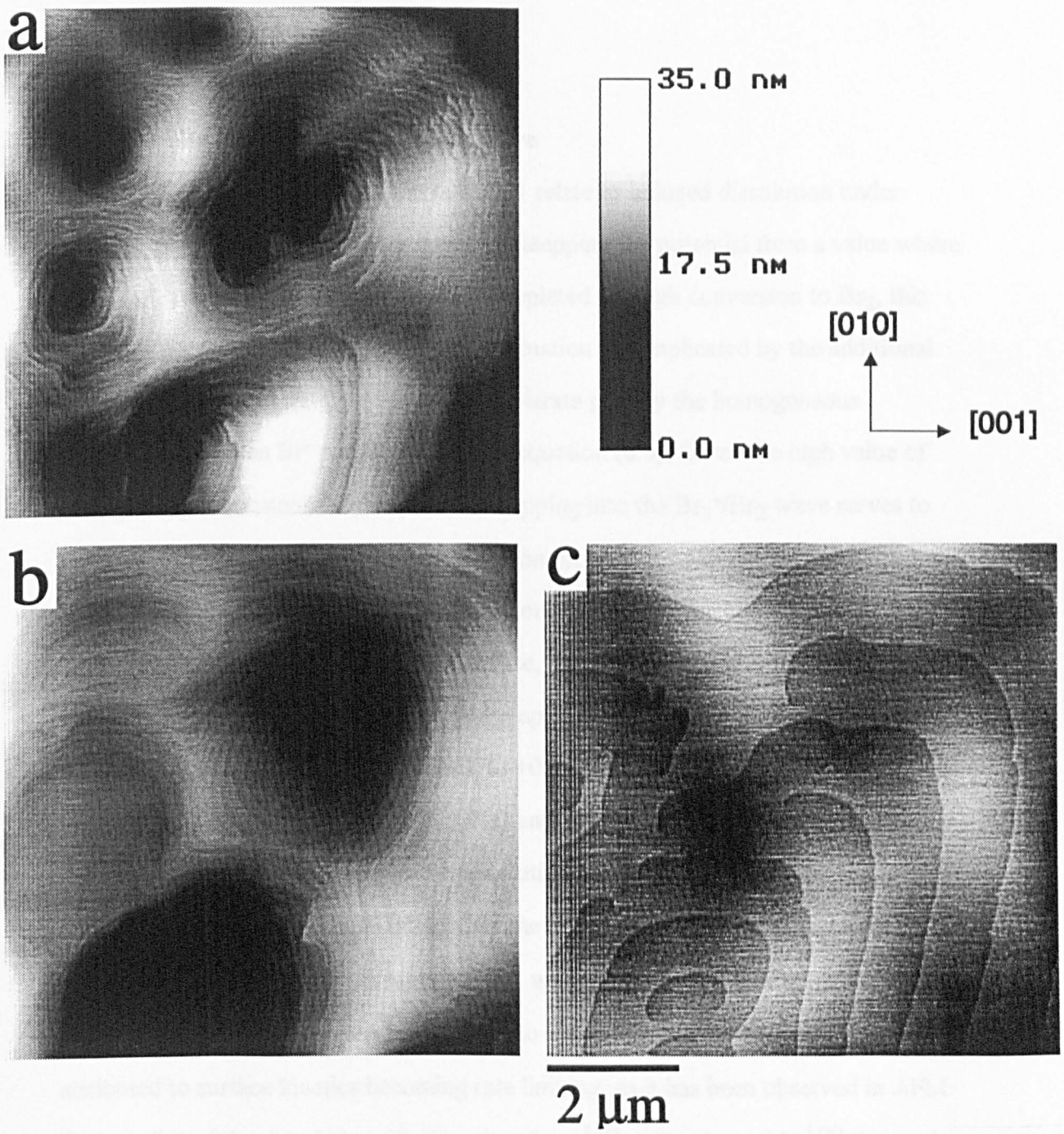

Figure 6.9. Height mode AFM images of the same area of the KBr (100) face as in Figure 6.7: (a) immediately after the application of a 1 s potential pulse (+0.5 V to +1.3 V) to the electrochemically active AFM probe; (b) *ca.* 60 s later; (c) *ca.* 180 s later.

very similar to that prior to all of the induced dissolution measurements, depicted in Figure 6.7(a).

6.4.2.2.2 The Br_3^- to Br_2 Oxidation Wave

The AFM images in section 6.4.2.2.1 relate to induced dissolution under effective conditions of diffusion control. By stepping the potential from a value where no electrolysis occurs to one where Br^- is depleted through conversion to Br_2, this assumption can no longer be made, as the situation is complicated by the additional titration of Br^-, from the IE-AFM probe/substrate gap, by the homogeneous equilibrium between Br^- and Br_2, shown in equation (6.6). Given the high value of the equilibrium constant for this process, stepping into the Br_3^-/Br_2 wave serves to exert a greater driving force on the dissolution process, with the consequence that the reaction is pushed towards greater surface control.

Figure 6.10(a) shows the KBr surface, depicted in Figure 6.9(a) immediately after the application of a 1 s potential pulse applied to the probe, from +0.5 V to +1.5 V (point D in Figure 6.6) and back to +0.5 V. Once again, the same dislocations are revealed as in Figures 6.8(a) and 6.9(a) and, as expected, penetrate deeper into the crystal surface, due to the greater dissolution driving force exerted on the crystal surface. In this instance, immediately after the potential step, lateral dissolution processes appear more prominent compared with Figure 6.9(a), as the width of the dislocations have also increased in addition to becoming deeper. This may be attributed to surface kinetics becoming rate limiting, as it has been observed in AFM flow studies of the dissolution of mineral surfaces[110] and amino acids,[109] that under the contrasting conditions of mass transfer control, lateral step motion has a tendency to become retarded.

Figures 6.10(b), (c) and (d) show the surface at times of 180 s, 240 s and 300 s post-application of the potential step. The change in the crystal morphology can

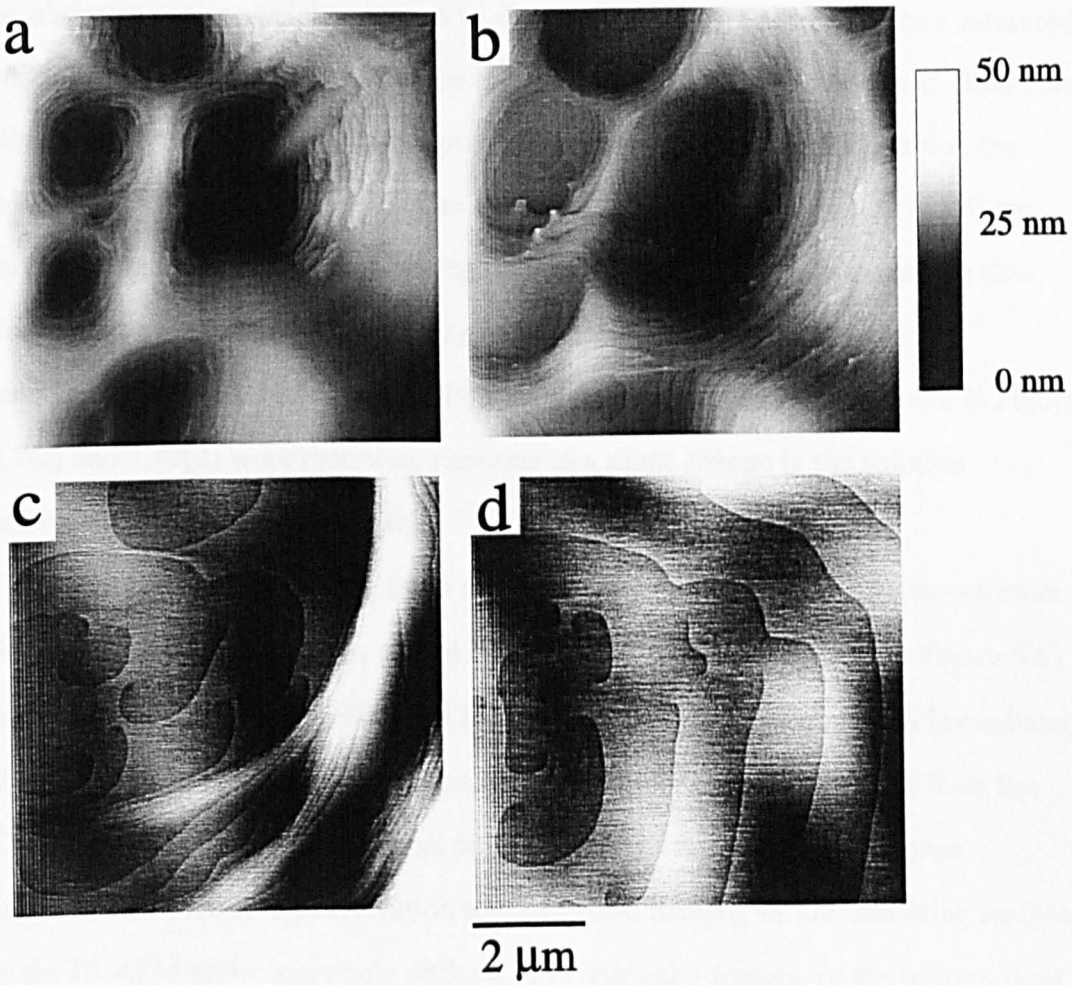

Figure 6.10. Height mode AFM images of the same area of the KBr (100) face as in Figure 6.7: (a) immediately after the application of a 1 s potential pulse (+0.5 V to +1.5 V) to the electrochemically-active AFM probe; (b) *ca.* 180 s later; (c) *ca.* 240 s later and (d) *ca.* 300 s later.

be observed as the crystal continues to dissolve, returning the solution to a saturated state. The final morphology is similar to that depicted in Figure 6.9(c) and differs only slightly from the original surface topography, shown in Figure 6.7(a), in that the width of the steps has increased. The measured width, in the range 950 -1250 nm, indicates that the slowly unwinding spiral is dissolving at an even slower rate than that shown in Figure 6.7(a). This may be due to very small variations in the temperature of the solution during the period over which the images shown in Figure 6.7(a) and 6.10(d) were recorded, resulting in a slight change in the solution saturation in the vicinity of the tip.

To increase the driving force exerted on the dissolution process even further, the potential of the probe was pulsed from +0.5 V to +1.7 V (point E in Figure 6.6) for 1 s and back to +0.5 V. Figure 6.11(a) shows the surface topography immediately after application of the potential pulse. The quantity of material removed from the KBr surface during the 1 s potential pulse has caused the surface to roughen considerably, making high resolution topographical imaging of the dissolving surface by the IE-AFM probe extremely difficult. The triangular feature, to the bottom right of Figure 6.11(a) is most probably an artefact of the imaging procedure, a common observation on very uneven surfaces, where lateral motion of the tip is impeded by prominent topographical surface features.[305]

Figure 6.11(b) shows the surface 120 s after application of the potential pulse to the IE-AFM probe. Continued dissolution has revealed high resolution features on the KBr surface. The centre of seven dislocations are displayed in Figure 6.11(b). These differ slightly in position from those in Figures 6.7 - 6.10 but given the substantial change in the surface topography, due to extensive dissolution, drift of the imaging position of the IE-AFM probe is not surprising. The nature of the exposed dislocations are different from those observed in Figures 6.7 - 6.10. In Figure 6.11(b) the screw dislocations can be seen to spiral down to hollow cores (cylindrical holes at

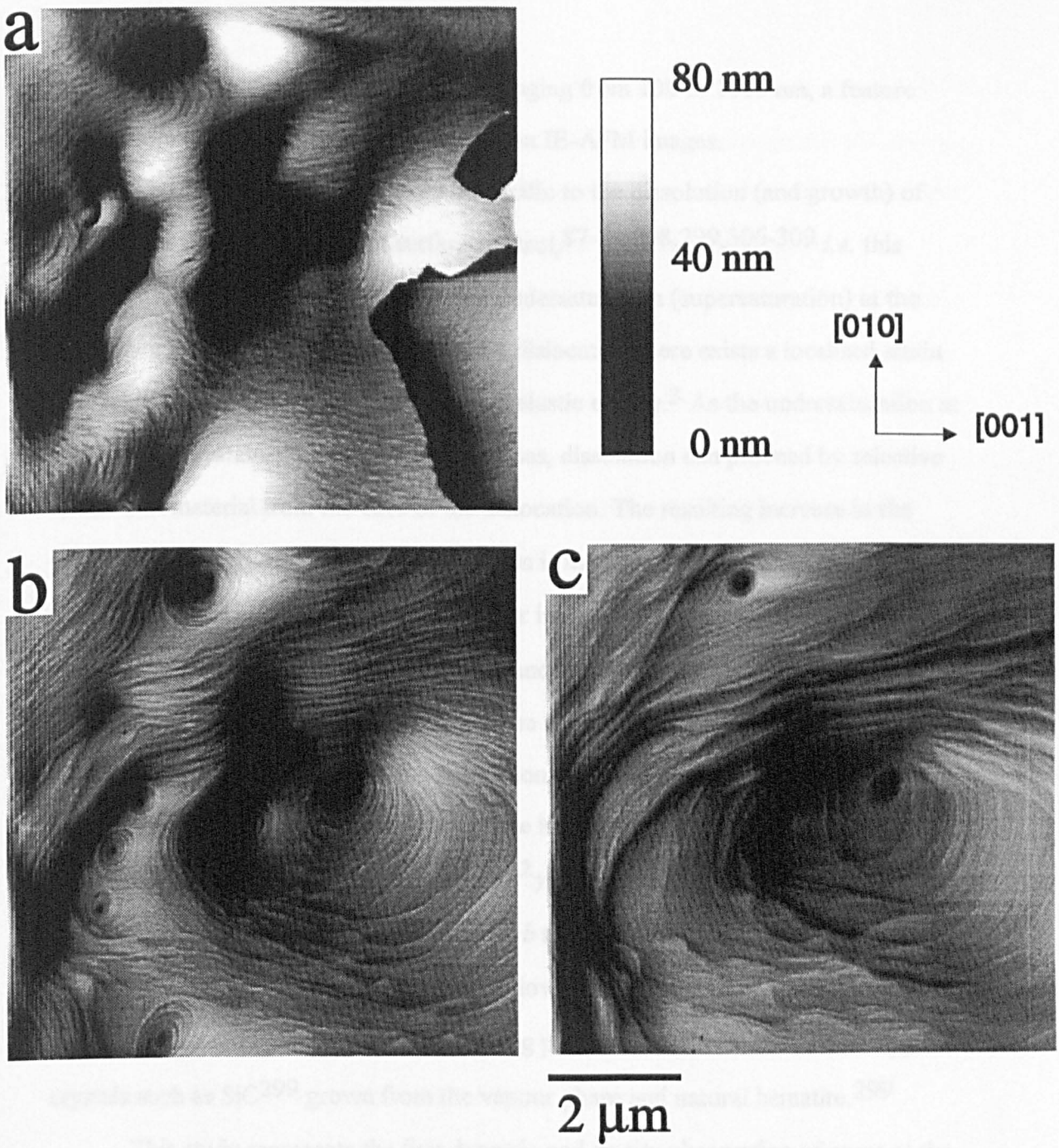

Figure 6.11. Height mode AFM images of the same area of the KBr (100) face as in Figure 6.7: (a) immediately after the application of a 1 s potential pulse (+0.5 V to +1.7 V) to the electrochemically active AFM probe; (b) *ca.* 120 s later and (c) *ca.* 240 s later.

the centre of each dislocation), with radii ranging from 100 to 1000 nm, a feature absent from all the previous screw dislocation IE-AFM images.

The presence of hollow cores is specific to the dissolution (and growth) of dislocations under conditions of surface control,[87-89,298,299,306-309] *i.e.* this feature is indicative of the existence of an undersaturation (supersaturation) at the solution/crystal interface. At the origin of a dislocation there exists a localised strain field which represents a region of excessive elastic energy.[3] As the undersaturation at a dislocated crystal/solution interface increases, dissolution can proceed by selective removal of material from the core of the dislocation. The resulting increase in the surface energy at the centre of the dislocation is more than compensated for by the removal of the existing strain energy. Further increase in the undersaturation leads to an increase in the radius of the hollow core and the eventual formation of etch pits.

The formation of a hollow core, at the centre of a dislocation, was first postulated by Frank[306] in 1951 for dislocations with a Burgers vector in excess of a critical value of 10 Å, where the radius of the hollow core, r_{hc}, was proposed as:

$$r_{hc} = \mu b^2 / 8\pi^2 \gamma \qquad (6.12)$$

In equation (6.12) μ is the rigidity modulus, b the magnitude of the Burgers vector and γ is the specific surface free energy. Hollow cores at the centre of dissolution spirals have since been observed *ex-situ* using positive phase contrast microscopy on crystals such as SiC[299] grown from the vapour phase and natural hematite.[299]

This study represents the first dynamic and *in-situ* observation of cores at the centre of revealed screw dislocations, characterised by low Burgers vectors (b = 6.6 Å), as shown by Figure 6.11(b). Although this observation is in disagreement with the prediction made by Frank, it should be noted that the theoretical treatment[306] (i) neglects the effect of the core energy associated with the centre of the dislocation and (ii) assumes that the elastic energy varies linearly with distance once outside the centre of the screw dislocation. Given that the core energy has now been recognised

to be an important factor in the dissolution behaviour of metals and ionic crystals[310-312] and depending on the nature of the material linear elastic behaviour is not always applicable,[313] for a complete theoretical treatment of the occurrence of hollow cores on the (100) face of KBr, it is necessary to account fully for both factors.

The existence of hollow cores at the centres of the dislocation spirals on the (100) face of KBr indicates the presence of an undersaturation at the interface and as expected under diffusion-controlled dissolution conditions, shown in Figures 6.7 - 6.9, these features were never observed. This suggests that upon stepping the potential to produce Br_2 at a maximum rate, the additional removal of Br^- in the probe/substrate gap by reaction with the produced Br_2 does act to promote surface-controlled dissolution.

Figure 6.11(c) shows the surface 240 s after the initial application of the 1 s potential pulse to the tip. As the surface continues to dissolve, as the solution returns to saturation and the interfacial undersaturation decreases, all cores become unstable and decrease in size. Those that have closed completely are likely to be the least highly strained in the 7 x 7 μm^2 area probed by the IE-AFM tip. The two which are featured in Figure 6.11(c), in the upper left corner and in the middle have decreased in diameter from 1060 nm ± 50 nm to 530 nm ± 50 nm and 860 nm ± 50 nm to 590 nm ± 50 nm. Over a period of thirty minutes this slow dissolution process continued with the smaller hole eventually disappearing.

6.5 Conclusions

The development of the IE-AFM probe has allowed the surface processes which accompany dissolution from the (100) face of a single crystal of KBr to be monitored in real time, under defined conditions identified from SECM kinetic measurements. Importantly, it has been established for the first time that, in the case of the (100) face of KBr in acetonitrile solution, a diffusion-controlled dissolution

process occurs via a spiral mechanism. Many of the surface dynamics observed during dissolution by this novel experimental approach are consistent with classical dissolution models. When the process is driven to surface-controlled dissolution, by removing Br^- in the probe substrate gap by electrochemical oxidation to Br_2, the appearance of hollow cores at the centre of the dissolving spiral dislocations becomes evident.

More generally, the AFM approach described opens up a new method of inducing and monitoring reactions at electrically insulating surfaces. For dissolution reactions, in particular, electrochemical control of the interfacial conditions and extent of reaction diversifies the range of surface activities that are accessible to study by AFM.

CHAPTER 7

INDUCED DISSOLUTION IN DISLOCATION-FREE REGIONS OF AN IONIC CRYSTAL SURFACE

The SECM has been used to induce and monitor dissolution from the (100) face of copper sulfate pentahydrate single crystals in regions of the surface where the average dislocation spacing is much greater than the size of the UME probe. The chronoamperometric characteristics for the reduction of Cu^{2+} at the probe electrode, positioned close to the crystal surface, indicate that the crystal is initially highly reactive towards dissolution. However, after a short period of time (*ca.* 0.1 - 0.3 s) the dissolution rate rapidly decreases until the solution adjacent to the crystal surface becomes sufficiently undersaturated to induce the dissolution process again. This is found to occur at a critical concentration ratio, c/c^* of 1.25 x 10^{-6}, where c is the concentration of Cu^{2+} and c^* is the concentration in the saturated solution. Thereafter, dissolution proceeds via a unique oscillatory process in which dissolution occurs in "bursts", each burst corresponding to the release of *ca.* 12.5 x 10^{-9} mol cm^{-2} of Cu^{2+} from the crystal. A simple theoretical model in which, in the absence of dislocations and steps, dissolution sites on the crystal surface are formed only when the interfacial saturation ratio is below the critical value is shown to account for the observed behaviour, and to successfully predict the period of the oscillations.

7.1 Introduction

A question of fundamental importance in understanding the dissolution of ionic crystals at the microscopic level is: what is the role of dislocations in controlling the rate and mechanism of dissolution? [3,5,11,22,53,314,315] It is

well-established that dissolution is usually initiated preferentially at sites on the crystal surface where dislocations emerge,[3] as demonstrated in Chapter 6 where IE-AFM images depicted the unwinding of steps at screw dislocations as the preferential pathway for dissolution from the (100) face of KBr. However, previous experimental dissolution studies,[11,22,53,314] have been unable to address quantitatively the comparative reactivities of dislocation vs. dislocation-free regions of a crystal surface, although theories for the nucleation of dissolution pits at these contrasting sites are available.[3]

The major shortcoming of the dissolution methodologies reviewed in this thesis is that the size of the probe used to monitor the dissolution process is too large to select spatially between dislocated and dislocation-free areas. Indeed most currently used techniques, as discussed in section 1.2.2, are only able to monitor the dissolution activity from the entire crystal face. Even with very high resolution scanned probe methods such as fluid-flow AFM (discussed in section 1.2.4.1), there have been no reports of the initiation of the dissolution process from dislocation-free areas. This is mostly like due to the inability of the technique to generate undersaturations at the crystal/solution interface which are large enough to drive the dissolution process via this mechanism.[3] In fact, as discussed in section 6.1, many of the reported AFM dissolution studies are for mass transfer-controlled processes only,[109-111] since low solution velocities have to be employed to ensure image stability.[105]

Through use of the high resolution and high mass transfer capabilities of the SECM, this chapter describes major advances in the understanding of dissolution mechanisms by providing the first direct experimental data for dissolution in an area free from dislocations. This is achieved through investigations of the dissolution activity in regions of an ionic crystal surface with a low density of dislocations.

The (100) face of copper sulfate pentahydrate single crystals, grown from aqueous solution, was chosen as a suitable substrate for the dissolution studies, as simple chemical etching treatments of the surface, described later in section 7.4.2, revealed that the dislocation density near the edges of the face was *ca.* 3×10^3 - 10^4 cm^{-2}, *i.e.* the mean dislocation spacing varied between 100 and 180 μm. By studying this region with a probe UME with a diameter of 25 μm, the probability of a dislocation emerging in the area probed by the SECM is low. This opens up the possibility of measuring the dissolution characteristics from an area effectively devoid of dislocations.

The value for the dislocation density at the edges of the (100) face of copper sulfate pentahydrate was significantly lower than in the centre of the face, where the dislocation density was estimated to be in excess of 1×10^8 cm^{-2}, *i.e.* the mean dislocation spacing was less than 1 μm. This spatial dependence on the dislocation density may be attributed to the nature of the growth process for solution grown ionic crystals.[314] Previous SECM induced dissolution studies, employing UMEs with a diameter of 25 μm, from the centre of the (100) face of copper sulfate pentahydrate in aqueous sulfuric acid solution,[219,220] determined a high and uniform dissolution reactivity in this area of the surface. This behaviour was expected for a heavily dislocated surface (see also section 4.5.2) where the average dislocation spacing was much smaller than the size of the probe and consequently material was supplied to the probe at a uniform rate, under the experimental conditions of low interfacial undersaturation.

7.2 Theory

In the light of the experimental results which follow, a simple model for the probe UME current-time response for dissolution induced by SECM in an area of the crystal which is devoid of dislocations, is developed. Experimental

conditions are set so that sulfuric acid is present at a sufficiently high concentration to buffer the sulfate ion concentration during a measurement, thus reducing the SECM problem to the consideration of Cu^{2+} only.

The UME response is calculated by solving the dimensionless axisymmetric cylindrical SECM diffusion equation subject to the appropriate boundary conditions as outlined by equations (2.2) to (2.6). For the present problem, the boundary condition at the crystal/solution interface is initially given by equation (2.74) up to $\tau = \tau_{in}$, *i.e.* the crystal is assumed to be dissolution active. The rationale for this is that although dissolution in an area of the crystal devoid of dislocations is being considered, for crystals grown from solution, in particular, the exposed faces are likely to contain a high density of growth steps within an area typically probed by the SECM, which will provide a source of dissolution sites. Indeed, macroscopic steps were observed on the $CuSO_4.5H_2O$ (100) face, when the surface was viewed with DIC light microscopy.

For simplicity, this source is considered to be constant for an initial period, since steps moving out of the tip/crystal domain, through SECM induced dissolution, may be replaced by steps moving into the tip/crystal domain, as illustrated schematically in Figure 7.1(a). The dimensionless boundary condition at the crystal/solution for this period, $0 < \tau < \tau_{in}$, can be written as follows:

$$Z = L,\ 0 < R \leq RG: \qquad \frac{\partial C}{\partial Z} = -K\left[1 - C^{1/2}\right]\theta \qquad (7.1)$$

$$0 < \tau \leq \tau_{in}: \qquad \theta = 1 \qquad (7.2)$$

where θ denotes the fraction of active dissolution sites, which is assigned a value of unity for an initially reactive surface. The normalised rate constant for dissolution is given by equation (2.75).

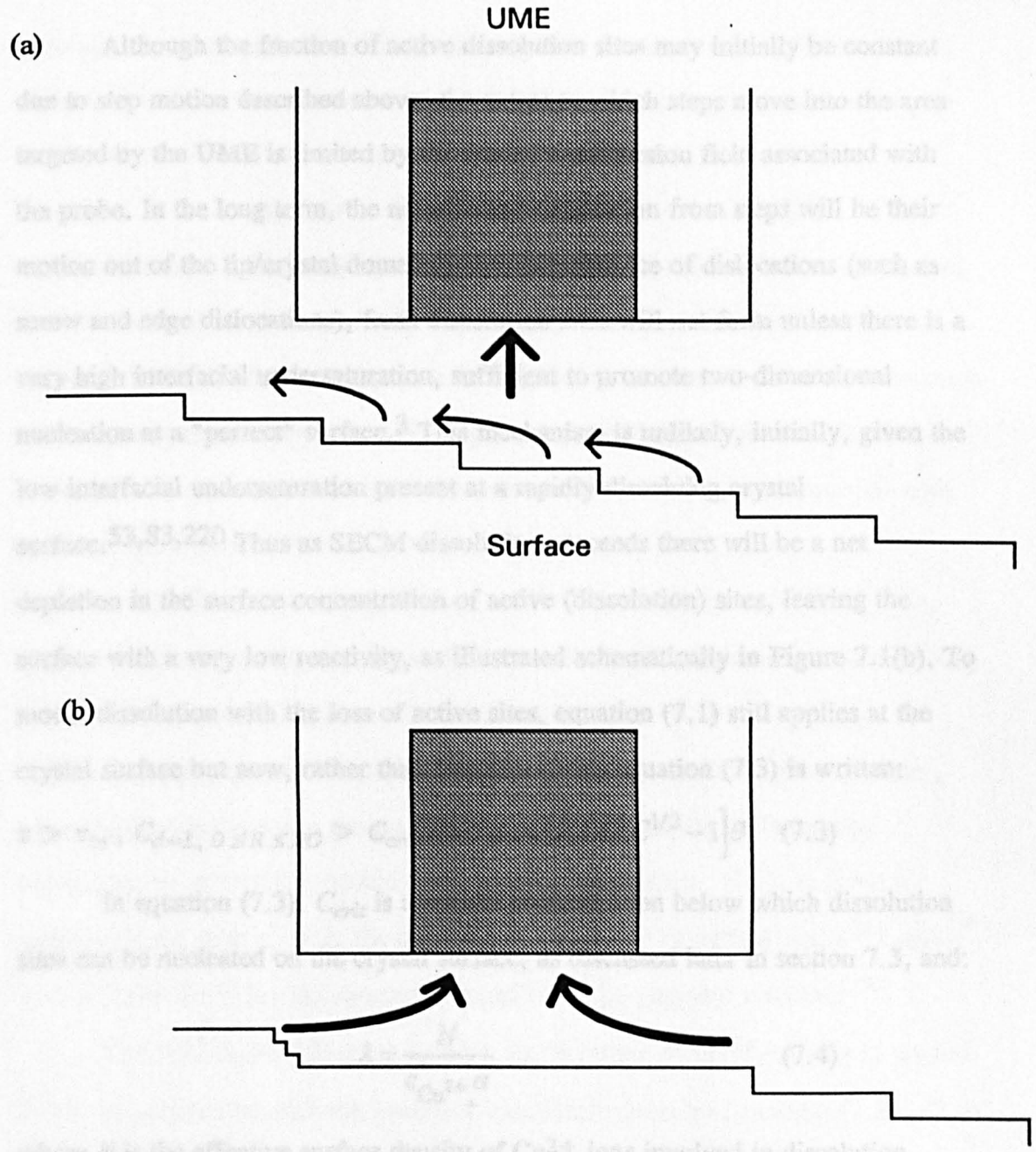

Figure 7.1. Schematic illustration of SECM induced dissolution. Initially steps provide a source of sites for dissolution which is detected at the UME (a). As dissolution proceeds, steps move out of the probe/crystal domain and the activity of the surface decreases. In this case (b) mass transfer tends towards that for an inert surface (hindered diffusion).[122] Note that this diagram is not to scale. The height of, and separation between, the steps has been significantly exaggerated: the surface is effectively flat on the scale of the probe/crystal geometry which, in this study is typically characterised by a probe/crystal separation of 1 μm, an UME diameter of 25 μm and an overall probe diameter of 250 μm.

Although the fraction of active dissolution sites may initially be constant due to step motion described above, the extent to which steps move into the area targeted by the UME is limited by the size of the diffusion field associated with the probe. In the long term, the net effect of dissolution from steps will be their motion out of the tip/crystal domain and, in the absence of dislocations (such as screw and edge dislocations), fresh dissolution sites will not form unless there is a very high interfacial undersaturation, sufficient to promote two-dimensional nucleation at a "perfect" surface.[3] This mechanism is unlikely, initially, given the low interfacial undersaturation present at a rapidly dissolving crystal surface.[53,83,220] Thus as SECM dissolution proceeds there will be a net depletion in the surface concentration of active (dissolution) sites, leaving the surface with a very low reactivity, as illustrated schematically in Figure 7.1(b). To model dissolution with the loss of active sites, equation (7.1) still applies at the crystal surface but now, rather than equation (7.2), equation (7.3) is written:

$$\tau > \tau_{in},\ C_{d=L,\ 0 \le R \le RG} > C_{crit}:\ d\theta/d\tau = (K/\lambda)\left[C^{1/2} - 1\right]\theta \qquad (7.3)$$

In equation (7.3), C_{crit} is a critical concentration below which dissolution sites can be nucleated on the crystal surface, as discussed later in section 7.3, and:

$$\lambda = \frac{N}{c^{*}_{Cu^{2+}}\, a} \qquad (7.4)$$

where N is the effective surface density of Cu^{2+} ions involved in dissolution during this period. Note that the value of N may be much greater than the density of Cu^{2+} ions in an atomically flat (100) surface, for reasons discussed in section 7.5.

The dependence of equation (7.3) on conditions for both *time* and the *interfacial concentration* reflects the fact that as the area of the crystal probed by the SECM becomes less reactive, due to the loss of steps, mass transfer in the

tip/crystal domain tends towards that for negative feedback with an inert surface.[122] Under these conditions, electrolysis serves to rapidly deplete the gap of electroactive material and the interfacial undersaturation, defined as:

$$\sigma_{Z=L} = 1 - C_{Z=L}^{1/2} \qquad (7.5)$$

rapidly increases. If the undersaturation reaches a value sufficient for spontaneous two-dimensional nucleation of dissolution sites,[3] the fraction of active sites will increase. To model this simply, the entire surface is allowed to become active once the undersaturation at any point on the surface exceeds a critical value for two-dimensional nucleation. Thus the following condition applies in conjunction with equations (7.1) and (7.3):

$$C_{d=L,\ 0 \le R \le RG} < C_{crit}: \quad \theta = 1 \qquad (7.6)$$

The justification for using equation (7.6) to model the increase in surface reactivity is discussed in section 7.3.

The quantity to be determined from the calculations is the UME current, normalised with respect to the steady-state current at infinite probe/crystal separation, as defined by equation (2.14). The denominator, $i(\infty)$, is given by equation (1.4), with $n_e = 2$, for the reduction of Cu^{2+} in sulfate media[316] and c^* = 0.125 mol dm^{-3} for the concentration of Cu^{2+} in saturated solution.[220]

The ADI finite-difference method, as discussed comprehensively in section 2.2.2, in conjunction with the boundary conditions given by equations (7.1) - (7.3) and (7.6), was adopted for the solution of this SECM problem.

7.3 Theoretical Results and Discussion

The dimensionless current-time response depends on a number of parameters: K, C_{crit}, λ, τ_{in}, L and RG. Rather than providing a systematic description of the effect of each of these parameters on the UME response, parameter values relevant to the experiments reported in section 7.5 are

considered. All theoretical results therefore relate to a probe/crystal geometry characterised by $RG = 10$ and $\log L = -1.10$ (for high sensitivity of the current response to the interfacial process[220]). Based on previous studies[220] of dissolution from the (100) face of $CuSO_4.5H_2O$, $K = 4$ and τ_{in} is fixed at 0.5, which is a sufficiently long period to ensure that the dissolution process effectively attains a steady-state during the initial part of the reaction.[220]

Typical current-time behaviour calculated for $C_{crit} = 1 \times 10^{-6}$ and $\lambda = 0.08$ (*i.e.* $c^{*}_{Cu^{2+}} = 0.125$ mol dm^{-3} [220] and $a = 12.5$ μm - values dictated by the experiments reported in section 7.5 - and $N = 12.5 \times 10^{-9}$ mol cm^{-2}) is shown in Figure 7.2. It can be seen that the current very quickly attains a steady-state value, which prevails up to $\tau = \tau_{in}$, but that at slightly longer times the current rapidly decreases and then oscillates with a regular periodicity. The initial decrease (for $\tau > \tau_{in}$) is a direct consequence of the loss of dissolution sites, described by equation (7.3). The effect of this boundary condition on the activity of the crystal surface can clearly be seen in Figure 7.3, which shows the dependence of θ on R for selected τ values in the period from τ_{in} to just before the first current surge, *i.e.* $0.51 \leq \tau \leq 0.61$. For the copper sulfate pentahydrate system, under the conditions of interest, this corresponds to a real time period (equation (2.8)) of only 34 ms (given $D = 4.58 \times 10^{-6}$ cm^2 s^{-1}).[220] It can be seen that in this very short period of time there is a rapid decrease in θ, particularly in the area of the crystal surface directly under the electrode ($0 \leq R \leq 1$) where the dissolution rate is initially most rapid. Further out in the radial direction, θ rises quickly and attains a limiting value of unity, for all times considered.

The corresponding change in the concentration profiles at the crystal/solution interface for the same period is shown in Figure 7.4. Qualitatively, the profiles are similar to those for θ, *i.e.* the probe UME has the greatest

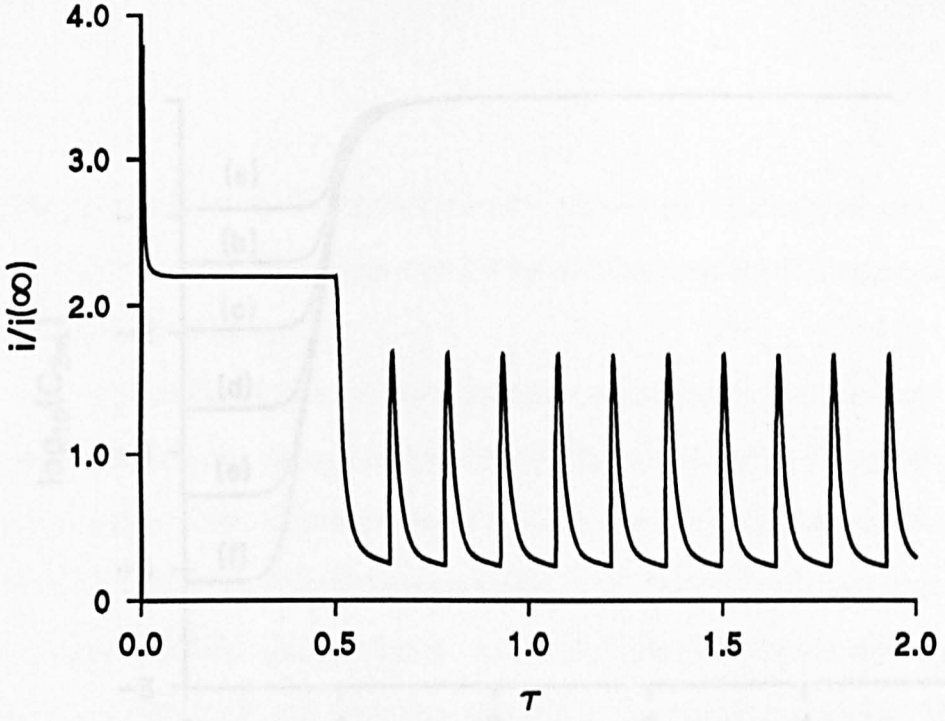

Figure 7.2. Normalised current-time characteristics calculated for C_{crit} = 1 x 10^{-6}, $\lambda = 0.08$, and $\tau_{in} = 0.5$. The remaining parameters used in the simulation are defined in the text.

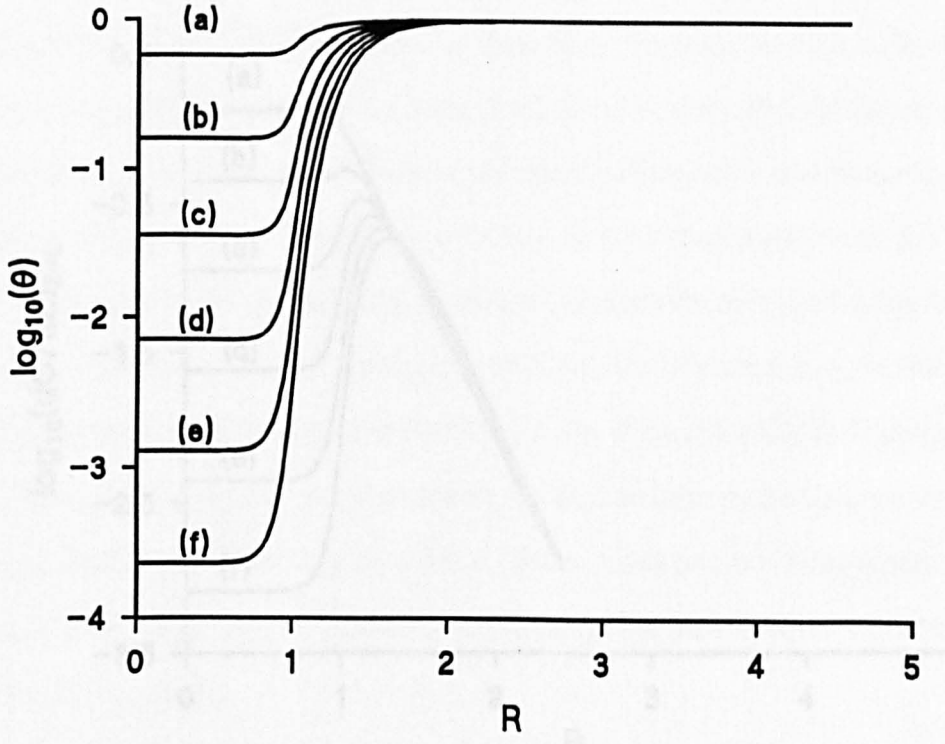

Figure 7.3. Profiles of log θ vs. R, for the current-time characteristics in Figure 7.2, at normalised times, τ, of (a) 0.51, (b) 0.53, (c) 0.55, (d) 0.57, (e) 0.59 and (f) 0.61.

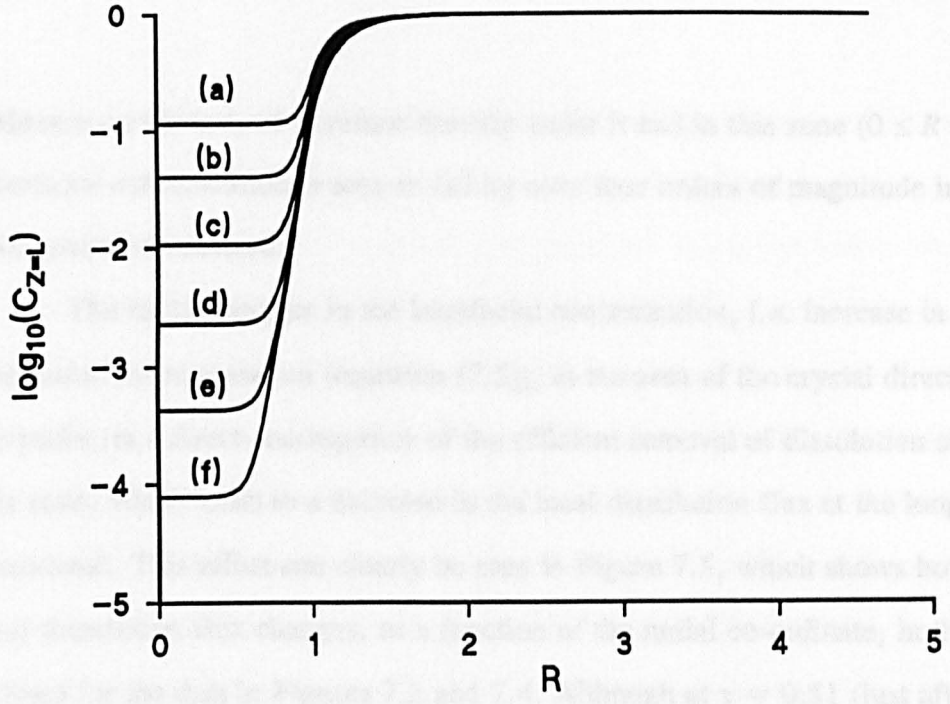

Figure 7.4. Profiles of log $C_{Z=L}$ vs. R, for the current-time characteristics in Figure 7.2, at τ = (a) 0.51, (b) 0.53, (c) 0.55, (d) 0.57, (e) 0.59 and (f) 0.61.

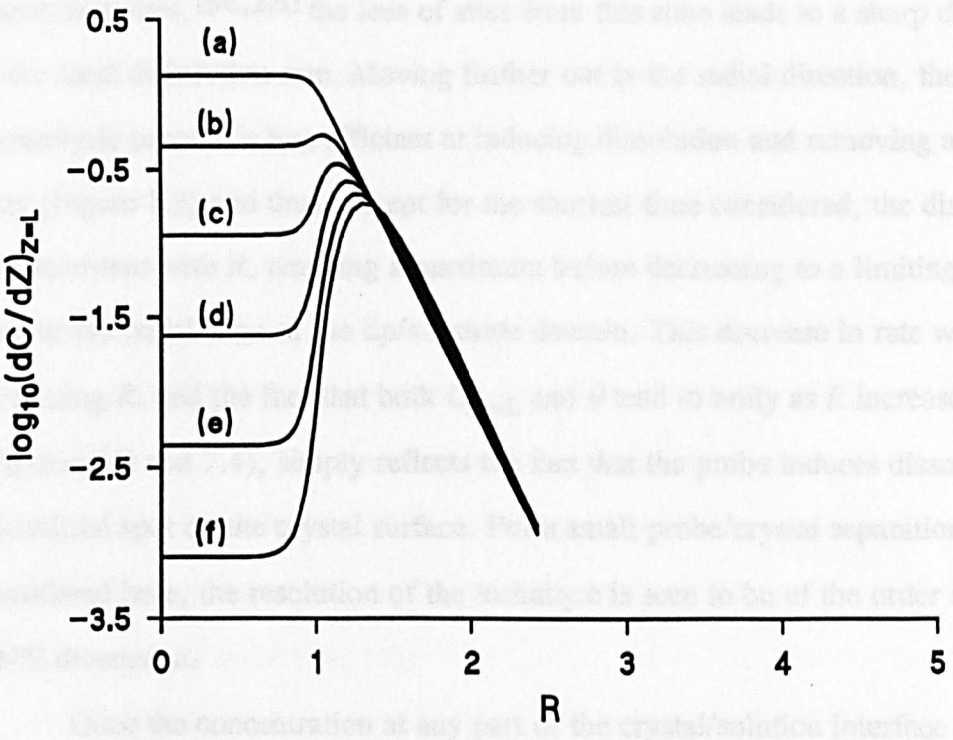

Figure 7.5. Profiles of local interfacial dissolution flux as a function of R, for the current-time characteristics in Figure 7.2, at τ = (a) 0.51, (b) 0.53, (c) 0.55, (d) 0.57, (e) 0.59 and (f) 0.61.

influence on the area of interface directly under it and in this zone ($0 \leq R \leq 1$), the interfacial concentration is seen to fall by over four orders of magnitude in the brief period considered.

The rapid decrease in the interfacial concentration, *i.e.* increase in the interfacial undersaturation (equation (7.5)), in the area of the crystal directly under the probe, is a direct consequence of the efficient removal of dissolution sites from this zone, which leads to a decrease in the local dissolution flux at the longer times considered. This effect can clearly be seen in Figure 7.5, which shows how the local dissolution flux changes, as a function of the radial co-ordinate, in the period defined for the data in Figures 7.3 and 7.4. Although at $\tau = 0.51$ (just after τ_{in}) the local dissolution rate (flux) is greatest in the area of the interface directly under the electrode ($0 \leq R \leq 1$), as found for dissolution with a constant density of dissolution sites,[198,220] the loss of sites from this zone leads to a sharp decrease in the local dissolution rate. Moving further out in the radial direction, the UME electrolysis process is less efficient at inducing dissolution and removing active sites (Figure 7.3) and thus, except for the shortest time considered, the dissolution rate increases with R, reaching a maximum before decreasing to a limiting value of zero at the radial edge of the tip/substrate domain. This decrease in rate with increasing R, and the fact that both $C_{Z=L}$ and θ tend to unity as R increases (Figures 7.3 and 7.4), simply reflects the fact that the probe induces dissolution in a localised spot on the crystal surface. For a small probe/crystal separation, as considered here, the resolution of the technique is seen to be of the order of the UME dimension.

Once the concentration at any part of the crystal/solution interface falls below the value required for the spontaneous nucleation of fresh dissolution sites, C_{crit}, (*i.e.* the interfacial undersaturation exceeds the critical value), the simple model outlined above assumes that the entire surface becomes active with the same

density of dissolution sites (equation (7.6)), and not just the part of the interface where the concentration reaches the critical value. The profiles of θ, $C_{Z=L}$ and interfacial flux in Figures 7.3 to 7.5, calculated for a time just before the critical undersaturation is reached ($\tau = 0.61$) suggest that this is a reasonable approximation. In particular, Figure 7.4 demonstrates that, once attained, the critical interfacial undersaturation will prevail over a reasonably long distance in the radial direction, *ca.* $0 \leq R \leq 0.5$. In this zone, θ is very small at the time of interest (Figure 7.3), but switches sharply to unity as R increases. This sharp transition, coupled with the dominant sensitivity of the UME to the area of the crystal directly under it (Figure 7.5) and the fact that sites formed in this particular zone will rapidly move out in the radial direction as dissolution proceeds, suggests that the use of equation (7.6) as a simple way to describe the nucleation of new sites is reasonable.

When the critical undersaturation is reached, the combination of equation (7.6) with the very high undersaturation prevailing at the crystal/solution interface leads to a tremendous increase in the dissolution rate, which subsequently decreases as sites for dissolution on the crystal surface are depleted, as discussed in section 7.2 (equation 7.3). This behaviour is transduced into a sudden current burst at the UME, followed by a period in which the current falls, until the interfacial undersaturation again exceeds the critical value, when the current surges again. Figure 7.2 indicates that this behaviour leads to a periodic oscillation in the UME current, corresponding to bursts in dissolution activity at the crystal/solution interface directly under the probe.

The period of the current oscillations resulting from SECM induced dissolution will clearly depend very strongly on the value of the critical saturation ratio (or undersaturation) required for the spontaneous nucleation of dissolution sites on the crystal. It follows, from the discussion above, that the lower the

interfacial undersaturation (*i.e.* the larger the interfacial concentration) needed to induce the nucleation of dissolution sites, the shorter will be the period between current surges. This predicted behaviour is born out in Figures 7.6(a), (b) and (c) which show the normalised current-time behaviour for C_{crit} values of 1×10^{-8}, 1×10^{-4} and 1×10^{-3}, respectively, with $\lambda = 0.08$. Comparison of the results in Figure 7.6 with those in Figure 7.2 suggest that the period of the oscillations could be used diagnostically to determine C_{crit}, if N is known.

In conjunction with Figure 7.2, Figures 7.7(a), (b), (c) and (d) show the effect of λ on the normalised current-time behaviour. The data in Figures 7.7(a) - (d) were generated using $C_{crit} = 1 \times 10^{-6}$, together with $\lambda = 0.1$, 0.05, 0.025 and 0.0125, respectively. It is clear that the value of λ has a significant effect on both the period of the oscillations and the normalised charge passed during each current surge. In particular, the lower the value of λ, the shorter is the period between oscillations and the smaller is the area under each current spike. This is expected given that λ is a measure of the ratio of the density of dissolution sites on the surface and the concentration of Cu^{2+} in solution (equation (7.4)).

As shown clearly in Figures 7.6 and 7.7, the period of the current oscillations is controlled by both C_{crit} and λ. However for a small change (*e.g.* 10 %) in the values of C_{crit} and λ (for constant values of K), the amount of normalised charge passed during the current surges depends much more strongly on λ than C_{crit}. Indeed, calculations carried out demonstrate that for $C_{crit} < 1 \times 10^{-4}$ there is only a small increase in the amount of charge passed during each current spike as C_{crit} decreases (for constant λ). The implications of these theoretical observations for experimental studies are that from experimental current-time behaviour, the amount of charge passed during a current spike can be used as a guide to λ (*i.e.* N), and C_{crit} can be deduced directly from the period of the current oscillations.

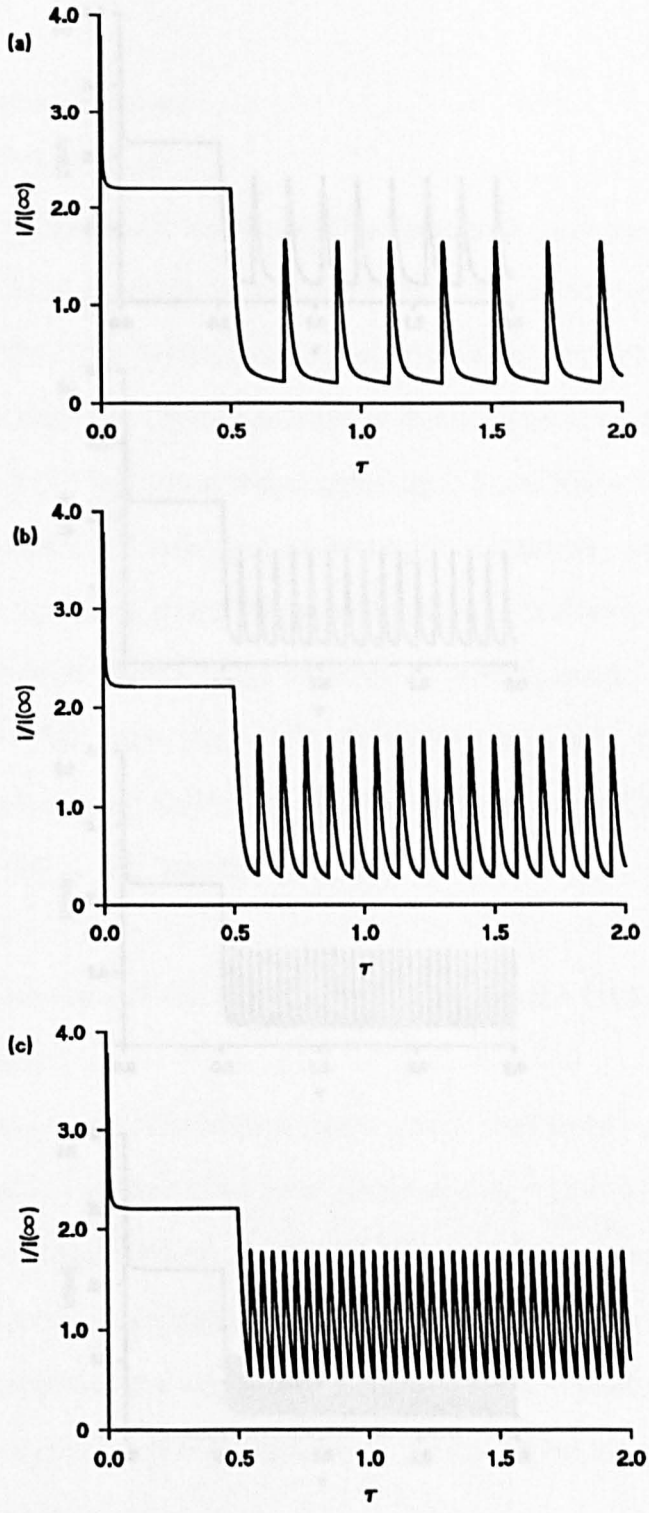

Figure 7.6. Normalised current-time characteristics calculated for $\lambda = 0.08$ and C_{crit} values of (a) 1×10^{-8} (b) 1×10^{-4} and (c) 1×10^{-3}. The remaining parameters used in the simulations are defined in the text.

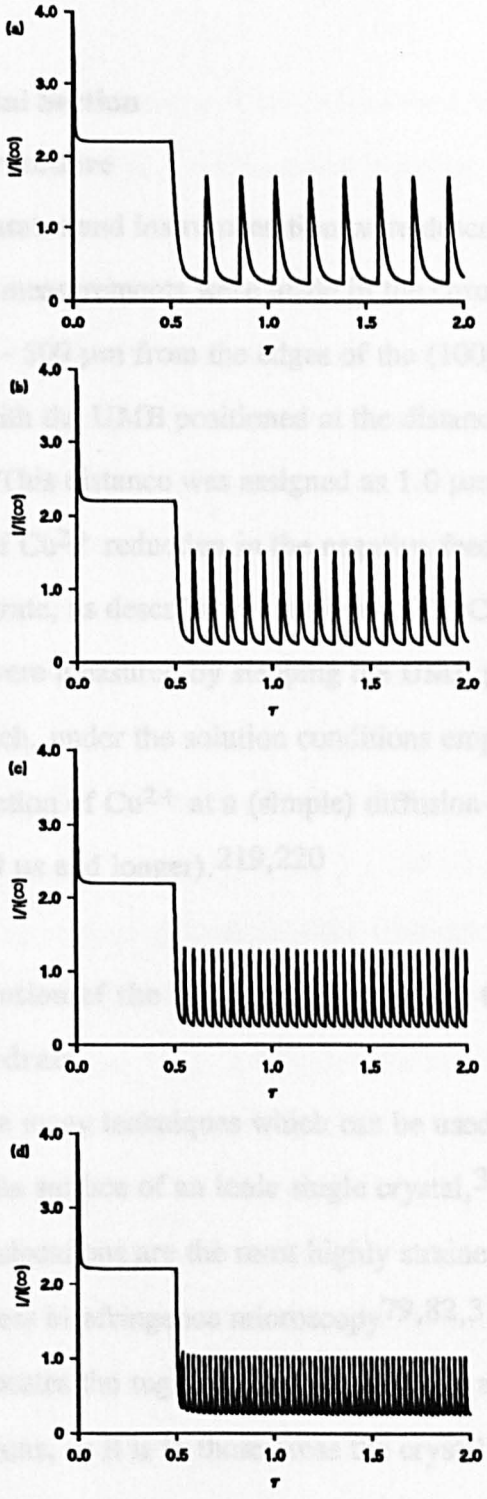

Figure 7.7. Normalised current-time characteristics calculated for C_{crit} = 1 x 10^{-6} and λ values of (a) 0.1 (b) 0.05 (c) 0.025 and (d) 0.0125. The remaining parameters used in the simulations are defined in the text.

7.4 Experimental Section

7.4.1 SECM Procedure

The apparatus and instrumentation were described previously in section 3.2. All SECM measurements were made in the chronoamperometric mode in regions *ca.* 300 - 500 μm from the edges of the (100) face of copper sulfate pentahydrate, with the UME positioned at the distance of closest approach to the crystal surface. This distance was assigned as 1.0 μm following calibration SECM measurements of Cu^{2+} reduction in the negative feedback mode with an inert glass disc as the substrate, as described in section 4.5.1. Chronoamperometric characteristics were measured by stepping the UME potential from -0.2 to -0.7 V vs. AgQRE which, under the solution conditions employed, has been shown to lead to the reduction of Cu^{2+} at a (simple) diffusion-controlled rate (on a timescale of 200 μs and longer).[219,220]

7.4.2 Determination of the dislocation density on the (100) face of copper sulfate pentahydrate

There are many techniques which can be used to reveal the sites of dislocations at the surface of an ionic single crystal,[3] most of which operate on the principle that dislocations are the most highly strained features on a crystal face. For example stress birefringence microscopy[79,82,314,317] (as discussed in section 1.2.3) locates the region of excess strain on a crystal surface and hence the sites of dislocations, as it is in these areas the crystal behaves anistropically and becomes double refracting.

In the case of the (100) face of copper sulfate pentahydrate, chemical etching[3] was employed due to its simplicity and effectiveness. The required crystal face of copper sulfate was placed into a stirred, slightly undersaturated copper sulfate solution for a few seconds. After immersion in the solution, the crystal face

was gently dried with lens tissue. Under these very low undersaturation conditions only the most active sites (*i.e.* dislocations) dissolve, resulting in the formation of etch holes or pits.

Figure 7.8(a) and (b) show DIC light micrographs of (a) the edge and (b) the centre of the (100) face of copper sulfate pentahydrate after a chemical etching treatment. The etched depressions on the crystal surface indicate the sites of dislocations, where dissolution has preferentially taken place. The pits are geometrically ill-defined, but this is likely to be due to the complex triclinic geometry of a unit cell of the copper sulfate pentahydrate crystal lattice[318] and the very low undersaturations present at the crystal/solution interface during the etching procedure.

The average dislocation density at the edges, (Figure 7.8(a)) as judged from the etch pit density, is typically *ca.* 3×10^3 - 10^4 cm^{-2}, *i.e.* the mean inter-dislocation spacing is much greater than the diameter of the UME, as discussed in section 7.1. In contrast in the centre of the face (Figure 7.8(b)) the etch pit density is in excess of 1×10^8 cm^{-2} and in this case the mean inter-dislocation spacing is now much less than the diameter of the UME.

7.5 Experimental Results and Discussion

Typical chronoamperometric characteristics for the reduction of Cu^{2+}, when the probe UME was positioned at a distance of 1.0 μm away from the copper sulfate pentahydrate (100) face, in a low dislocation region of the surface, are shown in Figures 7.9 and 7.10. Also shown are the best fits of the theoretical model, outlined in section 7.3, to the data (discussed below) and the theoretical behaviour predicted for an inert surface.[122,135,147,149] In these figures the UME current has been normalised with respect to the steady-state current obtained at effectively infinite tip/crystal separation, where $i(\infty) = 1.88$ μA. In

(a)

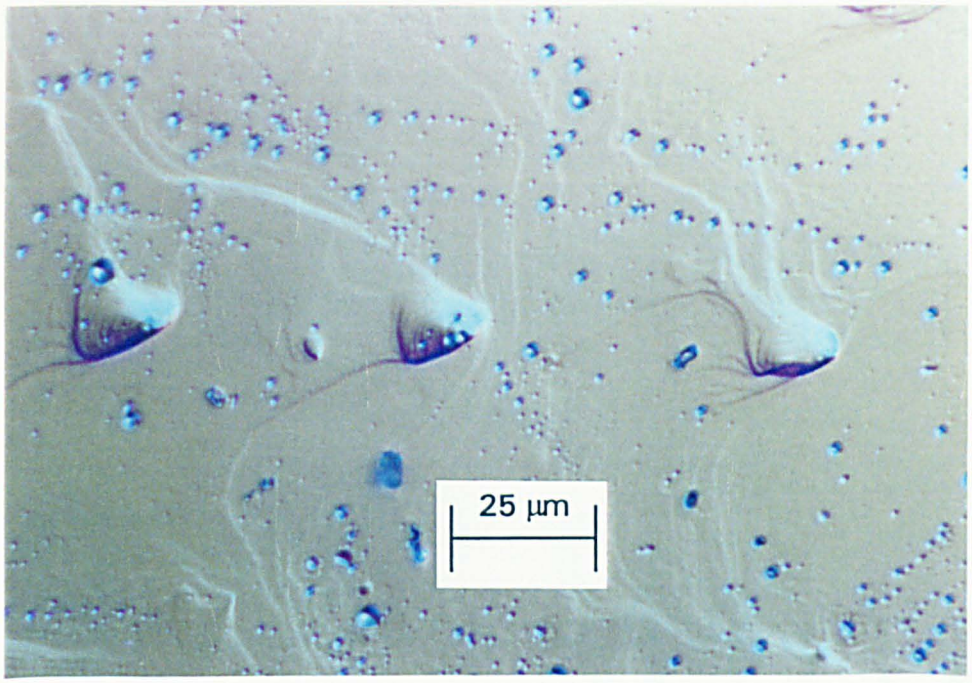

(b)

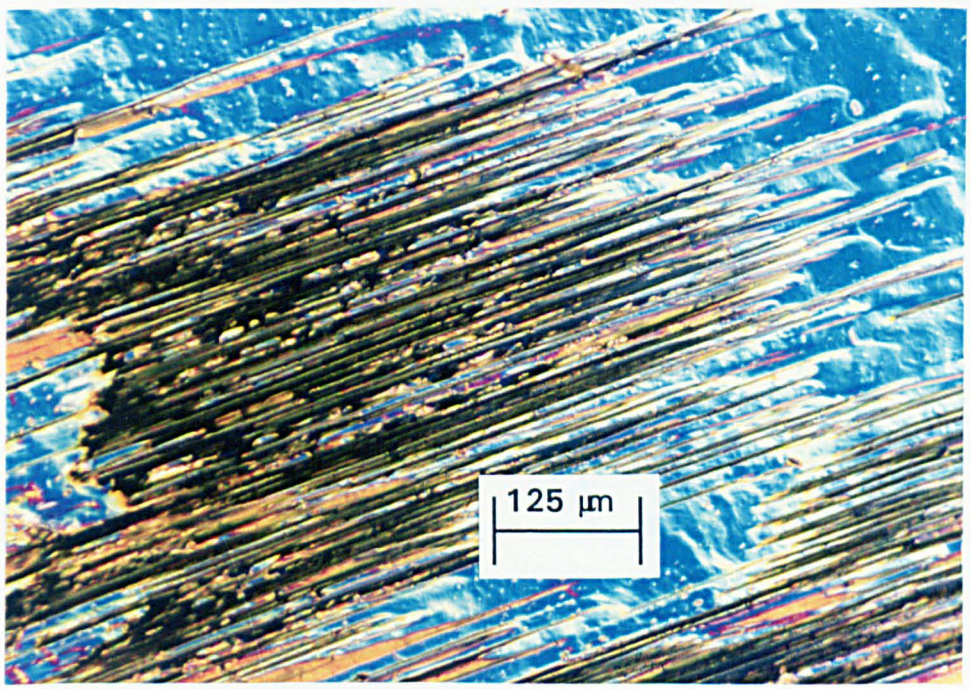

Figure 7.8. Nomarski DIC light photomicrographs of (a) the edge, magnification x 750 and (b) the centre, magnification x 150 of the (100) face of copper sulfate pentahydrate.

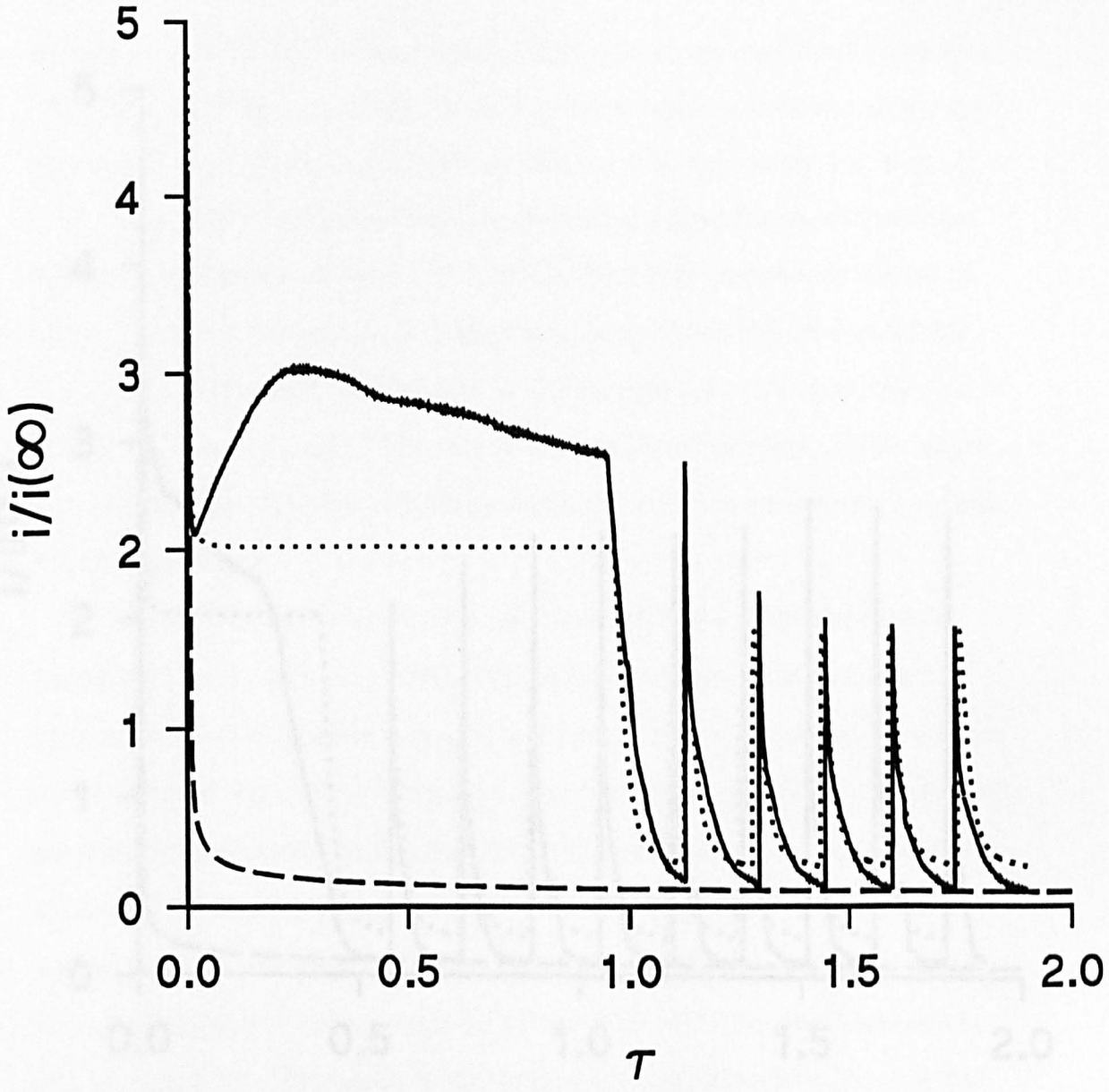

Figure 7.9. Experimental current-time characteristics (___) for the reduction of Cu^{2+} at a probe UME located 1.0 μm from the copper sulfate pentahydrate (100) face, in an area of the crystal with a low dislocation density. The experimental characteristics have been normalised using the steady-state current measured at an effectively infinite probe/crystal separation, $i(\infty)$ = 1.88 μA., The values of D and a are cited in the text. The best fit of the theoretical model (····) to the experimental data was calculated using the following parameters: τ_{in} = 0.967, K = 3.5, C_{crit} = 1.25 x 10^{-6} and N = 12.5 x 10^{-9} mol cm^{-2}. Values for the remaining parameters are dictated by the experimental conditions defined in the text. The theoretical behaviour predicted for an inert surface[220,135,147,149](----) is shown for comparison.

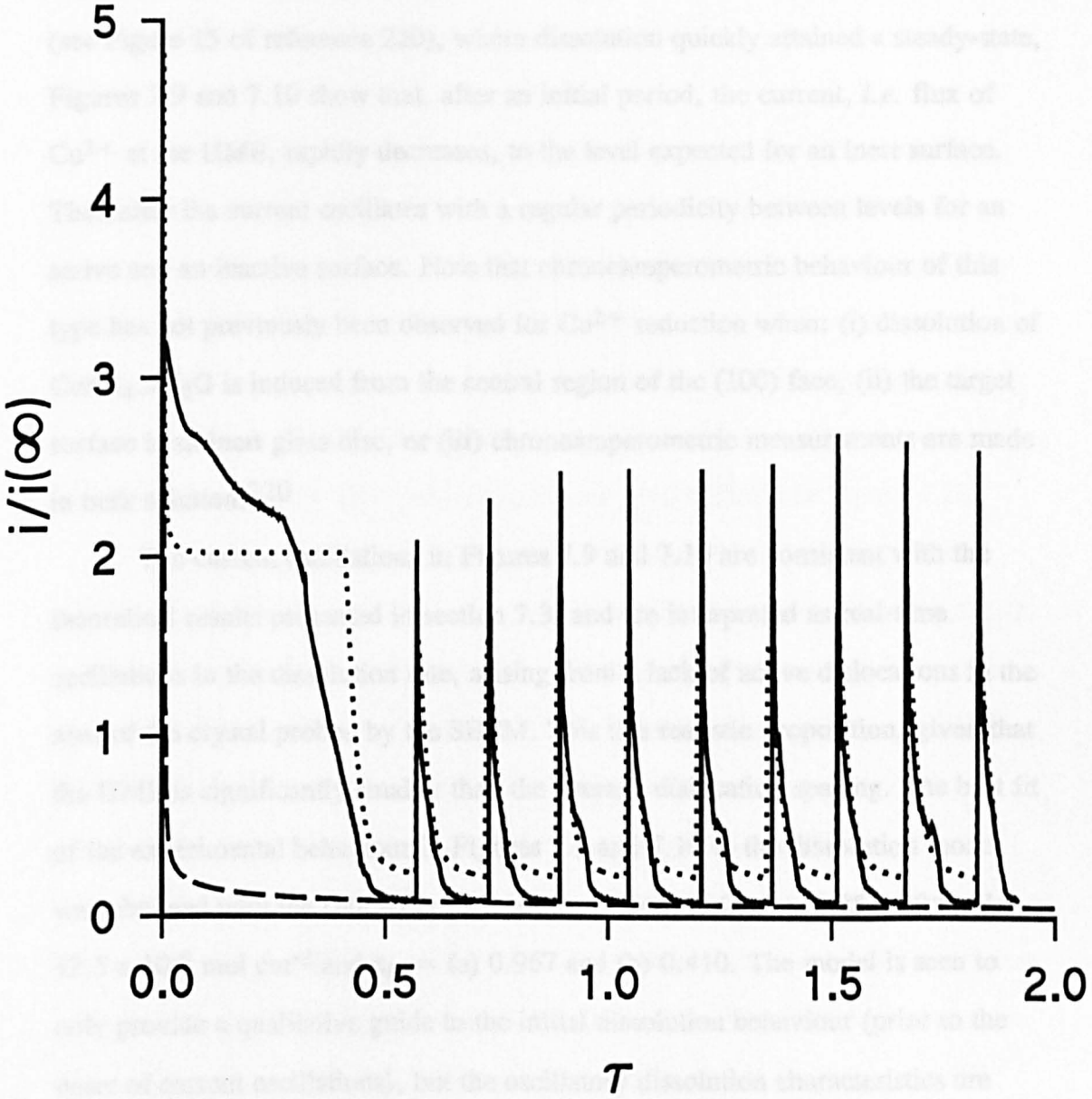

Figure 7.10. Experimental current-time characteristics (___) for the reduction of Cu^{2+} at a probe UME located 1.0 μm from the copper sulfate pentahydrate (100) face, in an area of the crystal with a low dislocation density. The experimental characteristics have been normalised as defined in the caption to Figure 7.9. The theoretical behaviour for SECM dissolution (····) was generated using τ_{in} = 0.410, with values for the remaining parameters as defined for Figure 7.9. The theoretical behaviour predicted for an inert surface[220,135,147,149] (----) is shown for comparison.

contrast to the behaviour measured in the highly dislocated regions of the surface (see Figure 15 of reference 220), where dissolution quickly attained a steady-state, Figures 7.9 and 7.10 show that, after an initial period, the current, *i.e.* flux of Cu^{2+} at the UME, rapidly decreases, to the level expected for an inert surface. Thereafter the current oscillates with a regular periodicity between levels for an active and an inactive surface. Note that chronoamperometric behaviour of this type has not previously been observed for Cu^{2+} reduction when: (i) dissolution of $CuSO_4.5H_2O$ is induced from the central region of the (100) face, (ii) the target surface is an inert glass disc, or (iii) chronoamperometric measurements are made in bulk solution.[220]

The current oscillations in Figures 7.9 and 7.10 are consistent with the theoretical results presented in section 7.3, and are interpreted as real-time oscillations in the dissolution rate, arising from a lack of active dislocations in the area of the crystal probed by the SECM. This is a realistic proposition, given that the UME is significantly smaller than the average dislocation spacing. The best fit of the experimental behaviour in Figures 7.9 and 7.10 to the dissolution model was obtained with the following parameters: $K = 3.5$, $C_{crit} = 1.25 \times 10^{-6}$, $N = 12.5 \times 10^{-9}$ mol cm^{-2} and τ_{in} = (a) 0.967 and (b) 0.410. The model is seen to only provide a qualitative guide to the initial dissolution behaviour (prior to the onset of current oscillations), but the oscillatory dissolution characteristics are reasonably well modelled with the simple theory proposed. The deviations between experiment and theory in the initial part of the current-time behaviour is attributed to the initial complexity of the crystal surface (irregularly spaced growth steps), as discussed in section 7.2. This period of SECM dissolution can effectively be regarded as an "electrochemically induced sputtering" of the surface, in which it is postulated that the majority of growth steps are removed from the crystal surface in the area directly under the UME, to leave a clean, essentially dislocation- and

step-free surface for longer time chronoamperometric measurements. Crucially, it is in this longer time period that the agreement between experiment and theory is most satisfactory.

Further evidence for the validity of the proposed dissolution model was revealed through microscopy of the crystal surface in areas of SECM measurements. Figure 7.11 is a DIC light micrograph of the dissolution pit corresponding to the transient in Figure 7.9. A series of *ca.* 5 ledges are visible inside the pit, *i.e.* the same total as the number of current surges in Figure 7.9. The formation of ledges of this type is clearly consistent with dissolution occurring in bursts, in a layer-by-layer fashion, as shown schematically in Figure 7.12.

The morphology of the pit in Figure 7.11 contrasts markedly with that resulting from dissolution in the central region of the (100) face of $CuSO_4.5H_2O$ (see Figures 16 and 18 in reference 220). SECM induced dissolution from this area resulted in a central pit, with additional significant pitting of the surrounding surface. The latter structure was shown to be diagnostic of a high dislocation density in the central region of the (100) face; the presence of dislocations allowing dissolution to occur at very low undersaturations.[220] In contrast, the lack of any pitting or roughening of the surface around the SECM induced pit in Figure 7.11 is consistent with a lack of dislocations in the area of the SECM measurement.

The question of the significance of the deduced values of C_{crit} and N naturally arises. First, the very small value of C_{crit} indicates that a high undersaturation is required to induce the dissolution reaction. The deduced value of $C_{crit} = 1.25 \times 10^{-6}$ is *ca.* 5 orders of magnitude smaller than the value typically required for the nucleation of observable dissolution etch pits at dislocation sites[53,83] Intuitively, this suggests that the value measured in this study is consistent with dissolution from an area of the crystal surface devoid of dislocations. In this case, the free energy change for the formation of a two-

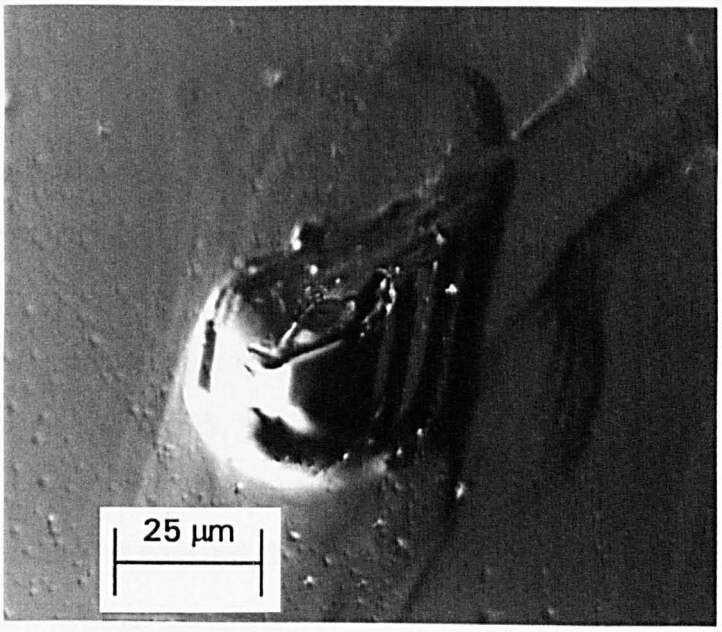

Figure 7.11. Nomarski DIC light micrograph of the SECM induced dissolution pit corresponding to the current-time characteristics in Figure 7.9. The scale bar denotes 25 μm.

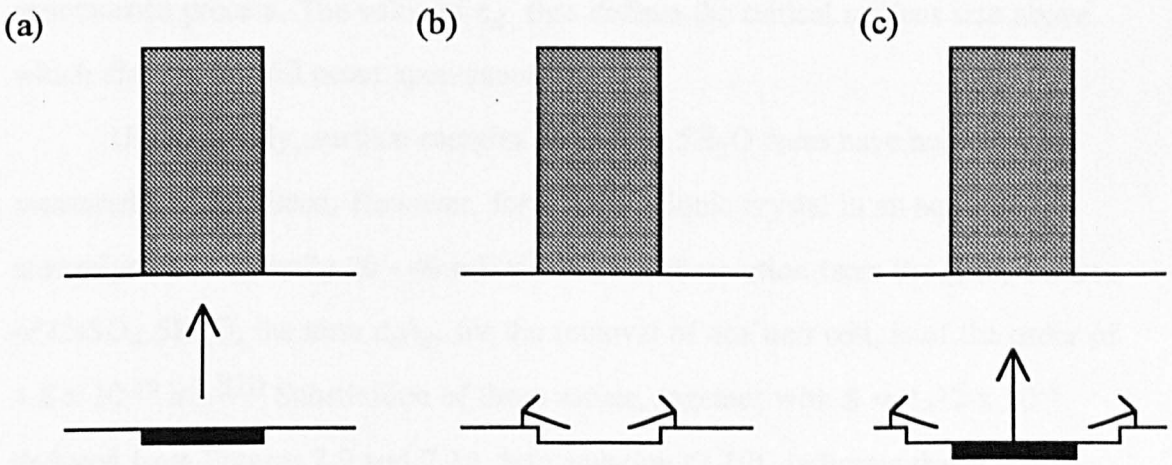

Figure 7.12. Schematic illustration of the formation of an SECM induced dissolution pit with terraced walls. The UME induces dissolution from the area directly under it (a), resulting in a current surge. The flux of material from this area then rapidly decreases (as illustrated in Figure 7.5), and slow dissolution occurs from the edge of the resulting pit (b), resulting in expansion. Concurrently, the area directly under the centre of the UME becomes increasingly undersaturated, until the critical value for the creation of fresh dissolution sites is attained, when there is a subsequent burst of material from the surface (c), producing a terraced structure within the pit. The overall process may then be repeated.

dimensional dissolution pit, ΔG_d, is the sum of contributions for the changes in the surface free energy, ΔG_s, and volume free energy ΔG_v:[3]

$$\Delta G_d = \Delta G_s + \Delta G_v \qquad (7.7)$$

For a square dissolution nucleus from which n_d units of area a_d^2 and height, h_d, have been removed, equation (7.7) can be written as

$$\Delta G_d = 4n_d^{1/2} a_d h_d \gamma + n_d kT \ln S \qquad (7.8)$$

where k is the Boltzmann constant, T is the temperature and S is the saturation ratio at the crystal/solution interface, *i.e.*

$$S = C_{Z=L}^{1/2} \qquad (7.9)$$

For dissolution ($S < 1$), ΔG_d is a maximum at $n_d = n_d'$

$$n_d' = \left(-2a_d h_d \gamma / kT \ln S\right)^2 \qquad (7.10)$$

i.e. for $n_d > n_d'$, $d(\Delta G_d)/dn_d < 0$, and under these conditions dissolution is a spontaneous process. The value of n_d' thus defines the critical nucleus size above which dissolution will occur spontaneously.

Unfortunately, surface energies of $CuSO_4.5H_2O$ faces have neither been measured nor calculated. However, for a soluble ionic crystal in an aqueous electrolyte, γ is typically 20 - 40 mJ/m^2.[319] For dissolution from the (100) surface of $CuSO_4.5H_2O$, the term $a_d h_d$, for the removal of one unit cell, is of the order of 4.8×10^{-19} m^2.[320] Substitution of these values, together with $S = 1.12 \times 10^{-3}$ deduced from Figures 7.9 and 7.10, into equation (7.10), indicates that n_d' is of the order of unity. The implication of this simple thermodynamic analysis is that, in the apparent absence of dissolution sites on the crystal surface, the undersaturation required to induce the dissolution process appears to be linked to a critical nucleus size of *ca.* one unit cell of $CuSO_4.5H_2O$. This implies that when the undersaturation is below the critical value, atomic or unit cell vacancies present on the crystal surface will not expand spontaneously through dissolution, but that

once the undersaturation reaches the critical value, dissolution from these sites is energetically favourable. The fact that, once this condition is met, there is a large and rapid dissolution flux from the crystal suggests that there must be a reasonable density of such vacancies available on the surface on the timescale of SECM detection, and that the rate of nucleus expansion is rapid.

Given that the above analysis is based on two-dimensional nucleation of dissolution sites, it first seems surprising that up to 24 monolayers of the (100) surface are removed in each current surge (given the deduced value of N = 12.5 x 10^{-9} mol cm^{-2} and the density of Cu^{2+} in the (100) surface is approximately 5.3 x 10^{-10} mol cm^{-2} [320]). The reason for the large value of N may be that, at a microscopic level, very rapid diffusion of material away from small dissolution pits expanding on the surface (consistent with rapid pit growth) may initially leave the solution adjacent to the exposed surface below sufficiently undersaturated with respect to the nucleation of further sites. This process could be self repeating until either the diffusion fields, associated with individual microscopic growing pits, overlap or the pits merge, with the associated material released into the solution inhibiting the further "nucleation" (and growth) of dissolution sites, until the solution is again depleted by electrolysis at the electrode. Overall, this process would lead to the effective loss of a significant number of monolayers of the (100) surface from the crystal during each period of dissolution activity, as observed.

7.6 Conclusions

The ability of the scanning electrochemical microscope to target selected small areas ($\leq 10^{-10}$ m^2) of a surface for kinetic measurements has been shown to be powerful for studying, for the first time, the dissolution characteristics of a region of a crystal surface effectively devoid of dislocation sites. In particular, it has been demonstrated that when the average inter-dislocation spacing is much

greater than the diameter of the UME probe, SECM induced dissolution from the (100) face of $CuSO_4.5H_2O$ occurs through a unique oscillatory rate process. Although oscillations in the rate of interfacial processes have been previously observed, for example in heterogeneous catalysis at the gas/solid interface[321,322] and in certain electrochemical reactions,[323-330] such as corrosion[331-334] and electrocrystallisation,[335-337] the results presented in this chapter represent the first observations of such behaviour in the dissolution of an ionic crystal.

After an initial period of dissolution activity, attributable to dissolution from growth steps present on the crystal surface, the dissolution rate rapidly decreases, until the solution adjacent to the crystal surface is sufficiently undersaturated to induce the reaction again. Thereafter dissolution occurs in a series of bursts, leading to oscillations in the UME current-time behaviour. The ability to quantitatively model mass transfer in the probe/crystal domain has allowed the value of the critical undersaturation, required to induce the dissolution process, to be estimated along with the amount of material released in each dissolution burst.

CHAPTER 8

DEVELOPMENT AND APPLICATION OF A MICROJET ELECTRODE: A HYDRODYNAMIC ULTRAMICROELECTRODE WITH HIGH MASS TRANSFER RATES

Chapters 4-7 considered the use of SECM as a technique for investigating the dissolution kinetics of ionic materials. This chapter introduces a new hydrodynamic technique - the microjet electrode - as a suitable methodology for studying reaction kinetics at solid/liquid interfaces. Initial emphasis is on processes at solid electrode/solution interfaces.

In the MJE, a jet of solution is fired at high velocities (up to 50 m s^{-1}) through a fine nozzle positioned directly over a disc UME, with the aid of micropositioners. This chapter describes the characterisation of the hydrodynamics of the MJE, which is shown to be capable of achieving mass transfer coefficients up to 0.82 cm s^{-1}, under laminar conditions. Through SECM mass transfer imaging, the mass transfer profile of the MJE is elucidated. The ability of the MJE to characterise fast surface processes is demonstrated, through studies of the kinetics of the oxidation of ferrocyanide ions at a Pt electrode. Finally, possible modifications to the MJE to facilitate the characterisation of dissolution processes are discussed.

8.1 Introduction

The ability to characterise surface reactions with increasingly faster kinetics continues to be a major challenge.[271,272,338] In order to quantitatively measure interfacial kinetics it is necessary to set the heterogeneous reaction of interest in competition with mass transfer and deduce the kinetics of the process from the

voltammetric or amperometric response. The availability, and further development, of techniques which are able to deliver the necessary high mass transfer rates, for the investigation of fast surface processes, under defined and controllable conditions, is thus of key importance.

Techniques which have been used to vary and control the mass transfer rate in dissolution studies have been reviewed in Chapter 1. One of the drawbacks of methods such as the RDM and CFMED is that typically they can only provide mass transfer coefficients of *ca.* 0.01 cm s^{-1} [73] and 0.05 cm s^{-1} [54,63] respectively, when employed with macroscopic substrates and electrodes. Although these mass transfer properties are suitable for studying intermediate kinetic regimes, they are not sufficient for fast kinetic analysis, as required for the ionic crystal dissolution systems investigated in Chapters 4-7. Recently, it has been demonstrated that the use of microband electrodes in channel flow under high pressure conditions allows the attainment of mass transfer coefficients approaching 1 cm s^{-1}.[339] Unfortunately this technique is limited, at present, to electrode processes only.

The geometry of an impinging jet, whereby a circular submerged jet collides perpendicularly with a planar surface has been found to be particularly attractive for a variety of applications due to its ability to deliver well-defined mass transfer rates.[340-344] In addition to its use as a flow-through detector for electroanalysis, the device is commonly used in electrochemical machining,[345] and erosion/corrosion studies.[346-348]

When the planar surface contains an embedded circular electrode, which has a diameter several times smaller than the diameter of the nozzle through which the solution flows, the system is termed a wall-tube electrode (WTE).[340,341,349,350] The WTE is an example of a uniformly accessible hydrodynamic electrode, akin to the rotating disc electrode,[73] described in section 1.2.2.1. Consequently, the WTE has found many applications as an electroanalytical tool[351-356] and is sometimes

preferred to rotating disc methodology, as no mechanical movement is required in the system.[340]

In this chapter, a new approach for achieving enhanced and variable steady-state mass transfer rates at UMEs, two orders of magnitude greater than the conventional diffusion rate at a 25 μm diameter UME, is proposed. This involves the use of a high velocity microjet of solution, which is fired through a small capillary positioned directly over the UME with the aid of micropositioners. Experimental conditions are set such that the diameter of the jet is *ca.* three to five times that of the disc electrode, thus the geometry represents a radical miniaturisation of the WTE. Initial studies are presented on the use of the MJE to characterise fast heterogeneous electron transfer kinetics, through studies on the $Fe(CN)_6^{3-}$ / $Fe(CN)_6^{4-}$ couple at a platinum electrode.

8.2 Apparatus and Instrumentation for MJE Studies

The apparatus and instrumentation used in the MJE studies was outlined in section 3.4. When it was necessary to use a simple manual positioner instead of the Burleigh closed loop system, a low cost system comprising a Newport Corp. (Fountain Valley, CA) 461 -*x y z* stage was employed. In this case the *z* axis was controlled by a differential micrometer (model DM-13) while fine adjustment screws (model AJS-1) were used to move the *x*- and *y*- axes. The stages were attached to an aluminium breadboard supported on polystyrene foam.

8.3 Experimental Procedures for Determining Mass Transfer in the MJE Geometry

In order to establish the nature of mass transfer to the MJE, experiments were concerned with determining the effect of the position and flow rate of the

impinging jet of solution on the transport-limited current at a UME for a simple electron transfer process. For this purpose, the oxidation of ferrocyanide ions:

$$Fe(CN)_6^{4-} - e^- \Leftrightarrow Fe(CN)_6^{3-} \qquad (8.1)$$

was studied at a 25 μm diameter platinum MJE, with a range of nozzle diameters and flow rates.

8.3.1 Effect of Lateral Position of the Jet on Mass Transfer Rate

The sensitivity of the electrode current to the lateral position of the jet was readily determined by first positioning the nozzle with respect to the UME in the region of maximum transport-limited current and then measuring the current as a function of displacement in the x or y direction. Typical results, showing the jet current, i_{MJE}, normalised with respect to the diffusion-limited current in stationary solution, i_{UME}, as a function of lateral displacement are shown in Figure 8.1. The data were obtained with a nozzle of diameter 95 μm, positioned 340 μm from the electrode surface and with an electrolyte flow rate of 0.0181 $cm^3\ s^{-1}$ (under gravity feed conditions).

Figure 8.1 demonstrates that impressive enhancements in current can be obtained with the impinging jet (even at moderate electrolyte flow rates), and suggests that the maximum enhancement in current with the MJE occurs when the nozzle is directly over the electrode. However, these results are at relatively low resolution, and for one-dimension only. In order to provide both complete information on the lateral positioning requirements of the MJE, and a unique insight into the nature of mass transfer from the impinging jet, a spatial two-dimensional map of mass transfer in the MJE geometry is necessary. This is provided by monitoring the current which flows at the UME as a function of the relative lateral displacement between the UME and the jet, as a jet of the solution is scanned over the UME surface in a raster pattern. The centre of the scan, assigned the co-ordinates, $x = 0$, y

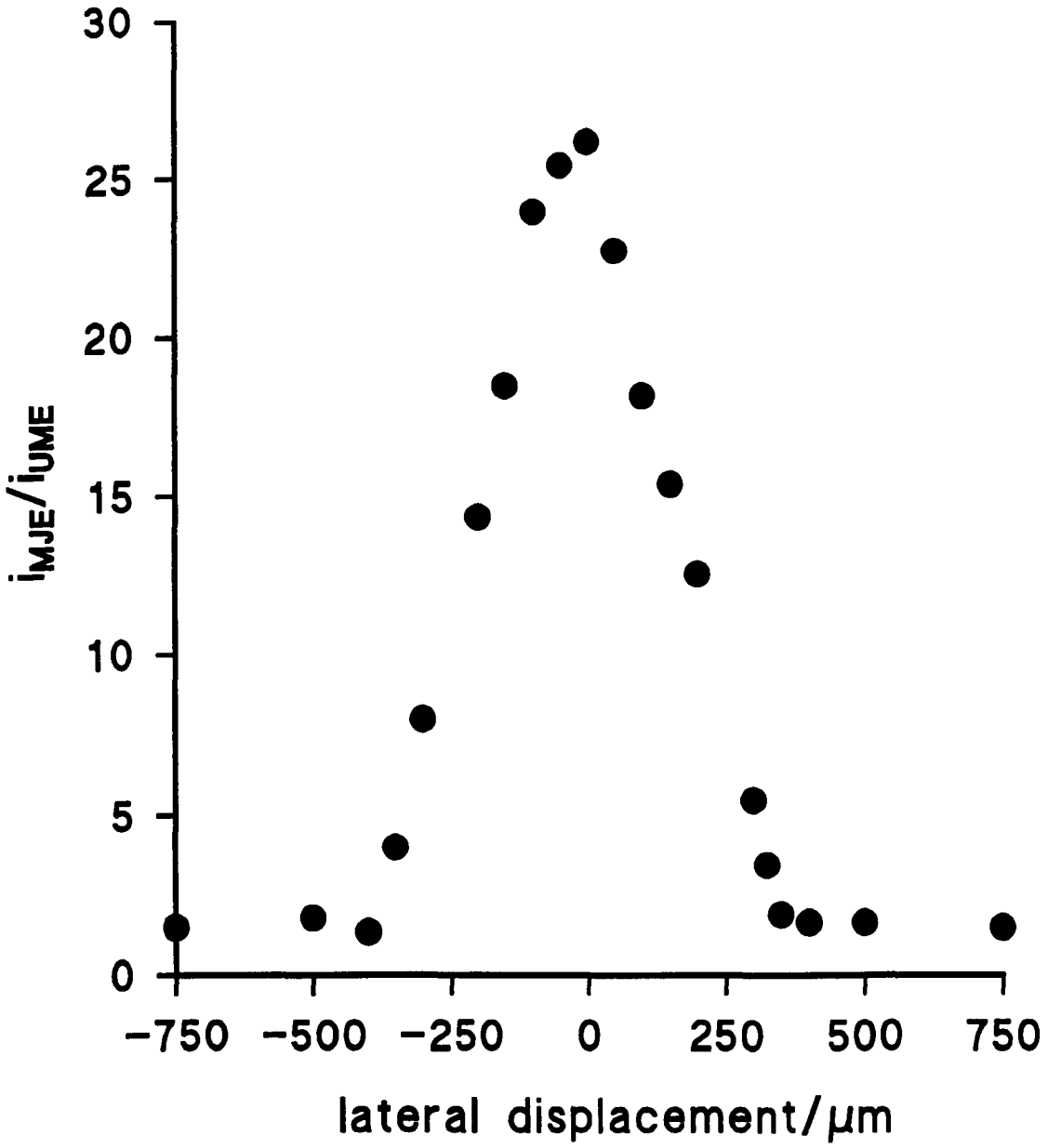

Figure 8.1. Effect of the lateral position of the nozzle, relative to the centre of the disc ultramicroelectrode, on the transport-limited current at the MJE. The end of the nozzle was positioned 340 μm above the electrode surface and a flow rate of 0.0181 $cm^3\ s^{-1}$ was employed.

= 0, qualitatively represents the position of maximum current as determined from a low resolution one-dimensional lateral scan.

Typical images of transport-limited current at the UME, as a function of nozzle displacement from the initial image centre, are shown in Figures 8.2 and 8.3. The data were obtained with a nozzle, of diameter d_n = 105 μm, which was positioned at distances above the UME surface, H, of 300 μm (Figure 8.2) and 1200 μm (Figure 8.3). To minimise solution consumption during the course of the data acquisition, these images were obtained with a moderate volume flow rate of 0.03 $cm^3\ s^{-1}$. The transport-limited current data, i_{MJE}, have been normalised with respect to the steady-state diffusion-limited current in stationary solution, i_{UME} = 1.51 nA.

Figures 8.2 and 8.3, in conjunction with Figure 8.1, again demonstrate that impressive enhancements in mass transport can be achieved with the MJE when the flow field from the nozzle encounters the UME. However, the high resolution contour plots in Figures 8.2(b) and 8.3(b), in conjunction with Figures 8.2(a) and 8.3 (a), suggest that the maximum enhancement in current does not occur when the nozzle of the MJE is directly centred over the electrode.

Although the point $x = 0, y = 0$ represents a point of highest current, this is not the only point where the current attains its maximum value. There is clearly a ring of maximum current, with an inner radius of *ca.* 25 μm and outer radius of *ca.* 50 μm, which surrounds a central circular area where the transport-limited current is slightly lower. The circular symmetry evident in Figures 8.2 and 8.3 suggests that this slight minimum, in the two-dimensional current distribution, represents the point at which the nozzle and the electrode are aligned. As the lateral (radial) displacement between the UME and nozzle increases from this position, the current increases slightly, reaching its maximum value when the axial centres of the jet and UME are offset laterally by about 50 μm. This applies when the nozzle is both close to (Figure 8.2), and far from (Figure 8.3) the planar surface containing the electrode. As the

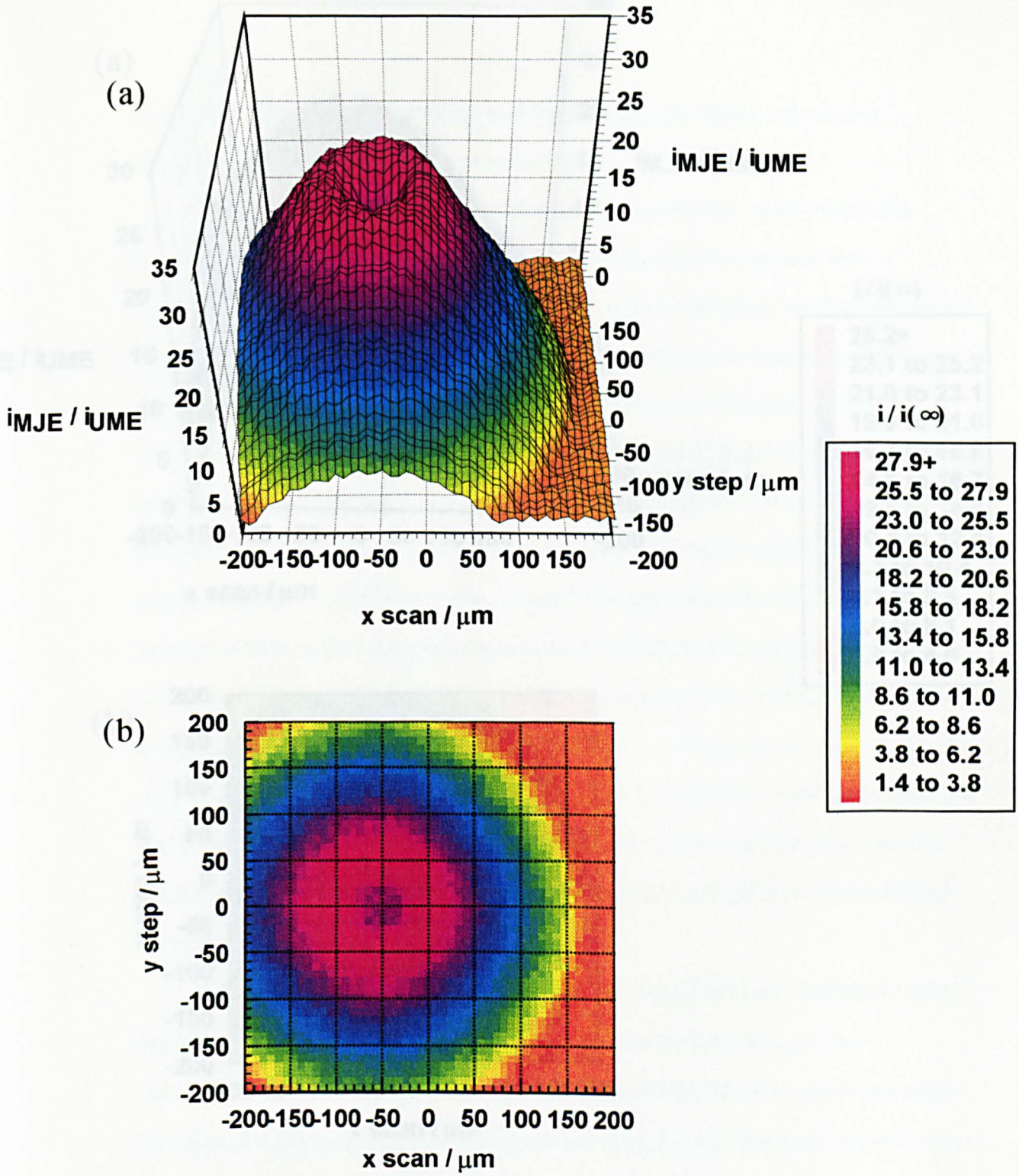

Figure 8.2. Variation of the transport-limited current at the MJE with the position of the nozzle (d_n = 105 μm) in the x, y plane at a distance H = 300 μm from the UME surface. Data are presented as a surface plot (a) and spectral plot (b) in order to emphasise both the minimum in the current at the centre of the image and the high degree of circular symmetry in the image. The image was obtained at a nozzle scan rate of 10 μm/s and comprises 51 equally spaced x-line scans. The colour bar represents values of $i/i(\infty)$.

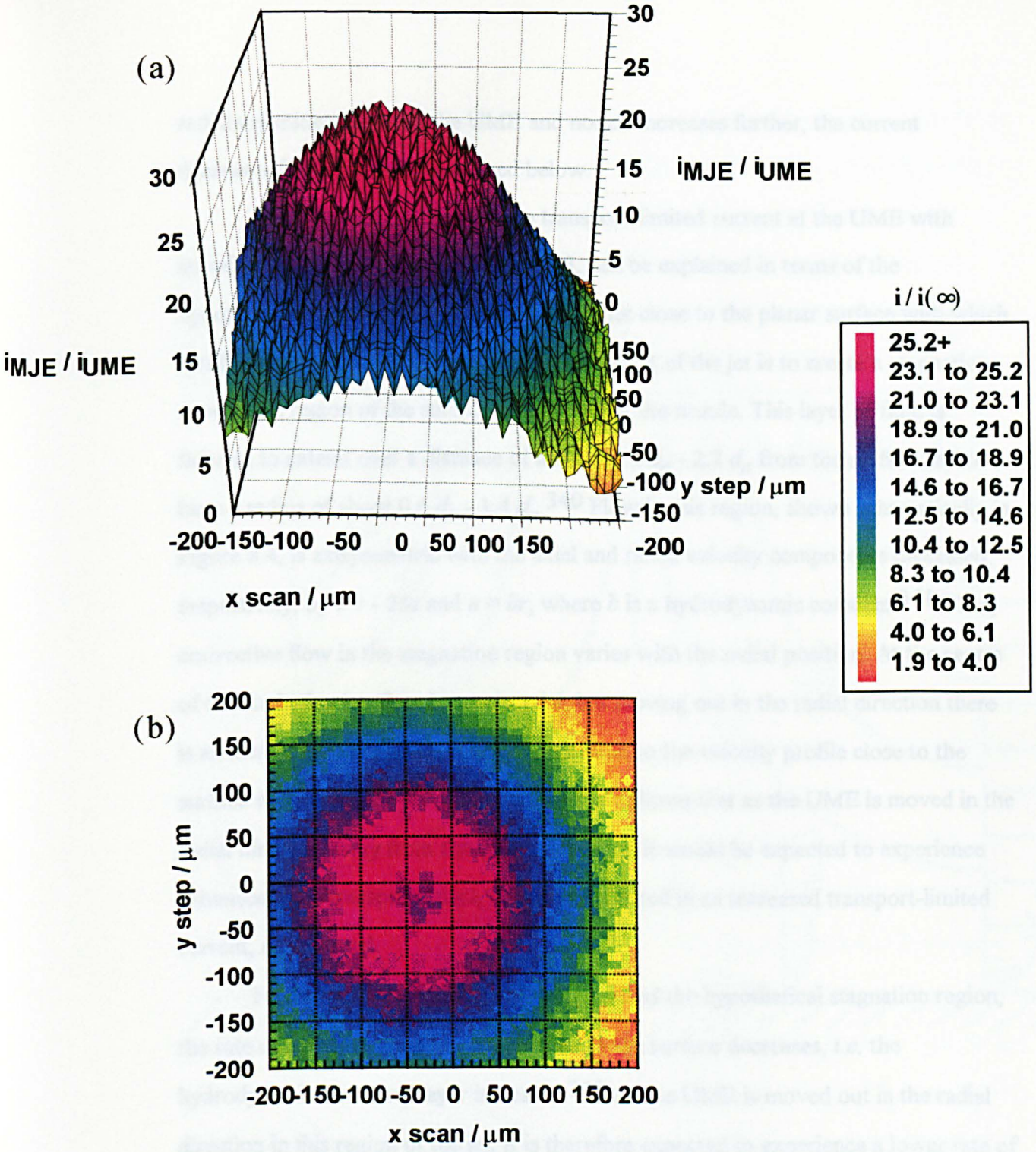

Figure 8.3. Variation of the transport-limited current at the MJE with the position of the nozzle (d_n = 105 μm) in the x, y plane at a distance H = 1200 μm from the UME surface. Data are presented as a surface plot (a) and spectral plot (b). The other experimental parameters used to obtain the image were as for Figure 8.2. The colour bar represents values of $i/i(\infty)$.

radial separation between the UME and nozzle increases further, the current decreases for the reasons discussed below.

The observed variation in the transport-limited current at the UME with lateral jet position, in Figures 8.2 and 8.3, can be explained in terms of the hydrodynamics of the submerged impinging jet close to the planar surface with which it collides.[340] It is well established that the effect of the jet is to create a stagnation zone in the region of the surface directly under the nozzle. This layer of fluid is thought to extend over a distance of around 1.6 d_n - 2.2 d_n from the surface and to have a radius of about 0.6 d_n - 1.4 d_n.[340] Flow in this region, shown schematically in Figure 8.4, is axisymmetric with the axial and radial velocity components described, respectively, by $v = -2bz$ and $u = br$, where b is a hydrodynamic constant.[341] Thus, convective flow in the stagnation region varies with the radial position. At the centre of the impinging jet, flow is purely axial, but moving out in the radial direction there is an increasingly important radial contribution to the velocity profile close to the surface with which the jet of fluid collides. It follows that as the UME is moved in the radial direction away from the centre of the jet, it would be expected to experience enhanced mass transport which would be reflected in an increased transport-limited current, as observed.

Further out in the radial direction, beyond the hypothetical stagnation region, the rate of convective mass transfer close to the surface decreases, *i.e.* the hydrodynamic boundary layer increases.[340] As the UME is moved out in the radial direction in this region of the jet, it is therefore expected to experience a lower rate of mass transfer, *i.e.* lower transport-limited currents, as observed for large radial displacements. The results in Figures 8.2 and 8.3, in which the UME current reaches a maximum when the centres of the jet and UME are offset laterally by about 50 μm, suggests that the stagnation zone extends over a region in the radial direction of about one nozzle radius from the centre of the jet.

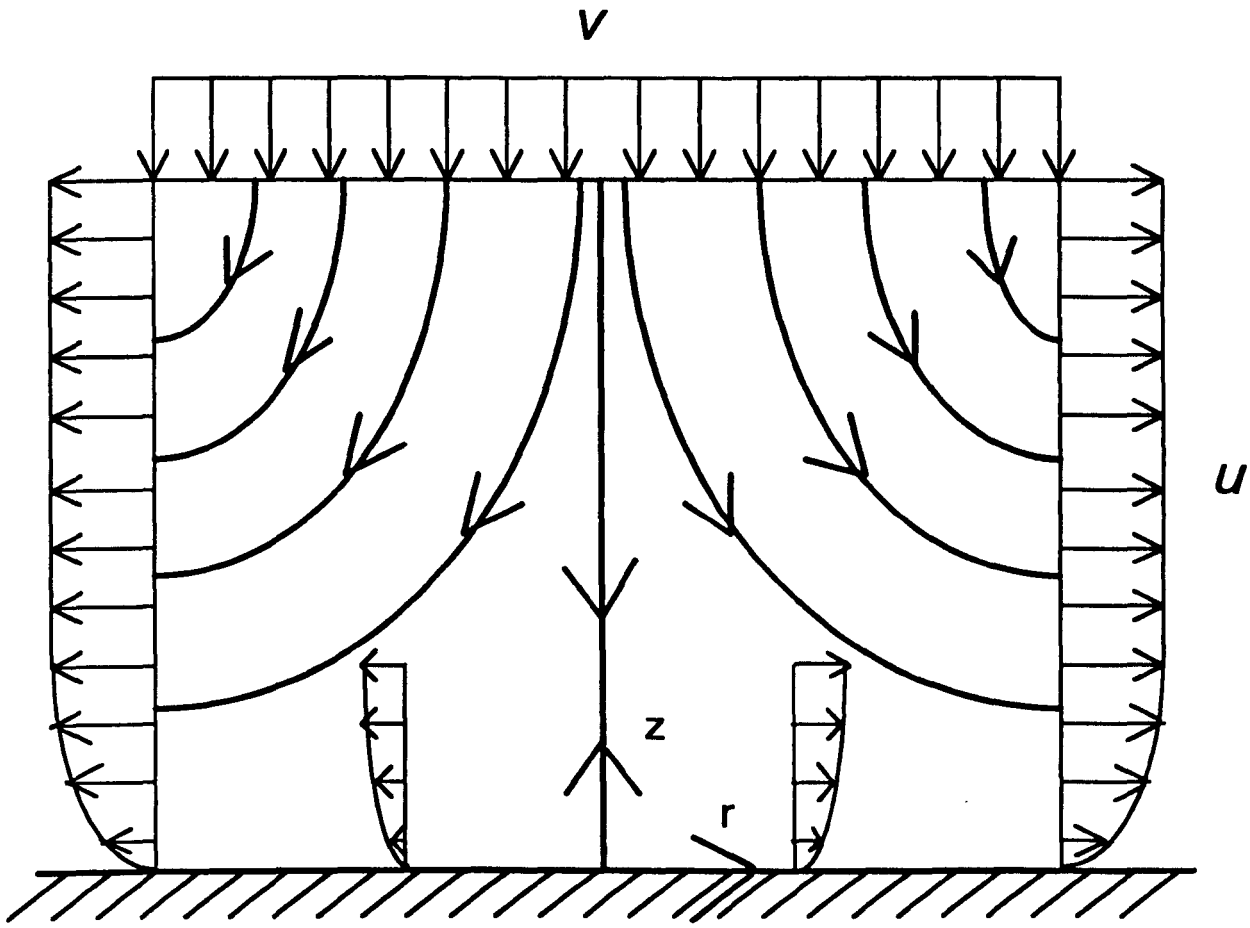

Figure 8.4. Schematic of the flow profile in the stagnation region of an impinging jet.

The differences in the mass transfer images in Figures 8.2 and 8.3 result from the different nozzle to electrode separations employed in each case. Comparison of Figures 8.2 and 8.3 clearly indicates that the maximum current enhancement is smallest when H is greatest. However, the current decays more slowly from its maximum value, with radial displacement between the UME and jet, for large H. These observations are in agreement with the general flow profile in the jet,[340] in which the electrolyte flowing from the nozzle mixes with the surrounding fluid. The mixing zone grows in width with distance from the nozzle exit and, while the volume flow rate stays constant, the solution velocity in the central region of the jet decreases. Thus when H is large, the width of the jet impinging on the surface will be large, and the electrode will "see" enhanced mass transfer to greater distances from the centre of the jet in the radial direction. However, the maximum current (or current when the axes of the jet and UME are aligned) will be lower than when smaller values of H are employed (for $H > 0.1\ d_n$[340]), due to the lower fluid velocity at the centre of the jet.

The implications of the above results for kinetic applications of the MJE are that for true alignment of the jet nozzle and UME, their relative positions should be adjusted until the transport-limited current at the UME is at a minimum with respect to all possible relative movements between the nozzle and UME in the x and y directions. In this configuration, the MJE is equivalent to the WTE and is expected to be uniformly accessible.[340] However, the profiles in Figures 8.2 and 8.3 demonstrate that the maximum current condition prevails over a lateral distance of at least one electrode diameter. Given the general jet flow profile,[340] these results suggest that when the MJE is set up in the configuration for maximum current, the UME appears to be effectively uniformly accessible. Hence, the MJE may be employed in either configuration for kinetic measurements. In contrast, if the UME is positioned outside the hypothetical stagnation region, the transport-limited current density on the

electrode is likely to be non-uniform, thus invalidating any analogy between the MJE and WTE.

8.3.2 Effect of Nozzle Exit -UME Separation on the Mass Transfer Rate

The effect of the distance between the nozzle exit and electrode surface on the transport-limited current at the MJE was investigated quantitatively by carefully placing the nozzle in contact with the electrode surface, having centred it to the position of maximum transport-limited current, and then measuring the current as a function of electrode-nozzle separation. The results of this exercise for a nozzle characterised by d_n = 110 μm, and flow rate, V_f, of 0.0338 $cm^3\ s^{-1}$ are given in Figure 8.5. The data have been normalised by dividing the MJE currents by the value measured at a distance $H = d_n$ (corresponding in this case to $i_{MJE}/i_{UME} = 30.8$), while the distance, H, has been normalised with respect to d_n. Figure 8.5 demonstrates that for most of the distances considered, there is only a weak dependence of the transport-limited current on H/d_n. This observation is in agreement with the extensive studies of Chin and Tsang, with conventional-sized WTEs under laminar flow conditions, who found (empirically) an $(H/d_n)^{-0.054}$ dependence of the transport-limited current for $0.2 < (H/d_n) < 6.0$.[340] For comparison with the experimental data, the behaviour predicted by Chin and Tsang is given by the solid line in Figure 8.5.

8.3.3 The Effect of Flow Rate on the Mass Transfer Rate

For experiments aimed at determining the effect of flow rate on the MJE transport-limited current, it was necessary to elucidate to what extent mass transfer can be described by existing models for WTEs.[340] For such electrodes, of conventional size, mass transfer, under laminar flow conditions, is described by expressions of the following general form:[340]

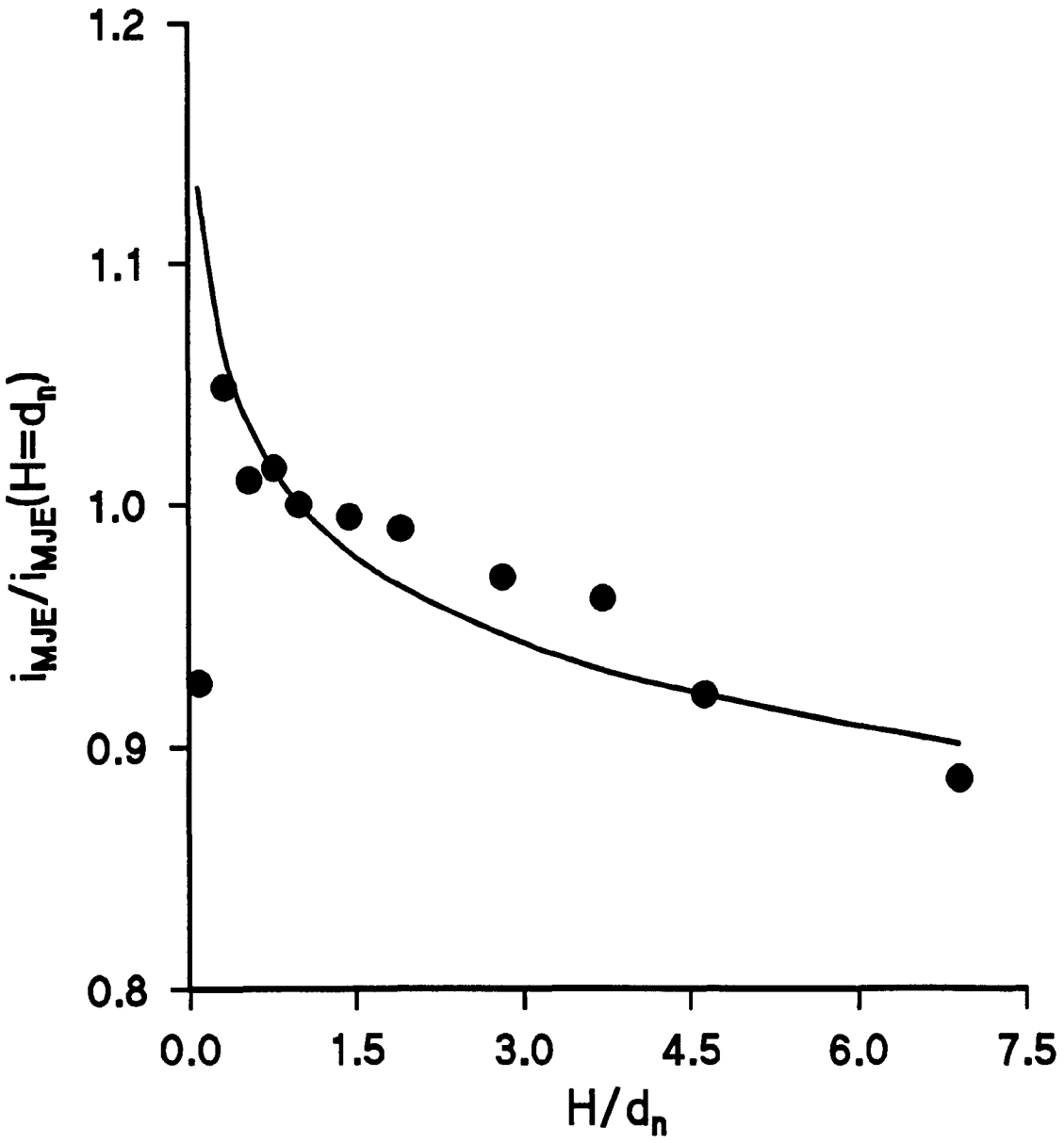

Figure 8.5. Effect of the distance, H, between the nozzle exit and electrode surface on the transport-limited current at the MJE. Measured currents, i_{MJE} (•) have been normalised with respect to that measured at a distance $H=d_n$, $i_{MJE}(H=d_n)$. Data relate to a nozzle of diameter, d_n = 110 μm and a solution flow rate of 0.0338 $cm^3\ s^{-1}$. The solid line represents the behaviour predicted for a conventional-sized wall tube electrode.[340]

$$Sh = \beta Re^{1/2} Sc^{1/3} f(H/d_n) \tag{8.2}$$

In equation (8.2), β is a constant coefficient and $f(H/d_n)$ is a distance dependent function; Sh and Sc are the Sherwood and Schmidt numbers, given by:

$$Sh = k_t d_n / D \tag{8.3}$$

$$Sc = \upsilon / D \tag{8.4}$$

The Schmidt number is a characteristic of the medium and is determined purely by the physical properties of the solution.

Laminar flow is ensured for Re < 2000,[340] where Re is given by:

$$Re = d_n \overline{U} / \upsilon \tag{8.5}$$

and $\overline{U}$ is the mean solution velocity.

The transport-limited current for the uniformly-accessible MJE is:

$$i_{MJE} = k_t n_e F(\pi a^2) c^* \tag{8.6}$$

and the diffusion-limited current at a UME is as given by equation (1.4).

It follows from equations (8.2) to (8.6) and (1.4) that for the MJE, under conditions of uniform accessibility:

$$\frac{i_{MJE}}{i_{UME}} = \beta f(H/d_n)(\pi/4)\overline{U}^{1/2} a D^{-1/3} \upsilon^{-1/6} d_n^{-1/2} \tag{8.7}$$

Given that

$$V_f = \pi (d_n/2)^2 \overline{U} \tag{8.8}$$

i_{MJE}/i_{UME} should be proportional to the square root of the volume flow rate.

Figure 8.6 shows data obtained from experiments with a 25 μm diameter electrode and two nozzle diameters, d_n = 90 and 116 μm, using a simple gravity feed system. In these cases, positioning was achieved using the closed loop system, and the nozzle/electrode separations were respectively 200 and 300 μm. It can be seen that over the range of flow rates investigated, a good linear relationship holds between i_{MJE}/i_{UME} and $V_f^{1/2}$. The slopes of the lines yield

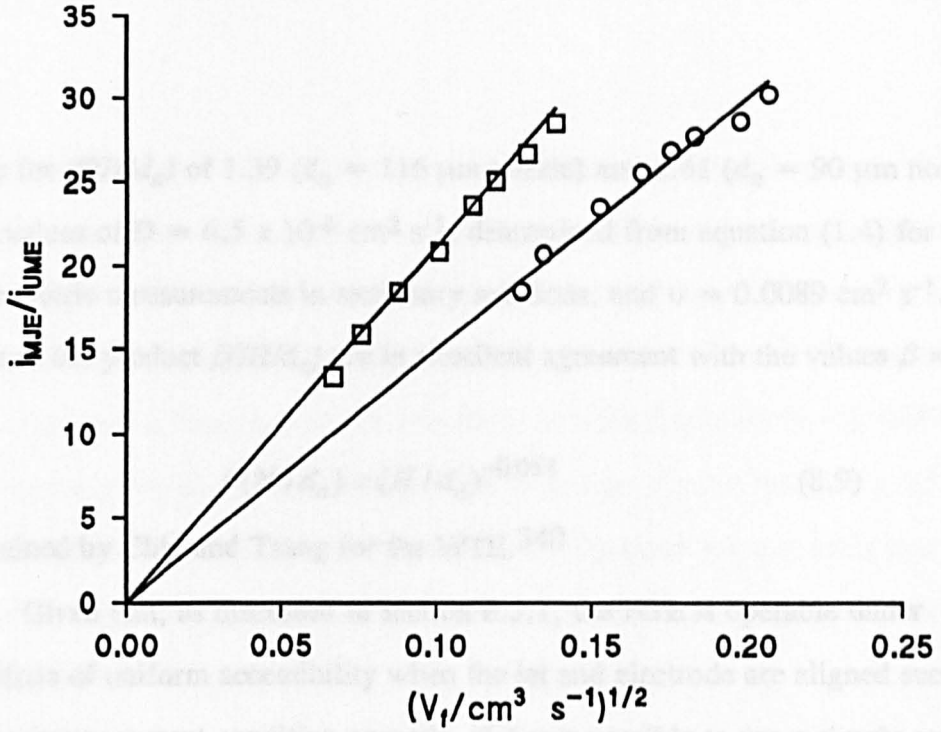

Figure 8.6. Analysis of the transport-limited current-flow rate data for the MJE in terms of equation (8.7). Data relate to: (□) d_n = 90 μm and H = 200 μm; (O) d_n = 116 μm and H = 300 μm.

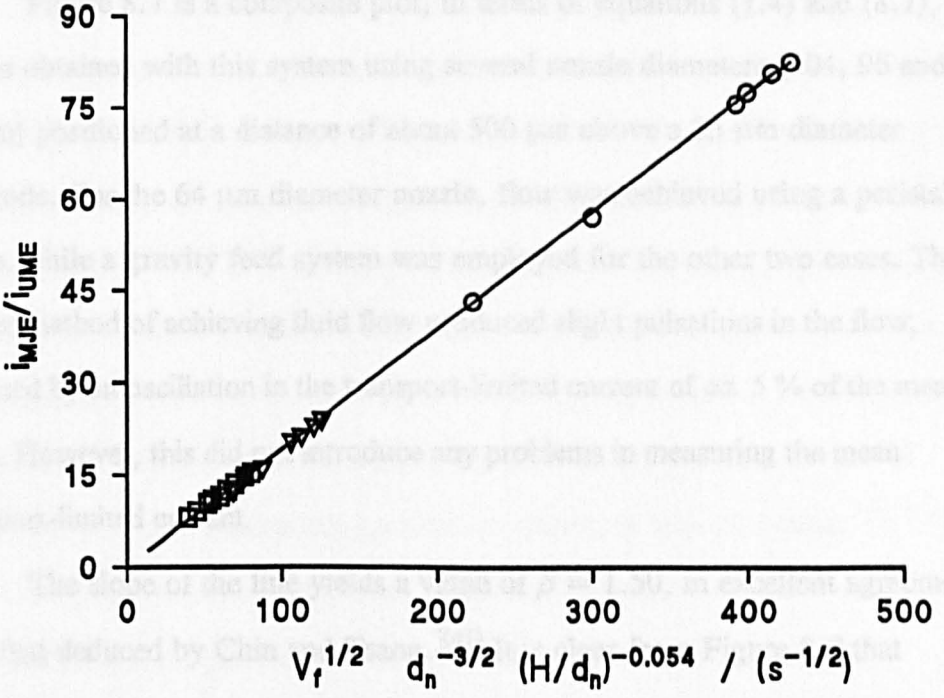

Figure 8.7. Analysis of the transport-limited current-flow rate data for the MJE in terms of equations (8.7) and (8.9). Data relate to d_n = (O) 64 μm; (▽) 96 μm and (□) 104 μm. In all cases the exit of the nozzle was about 500 μm above the electrode surface.

values for $\beta f(H/d_n)$ of 1.39 (d_n = 116 μm nozzle) and 1.41 (d_n = 90 μm nozzle), using values of $D = 6.5 \times 10^{-6}$ cm^2 s^{-1}, determined from equation (1.4) for voltammetric measurements in stationary solutions, and $\upsilon = 0.0089$ cm^2 s^{-1}. Both values of the product $\beta f(H/d_n)$ are in excellent agreement with the values $\beta = 1.51$ and

$$f(H/d_n) = (H/d_n)^{-0.054} \qquad (8.9)$$

determined by Chin and Tsang for the WTE.[340]

Given that, as discussed in section 8.3.1, the MJE is operable under conditions of uniform accessibility when the jet and electrode are aligned such that the maximum current condition prevails, if it was possible to use a simple manual positioner to align the two, this would reduce experimental costs greatly and make the MJE technique more commercially attractive.

Figure 8.7 is a composite plot, in terms of equations (1.4) and (8.7), of the results obtained with this system using several nozzle diameters (104, 96 and 64 μm) positioned at a distance of about 500 μm above a 25 μm diameter electrode. For the 64 μm diameter nozzle, flow was achieved using a peristaltic pump, while a gravity feed system was employed for the other two cases. The former method of achieving fluid flow produced slight pulsations in the flow, reflected by an oscillation in the transport-limited current of *ca.* 5 % of the mean value. However, this did not introduce any problems in measuring the mean transport-limited current.

The slope of the line yields a value of $\beta = 1.50$, in excellent agreement with that deduced by Chin and Tsang.[340] It is clear from Figure 8.7 that enhancements of almost two orders of magnitude ($i_{MJE}/i_{UME} = 82.5$) in the diffusion-limited current at an UME can be achieved through the addition of convection in the form of an impinging jet. By using a HPLC pump, to control the volume flow rate, as discussed later in section 8.3.4 it is possible to obtain even

higher enhancements, where i_{MJE}/i_{UME} = 120. It follows from equation (8.6) and (1.4) that the highest mass transfer rate achievable under these conditions *i.e.* (i_{MJE}/i_{UME} = 120) corresponds to a mass transfer coefficient of about 0.82 cm s^{-1}. A UME with a radius of *ca.* 100 nm would be required to achieve the same mean rate of mass transfer in stationary solution (equation (1.4)), while a rotating disc electrode would have to rotate at speeds of more than 4.3 x 10^5 Hz in order to achieve the same mass transfer rate.[73] The latter value is more than three orders of magnitude greater than the maximum rotation speed typically attainable with commercial devices.

8.3.4 MJE Voltammetry

Given that the mass transfer characteristics of the MJE have been fully characterised it is necessary to test the capability of the device in studying fast heterogeneous processes. This was readily achieved through studies on the $Fe(CN)_6^{4-}$ / $Fe(CN)_6^{3-}$ redox couple at a platinum electrode. This system has previously received considerable attention, particularly using UME voltammetry.[256,257,357] Although often considered to be a simple outer sphere one electron transfer process, under certain conditions the electrode reaction is complicated by side reactions which can lead to irreproducible voltammetric responses.[256] However, it has recently been demonstrated that the use of strontium nitrate as a supporting electrolyte prevents such problems.[256] For a supporting electrolyte concentration of *ca.* 0.1 mol dm^{-3}, the standard rate constant for the couple, deduced from steady-state and fast scan UME voltammetry, is reported to be in the range 0.3 - 0.4 cm s^{-1},[256] well within the mass transfer limits of the MJE.

A typical voltammogram for the oxidation of ferrocyanide at a 25 μm diameter Pt disc UME, obtained by scanning the electrode potential at a rate of 2 mV s^{-1} between +0.1 V and +0.4 V vs. a saturated calomel reference electrode (SCE), is shown in Figure 8.8. Analysis of the diffusion-limited current in terms of equation (1.4) yields a value for $D_{Fe(CN)_6^{4-}}$ of 6.2 x 10^{-6} cm^2 s^{-1}. This value is in very good agreement with that previously reported under similar conditions.[256,357] Analysis of the shape of the wave reveals that the difference between the quarter-wave and three-quarter wave potentials ($E_{3/4} - E_{1/4}$) is 57 mV, which is very close to the theoretical value of 56.5 mV predicted for a reversible one-electron transfer process at a disc UME.[358] This result indicates that the standard rate constant, k_o, for the oxidation of ferrocyanide under the conditions of the experiment is much greater than the mass transfer rate attainable from simple steady-state diffusion at the UME.

Figure 8.9 shows a typical series of steady-state voltammograms obtained when the UME was placed in the MJE configuration and a jet of solution was fired directly at its surface at a range of velocities. These results were obtained with a nozzle of diameter, d_n = 85 μm, positioned directly over the UME at H = 300 μm from its surface. It can be seen that as the solution flow rate is increased the wave becomes more irreversible, as the diffusion-limited plateau is shifted to more oxidising potentials. This is due to the increasing significance of k_o compared to k_t, as the surface electron transfer process becomes rate limiting.

As established previously in section 8.3.3, for practical solution flow rates, mass transfer to the MJE is analogous to that at the WTE,[340] *i.e.* the diffusional edge effect is effectively suppressed and the electrode behaves as a uniformly accessible electrode. Under laminar flow conditions, the dependence of the transport-limited current at the MJE on solution flow rate follows equation (8.7): Analysis of the data in Figure 8.9 in terms of equations (8.7) and (8.8) is given in Figure 8.10.

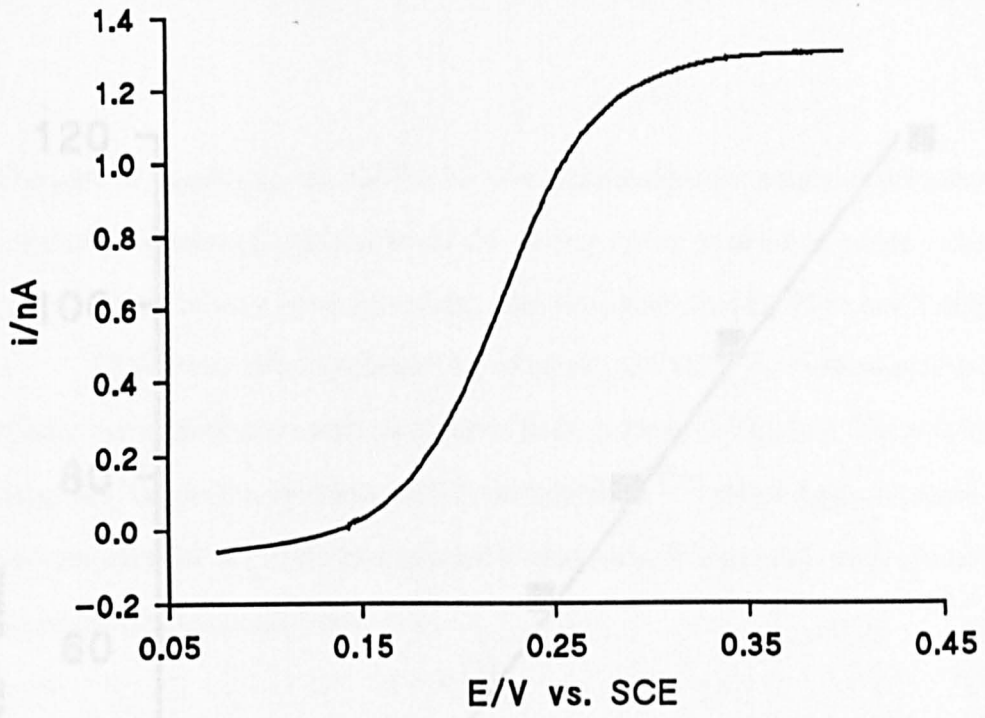

Figure 8.8. Typical steady-state voltammogram for the oxidation of ferrocyanide ions (*ca.* 5 x 10^{-4} mol dm^{-3}) at a Pt UME in stationary solution.

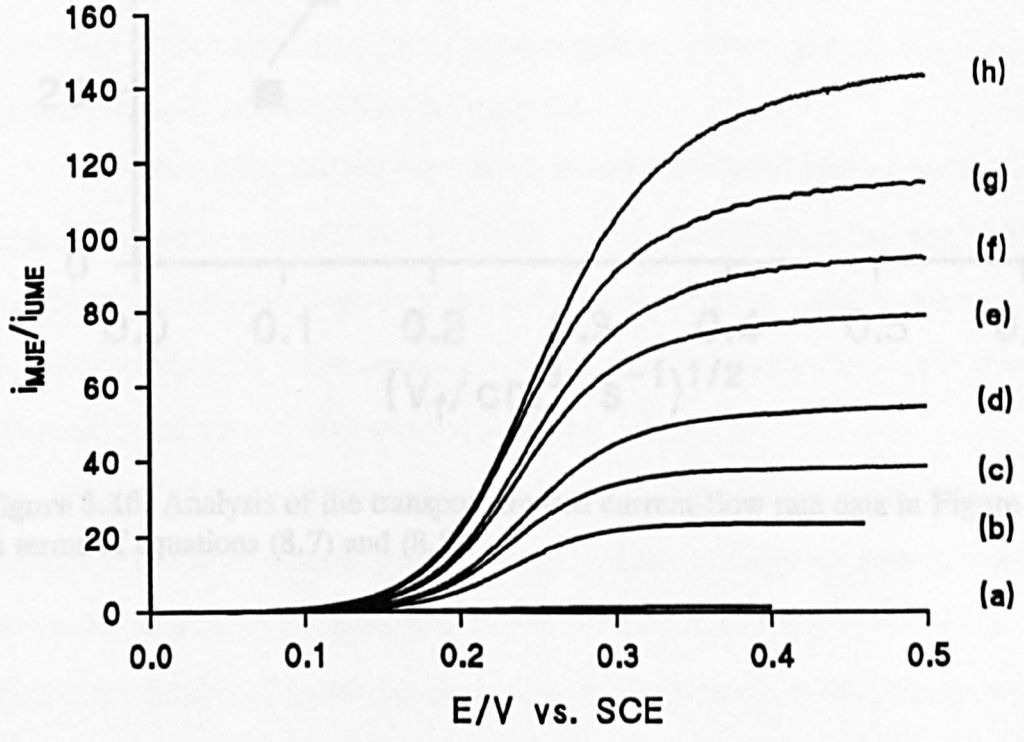

Figure 8.9. Steady-state voltammograms for the oxidation of ferrocyanide ions at a Pt MJE employing solution flow rates of: (a) 0, (b) 0.0083, (c) 0.0167, (d) 0.033, (e) 0.067, (f) 0.100, (g) 0.133, (h) 0.267 cm^3 s^{-1}. Data were obtained with a nozzle of diameter, d_n = 85 μm, positioned 300 μm from the UME surface.

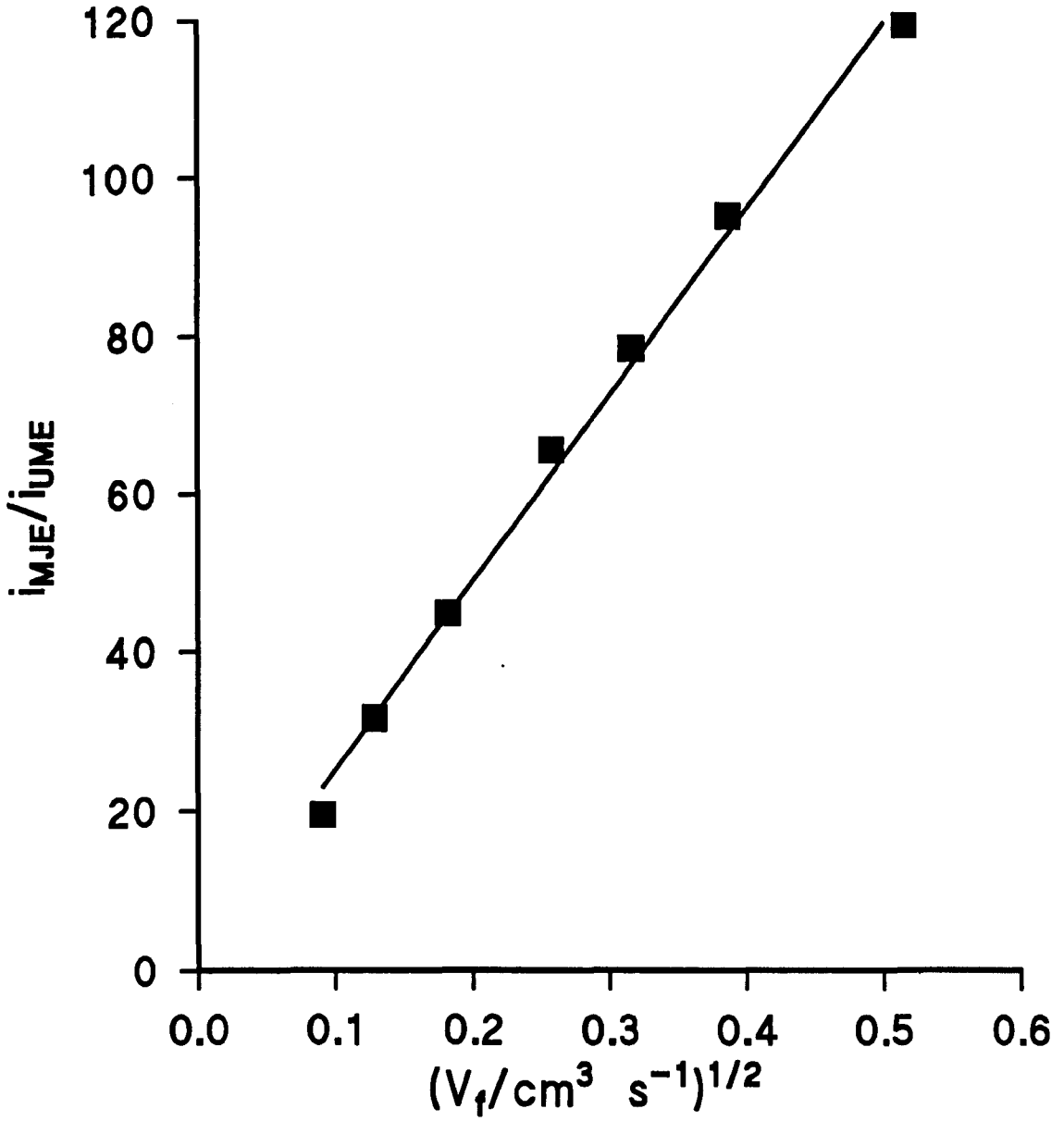

Figure 8.10. Analysis of the transport-limited current-flow rate data in Figure 8.9 in terms of equations (8.7) and (8.8).

The plot of i_{MJE}/i_{UME} vs. $V_f^{1/2}$ is linear and intercepts the origin, confirming the validity of equation (8.7). Moreover, linear regression of the data yields a value for β of 1.51, again in very good agreement with the value cited by Chin and Tsang.[340]

Given the uniform accessibility of an aligned MJE, the determination of kinetic parameters from voltammograms such as those in Figure 8.9 is simplified. By using the comprehensive tables of Mirkin and Bard,[179] which apply to steady-state voltammetry for any uniformly accessible electrode, it is possible to determine the normalised kinetic parameter,

$$\chi = k_o / k_t \qquad (8.9)$$

and transfer coefficient directly by measuring the separations between the quarter-wave and half-wave potentials, $\Delta E_{1/4} = |E_{1/4} - E_{1/2}|$ and between the three-quarter wave and half-wave potentials, $\Delta E_{3/4} = |E_{3/4} - E_{1/2}|$. Tables 8.1 - 8.3 provide a compilation of the kinetic analysis of voltammograms measured in several experimental runs, including those in Figure 8.9.

The values of k_o derived from the voltammetric data fall within a narrow range, with a mean value of 0.76 ± 0.11 cm s^{-1}. The value of α is in the range 0.35 - 0.55. There is a relatively large variation in the latter parameter since the chosen method of steady-state voltammetric analysis can result in a large variation in α even with a very small error in the measured potentials.[179]

The value of the standard rate constant for the ferro/ferricyanide couple measured in this study is about twice the value measured using (predominantly fast scan cyclic) voltammetry at stationary UMEs.[256] In part, this may be due to the higher concentration of supporting electrolyte employed in our system. However, the results also support the conclusions of Bard and co-workers[153] who suggested that fast scan cyclic voltammetry "even with quite careful (ohmic) compensation, tends to underestimate the rate constant for very rapid reactions." A further reason for the higher value of k_o may be due to the flow through nature of the MJE configuration.

Table 8.1. Kinetic Analysis of Voltammetric Data for Ferrocyanide Oxidation at a MJE with d_n = 85 μm and H = 300 μm.

V_f / cm^3 s^{-1}	$\frac{i_{MJE}}{i_{UME}}$	k_t / cm s^{-1}	$\Delta E_{1/4}$ / mV	$\Delta E_{3/4}$ / mV	α	χ	k_o / cm s^{-1}
0.0083	18.5	0.119	28.0	30.0	___	___	___[a]
0.017	31.7	0.194	31.0	33.0	0.50	3.74	0.72
0.033	44.8	0.274	33.0	38.0	0.39	2.74	0.75
0.067	65.6	0.400	34.0	38.5	0.46	1.97	0.79
0.100	78.5	0.480	36.0	41.0	0.49	1.36	0.65
0.133	95.3	0.582	36.0	42.0	0.45	1.50	0.87
0.200	107	0.654	38.0	46.0	0.42	1.28	0.84
0.267	120	0.734	38.0	47.0	0.44	1.12	0.82

[a] waveshape too close to reversible behaviour for accurate kinetic analysis

Table 8.2. Kinetic Analysis of Voltammetric Data for Ferrocyanide Oxidation at a MJE with d_n = 60 μm and H = 500 μm.

V_f / cm^3 s^{-1}	$\frac{i_{MJE}}{i_{UME}}$	k_t / cm s^{-1}	$\Delta E_{1/4}$ / mV	$\Delta E_{3/4}$ / mV	α	χ	k_o / cm s^{-1}
0.0042	12.0	0.073	28.5	30.0	___	___	___[a]
0.0083	20.6	0.126	28.5	31.0	___	___	___[a]
0.017	35.6	0.218	31.5	34.5	0.43	3.65	0.79
0.033	57.4	0.351	32.5	35.0	0.55	2.20	0.77
0.067	77.2	0.472	34.5	38.0	0.53	1.51	0.71
0.100	86.8	0.531	36.0	41.0	0.49	1.36	0.72

[a] waveshape too close to reversible behaviour for accurate kinetic analysis

Table 8.3. Kinetic Analysis of Voltammetric Data for Ferrocyanide Oxidation at a MJE with d_n = 85 μm and H = 900 μm.

V_f / cm^3 s^{-1}	$\frac{i_{MJE}}{i_{UME}}$	k_t / cm s^{-1}	$\Delta E_{1/4}$ / mV	$\Delta E_{3/4}$ / mV	α	χ	k_o / cm s^{-1}
0.067	60.7	0.371	35.0	43.0	0.35	2.09	0.78
0.100	71.9	0.439	36.0	43.0	0.42	1.63	0.72
0.133	82.6	0.505	36.0	42.0	0.45	1.50	0.76
0.167	93.0	0.569	38.0	46.0	0.42	1.28	0.73
0.200	101	0.617	38.0	46.0	0.42	1.28	0.79

Provided that the electrolyte source from the jet is clean, the action of the jet effectively serves to wash the electrode surface during the course of a measurement. This ensures that products which might inhibit the electrode reaction are carried to waste and do not build up on the electrode surface or in the solution. This is a particularly advantageous feature of the MJE for systems, such as the ferro/ferricyanide couple, which may be prone to complications from adsorbed products.

8.4. Discussion on How the MJE could be Modified to Enable the Study of Fast Dissolution Processes

In sections 8.3.3 and 8.3.4, the MJE was shown to be capable of providing mass transfer coefficients up to 0.82 cm s^{-1} for the study of electrode processes. It is thus useful to consider how this technique could be adapted to probe reactions occurring at non-conducting surfaces, in particular for the study of the dissolution kinetics of ionic crystals.

Figure 8.11 shows a schematic diagram of a proposed dissolution methodology employing a modified MJE. In contrast to Figure 3.5, the Pt UME is now replaced by the crystal surface of interest and the capillary through which solution is flowed has been modified to incorporate a ring electrode. In order to achieve the most sensitive collection of dissolution products or reactants at the ring electrode, the capillary must be placed very close to the surface of the crystal. In this situation the geometry is very similar to a thin layer cell.

For ionic salts such as those discussed in Chapters 4-7, dissolution could be induced locally by flowing an undersaturated solution through the capillary. Electroactive dissolution products would be detected at the ring electrode and the current response would provide information on the dissolution kinetics and mechanism, once the corresponding mass transfer problems has been modelled theoretically. Due to the flow-through nature of the methodology, problems from the build up of dissolution products in the capillary/substrate gap, serving to impede the dissolution or electrochemical reaction, would be eradicated. Hence the proposed technique, given that it is capable of delivering high mass transfer rates, provides an alternative to the SECM induced dissolution methodology.

8.4 Conclusions

The MJE represents a new approach for achieving significantly enhanced and variable mass transfer rates at UMEs (over two orders of magnitude greater, with a 25 μm diameter electrode, than the diffusion rate in stationary solutions). The electrode is characterised by well-defined mass transfer which, under most conditions, is similar to that for the conventionally sized wall tube electrode *i.e.* the electrode is "uniformly accessible", which greatly simplifies the description of mass transfer. At present the highest mass transfer coefficient attainable with the MJE is in excess of 0.8 cm s^{-1} (for a typical value of

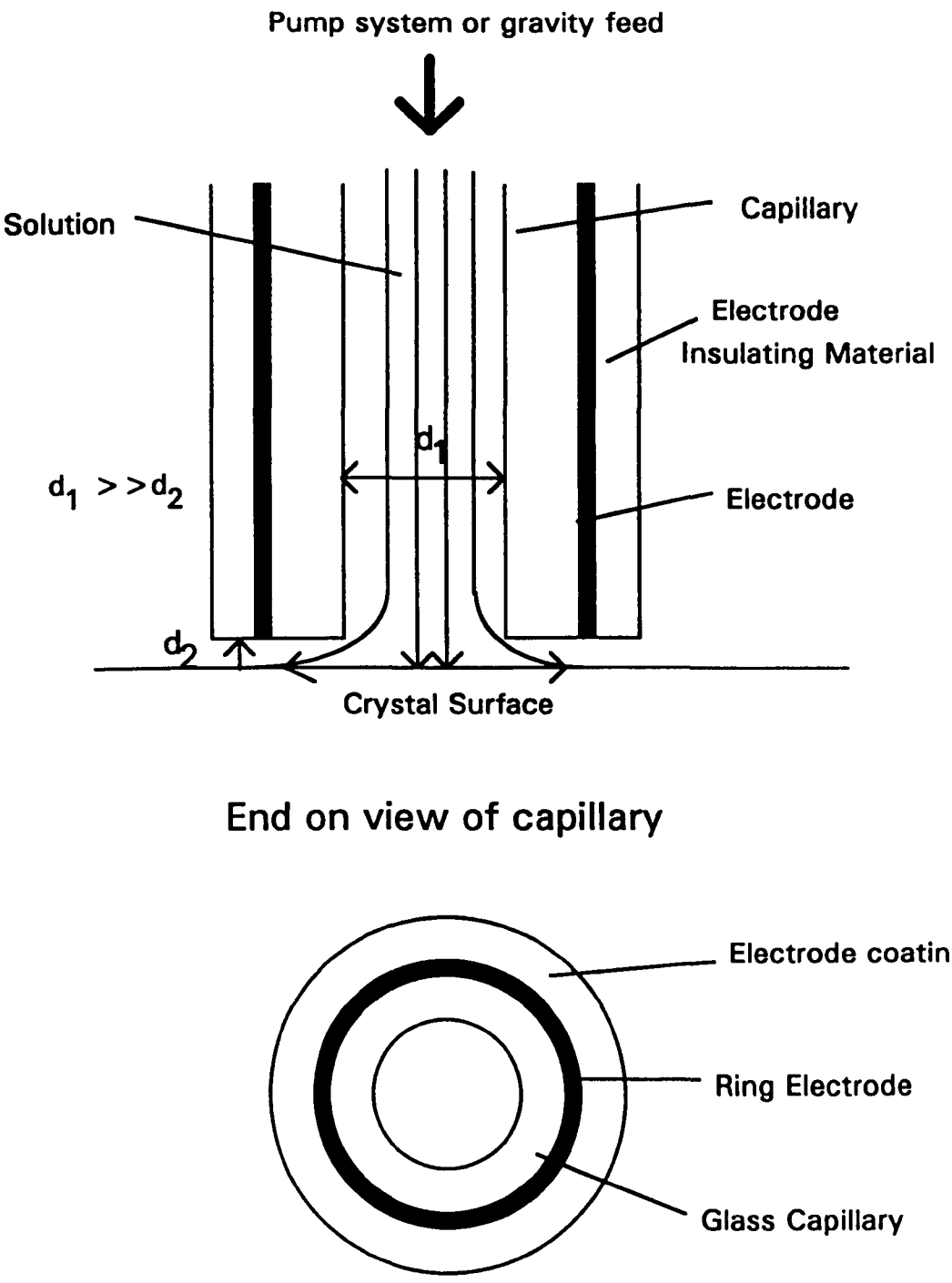

Figure 8.11. Schematic of the modified MJE employed in the proposed study of the dissolution of ionic materials.

$D = 6.5 \times 10^{-6}$ cm^2 s^{-1}), making the MJE attractive for the study of fast reactions. In particular, results from MJE voltammetry demonstrate that the MJE is a useful device for characterising rapid electron transfer kinetics under steady-state voltammetric conditions. Under these conditions the standard rate constant for the oxidation of ferrocyanide ions, at a Pt electrode, in 0.2 mol dm^{-3} strontium nitrate solutions was measured as 0.76 ± 0.11 cm s^{-1}, with a transfer coefficient in the range 0.35 - 0.55.

There is considerable scope for further increasing mass-transfer rates with the MJE, for example, by employing smaller nozzles and electrodes along with pumping systems which can deliver faster solution flow rates against high back pressures. These developments should enable the study of both very fast heterogeneous electron transfer processes and coupled solution reactions, under steady-state conditions which are largely free of complications from capacitative and resistive effects.

The possible modification of the MJE to incorporate a ring electrode, operating in a variable thin layer cell arrangement, represents a new, potentially powerful methodology for studying dissolution reactions of ionic crystals under very high and well-characterised mass transfer conditions.

List of Abbreviations

ADI	Alternating direction implicit
AFM	Atomic force microscope
AgQRE	Quasi silver reference electrode
BCF	Burton, Cabrera and Frank
CFMED	Channel flow method with electrochemical detection
DCE	Double channel electrode
DICM	Differential interference contrast microscopy
EC	Electron transfer preceding a chemical step
EM	Electron microscopy
et	Electron transfer
fcc	Face centred cubic
FEM	Finite element method
GC	Generation collection
GO	Glucose Oxidase
HDPE	High density polyethylene
IE-AFM	Integrated electrochemical-atomic force microscope
LSV	Linear sweep voltammogram
MI	Michelson interferometry
MIE	Multi-dimensional integral equation
MJE	Microjet electrode
MZ	Mach-Zender interferometry
Ox	Oxidised form of the redox couple
PM	Polarising light microscopy
PCM	Phase contrast microscopy
PSM	Phase shift microscopy
RDM	Rotating disc method

rds	Rate determining step
Red	Reduced form of the redox couple
RRDE	Rotating ring disc electrode
SECM	Scanning electrochemical microscope
SECMID	Scanning electrochemical microscope induced desorption
SCE	Saturated calomel electrode
SG/TC	Substrate generation/tip collection
SPM	Scanned probe microscope
STM	Scanning tunnelling microscope
TG/SC	Tip generation/substrate collection
TPM	Tip position modulation
UME	Ultramicroelectrode
WTE	Wall tube electrode

<u>List of Symbols</u>

a	Electrode radius
a_d	Area of the unit cell comprising a square dissolution nucleus
a_i	Activity of species *i*
A	Electrode area
b	Magnitude of the Burgers vector
c	Concentration of the mediator
c^*	Bulk concentration of the mediator
C	Normalised concentration
C_{crit}	Normalised interfacial concentration, below which a perfect surface becomes active to dissolution
d	Tip/substrate separation
d_n	Nozzle diameter

D_i	Diffusion coefficient of species *i*
$\Delta E_{1/4}$	Quartile potential
$\Delta E_{3/4}$	Quartile potential
E_s	Substrate potential
F	Faraday's constant
ΔG_d	Net change in free energy for a two-dimensional nucleus on a perfect surface
ΔG_s	Free energy change per unit area of surface of dissolved solid
ΔG_v	Free energy change per unit volume of solid dissolved in an undersaturated medium
h_d	Height of the unit cell comprising a square dissolution nucleus
H	Distance between the nozzle exit and the electrode surface
i	Current
$i(\infty)$	Bulk steady-state current
i_{MJE}	Steady-state current in the microjet electrode configuration
i_p	Peak current
i_{UME}	Steady-state current at an ultramicroelectrode
I_p	Ionic activity product
j	Notation for grid points in the radial direction
j_i	Flux of species *i*
k	Notation for grid points in the normal direction
k'	Dissolution rate constant
$k_{b,s}$	Potential dependent rate constant for the substrate reaction
k_c	Rate of decomposition
$k_{f,t}$	Potential dependent rate constant for the electrode reaction
k_n	Dissolution rate constant
k_o	Standard heterogeneous rate constant

k_t	Mass transfer coefficient
K_n	Normalised dissolution rate constant
K_s	Solubility product
L	Normalised tip/substrate separation
n	Order of the dissolution process
n_d	Number of unit cells in a square dissolution nucleus
n_e	Number of electrons transferred
n_α	Number of electrons transferred up to and including the rate determining step
N	Effective surface density of metal atoms
NE	Number of grid points over the electrode
NG	Number of grid points over the glass sheath
N_i	Flux of species *i* in the presence of diffusion and migration
NZ	Number of grid points in the normal direction
r	Cylindrical co-ordinates in the radial direction, to the electrode surface
r_{hc}	Radius of the hollow core
r_s	Radius of the glass sheath plus the electrode
R	Normalised radial direction
Re	Reynolds number
$\mathbf{Re}_{\mathbf{crit}}$	Critical reynolds number above which flow is turbulent
RG	Ratio of the radius of the probe to the radius of the electrode
S	Saturation ratio
Sc	Schmidt number
Sh	Sherwood number
t	Time
t_d	Tip/substrate diffusion time
t_i	Transference number of species *i*

t_{ind}	Induction time
t_{res}	Residence time
T	Temperature
u_i	Mobility of species *i*
$\overline{U}$	Mean solution velocity
υ	Solution viscosity
v_{scan}	Scan speed
v	Number of ions in the formula unit of an ionic salt
V	Potential scan rate
V_f	Volume flow rate
W	Rotation frequency
z	Cylindrical co-ordinates in the normal direction, to the electrode surface
z_i	Charge number of the species *i*
Z	Normalised normal direction
α	Transfer coefficient
β	Constant coefficient
γ	Surface Free Energy
γ_i	Activity coefficient of species *i*
η_i	Ionic equivalent conductance of species *i*
λ_i	Ratio of diffusion coefficients
μ	Rigidity modulus
ρ	Radial compression
υ	Solution viscosity
σ_b	Bulk undersaturation
σ_s	Surface undersaturation
τ	Normalised time

τ_{in}	Normalised time at which surface becomes insulating
Φ	Electric potential in solution
χ	Ratio of the standard heterogeneous rate constant to the mass transfer coefficient

APPENDIX 1
The Thomas Algorithm

The Thomas Algorithm[234,235,243] is an efficient method by which the matrix equation:

$$[T][u] = [d] \tag{A1.1}$$

may be solved for $[u]$, where $[T]$ denotes a tridiagonal matrix and $[u]$ and $[d]$ are vector quantities. The algorithm operates by factorising the tridiagonal matrix of $(i\text{-}1)^2$ elements, where T takes the form;

$$[T] = \begin{bmatrix} b_1 & c_1 & & & 0 \\ a_2 & b_2 & c_2 & & \\ & \ddots & \ddots & \ddots & \\ & & \ddots & \ddots & \ddots \\ & & & \ddots & \ddots \\ & & & a_{i-2} & b_{i-2} & c_{i-2} \\ 0 & & & a_{i-1} & b_{i-1} \end{bmatrix} \tag{A1.2}$$

Using the standard rules of matrix multiplication, $[T]$ can be separated into the components:

$$[T] = [T_L]\,[T_U] \tag{A1.3}$$

where;

$$[T_L][T_U] = \begin{bmatrix} \alpha_1 & & 0 \\ a_2 & \alpha_2 & \\ & \ddots & \ddots \\ & & a_{i-2}\alpha_{i-2} \\ 0 & & a_{i-1}\alpha_{i-1} \end{bmatrix} \begin{bmatrix} 1 & \beta_1 & 0 \\ & 1 & \beta_2 \\ & & \ddots \\ & & 1 \\ 0 & & 1 \end{bmatrix} \quad \text{(A1.4)}$$

for which α_i and β_i are readily determined as:

$$\alpha_1 = b_1 \quad \text{(A1.5)}$$

$$\beta_1 = c_1 / \alpha_1 \quad \text{(A1.6)}$$

$$\alpha_i = b_i - a_i\beta_{i-1} \quad i = 2,3.....i-1 \quad \text{(A1.7)}$$

$$\beta_i = c_i / \alpha_i \quad i = 2,3.....i-2 \quad \text{(A1.8)}$$

Writing;

$$[f] = [T_U][u] \quad \text{(A1.9)}$$

allows $[d]$ to be expressed in terms of $[f]$ as

$$[d] = [T_L][T_U][u] \quad \text{(A1.10)}$$

and therefore:

$$[d] = [T_L][f] \quad \text{(A1.11)}$$

Again, since the components of the matrices $[d]$ and $[T_L]$ are known, it is possible to determine the elements of $[f]$, where:

$$f_1 = d_1 / \alpha_1 \quad \text{(A.12)}$$

$$f_i = (d_i - a_i f_{i-1}) / \alpha_i \quad i = 2,3.....i-1 \quad \text{(A1.13)}$$

From equation (A1.9) since $[T_U]$ and $[f]$ are known an expression for the components of $[u]$ can now be formulated where:

$$u_{i-1} = f_{i-1} \quad i = 1 \quad \text{(A1.14)}$$

$$u_i = f_i - \beta_i u_{i+1} \quad i = i-2, i-3.....1 \quad \text{(A1.15)}$$

In this way $[u]$ is obtained from $[d]$.

APPENDIX 2

The SECM Negative Feedback Simulation

```
C MODIFIED SECM PROGRAM
C INSULATOR (NEGATIVE FEEDBACK SIMULATION)
C WITHOUT K SPACE COMPRESSION

      IMPLICIT DOUBLE PRECISION(A-H,O-Z)
      DOUBLE PRECISION LL,LLOG,LAMP(200),LAMQ(200),LAMZ
      INTEGER NP,NZ,NQ


      DIMENSION CO(0:200,0:200),F(200),ALR(200),BER(200),ALZ(200)
     >,BEZ(200),ALZG(200),BEZG(200),D(200),H(200),CN(0:200,0:200)
     >,RR(100),CCOMP(0:200)

C.....CREATION OF THE INITIAL GRID

C.....VALUE OF THE HALF TIMESTEP
      DELT=5.E-7
C.....NUMBER OF POINTS OVER ELECTRODE IN J SPACE (NQ)
      NQ=80
C.....NUMBER OF POINTS OVER GLASS IN J SPACE (NP)
      NP=80
C.....NUMBER OF POINTS IN K SPACE (NZ)
      NZ=100
C.....VALUE OF ELECTRODE RG
      RG=10.
C.....VALUE FOR (d/a) IN REAL SPACE (LL)
      LLOG=0.4
 501  LL=10.**LLOG
C.....SET VALUE FOR CONSTANT (F)
      FF=3.
      QT=LOG(1.+FF)
C.....DELQ IS (RHO) OVER THE ELECTRODE
      DELQ=QT/NQ
C.....SET VALUE FOR [1-R] OVER THE ELECTRODE (REXT)
      REXT=(1.-EXP(-DELQ))/FF
C.....SET VALUE FOR 'G' OVER THE GLASS TO MATCH GRIDS
      GG=0.1
      DIFF=0.1
 138  RES=NP*LOG(1.+(REXT*GG))-LOG(1.+((RG-1.)*GG))
      IF(RES.GT.0.00001)THEN
```

```
      GG=GG-DIFF
      DIFF=DIFF/10.
      GOTO 138
      ENDIF
      IF(RES.LT.-0.00001)THEN
      GG=GG+DIFF
      GOTO 138
      ENDIF
      PT=LOG(1.+(GG*(RG-1.)))
C.....DELP IS (RHO) OVER THE GLASS
      DELP=PT/NP
C.....SET GRID CONSTANTS OVER K SPACE
      DELZ=LL/NZ
      CURROLD=(DELZ**-1.)*3.142
C.....OPEN DATA FILE
      OPEN (67, FILE='calc.dat', STATUS='unknown')
C.....SETTING INITIAL BULK CONNCENTRATION VALUES
      DO 201 J=0,NQ+NP
      DO 202 K=0,NZ
      CO(J,K)=1.
 202  CONTINUE
 201  CONTINUE
C.....SETTING INITIAL SURFACE CONCENTRATIONS (OVER ELECTRODE)
      DO 30 J=0,NQ
      CO(J,0)=0.
      CCOMP(J)=1.
 30   CONTINUE
C.....CALCULATING LAMQ, LAMP, LAMZ CONSTANTS
C.....LAMZ (K SPACE)
 500  DO 150 K=1,NZ-1
      LAMZ=0.5*DELT/(DELZ*DELZ)
 150  CONTINUE
C.....LAMP (GLASS AREA) (J SPACE)
      DO 151 J=1,NP-1
      LAMP(J)=(0.5*GG*GG*DELT*(EXP(-2.*DELP*J)))/(DELP**2.)
 151  CONTINUE
C.....LAMQ (ELECTRODE AREA) (J SPACE)
      DO 190 J=1,NQ
      LAMQ(J)=0.5*FF*FF*DELT*(EXP(2.*(-QT+(J*DELQ))))/
     >(DELQ*DELQ)
 190  CONTINUE

C.....CONSTANTS FOR THE THOMAS ALGORITHM
C.....CONSTANTS WHEN VECTORS ARE RADIAL
C.....BOUNDARY (J=1) VALUES
```

```
      ALR(1)=1.+LAMQ(1)*(1.+(DELQ/2.)+(0.5*DELQ*(EXP(QT-DELQ))/
     >(FF+1.-(EXP(QT-DELQ)))))
      BER(1)=-LAMQ(1)*(1.+(DELQ/2.)+(0.5*DELQ*(EXP(QT-DELQ))/
     >(FF+1.-(EXP(QT-DELQ))))))/ALR(1)

C.....J SPACE OVER THE ELECTRODE
      DO 100 J=2,NQ
      ALR(J)=1.+(2.*LAMQ(J))+
     >(LAMQ(J)*(1.-(0.5*DELQ)-
     >(0.5*DELQ*(EXP(QT-(DELQ*J)))/(FF+1.-EXP(QT-(J*DELQ))))))*BER(J-1))
      BER(J)=-LAMQ(J)*(1.+(0.5*DELQ)+(0.5*DELQ*(EXP(QT-(J*DELQ)))/
     >(FF+1.-(EXP(QT-(J*DELQ))))))/ALR(J)
 100  CONTINUE

C.....J SPACE OVER THE INSULATOR
      DO 160 J=NQ+1,NQ+NP-2
      ALR(J)=1.+(2.*LAMP(J-NQ))+(LAMP(J-NQ)*BER(J-1)*
     >(1.+(DELP/2.)-(DELP*0.5*EXP((J-NQ)*DELP))*(((EXP((J-NQ)
     >*DELP))-1.+GG)**-1.)))
      BER(J)=LAMP(J-NQ)*(-1.+(DELP/2.)-(0.5*DELP*(EXP((J-NQ)*DELP))
     >*(((EXP((J-NQ)*DELP))-1.+GG)**-1.)))/ALR(J)
 160  CONTINUE

C.....J SPACE AT ELECTRODE EDGE
      ALR(NQ+NP-1)=1.+(LAMP(NP-1)*(2.+(BER(NQ+NP-2)*(1.+(DELP/2.)-
     >(DELP*0.5*(EXP((NP-1)*DELP)))*(((EXP((NP-1)*DELP))-
     >1.+GG)**-1.)))))

C.....CONSTANTS WHEN VECTORS ARE DOWN (K)
C.....BOUNDARY (K=1) OVER THE ELECTRODE
      ALZ(1)=(2.*LAMZ)+1.
      BEZ(1)=-(LAMZ*(1.-(0.5*DELZ)))/ALZ(1)

C.....K SPACE OVER THE ELECTRODE
      DO 300 K=2,NZ-2
      ALZ(K)=((2.*LAMZ)+1.)+(LAMZ*(1.+(0.5*DELZ))*BEZ(K-1))
      BEZ(K)=-(LAMZ*(1.-(0.5*DELZ)))/ALZ(K)
 300  CONTINUE

C.....K SPACE AT SUBSTRATE BOUNDARY (ELECTRODE)
      ALZ(NZ-1)=1.+(LAMZ*(1.+(0.5*DELZ)))+(LAMZ
     >*(1.+(0.5*DELZ))*BEZ(NZ-2))

C.....BOUNDARY (K=1) OVER THE GLASS
      ALZG(1)=LAMZ+1.-(DELZ*0.5*LAMZ)
```

```
      BEZG(1)=-(LAMZ*(1.-(0.5*DELZ)))/ALZG(1)

C.....K SPACE OVER GLASS
      DO 301 K=2,NZ-2
      ALZG(K)=((2.*LAMZ)+1.)+(LAMZ*(1.+(0.5*DELZ))*BEZG(K-1))
      BEZG(K)=-(LAMZ*(1.-(0.5*DELZ)))/ALZG(K)
  301 CONTINUE

C.....K SPACE AT SUBSTRATE BOUNDARY (GLASS)
      ALZG(NZ-1)=1.+(LAMZ*(1.+(0.5*DELZ)))+(LAMZ
     >*(1.+(0.5*DELZ))*BEZG(NZ-2))

C.....SAVING ALL CONSTANTS IN A DATA FILE
      OPEN (66, FILE='grid.dat', STATUS='unknown')
      WRITE (66,81) DELT, NP, NQ, NZ, RG, LL, FF, QT, DELQ, REXT
     >,GG, RES, DELP, BB, DELZ, CO
   81 FORMAT (/E12.5/3(I4/),10(E12.5/),E12.5//A2//(5(E12.5,2X)/))
      WRITE (66,82) 'ORDER: LAMZ, LAMQ, LAMP, ALR, BER, ALZ, BEZ
     >,ALZG, BEZG', LAMZ, LAMQ, LAMP, ALR, BER, ALZ, BEZ, ALZG
     >,BEZG
   82 FORMAT (/A40//(5(E12.5,2X)/))
      CLOSE(66)


C.....FIRST HALF TIMESTEP CALCULATION
C.....(K=OLD) AND (J=NEW)
C.....
  200 DO 1 K=1,NZ-1
      DO 2 J=1,NQ+NP-1
      D(J)=(LAMZ*(1.+(0.5*DELZ))*CO(J,K-1))-(((2.*LAMZ)-1.)
     >*CO(J,K))+(LAMZ*(1.-(0.5*DELZ))*CO(J,K+1))
    2 CONTINUE
C.....
      D(NQ+NP-1)=D(NQ+NP-1)+(LAMP(NP-1)*(1.-(DELP/2.)+
     >(0.5*DELP*(EXP((NP-1)*DELP))*(((EXP((NP-1)*DELP))-1.+GG)**-1.))))
C.....
      F(1)=D(1)/ALR(1)
      DO 3 J=2,NQ
      F(J)=(D(J)+(LAMQ(J)*(1.-(DELQ/2.)-(0.5*DELQ*(EXP(QT-(J*DELQ)))
     >/(FF+1.-(EXP(QT-(J*DELQ))))))*F(J-1)))/ALR(J)
    3 CONTINUE
C.....
      DO 41 J=NQ+1,NQ+NP-1
      F(J)=(D(J)+((LAMP(J-NQ)*(1.+(0.5*DELP)-
     >((0.5*DELP*(EXP((J-NQ)*DELP)))
```

```
     >*(((EXP((J-NQ)*DELP))-1.+GG)**-1.))))*F(J-1)))/ALR(J)
  41 CONTINUE

C.....CALCULATION OF NEW CONCENTRATIONS
     CN(INT(NQ+NP-1),K)=F(INT(NQ+NP-1))
C.....
     DO 4 J=NQ+NP-2,1,-1
     CN(J,K)=F(J)-(BER(J)*CN(J+1,K))
  4  CONTINUE
  1  CONTINUE

C.....UPDATING BOUNDARY CONDITIONS
     DO 101 J=NQ+1,NP+NQ-1
     CO(J,0)=CN(J,1)
  101 CONTINUE
     DO 102 J=1,NP+NQ-1
     CO(J,NZ)=CN(J,NZ-1)
  102 CONTINUE

C.....UPDATING REST OF CONCENTRATION VALUES
     DO 103 J=1,NP+NQ-1
     DO 104 K=1,NZ-1
     CO(J,K)=CN(J,K)
  104 CONTINUE
  103 CONTINUE

C.....CALCULATIONS IN OTHER DIRECTION
C.....(J=NEW OLD) AND (K=NEW NEW)
C.....
     DO 12 K=1,NZ-1
     H(K)=((1.-LAMQ(1)-(0.5*DELQ*LAMQ(1))
    >-(0.5*LAMQ(1)*DELQ*(EXP(QT-DELQ))/(FF+1.-(EXP(QT-DELQ)))
    >))*CO(1,K))+(LAMQ(1)*(1.+(0.5*DELQ)+(0.5*DELQ*(EXP(QT-DELQ))
    >/(FF+1.-EXP(QT-DELQ))))*CO(2,K))
  12 CONTINUE
C.....
     F(1)=H(1)/ALZ(1)
C.....
     DO 13 K=2,NZ-1
     F(K)=(H(K)+(LAMZ*(1.+(0.5*DELZ))*F(K-1)))/ALZ(K)
  13 CONTINUE
     CN(1,NZ-1)=F(NZ-1)
     DO 14 K=NZ-2,1,-1
     CN(1,K)=F(K)-(BEZ(K)*CN(1,K+1))
  14 CONTINUE
```

```
C.....
      DO 50 J=2,NQ
      DO 51 K=1,NZ-1
      H(K)=(LAMQ(J)*(1.-(0.5*DELQ)-(0.5*DELQ*(EXP(QT-(DELQ*J)))/
     >(FF+1.-(EXP(QT-(DELQ*J))))))*CO(J-1,K))+(CO(J,K)*
     >(1.-(2.*LAMQ(J))))
     >+(LAMQ(J)*(1.+(0.5*DELQ)+(0.5*DELQ*(EXP(QT-(J*DELQ)))/
     >(FF+1.-EXP(QT-(J*DELQ)))))*CO(J+1,K))
 51   CONTINUE
C.....
      F(1)=H(1)/ALZ(1)
      DO 53 K=2,NZ-1
      F(K)=(H(K)+(LAMZ*(1.+(0.5*DELZ))*F(K-1)))/ALZ(K)
 53   CONTINUE
      CN(J,NZ-1)=F(NZ-1)
      DO 54 K=NZ-2,1,-1
      CN(J,K)=F(K)-(BEZ(K)*CN(J,K+1))
 54   CONTINUE
 50   CONTINUE

C.....
      DO 60 J=NQ+1,NQ+NP-1
      DO 61 K=1,NZ-1
      H(K)=(LAMP(J-NQ)*(1.+(DELP*0.5)-(DELP*0.5*
     >(EXP((J-NQ)*DELP))*((EXP((J-NQ)*DELP))-1.+GG)**-1.))
     >*CO(J-1,K))+(CO(J,K)*(1.-(2.*LAMP(J-NQ))))
     >+(LAMP(J-NQ)*(1.-(0.5*DELP)+
     >(0.5*DELP*EXP((J-NQ)*DELP)*((EXP((J-NQ)
     >*DELP))-1.+GG)**-1.))*CO(J+1,K))
 61   CONTINUE
C.....
      F(1)=H(1)/ALZG(1)
      DO 63 K=2,NZ-1
      F(K)=(H(K)+(LAMZ*(1.+(0.5*DELZ))*F(K-1)))/ALZG(K)
 63   CONTINUE
      CN(J,NZ-1)=F(NZ-1)
      DO 64 K=NZ-2,1,-1
      CN(J,K)=F(K)-(BEZG(K)*CN(J,K+1))
 64   CONTINUE
C.....
 60   CONTINUE
      DO 360 J=1,NQ
      IF(CURR.GT.2.)THEN
      COM=0.95*CCOMP(J)
      ELSE IF(CURR.GT.1.)THEN
```

```
      COM=0.98*CCOMP(J)
      ELSE IF(CURR.GT.0.5)THEN
      COM=0.995*CCOMP(J)
      ELSE
      COM=0.999*CCOMP(J)
      ENDIF
      IF(CN(J,1).GT.COM)THEN
      KLM=KLM+1
      ENDIF
  360 CONTINUE

C.....
      DO 401 J=NQ+1,NQ+NP-1
      CO(J,0)=CN(J,1)
  401 CONTINUE
      DO 402 J=1,NQ+NP-1
      CO(J,NZ)=CN(J,NZ-1)
  402 CONTINUE
      DO 403 J=1,NQ+NP-1
      DO 404 K=1,NZ-1
      CO(J,K)=CN(J,K)
  404 CONTINUE
  403 CONTINUE

C.....
      DO 900 J=1,NQ
      CCOMP(J)=CN(J,1)
      IF(CO(J,1).LT.0.0.AND.III.EQ.0)THEN
      III=1
      ENDIF
  900 CONTINUE

C.....CONVERSION OF DELR TO DELQ
      DO 880 J=1,NQ-1
      RR(J)=1.-(((EXP(QT-((J+0.5)*DELQ)))-1.)/FF)
  880 CONTINUE
      RR(NQ)=1.
      FLUX=(CN(1,1)/DELZ)*((RR(1))**2.)
      DO 689 J=2,NQ-1
      FLUX=FLUX+(((RR(J))**2.)-((RR(J-1))**2.))
     >*CN(J,1)/DELZ
  689 CONTINUE
      FLUX=FLUX+(((RR(NQ))**2.)-((RR(NQ-1))**2.))
     > *CN(NQ,1)/DELZ
```

```
C.....NORMALISED CURRENT - CALCULATION
      CURR=FLUX*(3.1419/4.)
      T=T+DELT
      PRINT*,CURR,T
      IF(KLM.EQ.NQ.AND.III.EQ.0)THEN
      DELT=DELT*2.
      ENDIF
      IF(III.EQ.1)THEN
      DELT=DELT/2.
      ENDIF
      CURROLD=CURR
      III=0
      KLM=0
      FLUX=0.
      FLUXA=0.
      KK=KK+1

C.....SAVING THE DATA
      WRITE (67,11) CURR, T

C.....CONTINUING THE CYCLE
      IF (T.LT.80.) GOTO 500
      CLOSE (67)

C.....FORMAT STATEMENTS (?)
 606  FORMAT(1X,4F12.6)
 11   FORMAT(2X,E12.6,2X,E12.6)
      STOP
      END
```

References

1. H. G. Linge, *Adv. Colloid Interface Sci.*, 14, **1981**, 239.

2. Z. Zhang and G. H. Nancollas, *Reviews in Mineralogy*, 43, **1990**, 365.

3. K. Sangwal, *Etching of Crystals: Theory, Experiment and Application*, North Holland, Amsterdam, 1987.

4. W. K. Burton, N. Cabrera and F. C. Frank, *Phil. Trans. R. Soc. Lond.*, A243, **1951**, 299.

5. A. E. Blum and A. Lasaga, in *Aquatic Surface Chemistry*, W. Stumm (ed.), Wiley, New York, 1989, pp 255-292.

6. W. Stumm and G. Furrer, in *Aquatic Surface Chemistry*, W. Stumm (ed.),Wiley, New York, 1989, pp 197-219.

7. R. B. Heimann, *Crystals: Growth, Properties and Applications*, Springer-Verlag, Berlin, 1982.

8. G. H. Nancollas (ed.), *Biological Mineralization and Demineralization*, Springer-Verlag, Berlin, 1982.

9. A. W. Adamson, *Physical Chemistry of Surfaces*, John Wiley, New York, 1990.

10. M. Ohara and R.C. Reid, *Modeling Crystal Growth Rates from Solution*, Prentice Hall, Englewood Cliffs, N. J., 1973.

11. J. Schott, S. Brantley, D. Crerar, C. Guy, M. Borcsik and C. Willaime, *Geochim. Cosmochim. Acta*, 53, **1989**, 375.

12. B. Simon, in *Interfacial Aspects of Phase Transformations*, NATO ASI, Ser. C, vol. 87, B. Mutaftschiev (ed.), D. Reidel, The Netherlands, 1982, p. 639.

13. I. G. Gorichev and N. A. Kipriyanov, *Russ. Chem. Rev.*, 53, **1984**, 1039.

14. U. Svensson and W. Dreybrodt, *Chem. Geol.*, 100, **1992**, 129.

15. D. M. S. Little and G. H. Nancollas, *Trans. Faraday Soc.*, 66, **1970**, 3103.

16. J. G. Acker and R. H. Byrne, *Am. J. Sci.*, 289, **1989**, 1098.

17. L. N. Plummer, T. M. L. Wigley and D. L. Parkhurst, *Am. J. Sci.*, 278, **1978**, 179.

18. C. H. Bovington and A. L. Jones, *Trans. Faraday Soc.*, 66, **1970**, 2088.

19. R. M. Cornell, A. M. Posner and J. P. Quirk, *J. Inorg. Nucl. Chem.*, 36, **1974**, 1937.

20. G. Berger, E. Cadore, J. Schott and P. M. Dove, *Geochim. Cosmochim. Acta*, 58, **1994**, 541.

21. R. M. Cornell and P. W. Schindler, *Clays and Clay Minerals*, 35, **1987**, 347.

22. W. H. Casey, M. J. Carr and R. A. Graham, *Geochim. Cosmochim. Acta*, 52, **1988**, 1545.

23. T. D. Waite and F. M. M. Morel, *J. Colloid Interface Sci.*, 102, **1984**, 121.

24. H. Ohmoto, K. Hayashi, K. Onuma, K. Tsukamoto, A. Kitakaze, Y. Nakano and Y. Yamamoto, *Nature*, 351, **1991**, 634.

25. E. Eurybiades and L. N. Plummer, *Am. J. Sci.*, 282, **1982**, 45.

26. D. Hofmann and F. Moll, *Eur. J. Pharm. Biopharm.*, 40, **1994**, 142.

27. H. Sverdrup and I. Bjerle, *Vatten*, 38, **1982**, 59.

28. J. Morse, *Am. J. Sci.*, 274, **1974**, 97.

29. J. W. Morse and R. A. Berner, *Am. J. Sci.*, 272, **1972**, 840.

30. A. F. White, M. L. Peterson and M. F. Hochella, *Geochim. Cosmochim. Acta*, 58, **1994**, 1859.

31. M. B. Tomson and G. H. Nancollas, *Science*, 200, **1978**, 1059.

32. T. K. Sherwood, R. L. Pigford and C. R. Wilke, *Mass Transfer*, McGraw-Hill, New York, 1975.

33. E. L. Sjoberg and D. Rickard, *Geochim. Cosmochim. Acta*, 47, **1983**, 2281.

34. M. Litt and G. Serad, *Chem. Eng. Sci.*, 19, **1964**, 867.

35. For a review see: A. F. M. Barton and S. R. McConnel, *Chem. Austral.*, 46, **1979**, 427.

36. A. F. M. Barton and S. R. McConnel, *Trans. Faraday Soc.*, 67, **1971**, 2847.

37. D. R. Boomer, C. C. McCune and H. S. Fogler, *Rev. Sci. Instrum.*, 43, **1972**, 225.

38. K. Lund, H. S. Fogler, C. C. McCune and J. W. Ault, *Chem. Eng. Sci.*, 28, **1973**, 691.

39. G. H. Nancollas and H. G. Linge, *Calcif. Tissue Res.*, 12, **1973**, 193.

40. K. Lund, H. S. Fogler, C. C. McCune and J. W. Ault, *Chem. Eng. Sci.*, 30, **1975**, 825.

41. R. G. Compton and P. J. Daly, *J. Colloid Interface Sci.*, 101, **1984**, 159.

42. D. E. Giles, I. M. Ritchie and B.-A. Xu, *Hydrometallurgy*, 32, **1993**, 119.

43. D. T. Rickard and E. L. Sjöberg, *Am. J. Sci.*, 283, **1983**, 815.

44. V. P. Karshin and V. A. Grigoryan, *Russ. J. Phys. Chem.*, 44, **1970**, 762.

45. L. A. Virtsava, Yu. R. Dzelme, Yu. E. Tilikis and L. T. Bugaenko, *Russ. J. Phys. Chem.*, 52, **1978**, 1638.

46. E. L. Sjöberg and D. T. Rickard, *Geochim. Cosmochim. Acta*, 48, **1984**, 485.

47. E. L. Sjöberg and D. T. Rickard, *Chem. Geol.*, 42, **1984**, 119.

48. E. L. Sjöberg and D. T. Rickard, *Chem. Geol.*, 49, **1985**, 405.

49. R. G. Compton, P. J. Daly and W. A. House, *J. Colloid Interface Sci.*, 113, **1986**, 12.

50. R. G. Compton and P. J. Daly, *J. Colloid Interface Sci.*, 115, **1987**, 493.

51. I. N. MacInnis and S. L. Brantley, *Geochim. Cosmochim. Acta*, 56, **1992**, 1113.

52. I. N. MacInnis and S. L. Brantley, *Chem. Geol.*, 105, **1993**, 31.

53. B. van der Hoek, W. J. P. van Enckevort and W. H. van der Linden, *J. Cryst. Growth*, 61, **1983**, 181.

54. R. G. Compton, K. L. Pritchard and P. R. Unwin, *J. Chem. Soc., Chem. Commun.*, **1989**, 249.

55. R. G. Compton, K. L. Pritchard, P. R. Unwin, G. Grigg, P. Silvester, M. Lees and W. A. House, *J. Chem. Soc., Faraday Trans. 1*, 85, **1989**, 4335.

56. A. J. Barwise, R. G. Compton and P. R. Unwin, *J. Chem. Soc., Faraday Trans.*, 86, **1990**, 137.

57. P. R. Unwin and R. G. Compton, *J. Chem. Soc., Faraday Trans.*, 86, **1990**, 1517.

58. R. Orton and P. R. Unwin, *J. Chem. Soc., Faraday Trans.*, 89, **1993**, 3947.

59. R. G. Compton, C. T. Walker, P. R. Unwin and W. A. House, *J. Chem. Soc., Faraday Trans.*, 86, **1990**, 849.

60. R. G. Compton and K. L. Pritchard, *Philos. Trans. R. Soc. London*, A330, **1990**, 47.

61. C. A. Brown, R. G. Compton and C. A. Narramore, *J. Colloid Interface Sci.*, 160, **1993**, 372.

62. R. G. Compton and C. A. Brown, *J. Colloid Interface Sci.*, 165, **1994**, 445.

63. R. G. Compton and P. R. Unwin, *Philos. Trans. R. Soc. London*, A330, **1990**, 1.

64. V. M. Gortikov and L. I. Panteleva, *J. Gen. Chem. U.S.S.R.*, 7, **1937**, 56.

65. V. G. Levich, *Acta Phys. -Chim. URSS*, 17, **1942**, 257.

66. V. G. Levich, *Physicochemical Hydrodynamics*, Prentice-Hall, Englewood Cliffs, N. J., 1973, pp 60 -70.

67. V. Yu Filinovskii and Yu. V. Pleskov, in *Comprehensive Treatise of Electrochemistry*, vol. 9, E. Yeager, J. O' M. Bockris, B. E. Conway and S. Sarangapani (eds.), Plenum Press, New York, 1984.

68. A. F. M. Barton and N. M. Wilde, *Trans. Faraday Soc.*, 67, **1971**, 3590.

69. M. Bayramoglu, N. Demircioglu and B. Keskinler, *Int. J. Miner. Process.*, 39, **1993**, 19.

70. H. Tominaga, H. Adzum and T. Isobe, *Bull. Chem. Soc. Japan*, 14, **1939**, 348.

71. A. F. M. Barton and S. R. McConnel, *J. Chem. Soc., Faraday. Trans.*, 70, **1974**, 355.

72. H. G. Linge and G. H. Nancollas, *Calc. Tiss. Res.*, 12, **1973**, 193.

73. A. J. Bard and L. R. Faulkner, *Electrochemical Methods*, John Wiley, New York, 1980, pp. 290-297.

74. R. G. Compton and K. L. Pritchard, *J. Chem. Soc., Faraday Trans.*, 86, **1990**, 129.

75. P. G. Vekilov, Yu. G. Kuznetzov and A. A. Chernov, *J. Cryst. Growth*, 102, **1990**, 706.

76. A. A. Chernov and L. N. Rashkovich, *J. Cryst. Growth*, 84, **1987**, 389.

77. A. A. Chernov and A. I. Malkin, *J. Cryst. Growth*, 92, **1988**, 432.

78. K. Onuma, K. Tsukamoto and I. Sunagawa, *J. Cryst. Growth*, 89, **1988**, 177.

79. K. Maiwa, K. Tsukamoto and I. Sunagawa, *J. Cryst. Growth*, 98, **1989**, 590.

80. K. Onuma, K. Tsukamoto and I. Sunagawa, *J. Cryst. Growth*, 98, **1989**, 384.

81. T. Azuma, K. Tsukamoto and I. Sunagawa, *J. Cryst. Growth*, 98, **1989**, 371.

82. K. Maiwa, K. Tsukamoto and I. Sunagawa, *J. Cryst. Growth*, 102, **1990**, 43.

83. K. Onuma, K. Tsukamoto and I. Sunagawa, *J. Cryst. Growth*, 110, **1991**, 724.

84. I. Sunagawa, *Aquatic Sci.*, 55, **1993**, 347.

85. S. Tolansky, *An Introduction to Interferometry*, Longman, London, p 113.

86. K. Tsukamoto and I. Sunagawa, *J. Cryst. Growth*, 71, **1985**, 183.

87. N. Cabrera and M. M. Levine, *Phil. Mag.*, 1, **1956**, 459.

88. B. van der Hoek, J. P. van der Eerden and P. Bennema, *J. Cryst. Growth*, 56, **1982**, 621.

89. B. van der Hoek, J. P. van der Eerden, P. Bennema and I. Sunagawa, *J. Cryst. Growth*, 58, **1982**, 365.

90. H. K. Wickramasinghe, *Sci. Am.*, 261, **1989**, 98.

91. S. R. Snyder and H. S. White, *Anal. Chem.*, 64, **1992**, R112.

92. R. J. Behm, N. Garcia and H. Rohrer (eds.); *Scanning Tunneling Microscopy and Related Methods,* NATO ASI Series; Kluwer, The Netherlands, 1990; Vol. 184.

93. R. Wiesendanger, *Scanning Probe Microscopy and Spectroscopy,* Cambridge Univ. Press, Cambridge, U. K., 1994.

94. D. A. Bonnell, (ed.); *Scanning Tunneling Microscopy and Spectroscopy: Theory, Techniques and Applications;* VCH: New York, 1993 and references therein.

95. D. Rugar and P. K. Hansma, *Physics Today,* October issue, **1990**, 23.

96. C. F. Quate, *Surf. Sci.,* 299/300, **1994**, 980.

97. G. Binning and F. Ohnesorge, *Science*, 260, **1993**, 1451.

98. M. Radmacher, M. Fritz, H. G. Hansma and P. K. Hansma, *Science*, 256, **1994**, 1577.

99. G. Binnig, C. F. Quate and C. Gerber, *Phys. Rev. Lett.*, 56, **1986**, 930.

100. J. P. Hirth and G. M. Pound, *J. Chem. Phys.*, 26, **1957**, 1216.

101. A. J. Gratz, S. Manne and P. K. Hansma, *Science,* 251, **1993**, 1343.

102. S. Kipp, R. Lacmann and M. A. Schneeweiss, *J. Cryst. Growth,* 141, **1994**, 291.

103. P. E. Hillner, A. J. Gratz, S. Manne and P. K. Hansma, *Geology*, 20, **1992**, 359.

104. P. E. Hillner, A. J. Gratz, S. Manne and P. K. Hansma, *Ultramicroscopy*, 42, **1992**, 1387.

105. W. U. Schmidt and R. C. Alkire, *J. Electrochem. Soc.*, 141, **1994**, L85.

106. A. C. Hillier and M. D. Ward, *Science,* 263, **1994**, 1261.

107. P. W. Carter, A. C. Hillier and M. D. Ward, *Mol. Cryst. Liq. Cryst.*, 242, **1994**, 53.

108. P. W. Carter, A. C. Hillier and M. D. Ward, *J. Am. Chem. Soc.*, 116, **1994**, 944.

109. S. Manne, J. P. Cleveland, G. D. Stucky and P. K. Hansma, *J. Cryst. Growth,* 130, **1993**, 333.

110. D. Bosbach and W. Rammensee, *Geochim. Cosmochim. Acta,* 58, **1994**, 84.

111. C. Hall and D. C. Cullen, *AIChE J.*, 42, **1996**, 232.

112. T. Prohaska, G. Freidbacher and M. Grasserbauer, *F. J. Anal. Chem.*, 349, **1994**, 190.

113. A. Putnis, J. L. Junta-Rosso and M. F. Hochella, *Geochim. Cosmochim. Acta*, 59, **1995**, 4623.

114. A. J. Bard, F. -R. Fan, D. Pierce, P. R. Unwin, D. O. Wipf and F. Zhou, *Science*, 254, **1991**, 68.

115. P. R. Unwin and J. V. Macpherson, *Chem. Ind.*, 21, **1995**, 874.

116. A. J. Bard, F. -R. Fan and M. V. Mirkin in Electroanalytical Chemistry, vol. 18, A. J. Bard (ed.), Marcel Dekker: New York, 1994.

117. M. V. Mirkin, *Anal. Chem.*, 68, **1996**, 177A.

118. M. Arca, A. J. Bard, B. R. Horrocks, T. C. Richards and D. A. Treichel, *Analyst*, 119, **1994**, 719.

119. R. C. Engstrom, M. Webber, D. J. Wunder, R. Burgess and S. Winquist, *Anal. Chem.*, 58, **1986**, 844.

120. R. C. Engstrom, T. Meaney, R. Tople and R. M. Wightman, *Anal. Chem.*, 59, **1987**, 2005.

121. A. J. Bard, F. -R. Fan, J, Kwak and O. Lev, *Anal. Chem.*, 61, **1989**, 132.

122. J. Kwak and A. J. Bard, *Anal. Chem.*, 61, **1989**, 1221.

123. D. T. Pierce, P. R. Unwin and A. J. Bard, *Anal. Chem.*, 64, **1992**, 1795.

124. D. T. Pierce and A. J. Bard, *Anal. Chem.*, 65, **1993**, 3598.

125. G. Wittstock, K. Yu, H. B. Halsall, T. H. Ridgway and W. R. Heineman, *Anal. Chem.*, 67, **1995**, 3578.

126. M.V. Mirkin, F. -R. F. Fan and A. J. Bard, *Science*, 257, **1992**, 364.

127. J. Kwak, C. Lee and A. J. Bard, *J. Electrochem. Soc.*, 137, **1990**, 1481.

128. C. Lee and A. J. Bard, *Anal. Chem.*, 62, **1990**, 1906.

129. M. H. T. Frank and G. Denuault, *J. Electroanal., Chem.*, 354, **1993**, 331.

130. C. I. Jeon and F. C. Anson, *Anal. Chem.*, 64, **1992**, 2021.

131. F. -R. F. Fan, M. V. Mirkin and A. J. Bard, *J. Phys. Chem.*, 98, **1994**, 1475.

132. P. R. Unwin and A. J. Bard, *J. Phys. Chem.*, 96, **1992**, 5035.

133. S. B. Basame and H. S. White, *J. Phys. Chem.*, 99, **1995**, 16430.

134. D. O. Wipf and A. J. Bard, *J. Electrochem. Soc.*, 138, **1991**, 469.

135. A. J. Bard, M. V. Mirkin, P. R. Unwin and D. O. Wipf, *J. Phys. Chem.*, 96, **1992**, 1861.

136. R. C. Engstrom, B. Small and L. Kattan, *Anal. Chem.*, 64, **1992**, 241.

137. T. Solomon and A. J. Bard, *Anal. Chem.*, 67, **1995**, 2787.

138. C. Wei, A. J. Bard and M. V. Mirkin, *J. Phys. Chem.*, 99, **1995**, 16033.

139. T. Solomon and A. J. Bard, *J. Phys. Chem.*, 99, **1995**, 17487.

140. R. J. Forster, *Chem. Soc. Rev.*, 23, **1994**, 289.

141. R. M. Wightman, *Science*, 240, **1988**, 415.

142. R. M. Penner and N. S. Lewis, *Chem. Ind.*, 21, **1991**, 788.

143. J. Heinze, *Angew. Chem. Int. Ed.*, 32, **1993**, 1268.

144. J. Newman, *J. Electrochem. Soc.*, 113, **1966**, 501.

145. Y. Saito, *Rev. Polarogr.*, 15, **1968**, 177.

146. A. J. Bard, G. Denuault, R. A. Friesner, B. C. Dornblaser and L. S. Tuckerman, *Anal. Chem.*, 63, **1991**, 1282.

147. P. R. Unwin and A. J. Bard, *J. Phys. Chem.*, 95, **1991**, 7814.

148. M. V. Mirkin, H. Yang and A. J. Bard, *J. Electrochem. Soc.*, 139, **1992**, 2212.

149. F. Zhou, P. R. Unwin and A. J. Bard, *J. Phys. Chem.*, 96, **1992**, 5035.

150. D. A. Treichel, M. V. Mirkin and A. J. Bard, *J. Phys. Chem.*, 98, **1994**, 5751.

151. A. J. Bard and L. R. Faulkner, *Electrochemical Methods*, Wiley: New York, 1980, p. 143.

152. J. Wang, L. Wu and R. Li, *J. Electroanal. Chem.*, 272, **1989**, 285.

153. M. V. Mirkin, T. C. Richards and A. J. Bard, *J. Phys. Chem.*, 97, **1993**, 7672.

154. M. V. Mirkin, L. O. S. Bulhoes and A. J. Bard, *J. Am. Chem. Soc.*, 115, **1993**, 201.

155. D. Mandler and A. J. Bard, *J. Electrochem. Soc.*, 137, **1990**, 1079.

156. Y. M. Wuu, F. -R. F. Fan and A. J. Bard, *J. Electrochem. Soc.*, 136, **1989**, 885.

157. I. Shohat and D. Mandler, *J. Electrochem. Soc.*, 141, **1994**, 995.

158. S. Meltzer and D. Mandler, *J. Electrochem. Soc.*, 142, **1995**, L82.

159. H. Sugimura, T. Uchida, N. Kitamura, N. Shimo and H. Masuhara, *J. Electroanal. Chem.*, 361, **1993**, 57.

160. C. Wei and A. J. Bard, *J. Electrochem. Soc.*, 142, **1995**, 2523.

161. D. Mandler and A. J. Bard, *J. Electrochem. Soc.*, 137, **1990**, 2468.

162. D. Mandler and A. J. Bard, *Langmuir*, 6, **1990**, 1489.

163. D. Mandler and A. J. Bard, *J. Electrochem. Soc.*, 136, **1989**, 3143.

164. O. E. Husser, D. H. Craston and A. J. Bard, *J. Vac. Sci. Technol.*, B6, **1988**, 1873.

165. S. Meltzer and D. Mandler, *J. Chem. Soc., Faraday Trans.*, 91, **1995**, 1019.

166. E. R. Scott, H. S. White and J. B. Phipps, *Anal. Chem.*, 65, **1993**, 1537.

167. E. R. Scott, H. S. White and J. B. Phipps, *J. Membrane Sci.*, 58, **1991**, 71.

168. E. R. Scott, A. I. Laplaza, H. S. White and J. B. Phipps, *Pharm. Res.*, 10, **1993**, 1699.

169. E. R. Scott, J. B. Phipps and H. S. White, *J. Invest. Derm.*, 104, **1995**, 142.

170. S. Nugues and G. Denuault, *J. Electroanal. Chem.*, 408, **1996**, 125.

171. J. V. Macpherson, M. A. Beeston, P. R. Unwin, N. P. Hughes and D. Littlewood, *J. Chem. Soc. Faraday Trans.*, 91, **1995**, 1407.

172. J. V. Macpherson, M. A. Beeston, P. R. Unwin, N. P. Hughes and D. Littlewood, *Langmuir*, 11, **1995**, 3959.

173. C. Lee, J. Kwak and A. J. Bard, *Proc. Natl. Acad. Sci.*, 87, **1990**, 1740.

174. H. Sugimira, N. Shimo, N. Kitamura and H. Masuhara, *J. Electroanal. Chem.*, 346, **1993**, 147.

175. F. -R. Fan and A. J. Bard, *Science*, 270, **1995**, 1849.

176. D. O. Wipf and A. J. Bard, *J. Electrochem. Soc.*, 138, **1991**, L4.

177. J. L. Gilbert, S. M. Smith and E. P. Lautenschlanger, *J. Biomed. Mater. Res.*, 27, **1993**, 1357.

178. A. T. Hubbard and F. C. Anson in *Electroanalytical Chemistry*, vol. 4, A. J. Bard (ed), Marcel Dekker: New York, 1970, p. 156.

179. M. V. Mirkin and A. J. Bard, *Anal. Chem.*, 64, **1992**, 2293.

180. D. O. Wipf, E. W. Kristensen, M. R. Deakin and R. M. Wightman, *Anal. Chem.*, 60, **1988**, 306.

181. A. M. Bond, T. L. E. Henderson, D. R. Mann, T. F. Mann, W. Thormann and C. G. Zoski, *Anal. Chem.*, 60, **1988**, 1878.

182. M. I. Montenegro, D. Pletcher, *J. Electroanal. Chem.*, 200, **1986**, 371.

183. M. V. Mirkin and A. J. Bard, *J. Electrochem. Soc.*, 139, **1992**, 3535.

184. T. C. Richards, A. J. Bard, A. Cusanelli and D. Sutton, *Organometallics*, 13, **1994**, 757.

185. F. Zhou and A. J. Bard, *J. Am. Chem. Soc.*, 116, **1994**, 393.

186. B. P. Jackson, S. M. Dietz and R. M. Wightman, *Anal. Chem.*, 67, **1995**, 115.

187. W. J. Albery and M. L. Hitchman, *Ring Disc Electrodes;* Oxford University Press: Oxford, UK, 1971.

188. P. R. Unwin and R. G. Compton in *Comprehensive Chemical Kinetics*, R. G. Compton and A. Hamnett (eds.), Elsevier: Amsterdam, 1989; Vol. 29, pp. 173-296.

189. M. Brannstrom, in *Sensory Mechanisms in Dentine*, D. J. Anderson (ed.), Pergamon Press, Oxford, 1962.

190. D. H. Pashley, J. A. O'Meara, E. E. Kepler, S. E. Galloway, S. M. Thompson and F. P. Stewart, *J. Periodontol.*, 55, **1984**, 522.

191. E. Maita, M. D. Simpson, L. Tao and D. H. Pashley, *Arch. Oral Biol.*, 36, **1991**, 103.

192. N. Vongsavan aand B. Matthews, *Arch. Oral Biol.*, 37, **1992**, 175.

193. N. Vongsavan aand B. Matthews, *Arch. Oral Biol.*, 36, **1991**, 641.

194. O. W. Reeder, R. E. Walton, M. J. Livingston and D. H. Pashley, *J. Dent. Res.*, 57, **1978**, 187.

195. D. H. Pashley, R. Nelson and E. L. Pashley, *Arch. Orals Biol.*, 26, **1981**, 707.

196. J. Millman, *Microelectronics*, McGraw-Hill, 1979.

197. B. Tuck and C. Christopoulos, *Physical Electronics*, Wiley, New York, 1986.

198. J. V. Macpherson, C. J. Slevin and P. R. Unwin, *J. Chem. Soc., Faraday Trans.*, in press

199. H. Kaesche, *Metallic Corrosion*, NACE, Houston, TX, 1985 and references cited therein.

200. D. O. Wipf, *Colloids and Surfaces A:Physicochemical and Eng. Aspects*, 93, **1994**, 251.

201. N. Casillas, S. Charlebois, W. H. Smyrl and H. S. White, *J. Electrochem. Soc.*, 141, **1994**, 636.

202. N. Casillas, S. Charlebois, W. H. Smyrl and H. S. White, *J. Electrochem. Soc.*, 140, **1993**, L142.

203. A. J. Bard, G. Denuault, C. Lee, D. Mandler and D. O. Wipf, *Acc. Chem. Res.*, 23, **1990**, 357.

204. H. Shiku, T. Takeda, H. Yamada, T. Matsue and I. Uchida, *Anal. Chem.*, 67, **1995**, 312.

205. R. M. Penner, M. J. Hearn, T. L. Longin and N. S. Lewis, *Science*, 250, **1990**, 1118.

206. C. Lee, D. O. Wipf, A. J. Bard, K. Bartels and A. C. Bovik, *Anal. Chem.*, 63, **1991**, 2442.

207. K. A. Ellis, M. D. Pritzker and T. Z. Fahidy, *Anal. Chem.*, 67, **1995**, 4500.

208. D. O.Wipf and A. J. Bard, *Anal. Chem.*, 64, **1992**, 1362.

209. D. O. Wipf, A. J. Bard and D. E. Tallman, *Anal. Chem.*, 65, **1993**, 1373.

210. K. Borgwarth, D. G. Ebling and J. Heinze, *Ber. Bunsenges. Phys. Chem.*, 98, **1994**, 1317.

211. K. Borgwarth, D. G. Ebling and J. Heinze, *Electrochim. Acta.*, 40, **1994**, 1455.

212. G. Denuault, M. H. Troise-Frank and L. M. Peter, *Faraday Disc. Chem. Soc.*, 94, **1992**, 23.

213. J. L. Luo, Y. C. Lu and M. B. Ives, *J. Electroanal. Chem.*, 326, **1992**, 51.

214. T. J. Kemp, P. R. Unwin and L. Vincze, *J. Chem. Soc., Faraday Trans.*, 91, **1995**, 3893.

215. B. R. Horrocks, M. V. Mirkin, D. T. Pierce, A. J. Bard, G. Nagy and K. Toth, *Anal. Chem.*, 65, **1993**, 1213.

216. C. Wei, A. J. Bard, G. Nagy and K. Toth, *Anal. Chem.*, 34, **1995**, 1346.

217. B. R. Horrocks, D. Schmidtke, A. Heller and A. J. Bard, *Anal. Chem.*, 65, **1993**, 3605.

218. J. V. Macpherson, Final Year Undergraduate Project, University of Warwick, 1993.

219. J. V. Macpherson and P. R. Unwin, *J. Chem. Soc., Faraday Trans.*, 89, **1993**, 1883.

220. J. V. Macpherson and P. R. Unwin, *J. Phys. Chem.*, 98, **1994**, 1704.

221. C. W. Davies and G. H. Nancollas, *Trans. Faraday Soc.*, 51, **1955**, 818.

222. J. R. Howard, G. H. Nancollas and N. Purdie, *Trans. Faraday Soc.*, 56, **1960**, 278.

223. A. L. Jones, *Trans. Faraday Soc.*, 59, **1963**, 2355.

224. P. Delahay, *New Instrumental Methods in Electrochemistry*, Interscience, New York, 1954.

225. R. S. Nicholson and I. Shain, *Anal. Chem.*, 36, **1964**, 706.

226. R. S. Nicholson and I. Shain, *Anal. Chem.*, 37, **1965**, 178.

227. R. S. Nicholson and I. Shain, *Anal. Chem.*, 37, **1965**, 667.

228. W. H. Reinmuth, *Anal. Chem.*, 33, **1961**, 667.

229. S. W. Feldberg, in *Electroanalytical Chemistry*, vol. 3, A. J. Bard (ed.), Marcel Dekker: New York, 1969, p. 199.

230. S. Pons, in *Electroanalytical Chemistry*, vol. 13, A. J. Bard (ed.), Marcel Dekker: New York, 1984, p. 115.

231. S. S. Rao, *The Finite Element Method in Engineering*, Permagon Press, New York, 1982.

232. K. J. Huebner and E. A. Thornton, *The Finite Element Method for Engineers*, 2nd ed., Wiley-Interscience, New York, 1982.

233. T. Joslin and D. J. Pletcher, *J. Electroanal. Chem.*, 49, **1974**, 172.

234. S. W. Feldberg, *J. Electroanal. Chem.*, 127, **1981**, 1.

235. A. J. Bard, J. A. Crayston, G. P. Kittlesen, T. Varco Shea and M. S. Wrighton, *Anal. Chem.*, 58, **1986**, 2321.

236. R. A. Friesner, L. S. Tuckerman, B. C. Dornblaser and T. V. Russo, *J. Sci. Comput.* 4, **1989**, 327.

237. M. V. Mirkin and A. J. Bard, *J. Electroanal. Chem.*, 323, **1992**, 1.

238. M. V. Mirkin and A. J. Bard, *J. Electroanal. Chem.*, 323, **1992**, 29.

239. D. W. Peaceman and H. H. Rachford, *J. Soc. Ind. Appl. Math.*, 3, **1955**, 28.

240. L. Lapdius and G. F. Pinder, *Numerical Solution of Partial Differential Equations in Science and Engineering*, Wiley, New York, 1982.

241. W. F. Ames, *Numerical Methods of Partial Differential Equations*, Wiley, New York, 1977.

242. J. Heinze, *J. Electroanal. Chem.*, 124, **1981**, 73.

243. J. Heinze and M. Störzbach, *Ber. Bunsenges. Phys. Chem.*, 90, **1986**, 1043.

244. J. Heinze, *Ber. Bunsenges. Phys. Chem.*, 85, **1981**, 1096.

245. P. R. Unwin and R. D. Martin, manuscript in preparation.

246. C. M. A. Brett and A. M. O. Brett, *Electrochemistry, principles, methods and applications*, Oxford University Press, Oxford, 1993, p. 94.

247. R. M. Wightman, *Science*, 240, **1988**, 415.

248. D. Britz, *Digital Simulation in Electrochemistry*, Springer-Verlag, New York, 1988, p. 93.

249. L. H. Thomas, *Watson Sci. Comput. Lab. Rep.*, Columbia University, New York, 1949.

250. D. Britz, *Anal. Chim. Acta.*, 19, **1987**, 277.

251. R. M. Wightman and D. O. Wipf, in *Electroanalytical Chemistry*, vol. 15, A. J. Bard (ed.), Marcel Dekker: New York, 1989, p. 267.

252. F. A. Cotton and G. Wilkinson, *Advanced Inorganic Chemistry*, Wiley, New York, 1988, p. 942.

253. M. E. Clark, J. L. Ingram, E. E. Blakely and W. J. Bowyer, *J. Electroanal. Chem.*, 385, **1995**, 157.

254. S. J. Slade and G. F. Pegg, *Ann. Appl. Bio.*, 122, **1992**, 233.

255. J. M. Diazcruz, M. Esteban, M. A. G. T. Vanderhoop and H. P. Vanleeuwan, *Anal. Chem.*, 57, **1992**, 1769.

256. C. Beriet and D. Pletcher, *J. Electroanal. Chem.*, 361, **1993**, 93.

257. S. A. Campbell and L. M. Peter, *J. Electroanal. Chem.*, 364, **1994**, 257.

258. A. Seidell and W. F. Linke, *Solubilities: Inorganic and Metal-Organic Compounds*, 4th edition, American Chemical Society: Washington D.C., 1958; vol. 2, pp.69-70, pp. 73-74.

259. R. N. Adams, *Electrochemistry at Solid Electrodes*, Marcel Dekker, New York, 1969.

260. NAG Fortran Library, Numerical Algorithms Group; Oxford, UK, 1988.

261. D. Shoup and A. Szabo, *J. Electroanal. Chem.*, 140, **1982**, 237.

262. M. W. Porter and R. C. Spiller, *The Barker Index of Crystals*, W. Heffer and Sons, Cambridge, UK, 1958, vol. 2 (part 2), pp. 83-84.

263. G. Denuault, M. V. Mirkin and A. J. Bard, *J. Electroanal. Chem.*, 308, **1991**, 27.

264. A. E. Nielsen, *Kinetics of Precipitation*, Macmillan, New York, 1964.

265. R. A. Berner and J. W. Morse, *Am. J. Sci.*, 274, **1974**, 108.

266. M. V. Mirkin, F. -R. F. Fan and A. J. Bard, *J. Electroanal. Chem.*, 328, **1992**, 47.

267. M. W. Verbrugge, and D. R. Baker, *J. Phys. Chem.*, 96, **1992**, 4572 and references therein.

268. K. B. Oldham, *J. Electroanal. Chem.*, 337, **1992**, 91.

269. D. R. Baker, M. W. Verbrugge and J. Newman, *J. Electroanal. Chem.*, 314, **1991**, 23.

270. D. B. Pendley, H. D. Abruna, J. D. Norton, W. E. Benson, and H. S. White, *Anal. Chem.*, 63, **1991**, 2766.

271. P. R. Unwin and J. V. Macpherson, *Chem. Soc. Rev.*, 24, **1995**, 109.

272. J. V. Macpherson and P. R. Unwin, *Prog. React. Kinet.*, 20, **1995**, 185.

273. S. A. Brown and D. A. MacInnes, *J. Am. Chem. Soc.* 57, **1935**, 459.

274. J. S. Newman, *Electrochemical Systems*, Prentice-Hall, Englewood Cliffs, NJ, 1991, ch. 11.

275. I. M. Kolthoff and J. J. Lingane, *Polarography*, Interscience, New York, 1965, ch. 7.

276. J. Xu and G. C. Farrington, *J. Electrochem. Soc.*, 143, **1996**, L44.

277. J. S. Newman, *Electrochemical Systems*, Prentice-Hall, Englewood Cliffs, NJ, 1991, p255.

278. R. R. M. Johnston and M. Spiro, *J. Phys. Chem.*, 71, **1967**, 3784.

279. A. Pinkus and P. Haurez, *Bull. Soc. Chim. Belg.*, 47, **1938**, 532.

280. A. A. Hoyen and R. M. Cole, *J. Colloid Interface Sci.*, 41, **1972**, 93.

281. T. Prohaska, G. Friedbacher and M. Grasserbauer, *Fres. J. Anal. Chem.*, 349, **1994**, 190.

282. F. J. Giessibl and G. Binnig, *Ultramicroscopy*, 42, **1992**, 281.

283. N. Nakajima, M. Kageshima, N. Ara, M. Yoshimira and A. Kawazu, *Appl. Phys. Letts.*, 62, **1993**, 1892.

284. K. Yase, N. Ara and A. Kawazu, *Molecular Crystals and Liquid Crystals Science and Technol. Sec.; Section A - Molecular Crystals and Liquid Crystals*, 247 **1994**, 183.

285. T. Mussini and G. Faita in *Encyclopedia of Electrochemistry of the Elements*, A. J. Bard (ed.), Marcel Dekker, N. J., 1973, p.81.

286. T. Iwasita and M. C. Giordano, M. C. *Electrochim. Acta*, 14, **1969**, 1045.

287. J. C. Marchon, *C. R. Acad. Sci. Paris, Ser. C.*, 267, **1968**, 1123.

288. S. J. O'Shea, R. M Atta, and M. E. Welland, *Rev. Sci. Instrum.*, 66, **1995**, 2508.

289. A. J. Bard and L. R. Faulkner, *Electrochemical Methods*, Wiley: New York, 1980, p. 222.

290. F. C. Frank, *Disc. Faraday Soc.*, 48, **1949**, 67.

291. S. Kipp, R. Lacmann, and M. A. Schneeweiss, *Ultramicroscopy*, 57, **1995**, 333.

292. B. Van Der Hoek, L. A. M. J. Letten and W. J. P. Enckevort, *J. Cryst. Growth*, 62, **1983**, 603.

293. K. Tsukamoto, *J. Cryst. Growth*, 61, **1983**, 199.

294. A. J. Gratz, P. E. Hillner, and P. K. Hansma, *Geochim. Cosmochim. Acta*, 57, **1993**, 491.

295. S. D. Durbin, W. E. Carlson and M. T. Saros, *J. Phys. D: Appl. Phys.* 26, **1993**, B128.

296. A. J. Malkin, Yu. G. Kuznetsov, W. Glantz and A. McPherson, *J. Phys. Chem.*, 100, **1996**, 11736.

297. A. C. Hillier, PhD Thesis, University of Minnesota, 1995.

298. P. Bennema, *J. Cryst. Growth*, 69, **1984**, 182.

299. I. Sunagawa, and P. Bennema, *J. Cryst. Growth*, 53, **1981**, 490.

300. I. Sunagawa, *Am. Mineral.*, 47, **1962**, 1332.

301. P. Hartman and W. Perdok, *Acta Cryst.* 8, **1955**, 49, 521.

302. P. Bennema, *J. Phys. D: Appl. Phys.* 26, **1993**, B1.

303. P. Hartmann and P.Bennema, *J. Cryst. Growth.* 49, **1980**, 145.

304. Z. Berkovitch-Yellin, *J. Am. Chem. Soc.*, 107, **1985**, 8239.

305. Nanoscope® Command Reference Manual, Digital Instruments, Santa Barbara, 1992, pp. 1-22 - 1-27.

306. F. C. Frank, *Acta. Cryst.*, 4, **1951**, 497.

307. N. Cabrera, M. M. Levine and J. S. Plaskett, *Phys. Rev.*, 96, **1954**, 1153.

308. J. P. Hirth and D. J. Srolovitz, *Philos. Mag. A.*, 69, **1994**, 341.

309. G-Z. Liu, J. P. Van Der Eerden and P. Bennema, *J. Cryst. Growth*, 58, **1982**, 152.

310. W. Schaarwächter, *Phys. Status Solidi.*, 12, **1965**, 375.

311. H. B. Huntington, J. E. Dickey and R. Thomson, *Phys. Rev.*, 100, **1955**, 117.

312. A. Englert and H. Tompa, *J. Phys. Chem. Solids*, 24, **1963**, 1145.

313. N. Cabrera, *J. Chim. Phys.*, 53, **1956**, 675.

314. W. J. P. Van Enckevort and W. H. Van der Linden, *J. Cryst Growth*, 47, **1979**, 196.

315. A. E. Blum, R. A. Yund and A. C. Lasaga, *Geochim. Cosmochim. Acta*, 54, **1990**, 283.

316. U. Bertocci and D. R. Turner, in *Encyclopedia of Electrochemistry of the Elements*, vol. 2, pp 383-497, A. J. Bard (ed.), Marcel Dekker, New York, 1974.

317. J. W. Mathews and T. S. Plaskett, 13, **1978**, 2029.

318. T. Tutton, *Crystallography and Practical Crystal Measurements*, Macmillan, London, 1922, p. 84.

319. A. E. Nielsen and O. J. Söhnel, *J. Cryst. Growth*, 11, **1971**, 233.

320. W. H. Baur and J. L. Rolin, *Acta Cryst.*, B28, **1972**, 1448.

321. See for example, K. S. Scott, *Chemical Chaos*, Oxford University Press, Oxford, 1991, ch. 10.

322. M. Hackar, M. C. Demartinez, A. Rakotondrainibe, B. Beden and C. Lamy, *J. Electroanal. Chem.*, 302, **1991**, 173.

323. M. T. M. Koper, *Electrochim. Acta.*, 37, **1992**, 177.

324. J. L. Hudson and T. T. Tsotsis, *Chem. Eng. Sci.*, 98, **1994**, 7613.

325. F. Raspel and M. Eiswirth, *J. Phys. Chem.*, 98, **1994**, 7613.

326. J. Petitjean, S. Aeiyach, C. A. Ferreira, P. C. Lacaze and H. Takenouth, *J. Electrochem. Soc.*, 142, **1995**, 136.

327. K. Krischer, M. Lubke, W. Wolf, M. Eiswirth and G. Ertl, *Electrochim. Acta.*, 40, **1995**, 69.

328. F. Beck, J. Jiang and H. Krohn, *J. Electroanal. Chem.*, 389, **1995**, 161.

329. V. Lehmann, *J. Electrochem. Soc.*, 143, **1996**, 1313.

330. Y. Mukouyama, H. Hommura, T. Matsuda, S. Yae and Y. Nakato, *Chem. Lett.*, 6, **1996**, 463.

331. F. N. Albahadily and M. Schell, *J. Chem. Phys.*, 88, **1988**, 4312.

332. J. L. Hudson and M. R. Bassett, *Rev. Chem. Eng.*, 7, **1991**, 109.

333. D. Sazou, M. Pagitsas and C. Geogolitos, *Electrochim. Acta.*, 38, **1993**, 2321.

334. O. E. Barcia, O. R. Mattos, N. Pebere and B. Tribollet, *J. Electrochem. Soc.*, 140, **1993**, 2825.

335. R. P. Rastogi, I. Das, A. Pushkarna and S. Chand, *J. Phys. Chem.*, 97, **1993**, 4871.

336. E. Lojou, M. Devaud, M. Troupel and J. Perichon, *J. Electrochem. Soc.*, 140, **1993**, 2157.

337. F. Argoul and A. Kuhn, *J. Electroanal. Chem.*, 359, **1993**, 81.

338. C. P. Andrieux, P. Hapiot and J. M. Saveant, *Chem. Rev.*, 90, **1990**, 723 and references therein.

339. N. V. Rees, J. A. Alden, R. A. W. Dryfe, B. A. Coles and R. G. Compton, *J. Phys. Chem.*, 99, **1995**, 14813.

340. D. T. Chin and C. H. Tsang, *J. Electrochem. Soc.*, 125, **1978**, 1461.

341. H. Schlichting, *Boundary Layer Theory*, McGraw-Hill, New York, 1960, pp. 78-83

342. M. B. Glauert, *J. Fluid Mech.*, 1, **1956**, 6.

343. F. E. Powell and A. G. Fogg, *Analyst*, 113, **1988**, 483.

344. J. M. Esteban, G. S. Hickey and M. E. Orazam, *Corrosion*, 46, **1990**, 896.

345. Y. Yamauchi, H. Soyama, Y. Adachi, K. Sato, T. Shindo, R. Oba, R. Oshima and M. Yamabe, *JSME Int. J. Series B -Fluids and Therm. Eng.*, 38, **1995**, 31.

346. A. D. Wilson, D. M. Groffman, D. R. Powis and R. P. Scott, *Biomaterials*, 7, **1986**, 55.

347. U. Meyer, C. C. Brosnan, K. Bremhorst, R. Tomlins and A. Artens, *Wear*, 176, **1994**, 163.

348. C. B. Diem and M. E. Orazem, *Corrosion*, 50, **1994**, 290.

349. W. J. Albery and S. Bruckenstein, *J. Electroanal. Chem.*, 144, **1983**, 105.

350. H. Matsuda, *J. Electroanal. Chem.*, 16, **1968**, 153.

351. A. F. Kapauan, *Anal. Chem.*, 60, **1988**, 2161.

352. M. Kamiti and T. G. M. Vandeven, *Colloids and Surfaces A - Phys. Eng. Aspects*, 100, **1995**, 117.

353. F. Giralt and O. Trass, *Can. J. Chem. Eng.*, 53, **1975**, 505.

354. F. Giralt and O. Trass, *Can. J. Chem. Eng.*, 54, **1976**, 148.

355. D. A. Dawson and O. Trass, *Can. J. Chem. Eng.* ,44, **1966**, 121.

356. V. V. Rao and O. Trass, *Can. J. Chem. Eng.*, 42, **1964**, 95.

357. J. Kuta and E. Yeager, *J. Electroanal. Chem.*, 59, **1975**, 110.

358. K. B. Oldham, J. C. Myland, C. G. Zoski and A. M. Bond, *J. Electroanal. Chem*, 270, **1989**, 79.